MAGNETIC MANIFESTATIONS FROM THE APPLICATION OF PERTURBATIONS ON THE DYNAMIC SPIN ICE $Pr_2Sn_2O_7$

by

PAUL MAXIMO SARTE

A thesis submitted to the Faculty of Graduate Studies of the University of Manitoba in partial fulfilment of the requirements of the degree of

MASTERS OF SCIENCE

Department of Chemistry
University of Manitoba
Winnipeg, Manitoba, Canada

Copyright © Paul Maximo Sarte, August 2015

Abstract

Magnetic Manifestations from the Application of Perturbations on the Dynamic Spin Ice $Pr_2Sn_2O_7$

The purpose of this study was to investigate the effects of two perturbations, the application of an external magnetic field and *randomised* chemical pressure through Ti^{4+}/Sn^{4+} substitution, on the dynamic spin ice state in $Pr_2Sn_2O_7$. We show through magnetometry, heat capacity and powder neutron diffraction that the dynamic spin ice state in $Pr_2Sn_2O_7$ is extremely fragile, requiring an external field of approximately 0.5 T to induce a transition into a long range ordered antiferromagnetic state, in accordance with the recorded behaviour of other spin ice materials. Similarly, the dynamic spin ice state in $Pr_2Sn_2O_7$ only required a doping percentage of less than 2.5 % to induce a transition away from the spin ice state. But instead of the predicted spin glass state, $Pr_2Sn_2O_7$ assumes a cluster-type magnetic structure with extremely weak intercluster antiferromagnetic interactions, a magnetic structure that persists even to the highest doping level of 30 %. The results of this thesis reveals that careful attention must be taken when selecting and placing the tetravalent cation in the 16*c* Wyckoff site in the pyrochlore structure, if one desires to have a spin ice state.

List of Figures

List of Tables

Acknowledgements & Dedication

First and foremost, I would like to convey my sincerest thanks to my supervisor, Professor Chris Wiebe. His constant and ardent support, concerning both my professional and personal lives, has proven invaluable for all my success throughout the last five years. Chris' immense amount of knowledge, unrelenting enthusiasm, innovative ideas and absolute dedication to my and all his students' successes is truly inspiring and for this inspiration, I cannot thank him enough. Ultimately, I must thank Chris for being a good friend, who helped me accomplish my dreams, no matter how impossible they must have seemed.

Throughout my last five years, I have been extremely fortunate to have an incredible supporting cast. These countless individuals have supported me through the good and through the bad, through the occasional crisis and everything in between. I would like to thank (past and present) members of the Quantum Materials Group at the University of Winnipeg: Harlyn Silverstein, Arzoo Sharma, Cole Mauws, Alannah Hallas, Micaela Zelensky, Brenden van Wyk, Kanisha Cruz-Kan, Alison Smith and Avi Stoller. I have to thank my very good friend and closest lab mate Arzoo Sharma. You were always willing to assist with measurements, listen to my troubles and help me during my struggles. For this immense support, I cannot thank you enough. I would also like to convey my sincerest gratitude to Joey Lussier and Professor Mario Bieringer for all their support concerning both compound synthesis and Rietveld refinements. Finally, I would like to thank Elizabeth Skoropata, Ryan Desautels, Mueed Mirza and their supervisor Professor Johan van Lierop for their immense contribution to the magnetometry measurements contained in this thesis. In particular, I would like to convey my sincere gratitude to Professor van Lierop for dedicating so much of his time teaching me how to ask the right questions.

Last but not least, behind every scientist, there is a loving support network that is rarely acknowledged but is absolutely critical to one's success. I would like to convey my sincerest thanks to my two families on both sides of the Atlantic. To my mother, Annabelle, thank you for providing me constant encouragement and support during these difficult times. To Ute Singh Kang and Shaminder Singh Kang, thank you for always being there for me and providing unconditional support during the most challenging chapter of my life.

Whenever I was tempted to give up, whenever I was tempted to accept failure and whenever I lost hope, your love and unconditional support provided me the strength to carry on. For staying by my side during both the good and the bad, for inspiring me whenever all hope seemed to be lost and for teaching me the power of true love, I dedicate to you, my dearest Tina, this thesis.

Declaration of Co-Authorship

I hereby declare that this thesis incorporates material that is result of joint research, as follows:

1. Elastic neutron scattering experiments on $Pr_2Sn_2O_7$ in field on the DCS at the NCNR that are the subject of Chapter 3 were performed with the assistance of Professor H.D. Zhou and Dr. Y. Qiu (NCNR).

2. DC and AC magnetometry measurements for the $Pr_2Sn_{2-x}Ti_xO_7$ series that are the subject of Chapter 4 were performed with a Quantum Design MPMS provided by Professor Johan van Lierop and under the supervision of Professor J. van Lierop, E. Skoropata, R. D. Desautels and M. Mirza at the University of Manitoba in the Department of Physics and Astronomy.

3. Elastic neutron scattering experiments on $Pr_2Sn_2O_7$ and $Pr_2Sn_{1.7}Ti_{0.3}O_7$ on C2 at the CNBC, Chalk River Laboratories that are the subject of Chapter 4 were performed with the assistance of H.J. Silverstein and Dr. R. Donaberger (NRC).

4. Synthesis of select members of the $Pr_2Sn_{2-x}Ti_xO_7$ pyrochlore series that are subject of Chapter 4 were performed with furnaces provided by Professor Mario Bieringer and J.A. Lussier at the University of Manitoba in the Department of Chemistry.

5. All structural refinements from pXRD used LaB_6(SRM 660) and Si powder 200 mesh (lot GD1) that were provided by Professor Mario Bieringer at the University of Manitoba - Department of Chemistry.

All other material, data and analysis constituting this thesis are solely my own work under the supervision of Professor C.R. Wiebe.

Contents

Chapter 1

Introduction

This chapter begins with a brief summary of relevant results concerning solid state magnetism from quantum mechanics. In particular, the concept of interactions between individual magnetic moments in a multi-body problem is addressed. Using these preliminary results concerning interacting magnetic moments, the reader will be introduced to a situation when there is a conflict of symmetry between these interactions and the spatial geometry imposed by the lattice, a conflict of symmetry and interactions known as *geometric frustration*. This intrinsic conflict of symmetry has been at the forefront of solid state chemistry for the past two decades, attributed to both (i) the sheer number and diversity of magnetic systems exhibiting such a conflict provided by the solid state chemistry community and (ii) the exotic and in many cases, *novel* magnetic ground states that result from such conflict of symmetry. One such system, the magnetic pyrochlore oxides, has particularly captured the attention of the condensed matter community attributed to its high propensity to geometric frustration, the diversity of elements that can be incorprated into its structure and the plethora of magnetic ground states observed. One such ground state, the spin ice state, a direct magnetic analog of the proton disorder in crystalline ice, represents the main focus of this thesis and will be the final topic of discussion for this introductory chapter. It should be noted that the results from quantum mechanics will be simply stated with no rigorous mathematical proof. Although beyond the scope of this introductory chapter, the reader is suggested to refer to Auerbach's *Interacting Electrons and Quantum Magnetism* [1] and White's *Quantum Theory of Magnetism* [2] if a more rigorous treatment is desired.

1.1 Localised Magnetic Systems

1.1.1 Diamagnetism

Diamagnetism is a form of magnetism that is exhibited by all substances [1–3]. Diamagnetism for an isolated atom is commonly described by the classical Langevin theory of diamagnetism [2]. The discussion of diamagnetism will be limited to the classical theory proposed by Langevin to describe closed shell atoms. Other types of diamagnetism including the quantum Landau and Pauli theory of diamagnetism are not included in the present discussion since both these theories involve non-localised magnetism. Langevin's theory of diamagnetism essentially treats the atom as a source of *induced* current I in response to the application of an external magnetic field $\mathbf{B}$. By Lenz's law,

$$\epsilon = -\frac{\partial \Phi}{\partial t}, \tag{1.1}$$

where ϵ and Φ are the electromotive force and the magnetic flux, respectively, the electromotive force will generate an electric current that will create itself create a magnetic field to oppose the changes in magnetic flux [2]. Consequently, by applying an external magnetic field $\mathbf{B}$, it may be shown that an electron will precess about the magnetic field with the Larmor frequency, ω_L, defined as

$$\omega_L = \frac{e|\mathbf{B}|}{2m}, \tag{1.2}$$

where e, $|\mathbf{B}|$ and m are the elementary charge, magnitude of the applied external magnetic field and mass, usually that of the electron, respectively. The form of the Larmor frequency is further discussed in the context of localised paramagnetism in the subsequent subsection. Since the number of revolutions per second, f, is defined as

$$f = \frac{\omega_L}{2\pi}, \tag{1.3}$$

then for an atom with Z number of electrons, the effective electric current, I, is given by

$$I = -\frac{Ze^2|\mathbf{B}|}{4\pi m}, \tag{1.4}$$

where the negative sign is a consequence of Lenz's law. By the definition of the magnetic moment $\boldsymbol{\mu}$, its magnitude is defined as

$$|\boldsymbol{\mu}| = I \cdot A, \tag{1.5}$$

where A is the area of the current loop. Assuming that the applied external magnetic field is directed parallel to the z-axis, the average area of the current loop (in cylindrical polar coordinates) will be $\pi\langle\rho^2\rangle$, where $\langle\rho^2\rangle$ is the average square distance of the electrons from the z-axis. Substituting equation 1.4 into equation 1.5 and redefining A, one obtains

$$|\boldsymbol{\mu}| = -\frac{-Ze^2|\mathbf{B}|\langle\rho^2\rangle}{4m}, \tag{1.6}$$

and since all four non-constants are strictly positive, the negative sign in front of equation 1.6 implies that the induced current and thus the induced magnetic moment and its associated magnetic field is antiparallel to the direction of the externally applied magnetic field. It is this antiparallel alignment, manifesting itself as a repuslive force away from the externally applied magnetic field, that defines diamagnetism [1].

Although diamagnetism is exhibited by all substances, its contribution to a material's net response to the application of an external applied magnetic field may in fact become negligible if other forms of magnetism are exhibited. Other forms of magnetism include paramagnetism — the second type of magnetism for an atom — which will be discussed in the next subsection and ferromagnetism, which will be discussed in section 1.2.

1.1.2 Paramagnetism

Unlike diamagnetism as discussed in subsection 1.1.1, certain materials exhibit a form of magnetism called paramagnetism. These paramagnetic materials are attracted by an externally applied magnetic field and the internal induced magnetic field is parallel to the direction of the externally applied magnetic field [3]. For a localised magnetic system (i.e. an atom), paramagnetism is reliant on the formation of a non-zero net magnetic moment, denoted as $\boldsymbol{\mu}$, whose magnitude was defined previously in equation 1.5. The magnetic moment $\boldsymbol{\mu}$ is the quantity that determines the torque $\boldsymbol{\tau}$ that the magnet will experience in an external applied magnetic field $\mathbf{B}$ [4]. If the net magnetic moment of the atom is in fact zero, then system would exhibit exclusively local diamagnetism. Using classical electromagnetic theory, in particular Maxwell's fourth equation (i.e. Ampère's law), electric charges in motion produce a magnetic field and thus possess a magnetic moment μ [5]. In an atom — using the analogy to classical electromagnetism — the electric charges of interest are electrons with charge q = -e (where e is the elementary charge of 1.602 x 10^{19} C), whose motions around the nucleus are described by their

angular momentum **L**. It can be shown [6] that the magnetic moment of such an electron due to its motion around the nucleus, described by **L**, assumes the value of

$$\boldsymbol{\mu_L} = \frac{-e}{2m_e}\mathbf{L}, \tag{1.7}$$

where m_e is the mass of the electron (9.11 x 10^{-31} kg). Since torque experienced by a magnetic moment $\boldsymbol{\mu}$ is given by

$$\boldsymbol{\tau} = \boldsymbol{\mu} \times \mathbf{B} = |\boldsymbol{\mu}||\mathbf{B}| \sin\theta, \tag{1.8}$$

where the second equality is given by the definition of the cross product. From the definition of torque, in terms of angular momentum **L** is given by

$$|\boldsymbol{\tau}| = \frac{\Delta \mathbf{L}}{\Delta t} = \frac{|\mathbf{L}| \sin\theta \Delta\phi}{\Delta t}, \tag{1.9}$$

where $\Delta\phi$ is the change of azimuthal angle in cylindrical polar coordinates, then if one combines equations 1.7 and 1.8,

$$|\boldsymbol{\tau}| = \frac{e}{2m_e}|\mathbf{L}||\mathbf{B}| \sin\theta, \tag{1.10}$$

and consequently, by comparing equation 1.10 to the second equality in equation 1.9, one can observe that

$$\frac{\Delta\phi}{\Delta t} = \frac{e|\mathbf{B}|}{2m}, \tag{1.11}$$

and this quantity is by definition the Larmor frequency ω_L, a quantity previously discussed in the context of classical Langevin diamagnetism. The Larmor frequency is a direct consequence of the orbiting electron possessing a magnetic moment $\boldsymbol{\mu}$. It should be noted that the theory of diamagnetism previously developed considers the atom a *reactionary* system with an *induced* current created to counteract the change in magnetic flux. Instead, the following discussion of paramagnetism considers the atom as a system that possesses a magnetic moment $\boldsymbol{\mu}$ due to the combination of orbital and instrinsic spin angular momentum of the unpaired electrons, and the magnetism derived from these angular momenta is present even without an externally applied magnetic field.

Although the following discussion of the magnetic moment is in the context of paramagnetism (i.e. assuming there exists some unpaired electrons in the atom), the conclusions derived are still valid even if there are no unpaired electrons, the expressions

simply reduce to trivial solutions. Since the orbital angular momentum is quantised *via* the Heisenberg Uncertainty Principle [7], the value of **L** assumes the values of

$$|\mathbf{L}| = \sqrt{l(l+1)}\hbar, \tag{1.12}$$

where l is the angular quantum number which assumes values of $l = 0 \ldots n$-1 in integer steps, where n is the principal quantum number and $\hbar$ is the reduced Planck's constant defined as

$$\hbar = \frac{h}{2\pi}, \tag{1.13}$$

where h is Planck's constant (6.626 x 10^{-34} J $\cdot$ s) [6]. Combining equations 1.7 and 1.12, the magnitude of the magnetic moment μ for an orbiting electron is given by

$$|\boldsymbol{\mu_L}| = \frac{e\hbar}{2m_e}\sqrt{l(l+1)} = \sqrt{l(l+1)}\mu_B, \tag{1.14}$$

where μ_B is defined as the Bohr magneton and is equal to 9.27 x 10^{-27} J T^{-1} [8]. It should be noted that from the Heisenberg Uncertainty Principle, the z-component of the angular momentum, denoted as L_z, is also quantised and assumes values of

$$|\boldsymbol{L_z}| = m_l\hbar, \tag{1.15}$$

where m_l is the magnetic quantum number which assumes values of -l $\ldots$ l in integer steps. Using the same logic from equations 1.12-1.14, the z-component of the magnitude of the magnetic moment from the circulating electron is given by

$$|\boldsymbol{\mu_{l,z}}| = m_l\mu_B \tag{1.16}$$

In 1922, two German physicists Otto Stern and Walther Gerlach [9] discovered a second (intrinsic) source of angular momentum for the electron, called spin and is denoted as **S**. This source of angular momentum is intrinsic to the electron and other quantum particles and is ultimately needed to describe the fine structure observed *via* spin-orbit coupling [7]. It can be shown [6] that a quantum particle of charge q, mass m with spin **S** has a corresponding magnetic moment attributed to its spin, $\boldsymbol{\mu_S}$, which assumes the value

$$\boldsymbol{\mu_S} = g\frac{q}{2m}\boldsymbol{S}, \tag{1.17}$$

where g is called the g-factor, more specifically for equation 1.17, the spin g-factor. The g-factor is a first order perturbation term that relates the value of the magnetic moment $\boldsymbol{\mu}$ and its corresponding generating angular momentum (e.g. $\boldsymbol{S}$) [7]. For the case of an electron, equation 1.17 can be rewritten as

$$\boldsymbol{\mu_S} = g_e\frac{-e}{2m_e}\boldsymbol{S}, \tag{1.18}$$

where g_e is called the electron spin g-factor or simply the electron g-factor and is equal to approximately 2 [2]. In an analogous fashion to $\mathbf{L}$ in equation 1.12, the magnitude of $\mathbf{S}$ is given by

$$|\boldsymbol{S}| = \sqrt{s(s+1)}\hbar, \tag{1.19}$$

where s, the spin quantum number is $\frac{1}{2}$ for an electron as deduced from the fine structure (i.e. the splitting of spectral lines into **2** sets), corresponding to a value of $\frac{\sqrt{3}}{2}\hbar$ for $|\boldsymbol{S}|$. Continuing the analogy to the orbital angular momentum, the z-component — analogous to equation 1.15 — of the spin angular momentum is given by

$$\boldsymbol{S_z} = m_s\hbar, \tag{1.20}$$

where m_s assumes values of -s ... s in integer steps and thus for an electron, the possible values of $\boldsymbol{S_z} = \pm\frac{1}{2}$, commonly denoted as spin up (+) and down (-) [6]. The analogy between the orbital angular momentum and the intrinsic spin angular momentum ends at the resulting magnetic moment $\boldsymbol{\mu}$, more specifically its z-component $\boldsymbol{\mu_z}$. From equation 1.16, one would expect — with equation 1.20 — the z-component of the magnetic moment to be $\pm\frac{1}{2}\mu_B$ but instead the measured magnetic moment $\boldsymbol{\mu_z}$ leading to the fine structure was actually off by approximately a factor of 2 [2], leading to the necessity to include the electron g-factor in equation 1.17 and its corresponding $\boldsymbol{\mu_z}$ as

$$|\boldsymbol{\mu_{s,z}}| = gm_s\mu_B, \tag{1.21}$$

where $g = g_e \approx 2$ and $\mathrm{m}_s = \pm\frac{1}{2}$ for the electron.

Instead of considering the individual angular momentum contributions (i.e. orbital and spin), a total angular momentum $\hat{\boldsymbol{J}}$ operator is defined as

$$\hat{\boldsymbol{J}} = \hat{\boldsymbol{L}} + \hat{\boldsymbol{S}}, \tag{1.22}$$

where $\hat{\boldsymbol{L}}$ and $\hat{\boldsymbol{S}}$ are the orbital and spin angular momentum operators, respectively. The norm of the total angular momentum is given by

$$|\boldsymbol{J}| = \sqrt{j(j+1)}\hbar, \tag{1.23}$$

where j is the total angular momentum quantum number and assumes values of $|l-s| \leq j \leq l+s$, in integer steps and where l and s are the orbital and spin angular momentum quantum numbers. Hund's rules [2, 6, 7] are then required to determine the value of j for the ground state. The z-component of the angular momentum is given by

$$J_z = m_j\hbar, \tag{1.24}$$

where m_j assumes values of -j ... j in integer steps. Consequently, in the absence of any mechanism to remove the degeneracy, the ground state will consist of a $2j+1$ multiplet (i.e. the m_j values) for the corresponding j value as determined by Hund's rules. In an analogous manner to equations 1.17 and 1.21, the magnitude of the magetic moment of the atom and the magnitude of the moment along the z-axis are

$$|\boldsymbol{\mu_j}| = g_j\sqrt{j(j+1)}\mu_B, \tag{1.25}$$

$$|\boldsymbol{\mu_{j,z}}| = g_j m_j \mu_B, \tag{1.26}$$

respectively and where g_j is called the Landé g-factor defined as [3, 6]

$$g_j = g_l\frac{j(j+1)-s(s+1)+l(l+1)}{2j(j+1)} + g_s\frac{j(j+1)+s(s+1)-l(l+1)}{2j(j+1)}, \tag{1.27}$$

where g_l and g_s are the orbital and spin g-factors. For the rest of this thesis, the value of g_l and g_s are assumed to be 1 (previously used to derive the Larmor frequency) and 2, respectively, corresponding to an orbiting electron [7]. It should be noted that in general, it is indeed the case that the magnetic moment arises from both orbital and spin angular momentum. Unfortunately, it is common in literature that magnetic moments are usually referred to in terms of the spin operator **S**. The reason for using **S** are two-fold. Firstly, magnetic materials whose magnetism is derived from transition metals have magnetic electrons located in extended d-orbitals. Due to the local crystal

field — the main topic of discussion in subsection 1.1.3 — the orbital contributions (i.e. **L**) to the magnetic momentum are quenched, meaning that the orbital contribution is rendered insignificant [3]. Consequently, the magnetism of these transition metals may be successfully described by solely the spin **S**. Quenching does not occur with the rare earth systems [10] for example, whose electrons are located very close to the nucleus and far away from the effects of the electric crystal field. Consequently, **J** and not **S** must be used, when referring to magnetic moments. As aforementioned, the operator **J** is not used — and the reader is warned about this confusing nomenclature that will appear in the next section — because another important quantity in describing magnetism in solids, called the magnetic exchange is also assigned the symbol J. The repetition of J may potentially provide some confusion and thus it is convention to refer to spins **S** and not **J**, despite the latter being ultimately more correct.

As a final note, the nucleus — in a similar manner to the electron — itself has an intrinsic spin **S** which does create a corresponding nuclear magnetic moment [3]. From equations 1.7 and 1.17, one can see that the magnetic moment corresponding to a particular value of angular momentum (orbital or intrinsic) is inversely proportional to the mass of the charged object. Since the mass of an individual nucleon is approximately three orders of magnitude larger than the electron, the magnetism dervied from the nucleus is usually (but not always) disregarded in the study of electronic magnetism in solids [2, 7].

1.1.3 Crystal Field and Crystal Field Effects

As alluded to in the conclusion of section 1.1.2, spin-orbit coupling is non-negligible for the heavy rare-earth cations, these cations will form the origin of the magnetism probed in this thesis. The appreciable interaction between the spin and orbital angular momenta of such heavy cations may be understood using a relativistic argument. Although **L** in the standard reference frame of the atom (i.e. that of the observer) naturally describes the motion of an electron orbiting the positively charged nucleus. Instead, if one refers to the reference frame of the electron, **L** can also be interpreted as describing the motion of a positively charged nucleus orbiting the electron. A natural extension of this change of reference frame is that the magnetic field created by an orbiting positively charge nucleus will interact with the electronic spins *via* the usual Zeeman interaction. Since the spin-orbit coupling term $\mathbf{L} \cdot \mathbf{S}$ does not commute with the individual operators **L** or **S** separately, the total angular momentum $\mathbf{J} = \mathbf{L} + \mathbf{S}$ is a good quantum number that must be used when investigating systems whose magnetism is derived from rare earth cations. A corollary of **J** being a good quantum number for describing rare earth cations is that the angular momentum and consequently, the magnetism will assume the

spatial dependence of the orbital degrees of freedom associated with **L**. In other words, the **J** eigenstates will possess anisotropy (directional dependence) for any cations that have $\mathbf{L} > 0$.

Since **J** is a good quantum number, for an isolated rare earth cation, the J_z eigenstates will exhibit a $(2J + 1)$ degeneracy and the (isolated) electronic ground state can be subsequently determined *via* Hund's rules. As the rare earth cation is placed in a lattice, the $(2J + 1)$ degeneracy is lifted *via* the Stark effect by the local crystalline environment's electric field — termed the crystal field (often denoted as CF) — yielding crystal field levels. The splitting of the $(2J + 1)$ degeneracy into the crystal field levels is ultimately what determines the low temperature ground state magnetic properties of the rare earth cations in the crystalline environment. The manner by which the degeneracy is lifted is described by the crystal field Hamiltonian — often denoted as the CEF Hamiltonian — and the ground state wavefunction of this CEF Hamiltonian will determine both the magnitude of the magnetic moment and its anisotropy, both characterised by the g-tensor which is quite similar to the g-factor (equation 1.27) but incorporates anisotropy as well.

Recall that the splitting of the $(2J + 1)$ J_z multiplet into crystal field levels is ultimately what allows the system to select a ground state with particular magnetic properties and this ground state will usually be unique. However, it should be noted that if the system possesses $(2n + 1)$ f electrons (where $n \in \mathbb{N}^0$), then by time reversal symmetry, the ground state is at least two-fold degenerate, a conclusion summarised by Kramers' theorem. Consequently, by reversing the value of the angular momentum, the system cannot achieve a lower energy state, hence the ground state consists of (at least) a doublet. This ground state doublet for a $(2n + 1)$ f electrons (where $n \in \mathbb{N}^0$) system (e.g. Sm^{3+}, $4f^5$) is called a Kramers' doublet while if there exists a ground state doublet for a system with $2n$ (where $n \in \mathbb{N}_{>0}$) f electrons (e.g. Pr^{3+}, $4f^2$), the ground state doublet is called a non-Kramers' doublet. In fact, in some cases, the energy splitting (Δ) between the ground state crystal field level(s) and the next excited crystal level(s) is very large ($\Delta \sim 10^2$ K) compared to the relevant energy scales (i.e. the interactions that lead to magnetism that will be the topic of discussion in the next section) and thus the ground state crystal field levels of such systems under investigation can be thought of as isolated and the only contributors to the magnetic properties of such systems.

It is important to note that the g-tensor will assume the point symmetry of the crystallographic site of interest. For example, the rare earth cation in a pyrochlore lattice — the main topic of discussion in subsection 1.3.2 — is placed in a crystallographic site with trigonal symmetry (D_{3d}). The trigonal symmetry implies that the g-tensor has two components: one parallel to the local trigonal axis (i.e. the $\langle 111 \rangle$ direction) and one

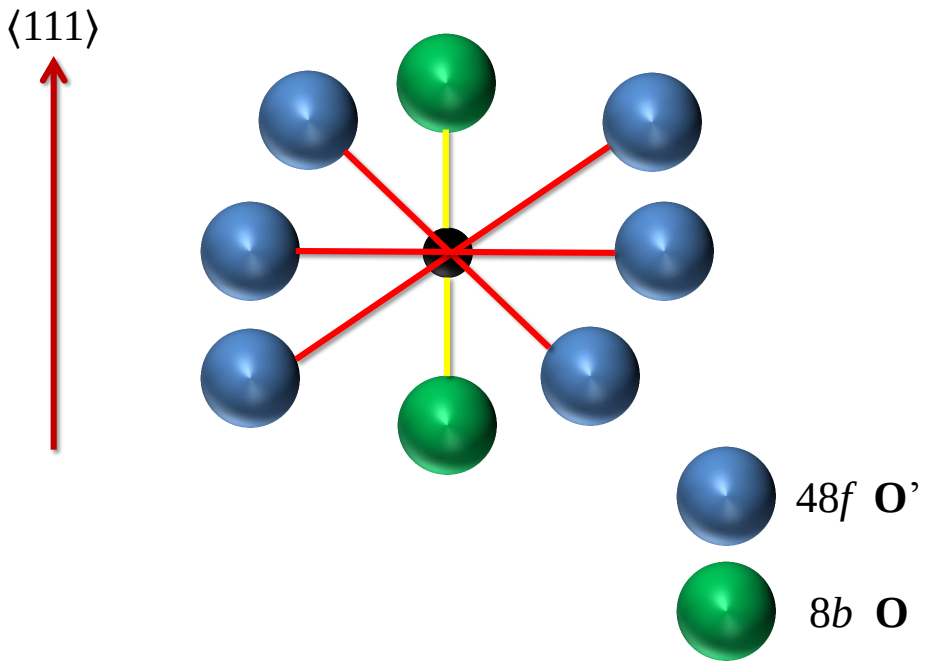

FIGURE 1.1: Pictorial representation of the coordination geometry of the 16*d* rare earth cation site in the cubic Fd$\bar{3}$m pyrochlore structure. The rare earth cation (black sphere) is coordinated with two 8*b* oxygen atoms (olive green spheres), forming a linear stick that is oriented normal to the average plane of the puckered six-membered ring formed from the rare earth cation and six 48*f* oxygen atoms (blue spheres). The average distance between the rare earth cation and 8*b* oxygen atoms (yellow bond) is the shortest distance observed between rare earths and oxygen anions, providing a pronounced axial symmetry along the local ⟨111⟩ direction. Adapted from Gardner *et al.* [11]

component in the plane orthogonal to the trigonal axis. The trigonal symmetry of the CF surrounding the rare earth's crystallographic site is pictorially shown in figure 1.1. The rare earth cation is surrounded by a puckered six-membered ring of oxygen atoms (denoted as O) with a bond distance of $\approx$ 2.4 to 2.5 Å while there are two additional oxygen atoms (denoted as O') that form a linear O'-rare earth-O' stick oriented normal to the puckered six-membered A-O ring. The distance between the rare earth and the O' axial oxygen atoms is exceptionally short with a bond distance of $\approx$ 2.2 Å which results in a pronounced axial symmetry along the local ⟨111⟩ direction. It is this pronounced axial symmetry that will determine much of the physics of the compounds probed in this thesis.

1.2 Interacting Magnetic Systems

Although the treatment of an individual isolated atomic system allows one to determine the magnitude of the magnetic moment and its orientation relative to a quantisation axis of one atom, the individual atomic treatment cannot account for the magnetic properties of a macroscopic ensemble of atoms constituting solids [12, 13]. In particular, the atomic magnetic moment alone cannot account for any magnetic ground state with any type of spatial coherence between magnetic moments. Simply put, the magnetism analysed by only considering a group of isolated atoms cannot explain why ordered magnetic states exist. Magnetic moments from isolated atoms would theoretically be allowed to orient themselves randomnly in space (within the symmetry restrictions imposed by the surrounding crystal field), possessing no spatial coherence and thus the average magnetisation, defined as the average magnetic moment per unit volume, would be zero in the absence of an applied magnetic field [3]. This state, called the paramagnetic state, is seen in all materials with unpaired electrons at a large enough temperature [13, 14]. Contrast this paramagnetic behaviour to diamagnetism — which is exhibited to a certain degree in all materials — which is a consequence of Lenz's law and is characterised by a negative magnetisation [1]. On the contrary, upon cooling, many materials' individual magnetic moments assume an ordered configuration, whereby individual magnetic moments are no longer oriented randomnly but assume an orientation that is consistent with either a global or local pattern defining their magnetic ground state. These ordered magnetic ground states are only possible if one considers that magnetic moments from individual atoms are not isolated but rather interact with one another with the type and strength of interactions between individual moments ultimately determining the magnetic ground state of the collective ensemble of atoms [15]. This treatment of interacting moments constitutes the basis of the modern theory of solid state magnetism [13, 14]. The types of interactions, although numerous, may be summarised concisely by the following [3, 15]:

- **Dipolar interactions**: From both classical electromagnetism and its subsequent quantum treatment, the (unpaired) electrons circulating in orbits as discussed in section 1.1.2, effectively form magnetic dipoles. Each magnetic dipole creates its own magnetic field — that one can calculate using the Biot-Savart law [12] — that interacts with the other magnetic dipoles. The dipole-dipole interaction is mathematically described by [3]

$$U = \frac{\mu_o}{4\pi r_{ij}^3} \left(\boldsymbol{\mu_i} \cdot \boldsymbol{\mu_j} - 3(\boldsymbol{\mu_i} \cdot \hat{\boldsymbol{r}}_{\boldsymbol{ij}})(\boldsymbol{\mu_j} \cdot \hat{\boldsymbol{r}}_{\boldsymbol{ij}}) \right), \tag{1.28}$$

  where $\boldsymbol{\mu_i}$, $\boldsymbol{\mu_j}$ are interacting magnetic dipole vectors, $\hat{\boldsymbol{r}}_{\boldsymbol{ij}}$ is the unit vector along the line joining the centres of the magnetic dipoles $\boldsymbol{\mu_i}$ and $\boldsymbol{\mu_j}$. The dipole-dipole

interaction is long ranged, attributed to its $\frac{1}{r_{ij}^3}$ dependence but is also quite weak, with an energy scale of approximately 1 K [3, 12].

- **Exchange interactions**: Equation 1.28 is seen as a classical explanation or interaction for magnetism and its characteristic energy scale is inadequate to explain the presence of magnetically ordered phases at much higher temperatures such as that seen for iron in lodestone at approximately 1000 K [16]. In fact, as alluded to in section 1.1.2, magnetism in solids can only be exclusively accounted for by quantum mechanics, a fact that is effectively summarised by the Bohr-van Leeuwen theorem [17]. Magnetism is now understood to be derived from the interaction between electronic orbitals [18]. This interaction between electronic orbitals, known as the exchange interaction, manifests itself in a variety of forms, depending on the detail concerning how the electronic orbitals interact between one another. Three types of exchange interactions exists but only one type, superexchange — which occurs as a result of an indirect overlap between two electronic orbitals from identical atoms through an intermediate orbital of a non-magnetic ion that mediates the exchange interaction — will be of relevance for work performed in this thesis.

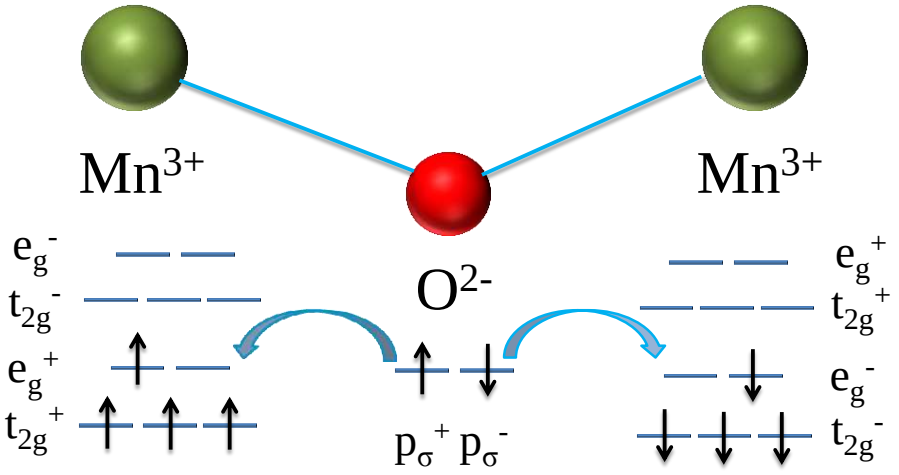

FIGURE 1.2: Schematic representation of the superexchange mechanism between two identical Mn^{3+} cations with a 180° placed in an octahedral crystal field through an intermediate diamagnetic O^{2-} anion. This particular superexchange interaction between e_g orbitals of Mn^{3+} and the p_σ orbital of O^{2-} results in antiferromagnetic coupling in accordance to the Goodenough-Kanamori rules. *Adapted from Mario Bieringer* [19].

Superexchange is usually mediated by the diamagnetic oxygen anion O^{2-} [3, 12, 18] as shown in figure 1.2 and is usually the dominant magnetic interaction for magnetic insulators whose orbitals are highly localised. This localisation of electronic orbitals is quite common in systems containing magnetic transition metal

components, whose localised d-orbitals prevent direct exchange, instead use the p-orbital of an intermediate O^{2-} to facilitate exchange. Furthermore, it should be noted that this localisation is even more prevalent with the lanthanides [12], whose f-orbitals lie deep inside the ions with the $5s$ and $5p$ orbitals being the most outershell atomic shells; thus, superexchange and not other forms of exchange is the dominant type of exchange interaction for these rare earth systems that will be the main focus for this thesis.

All types of exchange interactions are often mathematically expressed as [18, 20]

$$H = -J \sum_{ij} \boldsymbol{S_i} \cdot \boldsymbol{S_j}, \tag{1.29}$$

where $\boldsymbol{S_i}$ and $\boldsymbol{S_j}$ are the values for the individual spins, the sum is taken over all i,j pairs and J is the exchange integral [14], defined as

$$J = \frac{e^2}{8\pi\epsilon_o} \int \psi_A^*(\boldsymbol{r_i})\psi_B^*(\boldsymbol{r_j}) \left(\frac{1}{r_{A,B}} + \frac{1}{r_{i,j}} - \frac{1}{r_{A,j}} - \frac{1}{r_{B,i}} \right) \psi_A(\boldsymbol{r_j})\psi_B(\boldsymbol{r_i}) d\boldsymbol{r_i}\boldsymbol{r_j}, \tag{1.30}$$

where e, ϵ_o, A, B, i and j are the elementary charge, permittivity of free space, atom label A, atom label B and electron label i and electron label j, respectively. From equation 1.29, the value of $J > 0$ imples the exchange interaction prefers a ferromagnetic interaction between spins while a value of $J < 0$ prefers a dominant antiferromagnetic interaction between the individual spins [21, 22]. The exchange interaction is purely quantum mechanical and is a consequence of the statistics that governs identical fermions [18]. Once wavefunctions ψ from neighbouring magnetic ions overlap spatially, there is a probability that electrons within these orbitals are *exchanged*. Systems consisting of fermions are defined as having their wavefunction being antisymmetric with respect to exchange [6]. Consequently, the requirement that the wavefunction describing a two fermion system must be antisymmetric imposes restrictions on the relative orientation of the neighbouring spins in these overlapping orbitals [6, 13]. Prediction of such restrictions (i.e. the relative orientation of the neighbouring spins) are complex, with its complexity derived from the fact that one must consider both the spatial and spin components of the wavefunction in the context of the antisymmetric requirement. For example, a set of empirical rules known as the Goodenough-Kanamori rules [23] that allows one to predict the type of interaction that would result from the superexchange interaction has had only limited success to transition metal oxide systems with a specific subset of bonding angles [14].

Consequently, a simple Hamiltonian that incorporates all relevant interactions between **only** nearest neighbours (n.n.) can be stated as the following

$$H = -J\sum_{i,j} \boldsymbol{S_i}\cdot\boldsymbol{S_j} + \frac{\mu_o}{4\pi r_{i,j}^3}\sum_{i,j}\left(\boldsymbol{m_i}\cdot\boldsymbol{m_j} - 3(\boldsymbol{m_i}\cdot\hat{\boldsymbol{r}}_{\boldsymbol{ij}})(\boldsymbol{m_j}\cdot\hat{\boldsymbol{r}}_{\boldsymbol{ij}})\right), \tag{1.31}$$

where J is the exchange integral between spins $\boldsymbol{S_i}$ and $\boldsymbol{S_j}$, μ_o is the permeability of free space and $r_{i,j}$ is the distance between moments $\boldsymbol{m_i}$ and $\boldsymbol{m_j}$. It should be noted that in literature, most Hamiltonians concerning magnetic interactions refer exclusively to spins [20, 24] and not the moments they create, thus the second term in equation 1.31 (i.e. the dipolar term and equation 1.28) can be rewritten in terms of spins $\boldsymbol{S_i}$ and $\boldsymbol{S_j}$ as

$$H = -J\sum_{i,j} \boldsymbol{S_i}\cdot\boldsymbol{S_j} + \frac{g^2\mu_B^2}{r_{i,j}^3}\sum_{i,j}\left(\boldsymbol{S_i}\cdot\boldsymbol{S_j} - 3(\boldsymbol{S_i}\cdot\hat{\boldsymbol{r}}_{\boldsymbol{ij}})(\boldsymbol{S_j}\cdot\hat{\boldsymbol{r}}_{\boldsymbol{ij}})\right), \tag{1.32}$$

where g is the Landé g-factor defined in equation 1.27. A common addition to equation 1.32 is the Zeeman splitting term [6, 12, 13] that incorporates the influence of the application of a magnetic field, effectively summarising how the ground state J multiplet will be split. This term was not included here because it is not *exclusively* an interaction term between individual spins.

Although equation 1.32 is a first approximation with only nearest neighbour interactions being considered, the Hamiltonian does provide some insight concerning how a magnetic system selects its magnetic ground state. From statistical thermodynamics, the free energy of the system (at a particular temperature T) is defined as [3]

$$F = U - TS, \tag{1.33}$$

where F is the free energy, U is the internal energy defined as a probability-weighted average of all eigenvalues from the Hamiltonian in equation 1.32 and S is the entropy of the microcanonical ensemble of particles since it is assumed (for this discussion) that the system is isolated. An implication from equation 1.33 is that there are two temperatures, or equivalently, energy scales to be considered. When the temperature is large, compared to energy scale of the interactions, the second term (i.e. the entropy) of the free energy equation will dominate and the magnetic system will be in its paramagnetic state where the spins are fluctuating randomly and the arrangement of spins (or moments) is disordered. Once the temperature is lowered such that the energy scale of the spin-spin interactions are comparable to the energy scale of the ambient temperature (i.e. k_BT), the system should attempt to form a magnetic state that attempts to lower the internal energy U so that F is minimised. It is this attempt to lower the internal

energy that drives the formation of the magnetic ground states and is only possible through interactions between moments, albeit, not necessarily limited to only nearest neighbouring spins [3, 14]. The types of magnetic ground states that form depend on the intricacies of the Hamiltonian that describes the interactions present in the magnetic system under investigation. For example,

- if spins $\boldsymbol{S_i}$, where $i = 1,2 \ldots$ were placed on a the vertices of a square lattice,
- only nearest neighbour interactions' temperature scale was relevant (i.e. consider the dipolar term or next-nearest neighbour terms negligible),
- the value of the nearest neighbour exchange integral $J > 0$,

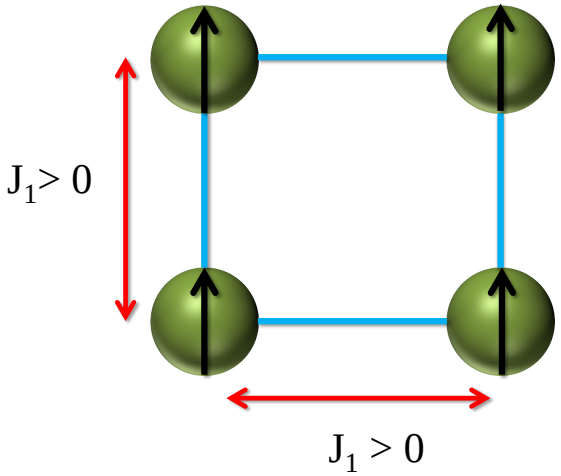

FIGURE 1.3: Magnetic moments placed on the vertices of a square lattice. The only relevant interaction between the magnetic moments are assumed to be the nearest neighbour exchange J_1. If $J_1 > 0$, the system assumes a collinear ferromagnetic long range ordered (LRO) state. Adapted from Greedan [21].

then the system would be expected to form a magnetic state where all spins were pointing parallel to one another [21]. This magnetic state is called a (collinear) ferromagnetic state as shown in figure 1.3 and in the case of $J < 0$, the spins would align anti-parallel to one another and would form an antiferromagnet. These magnetic ground states are called long range ordered (LRO) magnetic states, named after the fact that the spins are arranged in an infinitely repeating pattern in space. Another example of an LRO magnetic state would be

- if spins $\boldsymbol{S_i}$, where $i = 1,2 \ldots$ were placed on a the vertices of a triangular lattice,
- only the nearest neighbour interactions' temperature scale was relevant (i.e. consider the dipolar term or next-nearest neighbour terms negligible),

- the value of the nearest neighbour exchange integral $J < 0$,
- the spins $\boldsymbol{S_i}$, where $i = 1,2 \ldots$ were allowed to assume any orientation in the plane defined by the triangular lattice,

then the system would be expected to form a non-collinear magnetic state called a 120^o structure where each triangle would have spins $\boldsymbol{S_i}$, where $i = 1,2,3$ oriented 120^o with respect to one another [22] as shown below in figure 1.4. The fourth condition defined the anistropy of the individual spins and is crucial when considering the symmetry of the lattice that the individual spins are placed on [11]. In the next section, the situation when spins with $J < 0$ are limited to one spatial degree of freedom and the additional complications this extra condition imposes on the ordering of the magnetic system will be discussed.

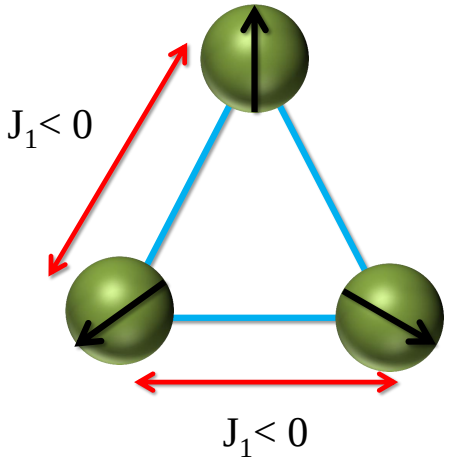

FIGURE 1.4: Heisenberg magnetic moments (three spatial degrees of freedom) placed on the vertcies of a trianglar lattice. The only relevant interaction between the magnetic moments are assumed to be the nearest neighbour exchange J_1. If $J_1 < 0$, the system assumes a two-dimensional 120^o long range ordered state. Adapted from Greedan [21].

Recall from equation 1.33, that as the temperature is lowered such that the energy scale set by the magnetic system's interactions are comparable to average thermal energy, the magnetic system will typically form a new magnetic arranagment from its paramagnetic or disordered arrangement, as an attempt to lower its free energy. This thermodynamic phase transition from a paramagnet to the new magnetic arrangement, occurs at a temperature denoted as T_C (Curie temperature) and T_N (Néel temperature) for ferromagnets and antiferromagnets, respectively [3]. The particular magnetic phase transition can be characterised as first or second order, whereas the former involves the order parameter being discontinuous at the phase transition while the latter has its first derivative of the order parameter (with respect to temperature) being discontinuous [3, 6, 13]. Examples of order parameters would be density ρ for a PT-phase

diagram or bulk magnetisation M for a HT-phase diagram [15]. A common method for determining both the magnitude and dominant type of spin-spin interactions involves studying the paramagnetic state *via* the DC susceptibility χ using a mean field approach summarised by the Curie-Weiss law [3],

$$\chi = \frac{C}{T - \theta_{CW}}, \tag{1.34}$$

where C and θ_{CW} are the Curie constant and Weiss temperature, respectively. The Curie-Weiss law (through its derivation, see *Kittel* [3]) describes a magnetic system in its paramagnetic regime (i.e. $\mathrm{k}_B\mathrm{T}$ is much larger than the spin-spin interaction energy scale) and where the individual spins see an ambient mean internal magnetic field created by its neighbouring spins. By taking the inverse of the DC susceptibility's temperature dependence,

$$\chi^{-1} = \left(\frac{1}{C}\right)(T) - \frac{\theta_{CW}}{C}, \tag{1.35}$$

both Curie-Weiss parameters C and θ_{CW} can be extracted. Using simple statistical mechanical arguments, one obtains [25]

$$\chi = \frac{Ng^2J(J+1)\mu_B^2}{3k_B(T - \theta_{CW})} + \alpha, \tag{1.36}$$

where N is the number of moments (usually $\mathrm{N} = \mathrm{N}_A$) being considered, α is a temperature-independent term with g, J, μ_B, k_B and θ_{CW} being the Landé g-factor, the total angular momentum quantum number, the Bohr magneton, Boltzmann constant and the Weiss temperature, respectively, as previously defined. As described in equation 1.34 and more explicitly in equation 1.36, the Weiss temperature θ_{CW} can be employed as a mean field estimate of the energy scale for the spin-spin interactions present in the system [26], given by

$$\theta_{CW} = \frac{2J(J+1)\sum\limits_{j>i} J_{ij}z_i}{3R}, \tag{1.37}$$

where R is the universal gas constant, J is the total angular momentum quantum number, J_{ij} is the exchange interaction between spins i and j and $\mathrm{z_i}$ is the number of neighbours for atom i. The value of θ_{CW} sets the temperature scale at which the Curie-Weiss law would be applicable [3, 15]. Its sign *via* equation 1.37 determines what type of spin-spin interactions dominate, if $\theta_{\mathrm{CW}} > 0$, then ferromagnetic interactions are dominant

and if $\theta_{\mathrm{CW}} < 0$, then antiferromagnetic interactions dominate. Finally, by comparing equations 1.34 and 1.36, the Curie constant C can be described by

$$C = \frac{Ng^2J(J+1)\mu_B^2}{3k_B}, \tag{1.38}$$

where one can define an effective magnetic moment μ_{eff} [3] as

$$\mu_{\mathrm{eff}} = \mathrm{g}\sqrt{\mathrm{J(J+1)}}\mu_{\mathrm{B}}, \tag{1.39}$$

which should not be confused with the definition provided for the magnetic moment of an atom given by equation 1.25. Therefore, the Curie constant C can be interpreted as a quantitative estimate of the magnitude of the magnetic moments that constitute the magnetic system.

1.3 Geometric Frustration

Although the quantitative precision of the Curie-Weiss law is limited — due to its mean field approach — the values of its parameters do provide estimates (up to a degree of magnitude) of what temperature a system of interacting moments, whose magnitude is given by C, will its spin-spin interactions' energy scale become comparable to thermal fluctuations and thus should theoretically order [3, 18]. In some materials, this is not the case, despite the interactions' energy scale being comparable or even greater than thermal fluctuations, no magnetic ordering is observed [11, 21, 22, 27]. In these materials, the spins are subject to multiple competing or contradictory interactions and the system is said to be *frustrated* [11, 21]. More precisely, a system is said to *frustrated*, if the system cannot satisfy all competing interactions **simultaneously** [11]. An example of such a situation would be the following:

- placing four spins $\boldsymbol{S_i}$ for i = 1,2,3 and 4 on the vertices of a square lattice,
- the nearest neighbour exchange J_{nn} or $\mathrm{J}_1 < 0$,
- the next nearest neighbour exchange J_{nnn} or $\mathrm{J}_2 < 0$,
- both the nearest neighbour and next nearest neighbour exchange energy scales are comparable with $\mathrm{J}_{nn} \approx \mathrm{J}_{nnn}$

with the first three conditions being commonly referred to as the J_1-J_2 model on the square lattice [21]. The fourth condition frustrates the lattice as shown in figure 1.5

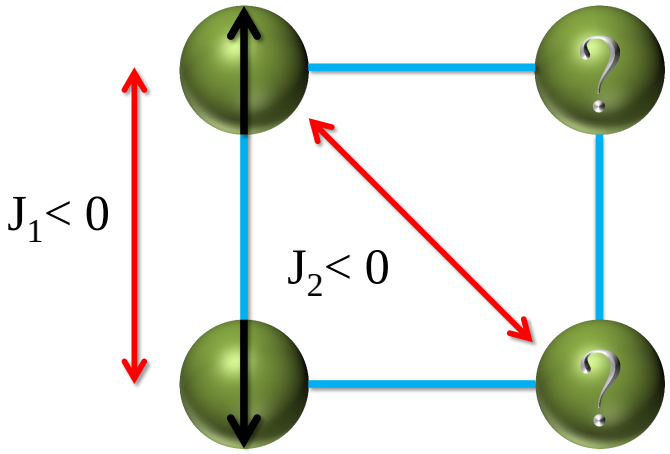

FIGURE 1.5: Pictorial representation of the J_1-J_2 model. Magnetic moments are placed on the vertices of a square lattice. Both the nearest neighbour and next neighbour neighbour interactions, J_1 and J_2 respectively have similar set energy scales (i.e. neither is negligible compared to the other). If both J_1 and $J_2 < 0$, there exists competing contradictory interactions between magnetic moments. This conflict between multiple interactions between moments *frustrates* the system, prohibiting the system from assuming a unique LRO magnetic state. Adapted from Greedan [21].

because both sets of interactions produce magnetic ground states that are on a comparable energy scale. In fact, if the $\frac{J_2}{J_1}$ =1, then both sets of interactions produce two magnetic ground states of equal energy and thus the system cannot select a unique magnetic ground state based simply on n.n. and n.n.n. exchange energetic considerations and will remain disordered, despite J_1 and J_2 being equal or even stronger compared to thermal fluctuations [21]. The J_1-J_2 model on the square lattice represents one particular example of a mechanism to produce a frustrated magnetic system. The particular mechanism, termed *geometric frustration*, has recently captured the attention of the solid state physics and chemistry communities and will be the focus of discussion for the remainder of this section.

1.3.1 Introduction & Motivation

Although the previous J_1-J_2 example consisted of **multiple** competing exchange interactions, magnetic frustration can also occur in the presence of a **single** exchange interaction between spins placed on a lattice whose symmetry is not compatible or conflicts with the aforementioned spin-spin interaction [11, 28]. It is this conflict of symmetries between the interactions between the spins and the lattice that the spins are placed onto that defines geometric frustration. For an excellent review of geometric

frustration, please refer to Ramirez [29] and Greedan [21, 22]. The canonical example would be Ising spins (i.e. spins that possess 1 spatial degree of freedom) placed on the corners of an equilateral triangle with a dominant $J_{nn} < 0$ [30] as shown in figure 1.6 below.

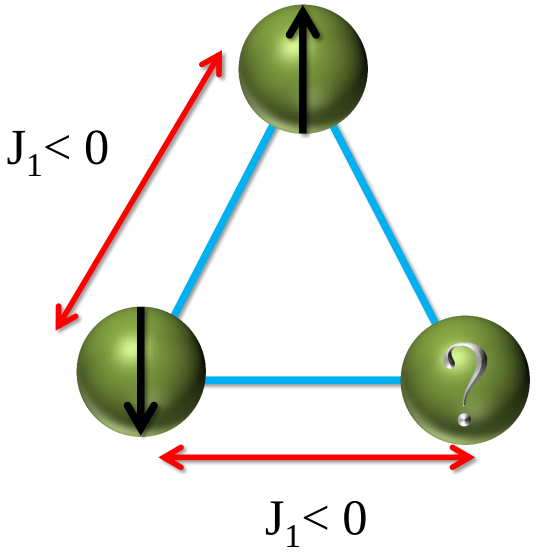

FIGURE 1.6: Ising magnetic moments (1 spatial degree of freedom) placed on the vertices of a triangular lattice with the nearest neighbour exchange interaction $J_1 < 0$. The conflict between the equilateral triangle geometry that constitutes the lattice and the nearest neighbour antiferromagnetic interaction between Ising spins is termed *geometric frustration* and prohibits the system from assuming a unique LRO magnetic state. Adapted from Gardner *et al.* [11].

The AFM interactions (i.e. the tendency of the spins to align antiparallel to one another) will only be satisfied for two of the three spins. This inability for all spins to have an antiparallel arranagement with respect to one another is a consequence of the conflict of the triangular symmetry and the AFM nearest neighbour spin-spin interactions between Ising spins, thus the system is said to be geometrically frustrated, as alluded to in the previous discussion of the 120^o degree structure when the spins instead possess XY anistropy. Geometric frustration is by no means limited to two dimensional structures or even triangular motifs [21]. The former situation is best illustrated by placing four spins $\boldsymbol{S_i}$ on the corners of a tetrahedron — a polyhedron consisting of four edge sharing triangles — with the $J_{nn} < 0$, whereby only two of out of the four spins have the antiparallel arrangement satisfied [11, 21]. The latter situation was already illustrated with the J_1-J_2 model on the *square* lattice, whereby the presence of two competing interactions is a consequence of the square's geometry. Although the preceding discussion was limited to the frustration of *individual* motifs such as the triangle, tetrahedon and square, lattices that are composed of such "frustrated" motifs will not only

naturally inherit the frustration from these individual motifs but will scale the frustration up to a macroscopic level. Examples of such lattices include the Kagomé lattice [21] that consists of a two-dimensional array of corner sharing triangles and the pyrochlore lattice [11], consisting of a three-dimensional array of corner sharing tetrahedra, that will be the focus of the next subsection.

Recall from section 1.2, a magnetic system, in the absence of magnetic frustration, should transition into an ordered magnetic state when the energy scale set by the interactions between spins (estimated by θ_{CW} through equation 1.37) is comparable to thermal fluctuations. Instead, when magnetic frustration is present, the system does not order, despite the energy scale of the spin-spin interactions being equal or stronger than thermal fluctuations and is a result of the inherent degeneracy as a result of the magnetic frustration [11, 20, 22]. This situation where there is degeneracy concerning the magnetic ground state is in clear violation of the third law of thermodynamics because there is finite entropy at 0 K [31]. Instead, magnetic systems must select a unique ground state if the third law is to be satisfied, albeit at much lower temperatures than predicted by mean field theory. Ramirez [29] popularised a quantiative descriptor of the degree of frustration present in the system, called the *frustration index*, denoted as f and defined as

$$f = \frac{|\theta_{CW}|}{T^*}, \tag{1.40}$$

where T^* is the Curie or Néel temperature, as previously defined or T_f for a spin glass transition and a magnetic system is defined as frustrated if $f > 10$ [11]. The method of selection and the magnetic ground state ultimately chosen by a geometrically frustated system forms the basis of interest in these particular compounds. Since frustration tends to prohibit the magnetic system from ordering at conventional temperature scales, weaker terms in the Hamiltonian, that are often not considered in conventional spin-spin interaction models such the model described by equation 1.32, ultimately dictate the selection of the magnetic ground state [11, 22, 28, 31, 32]. Examples of these weaker terms include beyond nearest neighbour interactions and long range dipolar interactions [20], where the latter will be an important component for the discussion in subsection 1.4. These weaker terms, although ultimately selecting a unique LRO magnetic state, also dictate the behaviour of these magnetically frustrated magnetic systems in a unique temperature regime before the formation of an LRO magnetic state. Specifically, a temperature regime that is well below the energy scale set by thermal agitation and thus are largely dominated by spin-spin interactions, a situation permitted only because the presence of frustration prohibits the formation of an LRO magnetic state. This unique temperature regime is an arena for rich physics [30], often yielding exotic and sometimes novel short range ordered (SRO) magnetic states as a consequence of energetic compromises in order to comply with the third law of thermodynamics [30, 33]. Such

SRO magnetic ground states include (but are not limited to) quantum spin liquids [27] and spin ices [21, 33, 34]. The former represents short ranged dynamic correlations, in an analogy to fluids, and its existence was first postulated by the prominent American physicist Anderson in 1973 [35], while the latter will be the main topic of discussion in section 1.4. The great diversity in observed magnetic states resulting directly from magnetic frustration, reflects the delicate balance between the weaker terms of the interaction Hamiltonian, and is best exemplified by the various magnetic states assumed by various members of one class of geometrically frustrated compounds, the magnetic pyrochlore oxides, the subject of the next subsection.

1.3.2 Magnetic Pyrochlore Oxides $A_2B_2O_7$

Within the past 25 years, there has been an explosion of interest in the magnetic properties of one particular class of geometrically frustrated magnets called the magnetic pyrochlore oxides, particularly of the form $A_2^{3+}B_2^{4+}O_7$ (the only form of the pyrochlores that will be considered in this thesis), where A is usually a trivalent f-block element and B is usually a tetravalent transition metal. With the A and B cations each forming a network of corner sharing tetrahedra, which is the quintessential framework for a geometrically frustrated lattice [11]. In combination with the pyrochlores' significant compositional diversity, the magnetic pyrochlore oxides provides the condensed matter community with a unique opportunity for systematic studies of the exotic and often novel macroscopic magnetic manifestations that directly result from frustrated magnetism [22].

The magnetic pyrochlore oxides are a family of magnetic compounds with the chemical formula $A_2B_2O_7$, with either the A cation, the B cation or both being magnetic, that assumes the pyrochlore lattice upon crystallisation [36]. The pyrochlore lattice — named after the naturally abundant solid solution pyrochlore $(Na,Ca)_2Nb_2O_6(OH,F)$ — is cubic (space group: $Fd\bar{3}m$, 227/230) with four unique crystallographic positions summarised in table 1.1 [37] and shown pictorially below in figure 1.7. The A cation in the $16d$ Wyckoff position is eight coordinate with respect to oxygen while the B cation in the $16c$ is six coordinate. The only variable positional parameter of the $48f$ O, x determines the specific nature of the coordination polyhedra for both the $16d$ and $16c$ sites. A value of $x = 0.3125$ represents perfect octahedral polyhedra BO_6 around the $16c$ while a value of $x = 0.375$ represents perfect cubic polyhedra AO_8 around the $16d$ site. Since a single value of x cannot satisfy both ideal coordination polyhedra simultaneously, the value of x assumes an intermediate value correlated to the unit cell's lattice parameter a [38], resulting in the distortion of both coordination polyhedra. In fact, the polyhedral distortion tends to be much larger for the $16d$ site [11]. An alternative view for the local coordination of $16d$ site consists of two $8b$ O' ligands located in the centre

of a tetrahedron defined by the 16*d* *A* cations and these O' ligands define the local ⟨111⟩ axis as previously discussed in subsection 1.1.3. The six remaining oxygen ligands form a puckered or buckled hexagon, whose degree of "buckling" is a direct manifestation of the polyhedral distortion [36]. This alternative view is important when considering the anistropy introduced by local crystal field effects as will be seen in section 1.4 when discussing spin ices. For an excellent introduction to the pyrochlore structure, please refer to a review of pyrochlore oxides by Subramanian *et al.* [39].

TABLE 1.1: Crystallographic positions for constituent atoms of the Fd$\bar{3}$m unit cell (space group: 227/230) $A_2B_2O_6O'$ with the origin at position 16*c* from the International Tables of Crystallography [40]

Atom	Wyckoff Position	Point Group Symmetry	Minimal Coordinates
A	16*d*	D_{3d}	$(\frac{1}{2}, \frac{1}{2}, \frac{1}{2})$
B	16*c*	D_{3d}	(0, 0, 0)
O	48*f*	C_{2v}	$(x, \frac{1}{8}, \frac{1}{8})$
O'	8*b*	T_d	$(\frac{3}{8}, \frac{3}{8}, \frac{3}{8})$

As aforementioned, the cations lying in the 16*c* and 16*d* Wyckoff positions, commonly referred to as the *B* and *A* site, respectively, each form a network of corner-sharing tetrahedra, which in turn interpenetrate one another and thus form the canonical geometrically frustrated lattice [11]. In fact, the propensity of the pyrochlore lattice towards geometric frustration can be further emphasised by viewing the pyrochlore lattice in the [111] crystallographic direction where the pyrochlore lattice's *A* and *B* cations each form alternating triangular and Kagomé layers [11, 22], two prototypical examples of two-dimensional frustrated motifs mentioned in section 1.3. Both the three-dimensional interpretation of the pyrochlore lattice consists of interpenetrating network of corner sharing tetrahedra or the interpretation of stacked two dimensional triangular and Kagomé motifs along the [111], illustrates a lattice highly susceptible towards geometric frustration and thus an excellent structural framework for the study of what results from this frustration.

The particular interest in these (magnetic) pyrochlore oxides, in contrast to many other known geometrically frustrated systems, stems from the great diversity of elements that *can* occupy the *A* and *B* site with more than 25 and 30 possible element choices occupying each site, respectively [11, 42]. It is worth noting that although this discussion will be limited to a trivalent rare earth *A* and tetravalent *p* or *d*-block *B*, another common alternative [11, 37] consists of a divalent *A* and a pentavalent *B* cation and is only mentioned for completion. Furthermore, although many elements *can* occupy the *A* and *B* site, the number of combinations that actually assume the pyrochlore

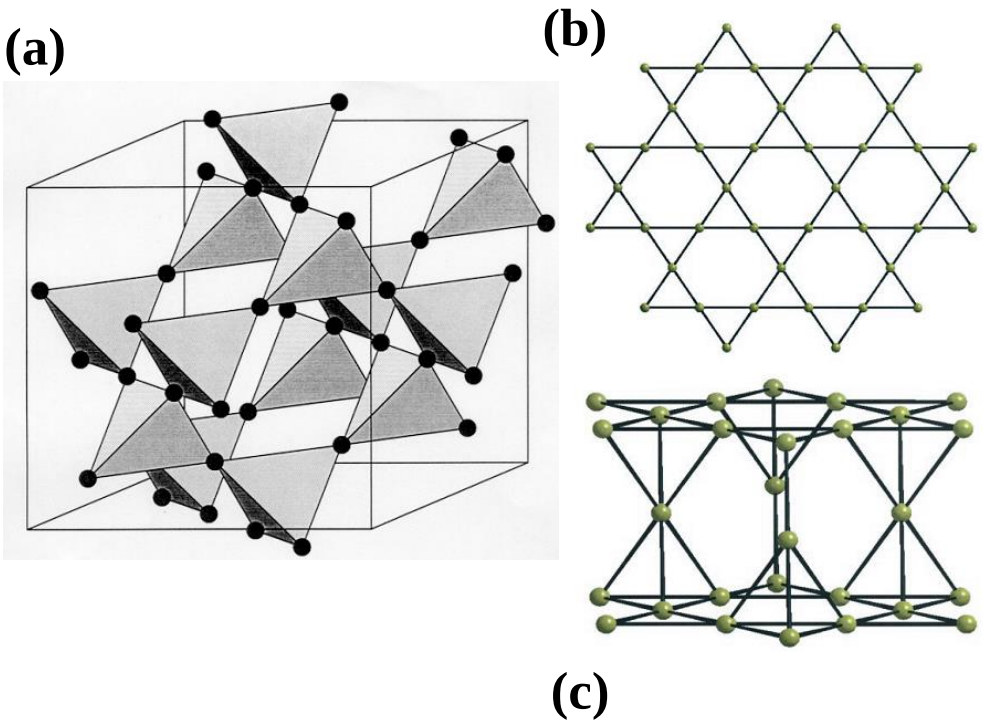

FIGURE 1.7: Pictorial representation of structural motifs of the cubic $Fd\bar{3}m$ pyrochlore structure. (a) The 16*d* and 16*c* Wyckoff site, commonly referred to as the *A*-site and *B*-site, respectively, consists of placing the atoms of each respective site on the vertices of a unique network of corner-sharing tetrahedra, with both *A* and *B* sublattices of corner-sharing tetrahedra interpenetrate one another. (b) Projection of either the *A* or *B* site onto the (111) plane yields the two dimensional Kagomé lattice. (c) Two dimensional Kagomé and triangular layers are alternately stacked along the [111] direction. All three triangular-based structural motifs demonstrates the pyrochlore lattice's tendency towards geometrically frustration. Adapted from Karunadasa *et al.* [41].

structure is limited as summarised in figure 1.8. The restriction placed on the possible combinations can be inferred from a simple argument concerning the relative size of the ions' ionic radii that consitute the structure, an argument that is by no means limited to the pyrochlores alone. A metric for determining the stability of a given A^{3+} /B^{4+} combination is given by the radius ratio [11, 43], denoted as RR and expressed as

$$RR = \frac{R_{A^{3+}}}{R_{B^{4+}}}, \tag{1.41}$$

where $R_{A^{3+}}$ and $R_{B^{4+}}$ are the ionic radii for the trivalent rare earth *A* and the tetravalent *p* or *d*-block *B*, respectively. Subramanian *et al.* [37] determined that the stability range of the magnetic pyrochlore oxides at ambient pressures can be defined as: $1.36 \lesssim RR \lesssim 1.71$. It should be noted that that this range is only approximate, with marginal stability expected as one approaches the upper/lower limits, and there are a few notable exceptions such as $Pr_2Ru_2O_7$ [44] with an *RR* of 1.82 assuming a stable pyrochlore

structure and yet $Pr_2Mo_2O_7$ [45] with an RR of 1.73 forms the monoclinic $P2_1$ structure. The consequences on the pyrochlore structure as one approaches either upper/lower boundary of the stability field has been a recent — and poorly appreciated — topic of research which includes ion conduction [46–49], nuclear waste disposal [50–52] and the cationic disorder present in two pyrochlores, $Pr_2Zr_2O_7$ [53] and $Yb_2Ti_2O_7$ [54]. Although the upper limit of the stability field is approximately 1.71, with recent advances of high pressure-high pressures synthesis techniques, the stability field can be artifically expanded to an $RR \approx 2.3$ to include smaller tetravalent p-block elements in the B-site such as germanium [32, 43] and vanadium [55].

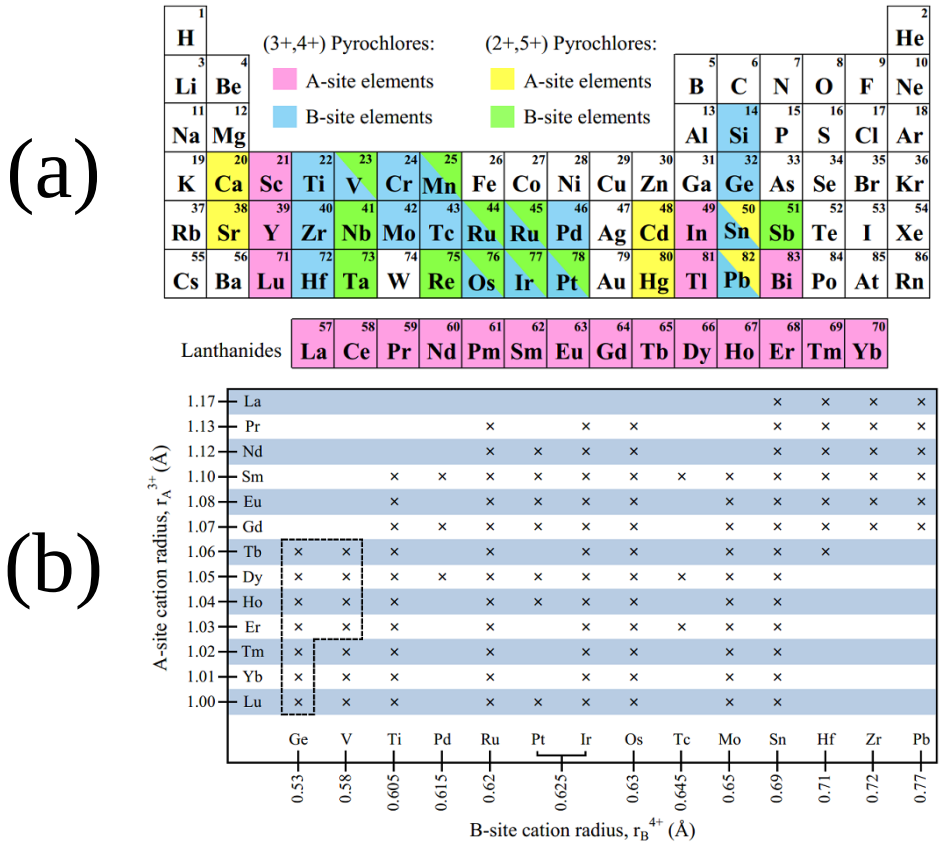

FIGURE 1.8: (a) Periodic table summarising reported elements occupying the A-site ($16d$) and B-site ($16c$ site) respectively for +3/+4 and +2/+5 cubic pyrochlores. (b) Reported stability field for the rare earth cubic pyrochlore phase. High pressure members (germanates and select members of the vanadates) are enclosed by the dashed lines. Adapted by Hallas [42] from Gardner *et al.* [11].

Ultimately, the plethora of exotic and sometimes novel magnetic behaviour that results from the combination of the canonical frustrated topology and a large and diverse stability field — characteristic of the pyrochlore structure — is what has captured the unparalleled interest of the condensed matter community. The magnetic ground states observed in these magnetic pyrochlore oxides vary significantly, depending on the specific A^{3+}/B^{4+} combination, from LRO magnetic states [56] to amorphous (disordered) spin glasses [57, 58] to SRO magnetic states that include spin liquids [59, 60] and spin

ices [31, 32, 61, 62], that will be the topic of the next section. For a comprehensive summary of the observed magnetic ground states exhibited by the magnetic pyrochlore oxides, please refer to Gardner *et al.* [11].

1.4 Spin Ice State and the Canonical and Dipolar Spin Ices

In this section, one of the novel and perhaps most exotic of the magnetic ground states resulting from geometric frustration in the magnetic pyrochlore oxides, the *spin ice* state, will be discussed. The spin ice state, a short range ordered magnetic state, represents (almost) ideal realisations of Pauling's model of proton disorder in water ice, has provided the condensed matter community with an arena with extremely rich physics. Theoreticians have explored many new aspects of the underlying physics concerning magnetic interactions in a highly geometrically frustrated magnetic system including novel magnetic states and corresponding exotic phase transitions. The discussion of the *spin ice* will provide the reader first with the historic problem of water ice and the statistical mechanical framework that was established to describe such problems. Then the reader will be introduced to the various experiments that led to the initial proposal by Harris *et al.* [62] that the *spin ice* state was present in $Ho_2Ti_2O_7$, representing the first *spin ice* candidate. Select subsequent experiments are discussed with the intention to provide the reader with a summary of the experimental features of such a state. Finally, one specific treatment to model the properties of the *spin ice state*, the *dipolar spin ice model* [20], is discussed. It should be noted that this discussion consists of a superficial treatment of dipolar spin ices for the sake of brevity. An exotic variant of the spin ice state, called the *quantum spin ice* state, is not included in the current dicussion but will be immediately addressed in Chapter 3 in the context of $Pr_2Sn_2O_7$, the main compound addressed in this thesis. If one desires a much larger comprehensive review of dipolar spin ices, please refer to Chapter 7 of Diep's *Frustrated Spin Systems* [24] and Bramwell *et al.* [63].

Between 1933-1936, Giauque and Stout [64] demonstrated that there was a small, but finite difference between the entropy that was retrieved by integrating calorimetric measurements they performed on water and the entropy release (ΔS) that was calculated using statistical mechanical arguments with energy levels retrieved from previous spectroscopic measurements. The discrepancy of 0.82 ± 0.05 Cal/K mol ice (3.4 ± 0.3 J/K mol ice) between both methods remained a particular mystery since it was theorised that both approaches would both yield the same results and both methods were performed with extremely high precision, in particular, the calorimetric measurements were extrapolated down to 0 K *via* Debye's model [65] for heat capacity that was just

recently introduced in 1912 to address the shortcomings of Einstein's model [14]. The discrepancy reported by Giauque and Stout was accounted for by Linus Pauling [66] in 1935 using statistical mechanical arguments concerning the proton H^+ disorder in water ice. Pauling's argument was as follows:

- Assume there are N O^{2-} anions present,
- By stoichometry, there are $2N$ H^+ cations present,
- Each H^+ can have 2 "positions" (i.e. close or far) in accordance to the 1933 Bernal-Fowler "ice rules" [67],
- Given a set of O^{2-} anion and the four surrounding H^+ protons, there are $\frac{6}{16}$ arrangements that satisfy the Bernal-Fowles rules,

and the number of possible configurations for the N ice molecules Ω is given by

$$\Omega = 2^{2N} \cdot \left(\frac{6}{16}\right)^N = \left(\frac{3}{2}\right)^N, \tag{1.42}$$

then by the statistical mechanical Boltzmann definition of entropy [30], the entropy for the N ice molecules system due to the intrinsic proton disorder in ice, termed S_o is given by

$$S_o = k_B \ln\Omega = N k_B \ln\left(\frac{3}{2}\right) \tag{1.43}$$

usually $N = N_A$ and instead of per mol of ice, S_o, is usually reported per mol of H^+

$$S_o = k_B \ln\Omega = \frac{N_A k_B}{2} \ln\left(\frac{3}{2}\right) = \frac{R}{2} \ln\left(\frac{3}{2}\right) \approx 1.7\,\mathrm{J/K\ mol \cdot H^+} \tag{1.44}$$

The introduction of the notion that the finite entropy difference was due to a source of configurational disorder that was inherent in the system and consequently would be present even at 0 K, not only solved the missing entropy problem but introduced the concept of a finite residual entropy, usually denoted as S_o where $S_o \neq 0$. The non-zero residual entropy is a direct consequence of frustration of internal degrees of freedom [20]. In particular, if one considers the protons as an Ising-like system and with the geometric constraints, represented by both the molecular integrity of H_2O and the Bernal-Fowles rules, the proton disorder in ice can be thought of as a nearest neighbour exchange interaction that is frustrated by geometry, in other words, the proton disorder present in ice is a consequence of geometric frustration [24]. This interpretation of geometric

frustration was in fact underappreciated — relative to Pauling's introduction of residual entropy — and would not be at the forefront of the geometrically frustrated magnetism community until the late twentieth century.

In the late 1990's, a magnetic pyrochlore oxide $Ho_2Ti_2O_7$ was hypothesised to be a frustrated antiferromagnet that would not exhibit an LRO magnetic state down to the lowest measurable temperatures. In order to pursue such a hypothesis, Harris *et al.* [68] performed μSR experiments at ISIS in 1996, revealing both no characteristic precessional oscillations in the relaxation signal, indicative of no well-defined distribution of internal fields as one would expect from an LRO magnetic state. In fact, $Ho_2Ti_2O_7$ exhibited no such oscillations and when a magnetic field was applied, the signal was "frozen", both implying the presence of spin freezing behaviour and confirming the original hypothesis that $Ho_2Ti_2O_7$ was a geometrically frustrated antiferromagnet. However, very precise DC magnetometry measurements by Harris *et al.* [62] on single crystals of $Ho_2Ti_2O_7$ revealed that the Weiss temperature θ_{CW} was in fact positive implying net dominant ferromagetic interactions. The value of $\theta_{CW} = 1.9 \pm 0.1$ K [62] was obtained only after measuring quasi-ellipsoidal samples of different aspect ratios to compensate for the large demagnetisation factor that led to the original antiferromagnetic hypothesis. The DC magnetometry result was puzzling because the pyrochlore lattice is not geometrically frustrated for nearest neighbour ferromagnetically coupled Heisenberg spins and thus should theoretically order at a finite temperature. Instead, the lack of magnetic ordering was later confirmed by mutliple neutron scattering experiments, revealing no LRO magnetic state down 50 mK but instead revealed a distinct buildup of low $\mathbf{Q}$ diffuse scattering, confirming net ferromagnetic interactions. At the same time the discovery of net ferromagnetic interactions in $Ho_2Ti_2O_7$ were made, Harris *et al.* [62] also performed powder magnetometry experiments that revealed that $Ho_2Ti_2O_7$ behaved (to an excellent approximation) as a large moment Ising-like system with a ground state doublet crystal field level being $|M_J = \pm 8\rangle$ with little admixture from $|M_J \neq J\rangle$ terms. This large moment Ising-like characteristic implied analogous behaviour to $LiHoF_4$ [69, 70] where the large holmium moments were Ising spins fixed along the local quantisation axis, in the case of the pyrochlores, the local quantisation axis would be the trigonal $\langle 111 \rangle$ axis. In 1997, Harris *et al.* [62] accumulated all their previous experimental data on $Ho_2Ti_2O_7$ – indicating (almost perfect) Ising-like spins bound to the $\langle 111 \rangle$ trigonal axis that were ferromagnetically coupled — but even went even further by establishing an analogy between $Ho_2Ti_2O_7$ and Pauling's original water ice model. Harris *et al.* [62] argued the following:

- since the ground state configuration of the aforementioned $\langle 111 \rangle$ Ising ferromagnet corresponds to a spin configration where two spins are pointing into the tetrahedron

and two spins are pointing out

- since the pyrochlore lattice was proven by Anderson to be the dual lattice (or medial lattice) of cubic ice [71]

then the ground state spin configuration on the vertices of the 16*d* Wyckoff site in $Ho_2Ti_2O_7$ would correspond to the Bernal-Fowles "ice rules" [67] and thus would map directly onto the Pauling model of water ice. Consequently, the 1997 paper from Harris *et al.* [62] concerning $Ho_2Ti_2O_7$ represented the first spin ice reported, a magnetic system whose spin configuration maps directly onto the proton arrangement in water ice. The spin ice model, or more precisely, the nearest neighbour ferromagnetic interaction model, provided a natural explanation for all the unusual magnetic properties that were previously reported. In particular, the model accounted for the absence of the formation of a LRO — despite dominant FM interactions on the pyrochlore lattice — and the distinct $\mathbf{Q} = 0$ diffuse scattering seen in neutron scattering, corresponding to a disordered spin structure with exclusively short range order. Furthermore, the "spin ice" model and its correspondence to water ice, naturally provided one key prediction concerning what should be seen in the isobaric heat capacity. Recall from the second law of thermodynamics [13, 14], it can be shown that

$$\Delta S = S_T - S_o = \int_{T=0K}^{T} \frac{C_p(T)}{T} dT. \tag{1.45}$$

Thus, by integrating the quotient of the isobaric heat capacity and temperaure over some definite temperature range, the entropy change can be determined. If one subtracts all non-magnetic components, one may retrieve the entropy associated exclusively with the magnetic moments. If the "spin ice" model was indeed correct, a spin ice compound would possess a finite amount of entropy, specifically Pauling's entropy, originating from the intrinsic disorder concerning the arrangement of spins in a direct analogy to proton disorder in water ice. Unfortunately, holmium exhibits a large hyperfine splittng (~ 0.35 K [73]) and many [74] interpreted the upward turn seen at base temperatures in the $\frac{C_p(T)}{T}$ plot as the high temperature tail of a Schottky anomaly implying the formation of a partially ordered magnetic state. Consequently, the presence of Pauling entropy by Ramirez *et al.* [75] was first directly measured in $Dy_2Ti_2O_7$ since dysprosium exhibits a much smaller hyperfine splitting (~ 50 mK [76], much lower than the base temperatures measured in conventional laboratory calorimetry experiments at the time). It should be noted that Pauling's entropy was also eventually measured in $Ho_2Ti_2O_7$ after Bramwell *et al.* [61] successfully accounted for the nuclear contribution to the isobaric heat capacity by analysing the heat capacity of an isostructural compound Ho_2GaSbO_7 measured by Blöte [77]. The motivation of Bramwell *et al.* [61] to pursue the measurement of the elusive Pauling entropy in $Ho_2Ti_2O_7$ stemmed from the fact that neutron experiments

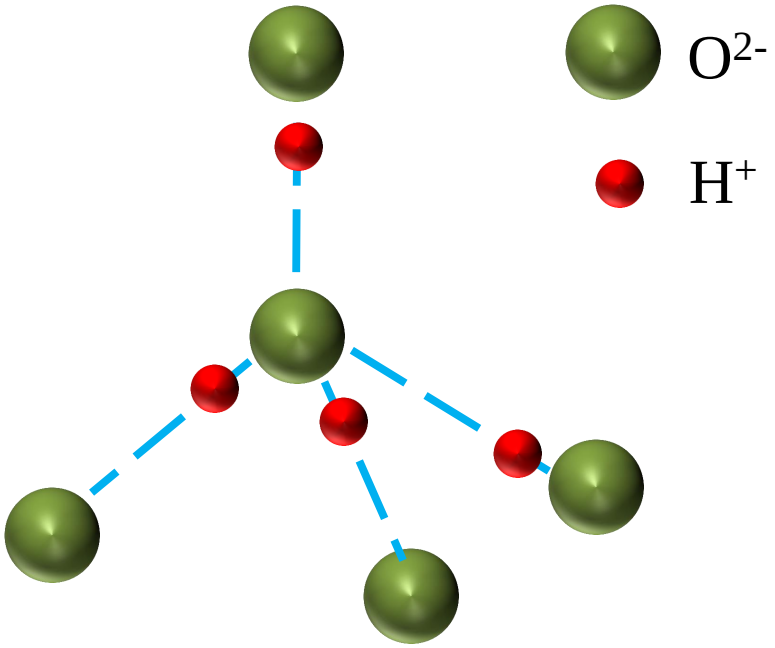

FIGURE 1.9: Pictorial representation of the 1933 Bernal-Fowler "ice rules" [67] with the restriction that for each oxygen anion (olive green sphere), there are two hydrogen cations H^+ (red spheres) close and two far, representing covalently bonded and hydrogen bonded H^+, respectively. Adapted from Bramwell and Gingras [72].

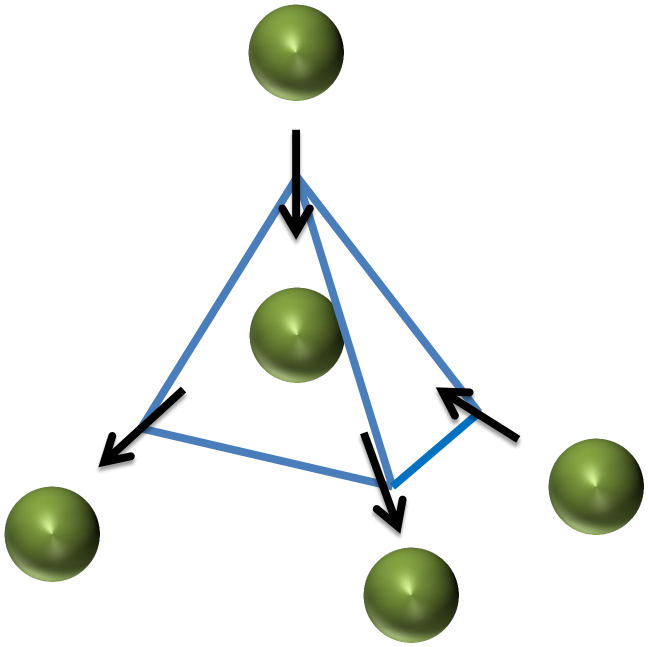

FIGURE 1.10: Pictorial representation of the "spin ice rules" [68]. The four magnetic moments (black arrows) placed on the vertices of the $16d$ or $16c$ Wyckoff site of the cubic $Fd\bar{3}m$ pyrochlore lattice are restricted along the local $\langle 111 \rangle$ axis due to strong crystal field effects (refer to subsection 1.1.3). When these moments are ferromagnetically coupled, the system's energy is minimised when the magnetic moments assume a "'two-in-two-out" configuration, representing a direct magnetic analog to the 1933 Bernal-Fowler ''ice rules" (two-close-two-far) in figure 1.9. Adapted from Bramwell and Gingras [72].

by both Bramwell *et al.* [61] and Kanada *et al.* [78] failed to indicate any indication of a partially ordered magnetic state proposed in lieu of the spin ice state. The recovery of Pauling entropy solidified $Dy_2Ti_2O_7$ as another "spin ice" candiate, confirmed the 1997 claim of $Ho_2Ti_2O_7$ as a spin ice and constitues one of the main experimental indicators of the presence of the spin ice state first reported by Harris *et al.* [62]. Other experimental necessary conditions of these first "spin ice" materials [72] are listed below for brevity:

- Almost pure $|M_J = \pm J\rangle$ thermally isolated (well-isolated) ground state doublet with little $|M_J \neq J\rangle$ admixture corresponding to (almost) ideal Ising-like spins bound to the $\langle 111 \rangle$ trigonal axis,
- If a magnetic field was applied along the [111] direction, the magnetisation should exhibit a plateau, occassionally referred to the "111 plateau", indicative of the formation of an anistropic version of the spin ice state called a Kagomé spin ice [79],
- Hysteretic behaviour (i.e. history dependence) of magneometry measurements due to freezing of the spins [80],
- Divergence of the spin relaxation time (i.e. rapid increase in τ with τ reaching $\sim$ 1 s) due to freezing of the spins at low temperatures [62],
- "Pinch points" in neutron scattering, indicative of the presence of the Coulomb phase which may be interpreted as a propogation of "defect" spins throughout the structure [81],
- A build-up of low $\mathbf{Q}$ diffuse neutron scattering [31, 82],
- The absence of long range order (e.g. no sharp anomalies should be present in the measurement of physical property measurements).

The absence of long range order is important to stress. The spin ice state is a short range ordered state which the magnetic system "freezes" into [20, 62, 68]. Although the magnetic system selects one particular spin ice state to freeze into, the spin ice state is in fact macroscopically degenerate [72]. This degeneracy is due to the fact that despite each tetrahedon satisfying the two-in-two-out requirement, which ultimately yields the Pauling entropy, knowledge of one particular component of the spin ice state will **not** provide information concerning all other components [62]. Despite the absence of a LRO magnetic state in the "spin ice" regime, as aforementioned, the spin ice state has represented a unique opportunity for the condensed matter community to explore underlying physics of magnetic interactions in highly geometrically frustrated correlated spin systems. Consequently, the development of the theoretical framework to account for

such an exotic state, quickly followed the initial report of the spin state in $Ho_2Ti_2O_7$ by Harris *et al.* [62].

Shortly after the discovery of the spin ice state in $Ho_2Ti_2O_7$ and $Dy_2Ti_2O_7$ by Harris *et al.* [62] and Ramirez *et al.* [75], respectively, Bramwell *et al.* [61] proposed the ferromagnetic (FM) interaction model of spin ices to explain the exotic spin ice ground state. The ferromagnetic interaction model of spin ices proposed that the spin ice state was created as a consequence of a combination of nearest neighbour ferromagnetic interactions coupled with strong single ion anistropy. Further measurements [83, 84] in the late 1990's indicated that the exchange in both $Ho_2Ti_2O_7$ and $Dy_2Ti_2O_7$ were in fact antiferromagnetic, thus providing an explanation for the small positive Weiss temperatures ($\theta_{CW} \sim 1$ K) for both $Ho_2Ti_2O_7$ and $Dy_2Ti_2O_7$. Furthermore, the low temperature behaviour of the heat capacity of $Ho_2Ti_2O_7$ was revealed to be completely inconsistent with the ferromagnetic spin ice model [74]. In the ferromagnetic spin ice model, the Ising-like system has a two-fold degeneracy (with a tetrahedron having all its spins pointing all in or all out depending on its orientation) if the system has nearest neighbour AFM interactions. While if the system has nearest neighbour FM interactions, then the system has a six-fold degeneracy whereby the ground state consists of tetrahedra satisfying the two-in-two-out arrangement (i.e. spin ice rule). Monte Carlo simulations proposed that by considering only the FM model and if the system was located in the spin ice manifold, a broad peak would appear at a temperature approximately equal to the exchange interaction energy. Contrarily, if the system was located in the antiferromagnetic manifold, a sharp peak would appear at a temperature roughly four times the interaction energy, reflecting the higher energy required for a spin flip. The heat capacity behaviour of $Ho_2Ti_2O_7$ initially reported by Bramwell *et al.* [61] did not agree with any of the two options proposed by the FM spin ice model, rather it exhibited a peak at a much lower temperature of 0.6 K relative to the energy scale of the nearest neighbour interactions. A possible explanation was provided by Siddharthan *et al.* [74], proposing that one must consider an antiferromagnetic superexchange component that may reduce the nearest neighbour dipolar coupling between spins and secondly, dipolar interactions cannot be truncated to nearest neighbour, rather one must consider the dipolar interactions as far out as to 5 nearest neighbours. Although the work performed by Siddharthan *et al.* did provide significant progress in modelling spin ices including indications of a transition into a LRO $\mathbf{Q} = 0$ AFM state, spurious features were present in their numerical simulations. These spurious features were eventually eliminated by the *dipolar spin ice model* proposed by den Hertog *et al.* [20] by avoiding the truncation of the dipolar interactions to 5 nearest neighbours. Instead, den Hertog *et al.* included up to 10 nearest neighbour dipolar interactions in their numerical simulations using the Ewald summation method.

The dipolar spin ice model — despite its inclusion of 10 nearest neighbour dipolar interactions — paramaterises phase space by nearest neighbour quantities, specifically the ratio of the nearest neighbour exchange interaction (D_{NN}) to the nearest neighbour dipolar interaction (J_{NN}) due to screening effects. Recall that the field generated by a magnetic moment $\boldsymbol{\mu}_1$ at the origin is given by [1, 3]

$$\mathbf{B}(\mathbf{r}) = \frac{\mu_o}{4\pi}\frac{3(\boldsymbol{\mu}_1 \cdot \mathbf{r})\mathbf{r} - r^2\boldsymbol{\mu}_1}{r^5}, \tag{1.46}$$

where μ_o and r are the permeability of free space and the magnitude of the vector $\mathbf{r}$ from the origin. Placing another moment $\boldsymbol{\mu}_2$ at $\mathbf{r}$, the energy associated with this moment is then

$$U_{\text{dip}} = -\boldsymbol{\mu}_2 \cdot \mathbf{B}(\mathbf{r}) = \frac{\mu_o}{4\pi}\frac{3(\boldsymbol{\mu}_1 \cdot \mathbf{r})(\mathbf{r} \cdot \mathbf{r}) - r^2\boldsymbol{\mu}_1 \cdot \boldsymbol{\mu}_2}{r^5}, \tag{1.47}$$

which is simply a restatement of equation 1.28. If one simplifies equation 2.4 by assuming the individual magnetic moments are both orthogonal to $\mathbf{r}$ and parallel to one another, then its value can be estimated by equation 1.48 [85]

$$D_{\text{NN}} = \frac{5 \cdot \mu_{\text{o}} \cdot \mu^2}{3 \cdot 4\pi \cdot (\text{R}_{\text{NN}})^3}, \tag{1.48}$$

where μ_{o} is the permeability of free space, μ is the magnetic moment and R_{NN} is the nearest neighbour distance, equal to $\frac{a\sqrt{2}}{4}$ for pyrochlores, while the nearest neighbour exchange interaction J_{NN} can be estimated by the Weiss temperature with equation 1.37 [86]. The factor of $\frac{5}{3}$ comes from the usual assumption that a general estimate of the nearest neighbour dipolar interaction between Ising spins placed on a pyrochlore lattice is $\frac{5U_{\text{dip}}}{3}$. It should also be noted that D_{NN} is commonly reported in degrees Kelvin which requires an additional factor of k_B to be placed in the denominator. The *dipolar spin ice model* proposes that the spin ice state will remain intact even if the nearest neighbour exchange is AFM. In fact, den Hertog *et al.* proposed that the spin ice state will remain intact to a $J_{\text{NN}}/D_{\text{NN}} \gtrsim$ -0.91 [20]. In other words, the spin ice state will remain intact until the AFM exchange interactions begin to dominate over the ferromagnetic dipolar interactions and once AFM exchange interactions dominate over the ferromagnetic dipolar interactions, the system will transition from the frustrated spin ice regime to an unfrustrated $\mathbf{Q} = 0$ AFM regime. The *dipolar spin ice model* has proven extremely successful for describing the magnetic properties for all four spin ices discovered between 1997 and 2002 [62, 75, 84]: $Ho_2Ti_2O_7$, $Dy_2Ti_2O_7$ and their stannate analogs $Ho_2Sn_2O_7$ and $Dy_2Sn_2O_7$, respectively. These four spin ice materials

are commonly referred to as canonical/dipolar spin ices [87]. These spin ices have the largest free moments (i.e. holmium and dysprosium with $\mu \sim 10\ \mu_B$ [3]) in their $16d$ Wyckoff site with a correspondingly small tetravalent B-cation (Ti^{4+} and Sn^{4+} with $R_{B^{4+}} \sim 0.7$ Å [88]) in their $16c$ site to reduce the lattice parameter a to increase the D_{NN} which goes as $\frac{1}{r_{NN}^3}$ in equation 1.48. All four compounds have weak AFM superexchange interactions (relative to the dipolar interactions), corresponding to a J_{NN}/D_{NN} ratio between -0.26 and -0.49 [11, 42]. Despite the enormous success of the *dipolar spin ice model*, no other spin ice candidate (at ambient presure) has successfully been proven to be described completely by the *dipolar spin ice model* [34, 36, 42, 82]. In particular, praseodymium-based spin ice candidates, whose spin ice physics are a result of the magnetism of a much larger Pr^{3+} cation with a much smaller moment of $\sim 3.5\ \mu_B$ [3], such as $Pr_2Sn_2O_7$, composing the main series discussed in this thesis.

Chapter 2

Experimental Methods

2.1 Diffraction

The first section of this chapter will consist of a general introduction to diffraction processes, followed by a general introduction to the two particular experimental probes used for diffraction: x-rays and neutrons. The discussion of neutron diffraction will then be further expanded into a discussion of magnetic neutron scattering formalism. Finally, a discussion of the Rietveld method, used in the refinement process of experimental diffraction data sets, will conclude the section.

2.1.1 Introduction to Diffraction

It may be argued that much of mankind's modern understanding of the structure of materials can be directly attributed to diffraction performed with electrons, neutrons and photons [89]. Diffraction refers to the collective phenomena when waves encounter either an obstacle or a slit [90]. The term diffraction was coined by the Italian Jesuit Francesco Maria Grimaldi through his observations of light passing through a small hole [91]. Grimaldi's work with light constituted the first recorded experimental observations of the phenomenon of diffraction and was used by physicists to show that light was in fact a wave. This wave theory of light was confirmed by the much-celebrated double slit experiment performed by the English polymath Thomas Young in 1801 [92]. The constructive and destructive interference patterns that constituted the diffraction pattern, confirmed that light indeed behaved as a wave, disproving Newton's corpuscular theory of light that dominated for almost a century before [93]. It took almost another 100 years for scientists to apply diffraction for the purpose of studying solids [94, 95]. In early 1912, the German physicist Max von Laue performed the first successful diffraction

experiment on a solid, using a copper sulfate crystal as a diffraction grating. In the latter part of 1912, two English scientists W.H. Bragg and his son W.L. Bragg performed various diffraction experiments on simple crystalline materials such as NaCl. Both the work of von Laue and the Braggs in 1912 led to the formulation of basic x-ray elastic diffraction theory. In particular, the Braggs observed that the diffraction pattern's lines (for powders) and singular peaks (for single crystals) recorded on the photographic plates were both characteristic of the material and the wavelength of the x-rays used. The Braggs explained their results by considering the lattice to be a three-dimensional diffraction grating, with an infinite number of parallel planes of atoms, separated by the interplanar distance d that would diffract the incoming x-ray beam. Using simple geometry and the wave theory of light as summarised in figure 2.1, the Braggs formulated a law describing the conditions necessary for constructive interference and consequently the appearance of the peaks in the diffraction pattern [95]. This law which bears their name, known as Bragg's law is stated as

$$2d \sin\theta = n\lambda, \tag{2.1}$$

where d, θ, λ and n are the interplanar spacing , the angle of incidence (or reflection), the wavelength of incoming radiation and a positive integer (i.e. order of reflection). It should be noted that the sinθ term in equation 2.1 is a mathematical confirmation of the observation that diffraction of waves only occurs when the the wavelength of the diffracted wave and the obstacle such as the width of a hole, are on the same order of magnitude [89]. In particular, since $0 < \sin\theta < 1$ (for diffraction), the wavelength λ must be exclusively less than $2d$ in order for Bragg's law to be applicable [96].

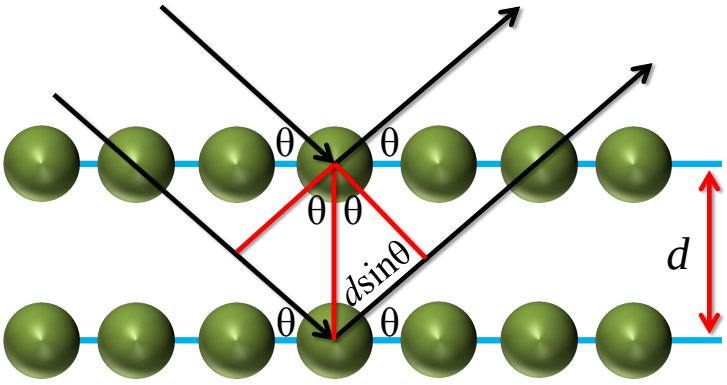

FIGURE 2.1: Derivation of Bragg's law (equation 2.1). The interplanar spacing d between parallel atomic planes (represented by the olive green spheres) introduces a phase difference between reflections from successive atomic planes. Constructive interference will only occur if the path difference $2d\sin\theta$ is equal to $m\lambda$ where $m \in \mathbb{N}_{>0}$, where θ is the angle of incidence and is assumed to equal to the angle of reflection. Adapted from Kittel [3].

Although Bragg's law provides a convenient way to determine the interplanar spacings d, one can imagine the difficulty of constructing a three-dimensional atomic array constituting the atomic lattice, simply from the values of d. Instead, it is much more convenient to approach the crystal lattice "problem" through a formulation called the von Laue formulation using the concept of reciprocal space [3]. The von Laue formulation of diffraction, unlike the Bragg formulation, does not have any particular sectioning of crystal planes. Instead, the formulation regards the crystal as composed of identical microscopic objects located at Bravais lattice sites $\mathbf{R}$, with each object at the lattice site re-radiating incident radiation in all directions, unlike the specular reflection assumption in the Bragg formulation [97]. According to von Laue, diffraction peaks will be observed in all directions where the re-radiated rays all constructively interfere with one another. By defining the problem through wavevectors $\mathbf{k}$, one can show with some geometry and Euler's identity that the reciprocal lattice is a natural and in some sense, more intuitive way of approaching a crystal lattice.

Beginning with the real space or Bravais lattice, one may define planes separated by an interplanar spacing d by their Miller indices [3, 94]. These Miller indices, conventionally denoted h, k and l, are the reciprocal values (in relative units) of where the plane intersects the $\mathbf{a}_1$, $\mathbf{a}_2$ and $\mathbf{a}_3$ axes for orthogonal symmetry. By transitioning into reciprocal space, each set of atomic planes, represented by a unique set of h, k, l values are treated as an individual point in the reciprocal lattice. In a similar manner to its real space counterpart, the recripocal lattice is also defined as a translationally invariant set of points, commonly denoted as

$$\mathbf{G} = h\mathbf{b_1} + k\mathbf{b_2} + l\mathbf{b_3}, \tag{2.2}$$

where $\mathbf{b}_i$ for $i = 1$, 2 and 3 are the reciprocal lattice basis vectors, defined as [3, 94, 97]:

$$\mathbf{b_1} = 2\pi \frac{\mathbf{a_1} \times \mathbf{a_3}}{\mathbf{a_1} \cdot (\mathbf{a_2} \times \mathbf{a_3})}, \tag{2.3}$$

$$\mathbf{b_2} = 2\pi \frac{\mathbf{a_3} \times \mathbf{a_1}}{\mathbf{a_1} \cdot (\mathbf{a_2} \times \mathbf{a_3})}, \tag{2.4}$$

and

$$\mathbf{b_3} = 2\pi \frac{\mathbf{a_1} \times \mathbf{a_2}}{\mathbf{a_1} \cdot (\mathbf{a_2} \times \mathbf{a_3})} \tag{2.5}$$

From definitions 2.3, 2.4 and 2.5, it can be shown that **G** in equation 2.2 is orthogonal to the (hkl) lattice plane it describes in real space and its interplanar spacing is the reciprocal of the interplanar spacing of (hkl) plane in real space [94]. Returning to the von Laue formulation, diffraction will only occur if **Q** = **k** - **k**', where **k** and **k**' are the incident and final wavevector, respectively, is equal to **G** in equation 2.2. **Q** is termed the scattering vector and from Euclidian geometry, one may deduce its magnitude is equal to $\frac{4\pi sin\theta}{\lambda}$ [3]. This necessity of **Q** = **G**, i.e. the momentum transfer or scattering vector being equal to a reciprocal lattice vector is commonly referred to as the Laue condition for diffraction [94]. An extremely elegant geometric consruct summarising the Laue condition was developed by the German physicist and crystallographer P.P. Ewald, known as the Ewald sphere [98]. The Ewald sphere, as shown in figure 2.2, consists of two vectors **k** and **k**' , constituting the incident and final wavevectors of the diffraction process, respectively, each with a magnitude of $\frac{2\pi}{\lambda}$, originating at the centre of sphere. Vectors **k** and **k'** subtend an angle 2θ, representing the angle of diffraction. The sphere construct is placed onto the set of points constituting the reciprocal lattice. By the Laue condition, i.e. if **k**'-**k** equals to the reciprocal lattice vector **G**, then diffraction will occur, consequently if the two wavevectors with the particular angle 2θ intersect (at their ends) with two points in reciprocal space, then diffraction will occur.

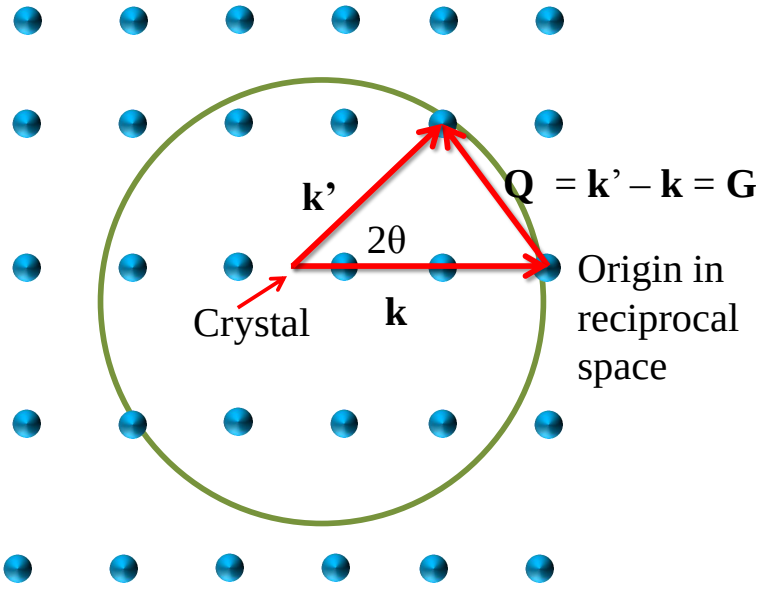

FIGURE 2.2: Pictorial representation of the two-dimensional Ewald sphere construction providing a geometric construct summarising the Laue condition for diffraction (i.e. **Q** = **k**' - **k** = **G**). Adapted from Wiebe [99].

The following section will continue with a discussion focussing on two types of radiation commonly employed for diffraction: x-rays and neutrons. Both x-rays and neutrons

have wavelengths of similar magnitude, making both suitable for the materials characterisation *via* diffraction. Furthermore, each probe has unique properties that provides some advantages over the other in certain circumstances, i.e. specific types of experiments.

2.1.2 X-Ray Diffraction

To this day, x-ray diffraction is still one of the most powerful and most commonly used experimental probes for crystal structure determination [94]. The ubiquity of the technique may be attributed to both its inexpensive nature and its relative ease of use, making x-ray diffraction an attractive probe for laboratory settings. The most common laboratory x-ray diffraction set-up consists of a sample being exposed to radiation with fixed wavelength λ while the location of peaks and their relative intensities are noted through a rotation in 2θ [90]. The conventional method for the production of x-rays in a modern x-ray diffractometer is quite similar to the inverse photoelectric effect method used by the German physicist Wilhelm Röntgen when he produced and detected the first man-made x-rays in November 1895 [100]. Conventional x-rays are produced by accelerating electrons — emitted from a heated metal filament (usually tungsten) *via* thermionic emission — through a potential difference in an evacuated tube towards a metal target, e.g. a copper target, thus producing an x-ray beam [101] as shown in figure 2.3. The x-ray beam has two components as shown in figure 2.4: (i) Bremsstrahlung and (ii) electronic transitions within the metal target. The first component or Bremsstrahlung component (from the German words *bremsen* and *Strahlung* meaning *to brake* and *radiation*) yields a low intensity white (continuous) background spectrum of x-ray radiation [90, 97]. The Bremsstrahlung radiation is a consequence of the rapid deacceleration of electrons as they experience both an electrostatic attraction force as they approach the positively charged nuclei and an electrostatic repulsion force as they approach the electrons that constitute the metal target. On the other hand, the second component of the x-ray beam is caused when the accelerated electrons (from the cathode) collide with an inner shell electron in the metal target which creates an inner core vacancy. Consequently, an outer shell electron will de-excite and fill the vacancy, thus requiring a reduction in energy that is achieved by the emission of x-ray radiation. Unlike the Bremsstrahlung x-ray radiation, since the electronic transitions have particular energy values due to energy quantisation at the atomic level, the x-rays that are produced through electronic transitions are not continuous but rather are fixed [3]. The x-ray radiation produced is characteristic of both the metal target (the anode) that is being bombarded with electrons and the energy levels of the metal target that are involved during the particular electronic transition. These particular electronic transitions

are labelled based on the notion of atomic shells involved in the electronic transition. A transition is labelled by the final "shell" (K, L and M for n = 1,2 and 3, respectively) where the de-excited electron fills the vacancy. A subscript is provided to indicate which shell where the de-excited electron originates from (α, β, γ for a difference of 1, 2 and 3 energy levels, respectively). An example — and most intense x-ray source from electronic transition — would be K_α, implying a $2p$ to $1s$ electronic transition. It should be noted that upon closer inspection that the K_α electronic transition is actually a doublet $K_{\alpha,1}$ and $K_{\alpha,2}$ as a consequence of spin orbit coupling for the $2p$ atomic orbital (i.e. $\frac{1}{2}$ and $\frac{3}{2}$ for L - S and L + S, respectively) [3]. Therefore, the x-ray spectrum from a typical laboratory source would contain intense sharp features — representing the discrete electronic transitions — overlaid on a low intensity continuous Bremsstrahlung background.

Since a typical laboratory x-ray diffraction set-up requires a fixed x-ray wavelength λ, one particular emission from the electronic transitions must be selected while the other characteristic emission lines and the majority of the continuous Bremsstrahlung must be filtered out. This filtering process is accomplished by the use of a monochromator (e.g. single crystal graphite or germanium) which selects a specific wavelength *via* diffraction and the monochromated beam is directed using high precision optics towards the sample [96]. It should be noted that the angular resolution — mathematically summarised in Bragg's law — may not be precise enough to separate closely space doublets such as $K_{\alpha,1}$ and $K_{\alpha,2}$.

The geometry concerning the interaction between the monochromated beam and the sample is of particular importance due to the high x-ray absorption cross section of many materials [102]. In order to minimise the effects of absorption, the x-ray diffraction patterns for samples placed in the Siemens D5000 diffractometer are collected in reflection geometry, also known as Bragg-Brentano mode [103]. For the Bragg-Brentano mode in the Siemens D5000 diffractometer, the sample consists of a thin homogenous layer placed on an amorphous stage which remains stationary. Both the monochromated beam and the scintillation counter in the detector are moved in order throughout 2θ and intensities are recorded as a function of angle. In the past, photographic film was used to record the positions of the Bragg peaks in combination with a Guinier-Hägg camera that provided an extremely focussed beam. The photographic film would be developed with the aid of a line scanner and the darkness of the film would be converted into a relative intensity. The usage of photographic film possesses numerous disadvantages including oversaturation of the photographic film and has provided stimulus for the development of advancements in detector technology including charge coupled devices and phosphor screens [94, 97, 104].

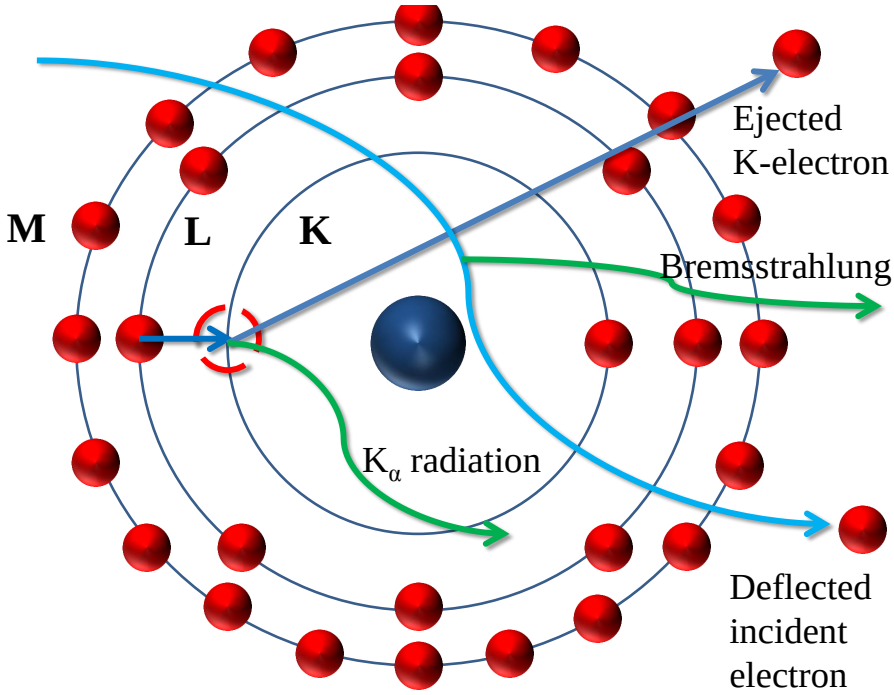

FIGURE 2.3: Pictorial representation of the mechanism for production of x-rays in modern laboratory sources *via* the bombardment of a metal target (e.g. Cu) by electrons accelerated through a potential difference. Characteristic radiation such as K_α is a result of electrons from higher energy shells filling inner shell vacancies created *via* the collision of the electrons on the metal target. A low intensity white background Bremsstrahlung component is a result of the rapid deacceleration of the incident electrons as they experience electrostatic forces *via* the metal target's constituent electrons and nucleus. Adapted from Hallas [42].

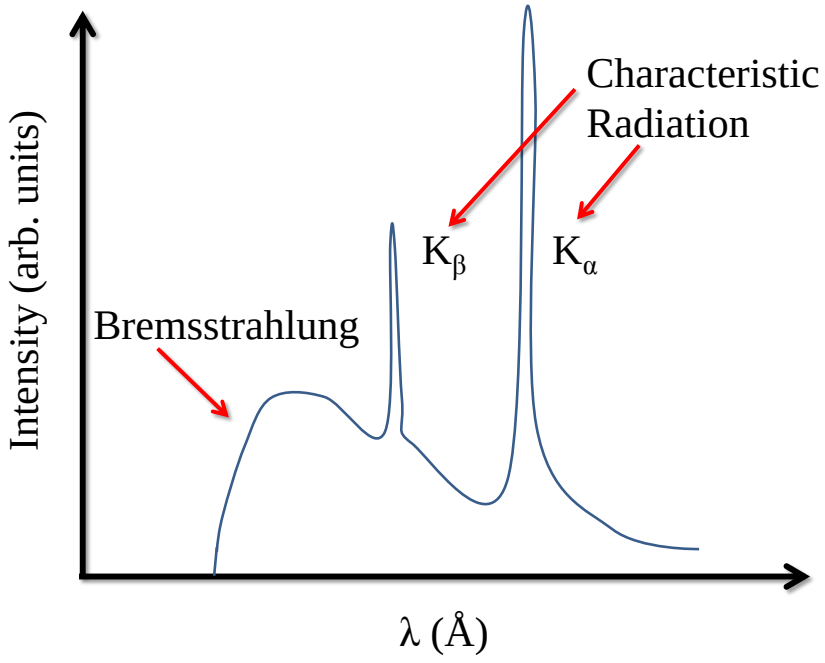

FIGURE 2.4: Pictorial representation of a sample spectrum produced by an x-ray tube used in conventional laboratory sources consisting of sharp characteristic radiation peaks (K_α, K_β, etc.) overlaid on a continuous Bremsstrahlung background. Adapted from Wiebe [99].

Although both Bragg's law (equation 2.1) or equivalently, Laue's condition for diffraction, provides the position of Bragg reflections, both statements do not provide any information concerning the relative intensities of these reflections. The relative intensities of Bragg reflections are provided by F, termed the structure factor, a mathematical function that describes the relative amplitude and phase of diffracted waves [104]. It should be noted that the intensity is proportional to the square modulus of the structure factor,

$$I \propto |F|^2, \tag{2.6}$$

where I is the relative intensity. Since the intensity is proportional to the square modulus of the structure factor, any information concerning phase is lost and this problem is commonly referred to as the *phase problem of diffraction* [105]. The structure factor is defined as

$$F = \sum_j f_j(2\theta) e^{i\mathbf{Q}\cdot\mathbf{r_j}}, \tag{2.7}$$

where $\mathbf{Q}$ is the scattering vector, r_j is the position in real space for atom j, f_j is called the scattering factor for atom j and sum is taken over all atoms j that form the basis. From equation 2.7, the scattering factor f_j may be interpreted as a mathematical tool to describe the scattering object, or more precisely, its spatial distribution in reciprocal space, effectively summarising its ability to scatter the incident radiation (e.g. x-rays). Since the scattering object for x-rays are electrons [3, 94], the x-ray scattering factor is defined as the Fourier transform of the real space electron density of the particular atom of interest,

$$f_j = \int \rho_{electronic}(\mathbf{r_j}) e^{i\mathbf{Q}\cdot\mathbf{r_j}} d\mathbf{r_j} \tag{2.8}$$

where $\rho_{\mathrm{electronic}}$ is the electronic density of atom j in real space and in the limit of $\mathbf{Q} \to 0$, the x-ray scattering factor in equation 2.8 becomes

$$f_j = \int \rho_{electronic}(\mathbf{r_j}) d\mathbf{r_j} = Z, \tag{2.9}$$

where Z is the atomic number since the integral is reduced to integrating the electronic density over all (real) space [3, 94, 104]. Since the $I \propto |F|^2$ (equation 2.6) and F is also a function of *f(j)* (equation 2.7) then since f_j for x-rays is a function of $\mathbf{Q}$, then F must possess an angular dependence, i.e. $F = F(2\theta)$. This angular dependence implies

that the measured intensities from x-ray diffraction will decrease as a function of **Q** or commonly stated as $\frac{sin\theta}{\lambda}$ to reflect its angular dependence explicitly [3].

Despite the historic importance and ubiquity in the modern day laboratory, x-ray diffraction does possess significant weaknesses compared to other diffraction probes [3, 90]. Since the intensity of a particular Bragg reflection is dependent on the electron density of the material being examined, there are two significant weaknesses of x-ray diffraction. Since the resulting intensities from x-ray diffraction depend on electron densities, elements of very similar electron density will provide similar relative intensities (within a certain 2θ range). Furthermore, elements with low atomic numbers such as hydrogen or oxygen will be "invisible" or have practically negligible intensities compared to the intensities of heavier elements such as f-block elements [3]. Consequently, if both light and heavy elements are present in a sample as is the case for $Pr_2Sn_2O_7$, the main compound of interest for this thesis, the structural properties of the lighter elements will be less accessible due to the presence of the heavier elements, attributed to their much higher electron density. Another weakness of x-ray diffraction is the fact that x-rays have the appropriate wavelength in order to probe interplanar distances (i.e. $\lambda \sim$ Å) but their energy, defined by the fundamental momentum-energy relationship

$$E_\lambda = \frac{hc}{\lambda}, \tag{2.10}$$

where h and c are Planck's constant and the speed of light in a vacuum, respectively, is too large for non-elastic processes [97]. In fact, the energy of x-rays can reach on the order of $\sim 10^3$ eV [101], an energy scale much larger than the energy required for average excitations in solid. Consequently, x-rays are a suitable probe for static or elastic processes but can rarely, if ever, be used for inelastic processes. Furthermore, the weak nature of the magnetic field in electromagnetic radiation, heavily limits the ability of using x-ray diffraction to probe, in particular, magnetic properties of materials, usually requiring very large and bright synchrotron sources [102]. On the other hand, neutron diffraction provides an excellent complementary diffraction probe, addressing some of the weaknesses of x-ray diffraction and will be the subject of the next two subsections.

2.1.3 Neutron Diffraction

After more than one decade from the pioneering work of Laue and the Braggs on establishing the principles of diffraction on solid state systems, a French physicist, Louis de Broglie proposed in his 1924 Ph.D. dissertation a revolutionary idea; the *wave-particle*

duality hypothesis or sometimes presented as the de Broglie hypothesis [106]. The *wave-particle duality* hypothesis can be simply interpreted — and is commonly presented — as the converse of Einstein's introduction of the photon for light. Since light, an entity which clearly exhibits wave-like properties, is composed of particles (i.e. photons), then particles, in fact, can and do exhibit wave-like properties. In particular, a consequence of the *wave-particle duality* hypothesis is that particles have an associated wavelength, termed the de Broglie wavelength λ, defined as

$$\lambda = \frac{h}{mv}, \tag{2.11}$$

where h, m and v are Planck's constant, mass and speed of the particle, respectively or alternatively expressed [96] as

$$E = \frac{h^2}{2m\lambda^2}, \tag{2.12}$$

where E is the energy of the particle, h, m and λ are Planck's constant, mass and wavelength of the particle, respectively, as previously defined. Equation 2.11 implies that not only x-rays and other forms of electromagnetic radiation can be used for diffraction experiments, but instead particles — if their λ is on the same order of magnitude of the obstacle (e.g. interplanar spacing) the wave is diffracting from — can also be probes for diffraction as well. The confirmation of the *wave-particle duality* hypothesis and the usage of particles, in particular electrons, was confirmed by two American physicists Clinton Davisson and Lester Germer at Bell labs. Their electron diffraction pattern from crystalline nickel matched the diffraction pattern predicted by Bragg's law [3, 107]. The use of another type of particle, the neutron, for the purposes of diffraction only occurred many decades after the Davisson-Germer experiment since the availability of neutrons was closely linked to the development of nuclear reactor technology. This technique was popularised by the American physicist Clifford Shull and Canadian physicist Bertram Brockhouse, both of whom would eventually win the Nobel Prize in 1994 for their pioneering work of the use of neutron scattering for studying condensed matter systems [108, 109]. The use of neutrons as diffraction probes, as opposed to (in particular) x-rays, provide numerous additional advantages and allow neutron scattering to be an extremely important complementary diffraction probe to the "traditional" and ubiquitous x-rays [96]. Such additional advantages include:

- unlike x-rays, that can only typically penetrate matter to $\sim \mu$m depth because they are scattered heavily by bound electrons, neutrons are electrically neutral

and can penetrate matter to a depth of $\sim$ centimetres. They are predominately scattered by nuclear interactions,

- unlike x-rays, that have wavelengths of the appropriate order of magnitude to observe diffraction in solids but have equivalent energies far above — sometimes, three orders of magnitude above — the typical excitations seen in solids; neutrons *via* equation 2.12 — a rearranged form of equation 2.11 — possess energies that are on the order of k_BT (i.e. the typical order of magnitude of excitations seen in solids) and thus can be used for to probe both elastic and inelastic processes,

- neutrons possess their own magnetic moment, allowing neutrons the ability to directly probe magnetic processes (e.g. magnetic ordering, magnons, etc.)

However, the production of neutrons is typically both more complicated and consequently, much more expensive to produce than x-rays [3, 96]. Currently, there are two methods for the production of neutrons for the purposes of diffraction [103]: (i) traditional reactor-based fission and (ii) spallation. Historically, neutrons used for diffraction were produced *via* nuclear fission reactions of ^{235}U in a nuclear reactor. The energy — or equivalently, wavelength or velocity — distribution of the neutrons produced would depend on the temperature of the moderator. The moderator is a cavity within the reactor itself with which the neutron is brought to thermal equilibrium. Consequently, the velocity distribution of the neutrons produced from the reactor-based fission process is a Maxwellian distribution profile dependent on the temperature of the moderator. For example, thermal neutrons would have a peak of the distribution at approximately 300 K, a heated graphite moderator would produce fast neutrons ($\sim 10^3$ K) while slow neutrons would be produced by a liquid ^1H or ^2H moderator ($\sim 10^1$ K) [90, 103]. A monochromator would be subsequently used to both (i) filter out higher order wavelengths and (ii) choose a particular wavelength to conduct an experiment with. An example would be selecting long wavelengths (i.e. large λ from a cold source) since these high λ neutrons provide excellent resolution at low $\mathbf{Q}$ where magnetic features are most prominent [110]. Despite the historic importance of reactor-based fission, spallation sources are becoming ever increasingly more popular due to higher flux demands and political/safety motivation [90]. Production of neutrons *via* spallation involves directing a pulsed beam of high energy particles (e.g. protons) — provided by an adjacent particle accelerator — at a heavy metal target (e.g. Hg or W). The high energy particles upon collision with the target activate the target's nuclei and the neutrons are a result of the subsequent nuclear decay process. Unlike reactor-based fission production of neutrons, the resulting neutron beam from spallation sources possess a characteristic time structure, a consequence of the particle accelerator's pulsing frequency [90]. The

neutron velocity distribution from these spallation sources contain a Maxwellian component but also has an additional lower λ epithermal neutron impurity which results from the gamma-activation process [110]. Once again, a monochromator and filters such as choppers are required to filter out higher order pollution and to select a particular wavelength that is required for the particular experiment.

It is now convenient to complete this particular subsection with a discussion of the basic concepts of neutron scattering. The following discussion is a concise summary of the introductory discussion in G.L. Squires' *Introduction to the Theory of Thermal Neutron Scattering* [111]. For most neutron experiments, a sample is immersed in a monochromatic beam of neutrons, the quantity that is measured is the (partial differential) neutron cross section as shown in figure 2.5. The total neutron cross section, denoted by σ_{tot}, is defined as

$$\sigma_{tot} = \frac{N}{\Phi}, \tag{2.13}$$

where N is the number of neutrons scattered per unit time and Φ is the incoming neutron flux, i.e. the number of incoming neutrons per unit area per unit time. Simple dimensional analysis will show that the units of σ are units of area and its value is proportional to the probability of a scattering event occuring.

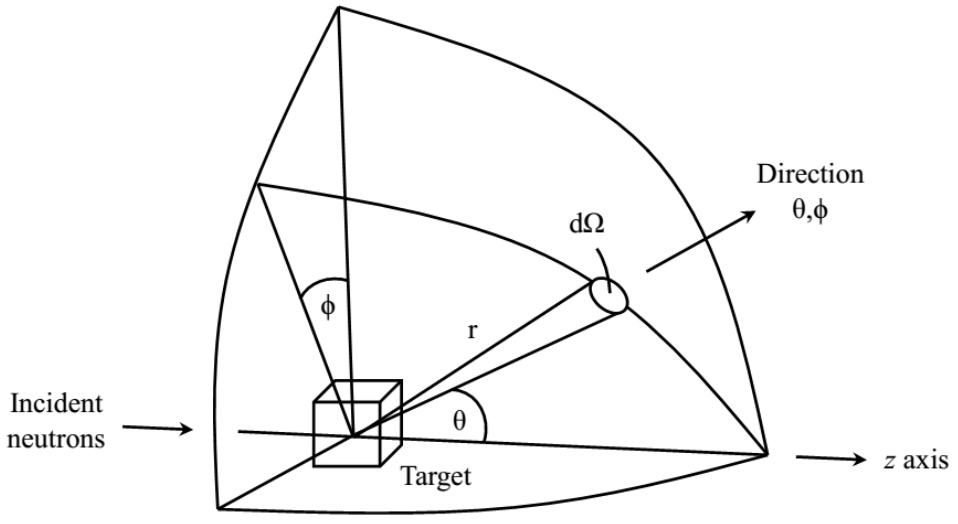

FIGURE 2.5: Pictorial representation of the geometry of a neutron scattering experiment in a spherical polar coordinate system. A sample (i.e. a general collection of atoms), also denoted as the *scattering system*, is immersed in a monochromatic beam of neutrons that are scattered in a general (θ, ϕ) direction and recorded by a detector subtending a solid angle dΩ at a distance r from the sample. Adapted by Hallas [42] from Squires [111].

It should be noted that in most neutron scattering experiments, it is in fact the partial differential neutron cross section that is measured. The partial differential neutron cross section, denoted by $\frac{d^2\sigma}{d\Omega dE_f}$, is defined as

$$\frac{d^2\sigma}{d\Omega dE_f} = \frac{N(\theta,\phi)}{\Phi d\Omega dE_f}, \tag{2.14}$$

where σ, Ω, E_f, $N(\theta,\phi,E_f)$ are the neutron cross section, solid angle, final energy and number of neutrons with a particular final energy scattered into a particular (θ,ϕ) direction per unit time, respectively. The concept of a partial differential cross section is necessary because in most conventional neutron scattering experiments, the number of neutrons incident on a detector that subtends a particular solid angle is the quantity recorded. Additionally, since neutron scattering can include both elastic and inelastic processes, the neutrons incident on a detector may have the same energy (elastic) or different (inelastic) energy as the incident neutron beam. Consequently, the total cross section σ_{tot} is simply the partial differential cross section integrated over all solid angles and over all possible energies,

$$\sigma_{tot} = \int_0^{\infty}\int_0^{4\pi} \frac{d^2\sigma}{d\Omega dE_f} d\Omega dE_f, \tag{2.15}$$

where the differential cross section is integrated over all 4π steradians and the final energy is integrated from 0 to ∞.

Since for non-magnetic neutron scattering, neutrons only interact with the nuclei, one may use the Fermi pseudo-potential $V(\mathbf{r})$ [112],

$$V(\mathbf{r}) = \frac{2\pi h^2}{m} b_i \delta(\mathbf{r}-\mathbf{R}_i), \tag{2.16}$$

to calculate the partial differential cross section defined in equation 2.14, where b_i is defined as the scattering length of a particular nucleus at $\mathbf{R}_i$. A conventional method to calculate the partial differential cross section is to use the Fermi pseudopotential in Fermi's golden rule [113],

$$\frac{d^2\sigma}{d\Omega dE_f} = \frac{k'}{k}\left(\frac{m}{2\pi\hbar^2}\right)^2 \sum_{\lambda} p_\lambda \sum_{\lambda'} |\langle k'\lambda'|V|k\lambda\rangle|^2 \delta(E_\lambda - E_{\lambda'} - E_i - E_f) \tag{2.17}$$

where k, E, p_λ denote the wave vector, energy and thermal population of the state λ of the system, while the primed variables are simply the corresponding variables after the scattering process. The resulting expression for the partial differential cross section is

$$\frac{d^2\sigma}{d\Omega dE_f} = \frac{k'}{k} N b^2 S(\mathbf{Q}, \omega), \tag{2.18}$$

where **Q** is the scattering vector defined as **k**'-**k**. The last term in equation 2.18 is called the dynamical structure factor and is the Fourier transform of the nuclear correlation function [110]. The dynamical structure factor is defined as

$$S(\mathbf{Q}, \omega) = \frac{1}{hN} \sum_{i,j} \int_{-\infty}^{\infty} e^{i\omega t} \langle e^{-i\cdot\mathbf{Q}\cdot R_j(0)} e^{i\cdot\mathbf{Q}\cdot R_i(\tau)} \rangle d\tau, \tag{2.19}$$

where $\mathbf{R}_i(\tau)$ is the position vector of atom i at time τ. In fact, it is the dynamic structure factor that is measured in inelastic neutron scattering experiments and the a.c. magnetic susceptibility [114]. If one considers a situation where there are multiple nuclei with scattering lengths b_i for the i^{th} nucleus, then if one does not restrict the sum in equation 2.19, one obtains the coherent partial differential cross section,

$$\left(\frac{d^2\sigma}{d\Omega dE_f}\right)_{coh} = \frac{k'}{k} N (\bar{b})^2 S_{coh}(\mathbf{Q}, \omega), \tag{2.20}$$

where $\bar{b}$ is defined as weighted average scattering length. On the contrary, if one restricts the sum in equation 2.19 to only considering the contributions of one atom, then one obtains the incoherent partial differential cross section,

$$\left(\frac{d^2\sigma}{d\Omega dE_f}\right)_{incoh} = \frac{k'}{k} N (\overline{b^2} - \bar{b})^2 S_{incoh}(\mathbf{Q}, \omega), \tag{2.21}$$

where $\overline{b^2}$ is defined as the weighted average of the square of the scattering length. From equation 2.20, the coherent partial differential cross section depends on both the correlation between the positions of the same nucleus at different times and on the correlation between the positions of different nuclei at different times [110]. Consequenty, coherent scattering gives interference effects and provides structural information *via* Bragg peaks for long range order or diffuse scattering for short range order. On the contrary, incoherent scattering probes the correlations between the same nucleus at different times, alternatively expressed as the self-correlation function, which typically manifests itself as a background function [112].

2.1.4 Magnetic Neutron Diffraction

The following subsection is a concise summary of selected topics concerning basic magnetic neutron diffraction theory developed by Squires [111] and Izyumov [110].

The neutron is an electrically neutral composite particle, possessing a magnetic moment of 1.913 μ_{N} where μ_{N} is the nuclear magneton [8]. Since the neutron itself possesses a magnetic moment, attributed to its quark structure, magnetic interactions imparts another scattering mechanism during neutron-matter interactions. In an analogous manner in section 2.1.3, a magnetic neutron diffraction experiment generally measures the (partial differential) magnetic scattering cross section. In a similar manner to the derivation of the partial differential cross section (equation 2.18), the Fermi pseudo-potential (equation 2.16) is replaced by a second rank tensor, commonly denoted as U and which mathematically describes the interaction between the magnetic moment of the neutron and the electrons in the solid. The term U is defined as

$$U = -\gamma \mu_N \sigma \cdot \mathbf{H}, \tag{2.22}$$

where γ , μ_{N} σ and $\mathbf{H}$ are the gyromagnetic ratio, the nuclear magneton, the Pauli spin operator and the magnetic field produced by the electrons, respectively. The expression for $\mathbf{H}$ is given by

$$\mathbf{H} = \nabla \times \frac{\mu \times \mathbf{R}}{|\mathbf{R}|^3} - \left(\frac{e}{c}\right) \frac{\mathbf{v_e} \times \mathbf{R}}{|\mathbf{R}|^3} \tag{2.23}$$

where μ is the magnetic moment operator, $\mathbf{R}$ is the position vector between the electron and the point of interest, e and c are the fundamental constants for the elementary charge and speed of light in a vacuum, respectively. The expression for $\mathbf{H}$ contains both the spin contribution and the orbital contribution summarised by the first and second term in equation 2.23, respectively. By substituting equation 2.22 into equation 2.17 — which was first performed successfully in 1939 by Halpern and Johnson [115] — one obtains

$$\frac{d^2\sigma}{d\Omega dE_f} = \left(\frac{k'N}{kh}\right) (\gamma r_o)^2 |F(\mathbf{Q})|^2 \sum_{\alpha,\beta} (\delta_{\alpha,\beta} - \hat{Q}_\alpha \hat{Q}_\beta) S^{\alpha\beta}(\mathbf{Q}, \omega), \tag{2.24}$$

where k, N, h, γ, r_{o}, $F(\mathbf{Q})$, $S^{\alpha\beta}(\mathbf{Q}, \omega)$ are the wave vector, number of particles considered, the gyromagnetic ratio, the classical radius of the electron ($\mathrm{r_o}$ = 2.818 x 10^{-15}

m) [8], the magnetic form factor and the magnetic scattering function, respectively. The magnetic scattering function is defined as

$$S(\mathbf{Q},\omega) = \frac{1}{2\pi}\sum_{R} e^{i\mathbf{Q}\cdot\mathbf{R}} \int_{-\infty}^{\infty} e^{i\omega\tau}\langle S_{0\alpha}(o)S_{R\beta}(\tau)\rangle d\tau, \tag{2.25}$$

where the term $S_{R\beta}(\tau)$ denotes the β component of the spin tensor at position $\mathbf{R}$ and at time τ. Comparing equations 2.24 and 2.25 to equations 2.18 and 2.19, four distinct differences are introduced when magnetism is considered. Firstly, the scattering length b is replaced by the constant γr_o reflecting the fact that magnetic neutron scattering is probing both the electrons and the magnetic fields these electrons produce. Secondly, the magnetic form factor is introduced. The magnetic form factor is analogous to the atomic form factor in equation 2.8 for x-rays. Recall that the form factor is a Fourier transform and in particular, the magnetic form factor is the Fourier transform of the spatial distribution of the magnetic moment instead of the electron density as is the case in x-rays. Thirdly, the term $\delta_{\alpha\beta} - \hat{Q}_\alpha\hat{Q}_\beta$, where the indices α and β refer to the spin components of the tensor, indicates that coupling between the neutron and the magnetic moments and/or spin fluctuations can only occur if they are orthogonal to the scattering vector $\mathbf{Q}$. This orthogonality requirement is quite important when eliminating possible symmetry groups for the magnetic unit cell *via* symmetry. Finally, the magnetic scattering function $S^{\alpha\beta}$ is the Fourier transform of the spin-spin correlation function and it is this quantity — just like equation 2.19 in the case of non-magnetic neutron scattering— that is measured when one extracts the partial differential magnetic cross section. The magnetic scattering function contains within it crucial information concerning both the spatial and temporal correlations between individual spins allowing one to determine magnetic structure, magnetic correlations (e.g. magnons), and many relevant quantities to solid state magnetism. A final observation is that since the magnetic neutron scattering function is the Fourier transform of the spin-spin correlation function, a conventional (elastic) magnetic neutron diffraction pattern will (usually) consist of sharp Bragg peaks overlaid on top of a broad diffuse background. The Bragg peaks are indicative of long range static — on the time scale of the neutron — spin-spin correlations. While the broad diffuse background, commonly referred to as diffuse scattering, are indicative of short range spin-spin correlations.

2.1.5 The Rietveld Method

Although both x-ray diffraction and neutron diffraction are excellent complementary techniques, both diffraction techniques still have the added complication of what is known as Bragg peak overlap — especially for systems possessing low symmetry —

when one attempts to solve the crystal structure from powder diffraction patterns [103]. Although the earliest experiments with diffraction by Laue and the Braggs used single crystals, many materials of interest do not exist in single crystal form due to various reasons and thus are only available in powder form [104]. For powder diffraction, instead of producing sharp single reflection spots of intensity (i.e. for a particular (hkl) Bragg reflection), one obtains so-called Debye "cones" [97]. These Debye cones of scattering are a result of powders being composed of numerous crystallites and these individual crystallites are oriented randomly in space; thus, for a given (hkl) plane, many different crystallites with different spatial orientations may satisfy Bragg's law and exhibit intensities. An additional complication of powder diffraction and the resulting Debye cones is the problem of Bragg peak overlap [116]. With high symmetry systems (e.g. cubic systems), certain crystallographic axes are equivalent (e.g. $a = b = c$ for cubic systems), powder diffraction patterns cannot distinguish between different Bragg reflections since these reflections are placed on a reduced 1-dimensional reciprocal axis but have the same d-spacing or 2θ value. This inability to distinguish these reflections when projected onto the common reciprocal axis in powder diffraction is called the Bragg peak overlap and represented a fundamental problem when solving crystal structures of samples only available in powder form.

The following discussion is a concise summary of the Rietveld refinement method as discussed by both Rietveld [117] and Egami *et al.* [116].

A solution to the Bragg peak overlap problem was proposed by the Dutch crystallographer H.M. Rietveld in 1967. Rietveld proposed a refinement method that involved fitting the entire data profile to a theoretical line profile derived from a model instead of individual reflections' intensities. This method, termed the Rietveld refinement method, is a least-squares refinement procedure involving the minimisation of the function F defined as

$$F = \sum_i w_i \left(y_{i,obs} - \frac{1}{c} y_{i,calc} \right)^2 , \tag{2.26}$$

where w_i, $y_{i,obs}$, $y_{i,calc}$ and c are a weighting factor (where $w_i = \frac{1}{y_{i,obs}}$, measured or observed experimental and calculated profile intensity from the input model and a scaling factor, respectively and the sum is taken over all profile points (i.e. over all 2θ, d or $|\mathbf{Q}|$). Consequently, the Rietveld method involves inputing an initial structural model and through the least squares refinement procedure, the model is modified so that the difference between the calculated profile intensities and the measured intensities are minimised, i.e. the function F is minimised.

The minimisation of F by adjustment of the structural model is accomplished by adjusting various parameters including both structural and instrumental. First, the raw observed intensities are corrected by a background function B,

$$y_{i,obs} = y_i - B_i, \tag{2.27}$$

where y_i and B_i are the raw observed intensity and background intensity for point i. Subsequently, the calculated (theoretical) pattern from the model is calculated and its parameters are adjusted to minimise F. The most basic form for the calculated model involves using a Gaussian peak shape function and is summarised below

$$y_{i,calc} = tS_k^2 j_k L_k \frac{2\sqrt{2ln2}}{H_k\sqrt{\pi}} e^{-4ln2\left(\frac{2\theta_i - 2\theta_k}{H_k}\right)^2} \tag{2.28}$$

where the subscript k represents a particular (hkl) reflection, t is the step width, j_k is the multiplicitly of the reflection, L_k is the Lorentz factor, H_k is the peak's FWHM, S_k is the structure factor (S was used instead of F to avoid confusion with equation 2.26) and $2\theta_k$ is calculated position of the Bragg reflection. The Lorentz factor L_k is a geometric correction which accounts for the amount of time that a point of the reciprocal lattce remains in the Ewald sphere during the measurement process [118]. The peak width function or commonly referred to as the resolution function, H_k is defined by the empirical Caglioti function [119],

$$H_k^2 = Utan^2\theta_k + Vtan\theta_k + W, \tag{2.29}$$

where U, V and W are instrumental and sample related parameters associated with the wavelength resolution, a combination of beam divergence and mosaic spread of the sample and a combination of incident beam cross section and sample diameter, respectively. With the development of much more complex Riteveld analysis software packages, many additional parameters such as peak asymmetry, preferred orientation and absorption coefficients can now be included whenever pertinent [103]. It should be noted that although many diffraction experiments' peak shapes can be properly accounted for by a simple Gaussian (up to a first order approximation) such as with continuous wave neutron sources, many other types of diffraction experiments such as time-of-flight (TOF) cannot be accounted for by a simple Gaussian.

The *goodness of fit* for the least squares refinement process in the Rietveld refinement process is quantified by several R parameters [120]. Some examples of indicators of *goodness of fit* are listed below:

- $\mathrm{R}_{wp} = \left(\frac{w_i(y_{i,obs}-y_{i,calc})^2}{\sum_i w_i(y_{i,calc})^2}\right)^{\frac{1}{2}}$: the R_{wp} parameter, also known as the weighted *R*-value, is a modified R_p parameter that includes angular dependence through an angular dependent statistical weighting factor w, which is a function of 2θ, i.e. $w = w(2\theta)$,
- $\chi^2 = \frac{R_{wp}^2}{R_{exp}^2}$: A rough "rule of thumb" is that a good refinement should have R_{wp} close to the value of R_{exp} (i.e. $\chi^2 \approx 1$) but the equality between R_{wp} and R_{exp} is not always the case such as with *R* values reported for magnetic structure refinements.

2.2 Susceptometry

The following section is a concise summary of fundamental concepts for both DC and AC magnetic susceptibility as discussed by Cullity & Graham [121].

2.2.1 DC Susceptometry

The magnetic susceptibility of a substance is defined as

$$\chi = \frac{\partial M}{\partial H}, \tag{2.30}$$

where M and H are the magnetisation and the magnetic field strength, respectively. The magnetic susceptibility χ is a proportionality constant that quantifies the degree of magnetisation in response to an applied magnetic field. Recall from Section 1.2., the magnetic susceptibility (or more precisely, the inverse of the magnetic susceptibility), provides an experimenter the ability to estimate (up to an order of magnitude), the strength and type of interactions between spins constituting a particular magnetic system through the Curie-Weiss law. Additionally, the temperature dependence of the magnetic susceptibility also provides the ability to identify magnetic transitions, in particular both the type of magnetic ordering that is occurring (e.g. AFM or FM) and its spatial coherence throughout the system (i.e. long ranged or short ranged) [122]. For example, for a magnetic system that assumes a long range ordered antiferromgnatic state, the magnetic susceptibility will exhibit a sharp cusp at the ordering temperature or the Néel temperature. If the antiferromagnetic state is only short ranged, the cusp would be broad instead of being sharp. In addition to identifying magnetic transitions, the nature of the magnetic ground state can also be determined by comparing hysteretic (history-dependent) behaviour [123]. For example, if the magnetic susceptibility differs between zero-field cooled (i.e. field is applied only at base temperature) and field-cooled

(i.e. field is applied throughout cooling), then the system may have a degenerate set of ground states (e.g. spin glasses) or this behaviour may imply the presence of rearranging domains. Both of these are possibilities and further experimental probes would be required to determine the true nature of the ground state.

The method used in this thesis for measuring the magnetic susceptibility of a substance consists of SQUID magnetometry [124]. SQUID magnetometry is an inductance method, where the magnetisation of the sample is not measured directly, rather the voltage is measured. This voltage is result of a current that is induced due to the movement of a sample inside a coil set. Consequently, the voltage, through the current and through Faraday's law determines the magnetic field produced from the sample and thus one can calculate the magnetic susceptibility from equation 2.30. The basis of SQUID magnetometry is the SQUID (**S**uperconducting **Qu**antum **I**nterference **D**evice), which is a device that can measure magnetic fields with extremely high precision. The ability of the SQUID to measure magnetic fields with such high precision is based on the Josephson effect that occurs within a Josephson junction consisting of two superconductors separated by a thin insulating layer. In 1962, American physicist B.D. Josephson discovered that the quantum mechanical wavefunctions that describe the Cooper pairs — that form the basis of superconductivity — leak into the forbidden insulating layer from either side [125]. Consequently, if the insulating layer is thin enough, the two leaked wavefunctions will overlap and the Cooper pairs will effectively tunnel together through the insulating layer, without breaking apart. The experimental manifestation from the Josephson effect is dependent on the bias across the Josephson junction. If there is no voltage present across the Josephson junction, the Cooper pairs will simply tunnel yielding a DC current. If there is a voltage present across the Josephson junction, the Cooper pairs will oscillate in the radio frequency (RF) range. Consequently, two types of SQUIDs — DC (direct current) and RF (radio frequency) — have been developed [126]. An RF SQUID consists of a single Josephson junction mounted upon a superconducting loop which is coupled to an LC circuit. Since the presence of a DC current in the SQUID results in Cooper pairs oscillating back and forth (i.e. the AC Josephson effect), if there is a change in the magnetic flux within the loop, the flow of the current (i.e. the flow of the Cooper pairs) will change as described by the Meissner effect. Since the Cooper pairs are both influenced by the AC Josephson effect and the Meisnner effect, the phase of the Cooper pairs will change and this change in phase will result in a change in the AC voltage in the loop that is detected by the LC circuit and it is this AC voltage change that allows the SQUID to be used as a high precision magnetometer [127].

The Quantum Design SQUID consists of three inductance coils that are wound in opposite directions that are connected *via* superconducting wires to the SQUID, enclosed

in a superconducting shield [126]. The superconducting shield serves two purposes: (1) it shields the SQUID from magnetic fields generated by the superconducting magnet and (2) it traps and stabilises the ambient laboratory magnetic field present when the SQUID and the superconducting shield were first cooled. The overall objective of the superconducting shield is to provide a very low and stable magnetic field in which the SQUID can operate within.

The DC magnetometry measurements performed in this thesis utilised the **v**ibrating **s**ample **m**agnetometry (VSM) option on the Quantum Design Dynacool^{TM} 9 T PPMS as shown in figure 2.6(a). For more information, please refer to the *Quantum Design Physical Property Measurement System - Vibrating Sample Magnetometer Option User Manual* [128]. A sample is placed on the end of a sample rod that is driven sinusoidally ($f \sim 40$ Hz) within a constant vertically applied magnetic field *via* a superconducting magnet. Consequently, since the sample is magnetised — due to the applied magnetic field — and it is oscillating, the magnetic flux is not constant and by Faraday's law of induction, a voltage V_{ind} will be induced,

$$V_{ind} = \frac{d\Phi}{dt} = \left(\frac{d\Phi}{dz}\right)\left(\frac{dz}{dt}\right), \tag{2.31}$$

where $d\Phi$, dt and dz are the differential of magnetic flux, time and vertical position, respectively. The VSM coil assembly will detect this voltage which will reflect the sinusoidal time dependence of the vertical drive of the sample and is mathematically summarised as

$$V_{ind} = 2A\pi fCm\sin(2\pi ft), \tag{2.32}$$

where f and A are the frequency and amplitude of oscillation, C is the coupling constant and m is the DC magnetic moment of the sample, respectively. By determining the leading coefficient of sinusoidal induced voltage expression 2.32, the desired value of m is retrieved.

2.2.2 AC Susceptometry

For this subsection, in addition to the concepts discussed by Cullity *et al.* [121], supplementary concepts from Bruce *et al.* [131] are included as well when relevant.

In contrast to DC magnetometry, the applied polarising magnetic field H that induces sample magnetisation for AC magnetometry possesses a sinusoidal time dependence, i.e.

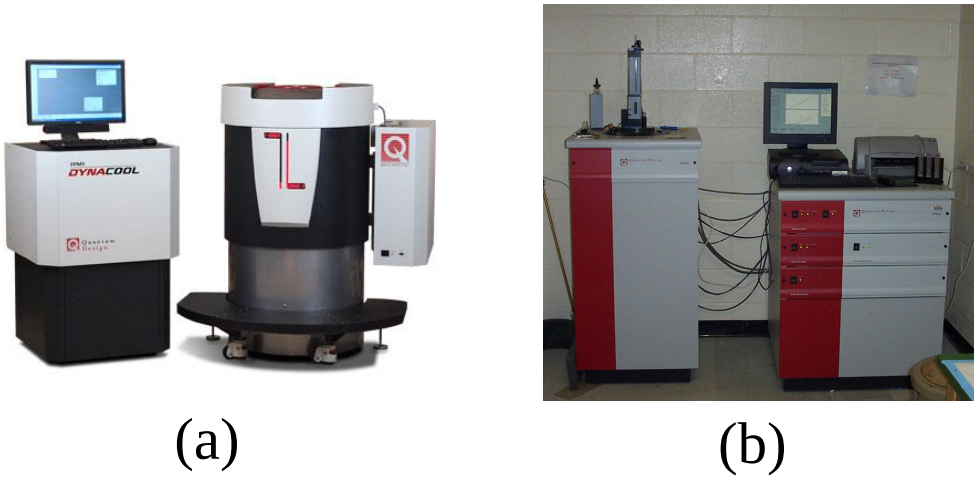

FIGURE 2.6: (a) Quantum Design Dynacool^{TM} 9 T PPMS from the Quantum Materials Group at the University of Winnipeg used for DC susceptometry and heat capacity measurements performed for this thesis [129]. (b) An example of a Quantum Design MPMS XL from the Nanomagnetism Research Group (NRG) at the University of Manitoba used for DC and AC susceptometry measurements for this thesis [130].

H is in fact $H(t)$ where

$$H(t) = H_{ac}cos(\omega t) + H_{dc}, \tag{2.33}$$

where ω, H_{ac}, H_{dc} are the angular frequency ($\omega = 2\,\pi\nu$), amplitude of the a.c. magnetic field and the amplitude of a static magnetic field component, respectively. It should be noted that the static magnetic field component H_{dc} is usually set to zero [132], as is performed for all a.c. magnetic susceptibility measurements performed in this thesis. The a.c. magnetometry measurements were performed using a Quantum Design MPMS XL (figure 2.6(b)) supplied by the Nanomagnetism group under the supervision of Professor J. van Lierop in the Department of Physics and Astronomy at the University of Manitoba.

Below a certain temperature and above a certain frequency, a magnetic system's local moments will eventually be unable to follow the sinusoidal driven a.c. magnetic field, resulting in the appearance of a phase shift for the sample's magnetisation,

$$M(t) = M_{ac}cos(\omega t - \phi), \tag{2.34}$$

where M_{ac} and ϕ are the induced magnetisation from the a.c. field and the phase shift, respectively. Using a double angle identity, equation 2.34 can be rewritten as

$$M(t) = M_{ac}(cos(\phi)cos(\omega t) + sin(\phi)sin(\omega t), \tag{2.35}$$

which can be further manipulated by using the definition of the magnetic susceptibility in equation 2.30,

$$M(t) = H_{ac}(\chi' cos(\omega t) + \chi'' sin(\omega t)), \tag{2.36}$$

introducing $\chi'$and χ'' as the in-phase and out-of-phase components of a complex a.c. susceptibility,

$$\chi = \chi' + i\chi'', \tag{2.37}$$

where the in-phase component χ' is defined as

$$\chi' = \frac{M_{ac}}{H_{ac}} cos(\phi), \tag{2.38}$$

reflecting the measurement of dispersive processes and the out-of-phase component χ" is defined as

$$\chi'' = \frac{M_{ac}}{H_{ac}} sin(\phi), \tag{2.39}$$

reflecting the measurement of absorption or irreversible processes [114].

Since the phase shift ϕ, depends on the driving frequency ω, a.c. magnetometry is a powerful tool for experimentalists to directly probe the dynamics of magnetic systems [133]. This can be seen through analysing the ω dependence of the a.c. susceptibility. By definition, as $\omega \to 0$, the a.c. susceptibility becomes the thermal susceptibility, denoted as χ_T, which is equivalent at $\omega = 0$ to the d.c. susceptibility. As $\omega \to \infty$, the a.c. susceptibility becomes the adibatic susceptibility, denoted as χ_S. Through some algebraic manipulation, one can show that

$$\chi = \chi_S + \frac{\chi_T - \chi_S}{1 + i\omega\tau}, \tag{2.40}$$

where τ is the characteristic relaxation time. Using the definition in equation 2.37, the in-phase can be rewritten as

$$\chi' = \chi_S + \frac{\chi_T - \chi_S}{1 + \omega^2\tau^2}, \tag{2.41}$$

and the out-of-phase component can be rewritten as

$$\chi'' = \frac{(\chi_T - \chi_S)\omega t}{1 + \omega^2\tau^2} \tag{2.42}$$

The ability of a.c. susceptibility to directly probe the dynamics of magnetic systems are summarised equations 2.41 and 2.42 because if $\omega\tau = 1$, then χ' will display an inflection point of $\frac{\chi_T+\chi_S}{2}$ while χ" will display a maximum of $\frac{\chi_T-\chi_S}{2}$. Consequently, for a fixed temperature, one can determine the value of τ by varying the frequency through ω and observing that

$$\tau = \omega(max[\chi'']), \tag{2.43}$$

where max[χ''] denotes the maximum of the out-of-phase component of the a.c. susceptibility. It should be noted that if the value of ω is fixed but the temperature is varied, the location of the inflection point in χ' corresponding to the maximum of χ" where $\omega\tau = 1$ will vary. The temperature where $\omega\tau = 1$ and how this temperature varies with frequency is inevitably dictated by the particular dynamics of the magnetic system under investigation. Therefore, simply put, a.c. magnetometry represents an experimental tool that can directly probe the dynamics of a magnetic system, through the characteristic relaxation time τ [134].

2.3 Heat Capacity

This section consists of a concise summary of the fundamental concepts from both classical and statistical thermodynamics relevant to the heat capacity measurements performed for this thesis. All included definitions and derivations were retrieved from Buchdahl [135], Münster [136], Waldram [137] and Hill [138].

The heat capacity of a substance, denoted by C (units: $\mathrm{J} \cdot \mathrm{K}^{-1}$), may be defined as the temperature change per unit heat transferred during a reversible process,

$$CdT = C(T)dT = \delta Q_{rev}, \tag{2.44}$$

where δQ_{rev} is the inexact differential of heat energy transferred, dT is the resulting change in absolute temperature and it is assumed that the heat capacity is a function of temperature. From the definition of entropy,

$$TdS = \delta Q_{rev}, \tag{2.45}$$

where dS is the exact differential of entropy and T is the absolute temperature, by equating the right hand side of equation 2.44 with the left hand side of equation 2.45, one obtains

$$TdS = C(T)dT, \tag{2.46}$$

and with further manipulation, one may show:

$$dS = \frac{C(T)}{T}dT, \tag{2.47}$$

consequently, if one integrates the quotient $\frac{C}{T}$ over a specific temperature range, one obtains the change in entropy over the specified temperature range of integration, given by

$$\Delta S = S(T_2) - S(T_1) = \int_{T_1}^{T_2} \frac{C(T)}{T}dT, \tag{2.48}$$

where T_1 and T_2 define the upper and lower limits of integration, respectively. It is convention in literature to normalise the heat capacity — and consequently the entropy — by the number of moles n; hence, equation 2.48 is usually written as

$$\Delta S_n = S_n(T_2) - S_n(T_1) = \int_{T_1}^{T_2} \frac{c(T)}{T}dT, \tag{2.49}$$

where the subscript n denoted these quantities have been normalised per mol of substance and c is called the molar (specific) heat capacity.

The heat capacity, defined by equation 2.44, can be specified more precisely, depending on the conditions present during the temperature change dT due to the energy transfer δQ. The heat capacity at constant volume, also known as the isochoric heat capacity, denoted as C_V is defined by

$$C_V = \left(\frac{\delta Q}{\partial T}\right)_V = \left(\frac{\partial U}{\partial T}\right)_V, \tag{2.50}$$

where U is the internal energy and the second equality is a consequence of a direct manipulation of the first law of thermodynamics,

$$dU = \delta Q + \delta W = \delta Q - pdV, \tag{2.51}$$

where W is work, p is the pressure and dV is the exact differential of volume while the second equality assumes only pressure-expansion work is present. The second type of heat capacity is the heat capacity at constant pressure, also known as the isobaric heat capacity, denoted as C_p and is defined as

$$C_p = \left(\frac{\delta Q}{dT}\right)_p = \left(\frac{\partial H}{\partial T}\right)_p, \tag{2.52}$$

where H is the enthalpy and the second equality is a consequence of a direct manipulation of the definition of enthalpy,

$$dH = \delta Q + V dp, \tag{2.53}$$

where dp is the exact differential of pressure. It can be shown *via* the fundamental thermodynamic relation,

$$dU = TdS - pdV, \tag{2.54}$$

that the isobaric and isochoric heat capacities are related by

$$C_p - C_V = T\left(\frac{\partial p}{\partial T}\right)_{V,n}\left(\frac{\partial V}{\partial T}\right)_{p.n}, \tag{2.55}$$

which can be rewritten as

$$C_p - C_V = V \cdot T \cdot \frac{\alpha^2}{\beta_T}, \tag{2.56}$$

where α is the coefficient of thermal expansion and β_T is the isothermal compressibility. It should be noted that for the samples that are of interest for this thesis, the values of α and β_T are considered negligible and thus it is assumed (as is common in literature [3, 89]) that the measured heat capacity can be characterised as isobaric or isochoric, and inferences from one or the other will be applied freely to the theory [3, 139] further developed in the section.

A general expression for the low temperature heat capacity temperature dependence of an arbitrary idealised material is

$$C_V = \gamma T + \beta T^3, \tag{2.57}$$

where the γ component represents the electronic contribution and β represents the phonon contribution to the heat capacity. The linear component (i.e.γ) in equation 2.57 is proportional to the density of states of the material's conduction electrons. Using free electron theory, it can be shown that

$$C_V = nk_B\frac{\pi^2}{2}\left(\frac{k_BT}{\epsilon_F}\right), \tag{2.58}$$

where n and ϵ_F are the density of states and the Fermi energy, respectively; while k_B and T are the Boltzmann constant and absolute temperature, respectively, as previously defined. Since the linear portion of the generalised low temperature behaviour of a material's heat capacity's temperature dependence is an indirect quantitative measure of the conduction electrons, the linear contribution for magnetic insulators such as the $Pr_2Sn_2O_7$, the compound of main interest for this thesis, will be very small compared to conductors. It is worthwhile to note that some magnetic insulators may in fact have a large γT contribution to its heat capacity. These insulators include those magnets that assume exotic magnetic states of spin glasses and quantum spin liquids, where the former's large ground state degeneracy and the latter's complicated Fermi surface containing a large low energy density of states, both contributing to the unexpected large γT contribution.

As aforementioned, the cubic component (i.e. β) in equation 2.57 is directly related to the phonon contribution to the heat capacity which can be seen directly through Debye's treatment of the isochoric heat capacity,

$$C_V = 9Nk_B\left(\frac{T}{T_D}\right)^3\int_0^{\frac{T_D}{T}}\frac{x^4e^x}{(e^x-1)^2}dx, \tag{2.59}$$

where x is an integration variable, defined as:

$$x = \frac{hc_sn}{2LkT}, \tag{2.60}$$

where c_s, L and n are the speed of sound, the physical dimension of the system and the resonating mode of the phonon, respectively. From equation 2.59, the temperature is normalised by T_D (also commonly labelled as θ_D), termed the Debye temperature and is defined as

$$T_D = \frac{hc_s}{2k_B}\sqrt[3]{\frac{6N}{\pi V}}, \tag{2.61}$$

where V and N are the volume and number of atoms present in the system, respectively. The Debye temperature may be intuitively interpreted as the temperature scale at which phonon modes begin to become frozen out (i.e. thermally inaccessible). If one assumes that T $<<$ T_D, in other words, if the system is placed in the low temperature regime, the expression in equation 2.59 becomes

$$C_V = Nk_B \frac{12\pi^4}{5} \left(\frac{T}{T_D} \right)^3, \tag{2.62}$$

revealing the celebrated Debye low temperature T^3 law and the second term in equation 2.57. Combining inferences from equations 2.58 and 2.61, at low temperatures (i.e. T $<<$ T_D), the heat capacity is dominated initially by the linear conduction electron contribution but is quickly overwhelmed by the Debye T^3 phonon contribution as the temperature is raised. This balance between the linear and cubic components of the heat capacity, summarised in equation 2.57 provided the solution to the observed discrepancy between Einstein's initial theory of solids and experimental results. Einstein's treatment assumed there was only one single frequency for the phonon modes and the resulting low temperature expansion implied an exponential low temperature behaviour for the heat capacity. Instead, Debye achieved his T^3 law by assuming that multiple possible phonon modes were present but there was an upper limit (i.e. the Debye temperature) of the modes the system could achieve. It should be noted that the quantiative precision of the Debye treatment for the isochoric heat capacity is only truly valid for highly symmetric, monoatomic materials and at very low temperatures due to the assumption that no optical modes are populated. Despite the limitations of the Debye model, its ability to account for the low temperature qualitative behaviour for many systems make the theory an excellent tool for first order approximations during the analysis of heat capacity.

From equation 2.57, the heat capacity of a material is a powerful tool to elucidate multiple properties of a particular material of interest. Such properties include the density of states for the conduction electrons, the nature of the phonon modes and most importantly, the identication of phase transitions [140]. For example, second order magnetic phase transitions are clearly identified by the presence of a lambda-type anomaly in the magnetic component of the heat capacity, consisting of a sharp and highly asymmetric peak, representing a large change in the absolute entropy of the system summarised in equations 2.47 and 2.48 [141]. For the purposes of this thesis, it is assumed that one may retrieve the magnetic component of the heat capacity by subtracting the heat capacity of a isostructural non-magnetic compound. This assumption is commonly used in frustrated magnetic systems due to two particular reasons:

- Since the compounds in this thesis are magnetic insulators, the first term in equation 2.57 will be very small compared to the phonon contribution (i.e. $\alpha << \gamma$),
- Since the γ term dominates and the γ term is directly related to the phonon contribution (i.e. the lattice vibrations), an isostructural compound should possess very similar phonon modes and thus provide a reasonable estimate for the second term in 2.57,

consequently, by subtracting the non-magnetic isostructural compound's heat capacity, only the magnetic component should remain.

From equation 2.44, the fundamental method to measure the heat capacity of a substance is to measure the corresponding change in temperature caused by a specific amount of input heat. There are traditionally two methods that are used to measure the heat capacity of a substance [142]: (1) the adiabatic calorimetic method and (2) the relaxation method. The latter method was utilized for the heat capacity measurements performed for this thesis using a Quantum Design Dynacool$^{\text{TM}}$ 9 T PPMS (figure 2.6(a)) He-3 Heat Capacity Option. The relaxation method involves placing a sample onto a sample platform that is only weakly connected to a thermal bath as shown in figure 2.7 below. The power that the system inputs in the form of a heat pulse is dependent on the final temperature of the system and it is the experimenter that sets the final temperature by defining $\Delta \mathrm{T}_o$. The heat pulses are such that they are equal to the heat lost of the sample when it reaches its final equilibrium temperature. The time it takes for the sample to achieve the final desired temperature, quantifed by the time consant τ, is directly related by the heat capacity summarised by first observing the time dependence of the temperature of the sample,

$$T(t) = T_1 + \Delta T_o(1 + e^{\frac{-t}{\tau}}), \tag{2.63}$$

where T_1 and ΔT_o are the initial temperature and desired temperature increase, respectively. The time for the system to achieve an increase of ΔT_o is summarised by

$$\tau = R_{TH}C, \tag{2.64}$$

where R_{TH} is the thermal resistance defined as:

$$R_{TH} = \frac{\Delta T_o}{\Delta P} \tag{2.65}$$

Unfortunately, the previous discussion of the relaxation method assumes that the sample and the platform are in good thermal contact and both possess identical temperatures. This is rarely the case during actual experiments where in fact the temperature of the sample and the sample stage differ by a non-negligible amount. To account for such a temperature difference, a modified form of the quasi-adiabatic relaxation approach introduced by Quantum Design, called the two-tau$^{\text{TM}}$ model was used for the heat capacity measurements performed for this thesis and is summarised briefly below. For a more detailed explanation of the two-tau$^{\text{TM}}$ model, please refer to the *Quantum Design Physical Property Measurement System - Heat Capacity Option User Manual* [129].

Since the process for measuring the heat capacity involves adhering the sample to the sample platform with grease and the sample platform is connected to the heat sink *via* wires, all four components must be considered when calculating the heat capacity. The two-tau method may be mathematically summarised by

$$C_p \frac{dT_p}{dt} = P(t) - K_w(T_p(t) - T_s(t)) + K_g(T_s(t) - T_p(t)), \tag{2.66}$$

and

$$C_s \frac{dT_s}{dt} = -K_g(T_s(t) - T_p(t)), \tag{2.67}$$

where the P, K, C and T are the power introduced for the heat pulse, thermal conductance, heat capacity and absolute temperature, respectively and the subscripts p, s, g and w denote the platform, sample, grease and the wires, respectively. The two-tau model method considers *via* equation 2.66, the thermal relaxation between the sample platform and the puck (the heat sink) and *via* equation 2.67, the thermal relaxation between the sample and the sample platform. Both thermal relaxation processes, quantified by τ_1 and τ_2, respectively are defined by

$$\tau_1 = \frac{1}{\alpha - \beta} \tag{2.68}$$

and

$$\tau_2 = \frac{1}{\alpha + \beta}, \tag{2.69}$$

where

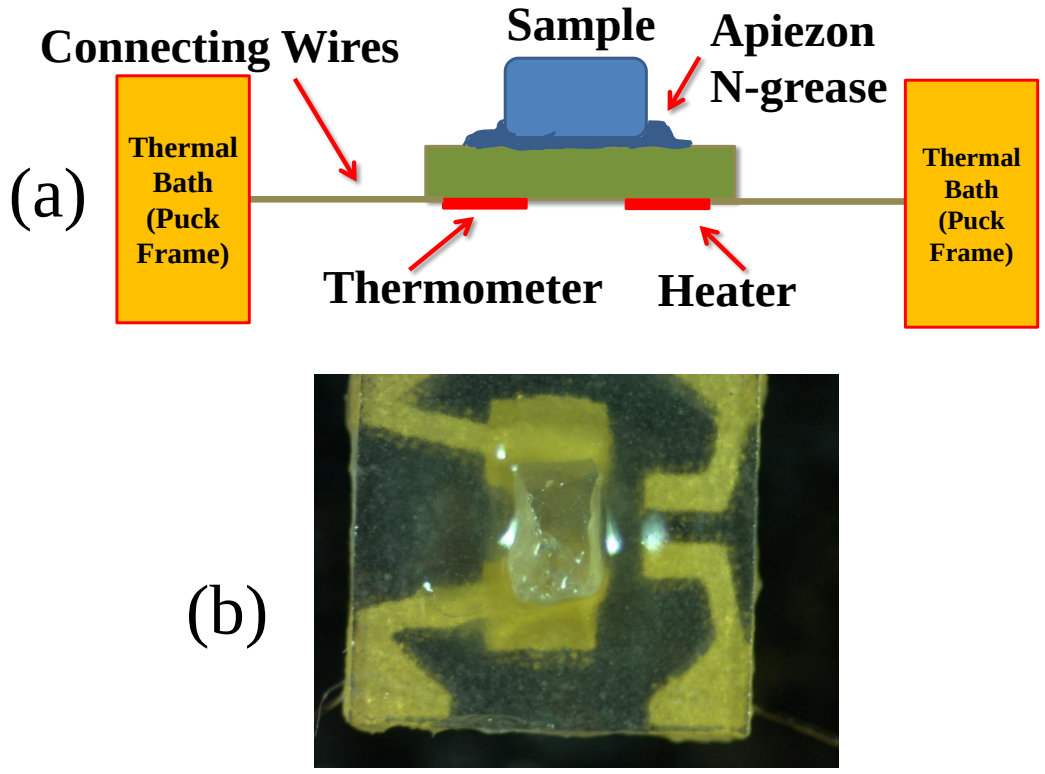

FIGURE 2.7: (a) Pictorial representation of the He-3 heat capacity mount for the Quantum Design Dynacool^{TM} 9 T PPMS adapted from [129]. (b) An example of a sample placed on the heat capacity stage. The sample is a single crystal of isotopically pure $^{154}Sm_2Ti_2O_7$ aligned along the [111] direction placed on the heat capacity stage for the Quantum Design Dynacool^{TM} 9 T PPMS He-3 Heat Capacity Option. Sample adhesion to the sample stage is accomplished by the addition of Apiezon^{TM} N-grease.

$$\alpha = \frac{K_w}{2C_p} + \frac{K_g}{2C_p} + \frac{K_g}{2C_s} \tag{2.70}$$

and

$$\beta = \frac{\sqrt{K_g^2C_s^2 + 2K_g^2C_pC_s + K_g^2C_p^2 + K_w^2C_s^2 + 2K_wC_s^2K_g - 2K_wC_sK_gC_p}}{2C_pC_s} \tag{2.71}$$

Both the values of τ_1 and τ_2 are retrieved by fitting the temperature response curve to an exponential decay model as described in equation 2.63 while the thermal conductance values are retrieved by the sample coupling between the sample and the stage. These values of τ_1 and τ_2 with the thermal conductance values, through their definitions summarised in equations 2.70 and 2.71, respectively, allow for an accurate calculation of the heat capacity of the sample.

Chapter 3

Perturbation of the Dynamic Spin Ice State *via* the Application of an External Field

3.1 Introduction and Project Motivation

$Pr_2Sn_2O_7$, like many other tin pyrochlores, has been at the forefront of condensed matter physics [34, 61, 62, 143, 144]. These pyrochlores possess two dimensional and three dimensional triangular structural motifs that make the structure highly susceptible to geometric frustration. These pyrochlores also possess a high versatility concerning the identity of the possible ions that form the structure [11]. This versatility has demonstrated to be a fruitful arena for theorists and experimentalists to investigate the roles played by properties such as single ion anistropy and crystal field interactions in the context of the selection of a magnetic ground state.

In 2008, Zhou *et al.* [31] using DC susceptometry, isobaric heat capacity, elastic and inelastic neutron scattering demonstrated that $Pr_2Sn_2O_7$ not only possessed a spin ice (SI) state but furthermore, the spin ice state was dynamic (i.e. non-static) on the neutron time scale. The spin ice conclusion was derived from the presence of diffuse scattering buildup as $\mathbf{Q} \rightarrow 0$, characteristic of spin ices [145]. An integration of the elastic channel along $\mathbf{Q}$ revealed a diffuse scattering pattern that agreed well with the expected behaviour from the dipolar spin ice model. The dynamic characteristic of the spin ice was deduced from both isobaric heat capacity and inelastic neutron scattering. The former provided a value of approximately 3.1 J/K mol Pr^{3+} for the magnetic entropy retrieved, representing a value that is significantly less than the expected value of R(2-$\frac{1}{2}$ ln$\frac{3}{2}$) $\approx$ 4.1 J/K mol for a spin ice [66]. The presence of a quantum tunneling regime was identified

through an Arrhenius plot derived from the FWHM of the quasi-elastic channel. The identification of the spin ice state in $Pr_2Sn_2O_7$ was not necessarily surprising due to Ising-like anistropy deduced from previous susceptometry results, in agreement with what one would expect from the crystal field scheme [146, 147]. The presence of the dynamic component in $Pr_2Sn_2O_7$ was surprising and represented a member of a new class of spin ices called *quantum spin ices*. These *quantum spin ices* are a large variety of magnetic systems that are characterized by a significant $\langle 111 \rangle$ anisotropy but more importantly, possess non-negligible quantum mechanical fluctuations [34, 82]. The source of these quantum mechanical fluctuations vary from system to system. For example, $Tb_2Ti_2O_7$ is an Ising-like system (below 10 K) that possesses a relatively large moment exhibiting significant quantum fluctuations. The origin of these fluctuations are attributed to a low lying crystal field state ($\Delta \approx 18$ K) that is in close proximity to the non-Kramers' doublet ground state $|M_j = 6\rangle$ ground state [145, 148]. For $Pr_2Sn_2O_7$, Princep *et al.* [149] demonstrated through a crystal field analysis that the source of quantum mechanical fluctuations in $Pr_2Sn_2O_7$ were not caused by virtual excitations to a low lying crystal field level. The crystal field analysis by Princep *et al.* confirmed the inelastic neutron scattering results from Zhou *et al.* that demonstrated $Pr_2Sn_2O_7$ is a well isolated non-Kramers' doublet system. Instead, the quantum mechanical fluctuations were caused by pollution of the ground state by non-axial $|M_J \ll J\rangle$ terms, reducing the axial anistropy characterisic of the classical dipolar spin ices. It is the presence of these quantum mechanical fluctuations that make $Pr_2Sn_2O_7$ —and its fellow *quantum spin ices* — of particular interest [34, 82, 150]. Despite the interest in these quantum spin ices, the magnetic properties of $Pr_2Sn_2O_7$ have not yet been explored in great detail [11, 144] beyond the low temperature structure in zero field.

This chapter explores the effects of perturbing the dynamic spin ice state in $Pr_2Sn_2O_7$ with the application of an external magnetic field. The motivation for perturbing the dynamic spin ice $Pr_2Sn_2O_7$ in an external magnetic field is based on the ambiguity present in the *dipolar spin ice model* phase diagram calculated by den Hertog *et al.* [20]. In particular, there is no experimental data that has directly probed what occurs at the transition between the ferromagnetic spin ice state and the proposed $\mathbf{Q} = 0$ long range ordered antiferromagnetic state (LRO AFM). This SI-AFM transition is of particular interest in the condensed matter community due to attempts by theorists to probe the dynamics of monopole-like elementary excitations within these spin ice systems, specifically the recondensation of these monopoles into the $\mathbf{Q} = 0$ LRO AFM state [151]. $Pr_2Sn_2O_7$ represents an excellent system to probe the boundary because Zhou *et al.* — confirmed by Princep *et al.* — deduced that the quantum mechanical exchange term dominates over the classical dipolar term. The former can be much more easily fine tuned by the application of a field and thus a shift towards the boundary

should be readily accomplished by the application of an external magnetic field [26]. There are three questions that this chapter attempts to address: (i) does the system form a LRO AFM state under an external magnetic field, (ii) if a LRO AFM state is formed, at what critical field does the transition occur and (iii) what is the mechanism that drives the transition?

3.2 Sample Preparation

Polycrystalline samples of $Pr_2Sn_2O_7$ were prepared by a standard solid-state reaction of stoichiometric amounts of Pr_6O_{11} (99.99 %, Alfa Aesar) and SnO_2 (99.99 %, Alfa Aesar) as described in equation 3.1 below.

$$Pr_6O_{11(s)} + 6\ SnO_{2(s)} \longrightarrow 3\ Pr_2Sn_2O_{7(s)} + O_{2(g)} \tag{3.1}$$

Both the powder reagents were mixed together, finely ground and pressed into a pellet form using a uniaxial press. The pellets were placed in an alumina crucible and were subjected to a heating routine adapted from Kennedy *et al.* [38]. The pellets were heated in air at 1000°C for 24 hours. The pellets were then reground, repelletised and heated in air at 1400°C for approximately 48 hours with intermittent grindings until powder x-ray diffraction measurements confirmed the absence of all starting reagents. The x-ray diffractogram and the subsequent Rietveld refinement with FULLPROF [152] are given in figure 3.1 below. The Rietveld refinement confirmed the presence of single phase pure $Pr_2Sn_2O_7$ possessing $Fd\bar{3}m$ symmetry with no discernible impurities. The refined lattice parameter of 10.6024(3) Å agrees within error with previously reported lattice parameters in literature [31, 38, 39].

The only adjustable crystallographic position parameter x of the 48f oxygen atom was refined to 0.33075(6), a value slightly smaller than 0.33148(5) measured by Kennedy *et al.* [38]. The smaller value of x is consistent with a larger unit cell parameter compared to the value measured by Kennedy *et al.* because they determined — through a systematic measurement of structural trends of tin pyrochlores ($A_2Sn_2O_7$) — that the oxygen positional parameter x decreases approximately linearly with lattice parameter [38]. The larger lattice parameter and smaller x parameter suggest a possibility of oxygen non-stoichiometry, attributed to the heating of samples at extremely high temperatures for long periods of time with no flowing $O_{2(g)}$. It should be noted that there is a possibility of oxygen non-stoichiometry and any conclusion derived from refinements concerning oxygen from powder x-ray diffraction is limited due to the large discrepancy between the x-ray scattering power of the high Z compounds of praseodymium and tin

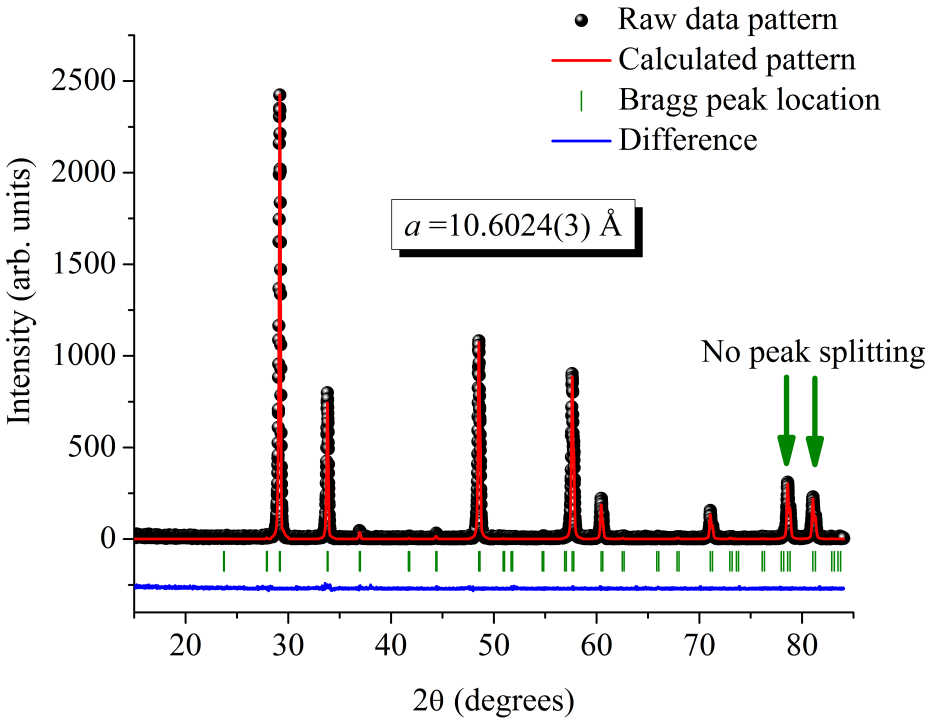

FIGURE 3.1: Measured, calculated and difference room temperature x-ray powder diffraction profiles for $Pr_2Sn_2O_7$ on a Siemens D5000 diffractometer with a $K_{\alpha_{1,2}}Cu$ source. The measured intensity is given by the black spheres, the calculated intensity is given by the red curve and the difference is given by the blue curve. The Bragg reflections' locations are given by the olive vertical lines. The lattice parameter of 10.6024(3) Å obtained from the Rietveld refinement is in agreement with lattice parameters reported in literature [31, 38, 39]. The absence of peak splitting (besides that attributed to $K_{\alpha,1/2}$) at high 2θ is noted, confirming the presence of a single pyrochlore phase.

compared to oxygen. The possibility of oxygen non-stoichiometry and sample preparation (in general) is always a concern when synthesising pyrochlores [153, 154] and has been receiving increasing attention after the recent discovery of significant sample dependence concerning the low temperature behaviour of $Yb_2Ti_2O_7$ [54].

3.3 Magnetic Susceptibility

As shown in figures 3.2 and 3.3, DC susceptiblity measurements down to 1.8 K with external magnetic fields from 0.01 to 9 T provided no anomalies corresponding to the formation of a long-ranged ordered state. The low temperature behaviour of the DC susceptibility is strongly correlated to the strength of the applied external magnetic field. The system exhibits simple paramagnetic behaviour in lower magnetic fields (down to 1.8 K) while under the application of larger external fields, the DC suceptibility saturates at a finite value, eventually to a value of appoximately 0.91(1) $J\cdot(T^2\cdot mol\ Pr^{3+})^{-1}$ under an

applied field of $\mu_o H = 9$ T. This change in behaviour — shown quite explicitly through a change in curvature of the susceptibility — is an indication of a possible field induced phase transition.

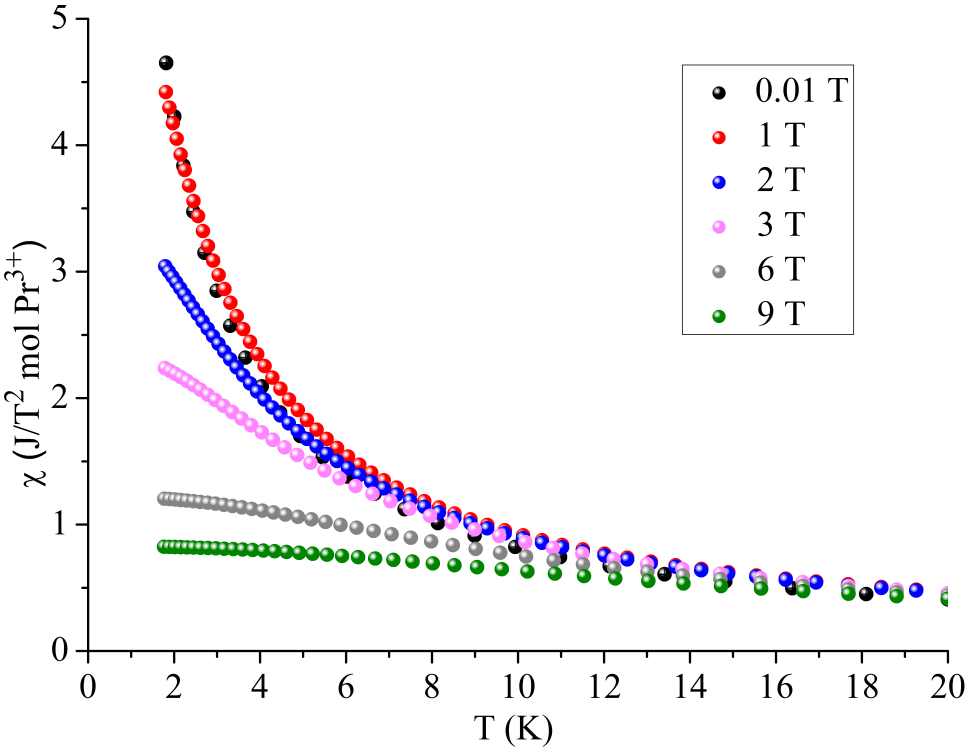

FIGURE 3.2: Molar DC ZFC magnetic susceptibility (M/H) of $Pr_2Sn_2O_7$ as a function of temperature for select applied magnetic fields.

This possibility of a phase transition is made even more evident by extracting the Curie-Weiss parameters, C and θ_{CW} from the temperature dependence of the inverse of the DC susceptibility for various applied magnetic fields. The evolution of the behaviour of C —presented as μ_{eff} as calculated by equation 3.3 from the value of C— and θ_{CW} as a function of applied magnetic field is summarized in figures 3.4 and 3.5. The Curie constant C and the Weiss temperature θ_{CW} are calculated using the Curie-Weiss law

$$\chi^{-1} = \frac{\mathrm{T}}{\mathrm{C}} - \frac{\theta_{\mathrm{CW}}}{\mathrm{C}}, \tag{3.2}$$

where χ is the DC magnetic suceptibility. The Curie constant calculated from equation 3.2 is presented as the effective magnetic moment μ_{eff}, defined as

$$\mu_{eff} = \sqrt{\frac{3k_B\chi T}{N_A}} = \sqrt{8 \cdot \mathrm{C}}, \tag{3.3}$$

where k_B, χ and N_A are the Boltzmann constant, DC magnetic susceptibility and Avogadro's number, respectively.

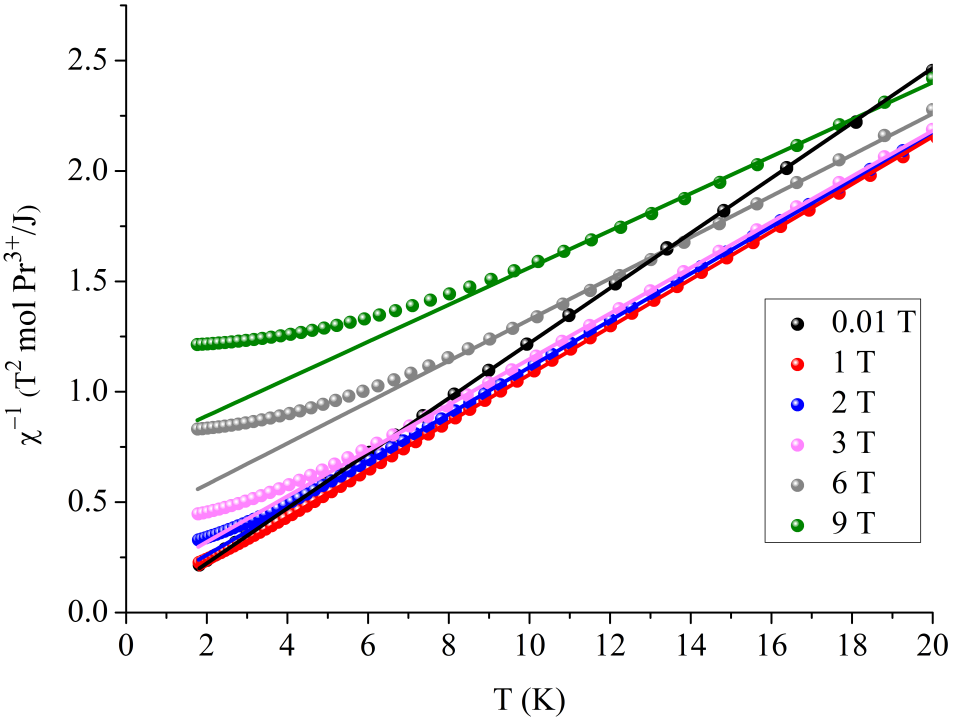

FIGURE 3.3: Inverse of the molar DC ZFC magnetic susceptibility of $Pr_2Sn_2O_7$ as a function of temperature for select applied magnetic fields with respective Curie-Weiss fits. As the external magnetic field is increased, the system's behaviour deviates from simple paramagnetic behaviour at higher temperatures as shown by the departure from linear behaviour (i.e. Curie-Weiss fits).

The ZFC (zero-field-cooled) and FC (field-cooled) behaviour of the Curie-Weiss parameters as a function of applied magnetic field were identical (within error) indicating no glassy behaviour, in agreement with previously reported behaviour in literature [31, 149]. Both the effective magnetic moment μ_{eff} and Weiss temperature θ_{CW} exhibit behaviours that are inconsistent with simple paramagnetic behaviour where both should vary linearly. Instead of varying linearly, the effective magnetic moment first experiences a drastic increase from an applied field of 0.01 to 0.1 T, increases slowly to a maximum value of 2.82(1) μ_{B} at a magnetic field of 0.5 T then decreases between 0.5 T and 0.75 T. The observed decrease is the opposite behaviour one expects from a simple paramagnet and is a possible indication of a field induced phase transition. After 0.75 T, the system appears to return to the expected linear behaviour, whereby the collection of spins become increasingly polarised with the application of a larger magnetic field, where the system will eventually saturate at the free ion moment of 3.5 μ_{B} [3].

The field dependent behaviour Weiss temperature — a measurement of the energy scale and type of spin-spin interactions — provides a possible explanation for the non-linear behaviour and consequent indication of a possible field-induced transition. Recall that the sign of θ_{CW} indicates either net ferromagnetic or antiferromagnetic interactions

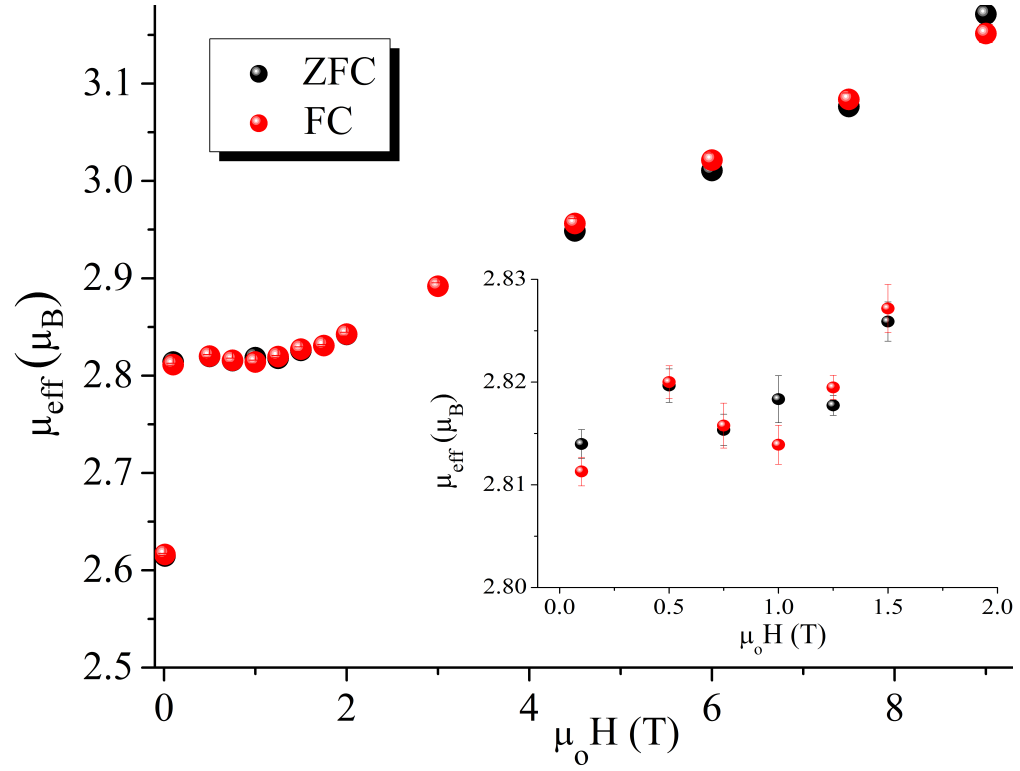

FIGURE 3.4: Calculated effective magnetic moment μ_{eff} as a function of applied external magnetic field for $Pr_2Sn_2O_7$; Inset: The effective magnetic moment's non-linear behaviour away from the dynamic spin ice state. The decrease from $\mu_o H = 0.5$ T to 0.75 T is an indication for a phase transition.

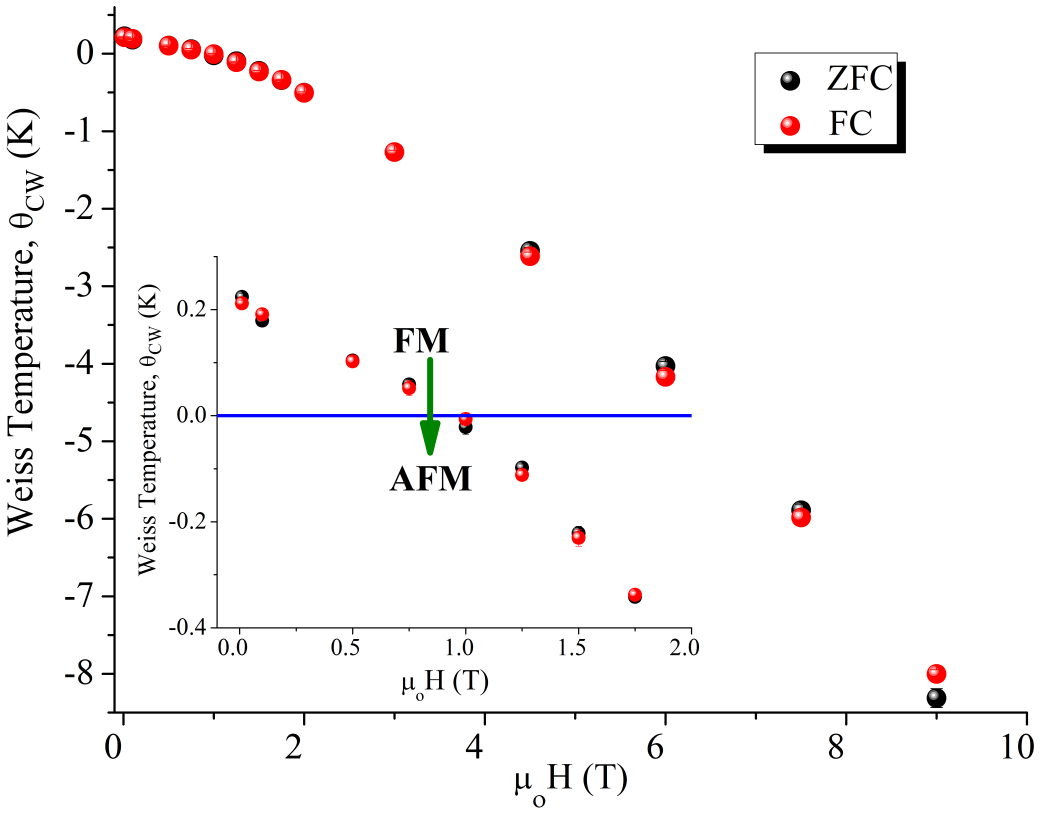

FIGURE 3.5: Calculated Weiss temperature, θ_{CW} as a function of applied field for $Pr_2Sn_2O_7$; Inset: The transition from a net ferromagnetic (FM) to net antiferromagnetic (AFM) regime occurring at $\mu_o H \approx 1$ T.

in the system [3, 20, 74, 148]. As shown in figure 3.5, the Weiss temperature decreases very quickly, representing a transition from a weak net ferromagnetic (FM) regime into a net antiferromagnetic (AFM) regime, a transition consistent with the possibility of a phase transition away from the spin ice (SI) state into an long-range-ordered (LRO) AFM state.

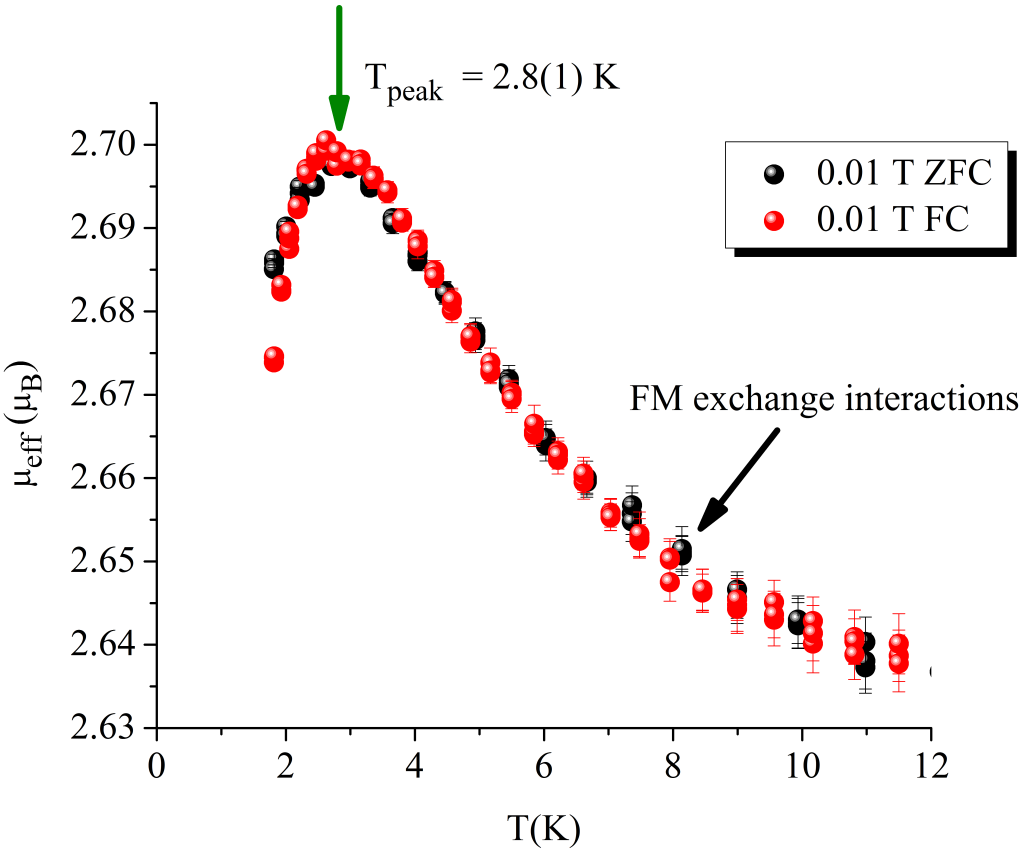

FIGURE 3.6: The effective magnetic moment μ_{eff} as a function of temperature for $\mu_o H = 0.01$ T. Two key features are noted: (1) the upward curvature is indicative of ferromagnetic interactions — required if the spin ice state is to exist — and (2) a peak that is indicative of the transition from a paramagnet to a spin ice state confirmed by elastic neutron scattering by Zhou *et al.* [31] and by magnetisation measurements in figure 3.9 using CF parameters calculated by Princep *et al.* [149].

By plotting μ_{eff} as a function of temperature, two key observations can be made. The first pertains to the high temperature tail. Recall that the term χT appears — multiplied by 3 constants — in the calculation of the effective magnetic moment. The positive curvature in figure 3.6 is indicative of net ferromagnetic interactions. As the field is increased from 0.1 T to 1 T in figure 3.7, the ferromagnetic tail consistently decreases in amplitude, eventually changing from an positive to negative curvature at 1 T, confirming the transition from net FM interactions to AFM interactions. Furthermore, the ferromagnetic tail begins to deviate from a flat paramagnetic pattern at lower temperatures at higher fields, implying the energy scale of the FM interactions are decreasing

as inferred by figure 3.5. As the magnetic field is progressively increased, the negative curvature becomes more prominent at higher temperatures — indicating stronger AFM correlations — supporting the conclusion that the system is no longer in the spin ice state as shown in figure 3.8. The second observation pertains to the low temperature peak at 2.8(1) K that is present at $\mu_o H = 0.01$ T in figure 3.6. This low temperature peak is indicative of a phase transition, specifically a transition from a paramagnet to a spin ice. The claim that the peak represents a transition from a paramgnetic state to a spin ice state is supported by both elastic neutron scattering by Zhou *et al.* [31] and crystal field calculations by Princep *et al.* [149]. Elastic neutron scattering by Zhou *et al.* on $Pr_2Sn_2O_7$ revealed strong evidence for spin ice correlations by approximately 2 K. These short range spin correlations manifest themselves as intense broad diffuse scattering — mathematicaly described by Mirebeau *et al.* [155] — that accumulates near $\mathbf{Q} \to 0$. Furthermore, Princep *et al.* using inelastic neutron time-of-flight spectroscopy and DC susceptometry, calculated the non-Kramers' doublet ground state in terms of the $\left|^{2S+1}L_J, M_J\right\rangle$ basis [149]. The ground state doublet and first excited state at 17.8(4) meV with Γ_3^+ and Γ_1^+ symmetries are shown in the $\left|^{2S+1}L_J, M_J\right\rangle$ basis as equations 3.4 and 3.5, respectively.

$$\begin{aligned}\Gamma_3^+ \text{ (0 meV)} &= 0.88\left|^3H_4, \pm4\right\rangle \pm 0.41\left|^3H_4, \pm1\right\rangle - 0.14\left|^3H_4, \mp2\right\rangle + 0.15\left|^1G_4, \pm4\right\rangle \\ &\quad \pm0.07\left|^1G_4, \pm1\right\rangle \mp 0.07\left|^3H_5, \pm4\right\rangle \pm 0.06\left|^3H_5, \mp2\right\rangle \end{aligned} \tag{3.4}$$

$$\begin{aligned}\Gamma_1^+ \text{ (17.8(4) meV)} &= 0.14\left|^3H_4, 3\right\rangle + 0.96\left|^3H_4, 0\right\rangle - 0.14\left|^3H_4, -3\right\rangle \\ &\quad +0.17\left|^1G_4, 0\right\rangle + 0.08\left|^3F_2, 0\right\rangle \end{aligned} \tag{3.5}$$

The ground state doublet proposed by Princep *et al.* is quite suggestive of not only a spin ice state but a dynamic or quantum spin state. The ground state non-Kramers' doublet possesses a strong axial $|M_J = 4\rangle$ component consistent with a $^3H_4$ Pr^{3+} ground state possessing Ising anistropy. Although small, as predicted by the arguments used in Stevens formalism, there is non-negligible pollution of the ground state by $|M_J \neq \pm J\rangle$, implying non-negligible quantum mechanical fluctuations [147]. This pollution of the ground state by non-axial terms is expected due to the significantly reduced moment and larger ionic radius of Pr^{3+} compared to Ho^{3+} and Dy^{3+} cations that constitute the canonical spin ices [149]. In fact, using a CEF method derived from Rosenkranz *et al.* [146], Princep *et al.* were able to deduce that the $\frac{\langle J_z\rangle}{\langle J\rangle}$ was approximately 0.98 and 0.97 for $Ho_2Ti_2O_7$ and $Dy_2Ti_2O_7$, respectively while $Pr_2Sn_2O_7$ exhibits a $\frac{\langle J_z\rangle}{\langle J\rangle} \approx 0.8$. This deviation from the value of 1, demonstrates that $Pr_2Sn_2O_7$ exhibits a significant

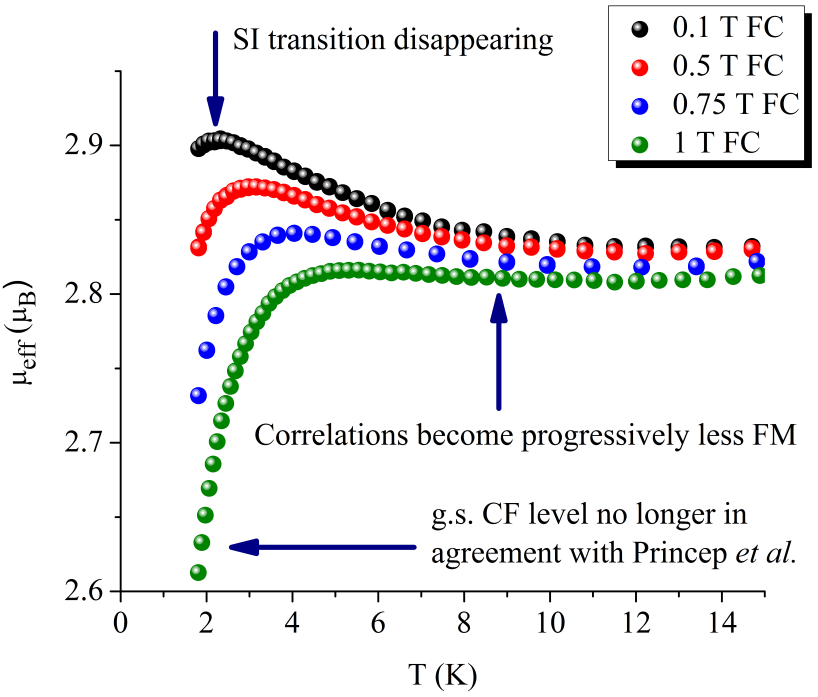

FIGURE 3.7: μ_{eff} as a function of temperature for various applied magnetic fields. As the $\mu_o H$ is increased, the FM correlations are pushed to lower temperatures, consistent with the shift of the spin ice peak to lower temperatures and eventually disappearing at approximately 0.75 T. By 1 T, the negative curvature confirms the system is in the AFM regime as inferred from figure 3.5. The μ_{eff} at base temperature is consistently reduced, significantly below the calculated moment deduced by Princep *et al.* [149] supporting the possibility of a change of CF levels, a change that would cause and accompany a field induced phase transition.

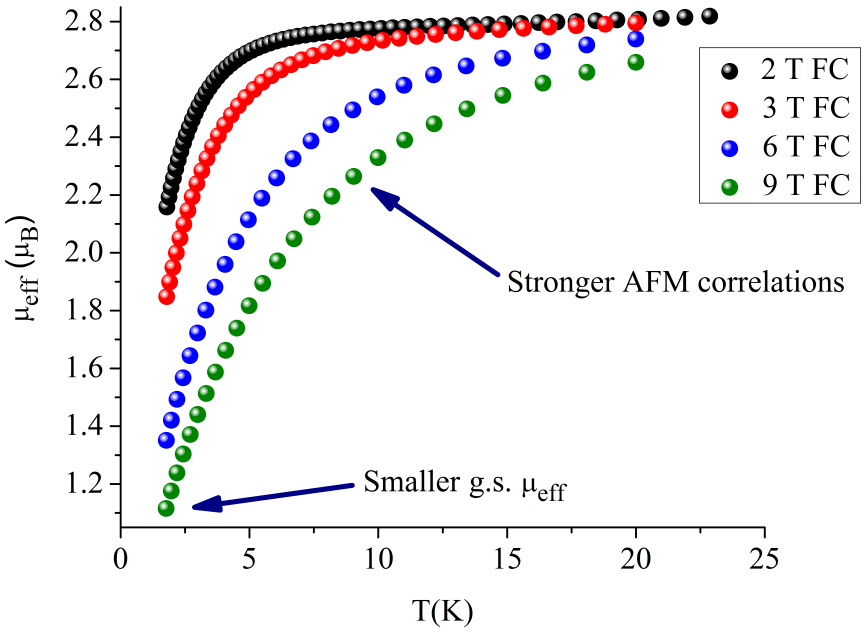

FIGURE 3.8: μ_{eff} as a function of temperature for various large applied magnetic fields. As the $\mu_o H$ is increased, the AFM magnetic correlations become stronger. Furthermore, the decrease in μ_{eff} supports the possibility of a change of CF levels causing and accompanying a field induced phase transition.

amount of XY character like $Yb_2Ti_2O_7$ [34] and $Pr_2Zr_2O_7$ [82]. The deviation away from ideal Ising-like behaviour may also be another contributing factor for the difficulty of placing $Pr_2Sn_2O_7$ in the presence of magnetic fields in the *dipolar spin ice model* phase diagram. Consequently, although the *dipolar spin ice model* does reflect experimental realities for the canonical spin ices, its applicability with respect to $Pr_2Sn_2O_7$ should correspondingly be viewed only as an approximation.

Using the convenience that Princep *et al.* expressed the ground state doublet in the $\left|^{2S+1}L_J, M_J\right\rangle$ basis set, one obtains a theoretical saturation magnetization - solely based on M_J alone - as 2.66704 μ_B/Pr^{3+} for the ground state doublet. As figure 3.6 demonstrates, as the temperature is decreased and the higher crystal field levels become thermally depopulated, the magnetic moment appears to approach a value that is proposed by Princep *et al.* for the ground state doublet. Further evidence of a spin ice transition at approximately 2 K is given by magnetization as a function of field measurements at 1.8 K shown in figure 3.9. It has been observed by Matsuhira *et al.* that polycrystalline samples of spin ices exhibit a saturation magnetisation — attributed to the two-in-two-out motif — that is approximately one half of the predicted magnetisation behaviour based on the M_J value(s) of the ground state crystal field level(s) [84]. As observed in figure 3.9, the magnetization behaviour cannot be described by a simple Brillouin function B_J (H,T) which assumes isotropic non-interacting spins [156]. Instead, the system approaches a moment of 1.32(2) μ_B/Pr^{3+}, representing half of the theoretical saturation magnetization in agreement with the behaviour predicted by Matsuhira *et al.*; thus, implying the system does possess the two-in-two-out motif by 1.8 K suggesting the spin ice state is present.

As shown in figures 3.7 and 3.8, the spin ice peak is pushed to progressively lower temperatures confirming the ferromagnetic interactions that create the state are becoming progressively weaker, in accordance to the dipolar spin ice model. Furthermore, the moment present at low temperatures progressively becomes smaller, eventually decreasing below the proposed moment by Princep *et al.* at approximately 0.75 T. This decrease in the magnetic moment at base temperature implies a significant change in the identity — specifically the constitutent $|M_J\rangle$ bases — of the ground state crystal field doublet. The continuous decrease in the moment at base temperature is consistent with an admixure of the ground state doublet Γ_3^+, which possesses a high amount of $|M_J = 4\rangle$ with the first excited crystal field Γ_1^+, which possesses many $|M_J \ll J\rangle$ non-axial terms. An admixture would be consistent with a decreased moment as $|\langle\Gamma| J_z |\Gamma\rangle|$ would decrease and is thus an indication of a phase transition.

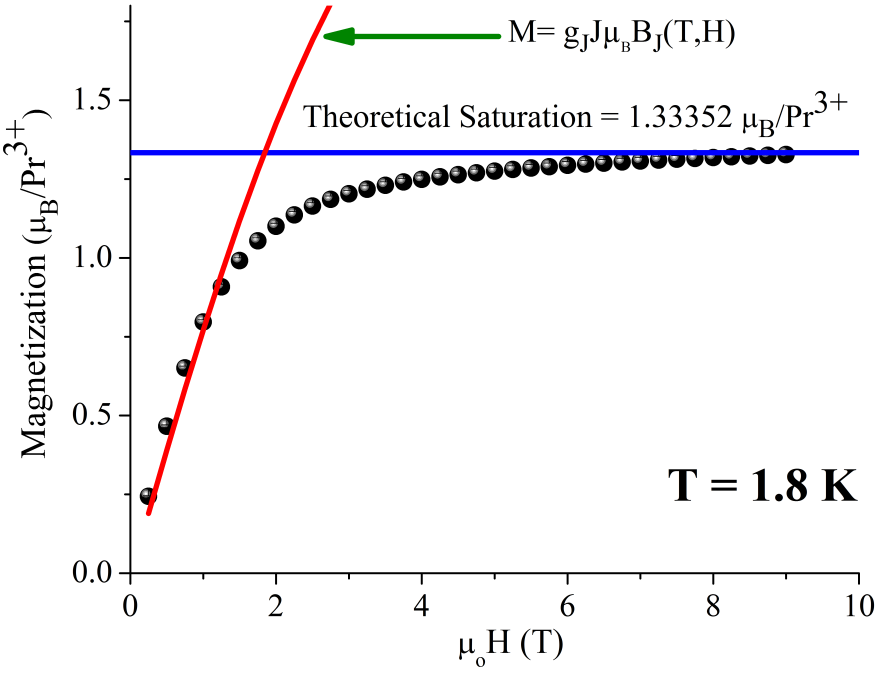

FIGURE 3.9: DC magnetisation of $Pr_2Sn_2O_7$ as a function of applied external magnetic field. The polycrystalline sample asymptotically approaches 1.33(2) μ_B/mol Pr^{3+} representing half of the theoretical magnetization limit based solely on $|M_J\rangle$ values of the constitutent crystal field level(s) as in agreement with Matsuhira *et al.* [84]. The magnetisation behaviour cannot be accounted for by a simple Brillouin function $M_J(H,T)$ for Pr^{3+} with $g_J = 0.8$, J = 4 at 1.8 K implying strong exchange interactions and single ion anisotropy.

3.4 Isobaric Heat Capacity

As an attempt to refine the value of the critical magnetic field at which the system crosses the critical $J_{NN}/D_{NN} \gtrsim$ -0.91 from the *dipolar spin ice model*, the isobaric heat capacity of polycrystalline $Pr_2Sn_2O_7$ was measured under multiple external magnetic fields. Phase pure $Pr_2Sn_2O_7$ was reground, repelleted and sintered at 1000°C for 12 hours in air to provide internal cohesion for the pellet. The isobaric heat capacity was then measured using the thermal relaxation method down to a temperature of 0.350 K under various applied magnetic fields ranging from $\mu_o H = 0.01$ T to 9 T. The mass normalized isobaric heat capacity for select magnetic fields are presented in figure 3.10.

The most striking feature in figure 3.10 is that there is no distinct sharp peak down to 0.350 K, even up to an applied magnetic field of 9 T. Instead of a sharp feature, there is a rapid increase of the heat capacity at base temperature. One can infer that the nuclear contribution to isobaric heat capacity is signficant and is the main contributor to the rapid increase at low temperatures. This inference resulted from the observation that at large fields, it became apparent that there were two Schottky-like anomalies present

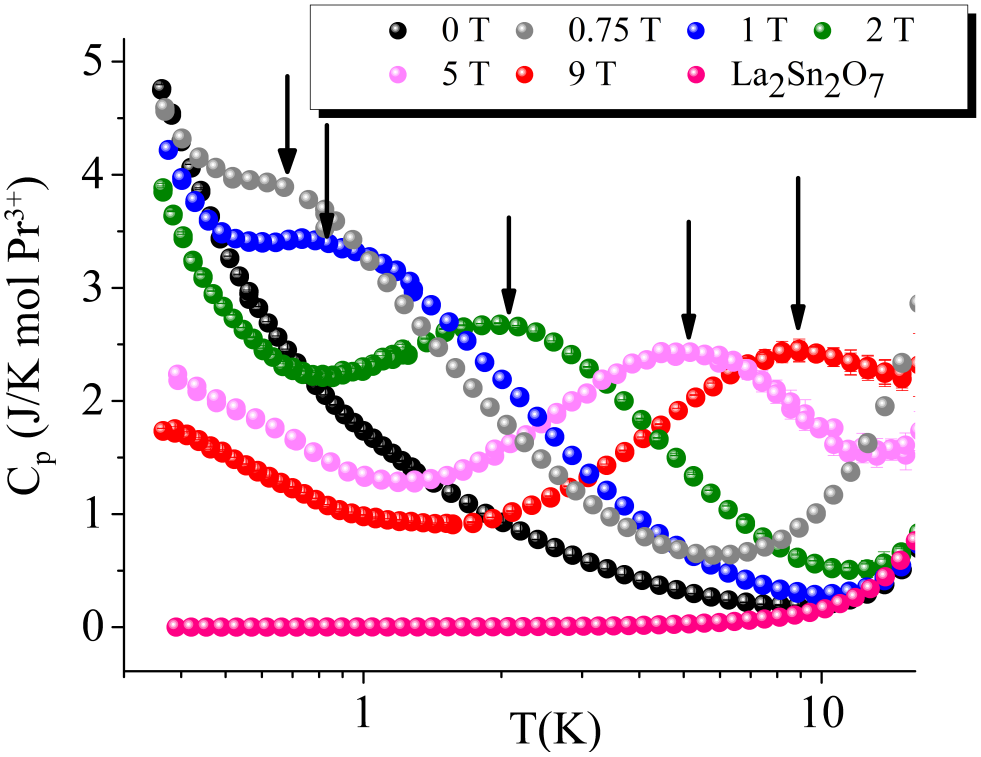

FIGURE 3.10: Mass normalized isobaric heat capacity for $Pr_2Sn_2O_7$ as a function of temperature for select applied magnetic fields. The isobaric heat capacity for the mass corrected non-magnetic isostructural $La_2Sn_2O_7$ is included as well for reference. As the external field is increased, two distinct Schottky-like anomalies become apparent. The second Schottky-like anomaly that distinctly appears and moves with the application of an external magnetic field is noted arrows for emphasis.

moving independently of one another. The first remaining relatively immobile at low temperatures while a second anomaly appears clearly after ≈ 0.75 T and moves linearly with applied magnetic field. The second Schottky-like anomaly's behaviour is distinctly magnetic with its linear dependence with respect to the applied magnetic field but the second is not purely magnetic and can only be speculated to be nuclear. The speculation that this low temperature feature is nuclear in origin is supported by similar behaviour by another praseodymium-based pyrochlore $Pr_2Zr_2O_7$, a quantum spin ice candidate which exhibits a similar mixture of nuclear and magnetic Schottky-like anomaly contributions to its low temperature isobaric heat capacity at small applied fields as shown by Kimura *et al.* [82].

In order to extract the magnetic component of the isobaric heat capacity $C_{p,mag}$, the isobaric heat capacity of a non-magnetic structural analog compound $La_2Sn_2O_7$ was measured as well. Since the isobaric heat capacity is an extensive quantity, the contribution from $La_2Sn_2O_7$ was scaled by multiplying its value by the ratio of the molar masses of $Pr_2Sn_2O_7$ to $La_2Sn_2O_7$. The scaled isobaric heat capacity of $La_2Sn_2O_7$ is also shown in figure 3.10 for reference. After subtracting the lattice component *via*

$La_2Sn_2O_7$ (i.e. the phonon component), the nuclear contribution to the isobaric heat capacity was estimated by a combination of techniques developed by Zhou *et al.* [31] and Kimura *et al.* [82]. The full form of the nuclear contribution to the isobaric heat capacity is given by

$$\mathrm{C_p} = \mathrm{R}\frac{\alpha^2}{4\mathrm{I}^2}\left(\frac{1}{\sinh^2(\frac{\alpha}{2\mathrm{I}})} - \frac{(2\mathrm{I}+1)^2}{\sinh^2\left(\frac{(2\mathrm{I}+1)\alpha}{2\mathrm{I}}\right)}\right), \tag{3.6}$$

where α is defined as

$$\alpha = \mathrm{A_{hf}}\left(\frac{\mu_{\mathrm{hyp}}^{\mathrm{Pr}}\mathrm{I}}{\mathrm{g_J k_B T}}\right), \tag{3.7}$$

where I is the nuclear spin number, A_{hf} is the hyperfine coupling constant, g_J is the Landé g-factor and μ_{hyp}^{Pr} is the static magnetic moment of the praseodymium electronic moments that the nucleus detects, causing the hyperfine field leading to the splitting of the nuclear spin energy levels. The value of I, A_{hf} and g_J are $\frac{5}{2}$, 0.078 and $\frac{4}{5}$, respectively and are all constants [157–159] with the only adjustable parameter being the static magnetic moment μ_{hyp}^{Pr} detected by the nucleus. The nuclear contribution *via* equation 3.6 was estimated by assuming that the last data points (i.e. those at base temperature) were completely attributed to the nuclear contribution and the magnetic component had a negligible component at base temperatures. This assumption, although significant, is completely valid for systems such as the canonical spin ices $Ho_2Ti_2O_7$ and $Dy_2Ti_2O_7$, whose magnetic contribution to the isobaric heat capacity at a temperature of approximately 350 mK is negligible. The extraction of the static magnetic moment $\mu_{\mathrm{hyp}}^{\mathrm{Pr}}$ with respect to the applied external magnetic field is presented in figure 3.11 below.

The behaviour of $\mu_{\mathrm{hyp}}^{\mathrm{Pr}}$ demonstrates that with the application of weak external magnetic fields, the nucleus experiences a growing hyperfine field. This increase in the hyperfine field may be attributed to the spins become increasingly polarized due to the external field. Furthermore, at approximately a critical field of $\mu_{\mathrm{o}}\mathrm{H} \approx 0.5$ T, the hyperfine field experiences a continuous decrease with the application of higher external magnetic fields. This decrease is signifiicant because it cannot be an artifact of the assumption made concerning the extraction of the nuclear Schottky. From the observations of Siddharthan *et al.* [74] and den Hertog *et al.*, as a spin ice system is pushed closer to the critical $\mathrm{J_{NN}/D_{NN}} \gtrsim$ -0.91, the spin ice anomaly in the isobaric heat capacity shifts to lower temperatures and increases in intensity, both characteristics attributed to the AFM exchange dampening the ferromagnetic dipolar interactions that stabilize the spin ice state. Consequently, as susceptometry clearly indicated, the application of the

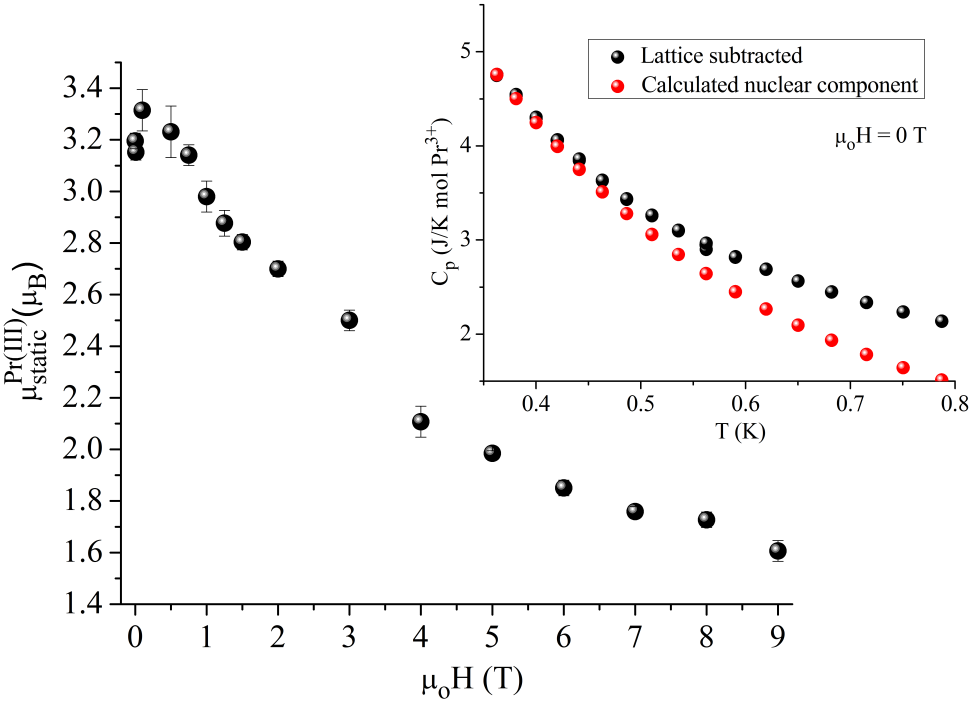

FIGURE 3.11: The static magnetic moment $\mu_{\text{hyp}}^{\text{Pr}}$ detected by the nuclear spin energy levels, calculated from equation 3.6, as a function of applied external magnetic field. The decrease from μ_{o}H = 0.5 T to 0.75 T provides support for a possible phase transition away from the spin ice state. Furthermore, the continuous decrease in $\mu_{\text{hyp}}^{\text{Pr}}$ as the external applied magnetic field increases further supports the conclusion — inferred from DC susceptometry — that the possible phase transition is driven by a change in crystal levels. Inset: The low temperature fit for a nuclear Schottky with a static Pr^{3+} moment of 3.196(3) μ_B to the $\mu_o H = 0$ T lattice subtracted isobaric heat capacity data.

field is analogous to tuning the J_{NN}/D_{NN} towards the critical boundary (i.e. away from net FM and towards net AFM); thus, one may speculate that the increase in the value for μ_{hyp}^{Pr} is simply an artifact of the increasing magnetic density at base temperatures in correspondence with the *dipolar spin ice model*. On the other hand, by applying an external magnetic field of approximately 0.75 T, the value of $\mu_{\text{hyp}}^{\text{Pr}}$ is clearly below that calculated for 0 T, implying a clear deviation of the *dipolar spin ice model*. In fact, this movement outwards is an indication of Schottky-like behaviour, which would only be present if the system was no longer in the spin ice regime. As previously noted, after the application of an external field of $\approx$ 0.75 T, the value of $\mu_{\text{hyp}}^{\text{Pr}}$ continuously decreases as the external applied magnetic field increases. This decrease is consistent with the hypothesis that the transition from a spin ice state to an LRO AFM state is driven by a change in the crystal field levels that constitute the ground state. Although it should be noted that another possibility is that the system could be populating higher crystal field levels with lower effective magnetic moments. Recall from figures 3.6, 3.7 and 3.8,

the magnetic moment of the ground state progressively decreases, to the point of its moments being well below the moment calculated by Princep *et al.* [149]. This decrease in the effective magnetic moment is clearly seen by the nuclear spin energy levels. In fact, if one were to compare the location of the higher temperature peak (i.e. the magnetic peak that appears at approximately 0.75 T), its location does not follow the expected behaviour from simple Zeeman splitting of the ground state doublet proposed by Princep *et al.* as shown in figure 3.12. Instead, the position of the peak assumes a linear pattern after a field of approximately 0.75 T and the linear pattern corresponds to a much weaker magnetic moment of approximately 1.2 μ_B which is again consistent with the hypothesis that the ground state crystal field level is being polluted by non-axial $|M_J \neq J\rangle$ terms.

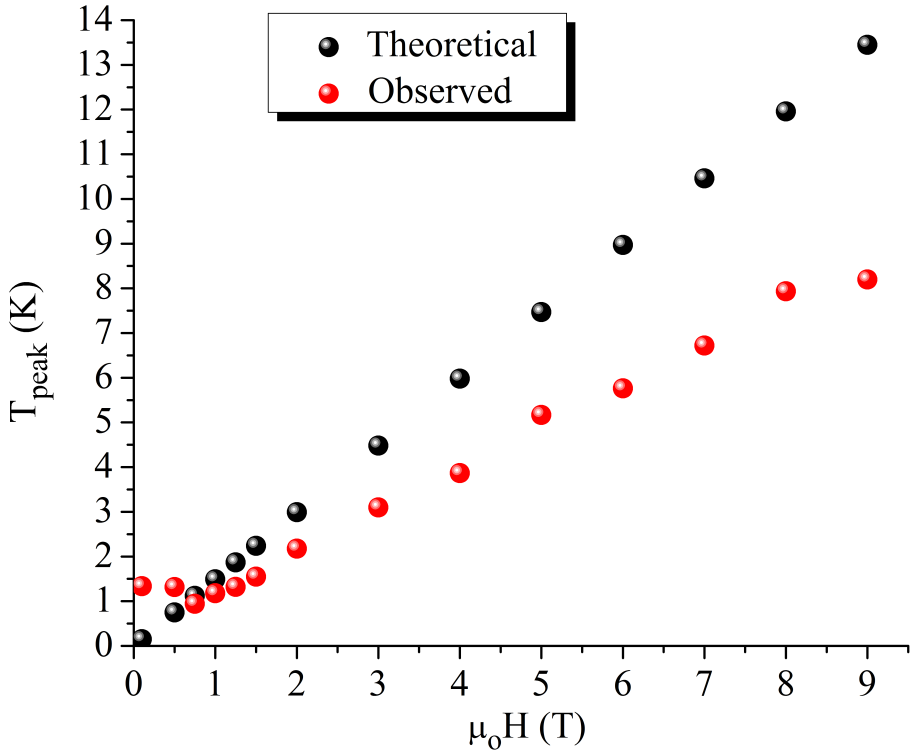

FIGURE 3.12: The location of the high temperature magnetic peak — as labelled in figure 3.10 — with respect to the external applied magnetic field. The behaviour becomes linear after approximately 0.75 T and the corresponding moment is significantly smaller ($\approx 1.2\ \mu_B$) than the moment calculated from Princep *et al.* [149]. The behaviour assuming simple Zeeman splitting of the ground state Γ_3^+ doublet calcualted by Princep *et al.* is included for comparison. This deviation away from the calculated value from Princep *et al.* once again supports the conclusion that the crystal field levels are changing — confirming conclusions inferred from figures 3.6, 3.7 and 3.8— supporting the claim for a phase transition.

The claim that a transition occurs in the vicinity of a critical magnetic external field of 0.75 T is supported by two key observations.

- By subtracting the nuclear component, as shown in figure 3.13, the evolution of a long ranged ordered magnetic state becomes quite clear. At 0 T, the system is a spin ice state, characterised by a broad feature at approximately 1 K. At 1 T, the low temperature feature has grown — to an intensity much larger than those observed in canonical spin ices — and exhibits a $\frac{1}{T^2}$ high temperature dependence, characteristic of a Schottky anomaly. As the field is increased to 9 T, a distinctly sharp feature appears at low temperatures (first appearing at an external magnetic field of 3 T as shown in figure 3.14). This sharp feature is an indication of the formation of a long range ordered magnetic state while there is increasing magnetic density present at higher temperatures, which further supports the claim that the peak at 1 T is a simple Schottky anomaly which is moving outward due to Zeeman splitting.

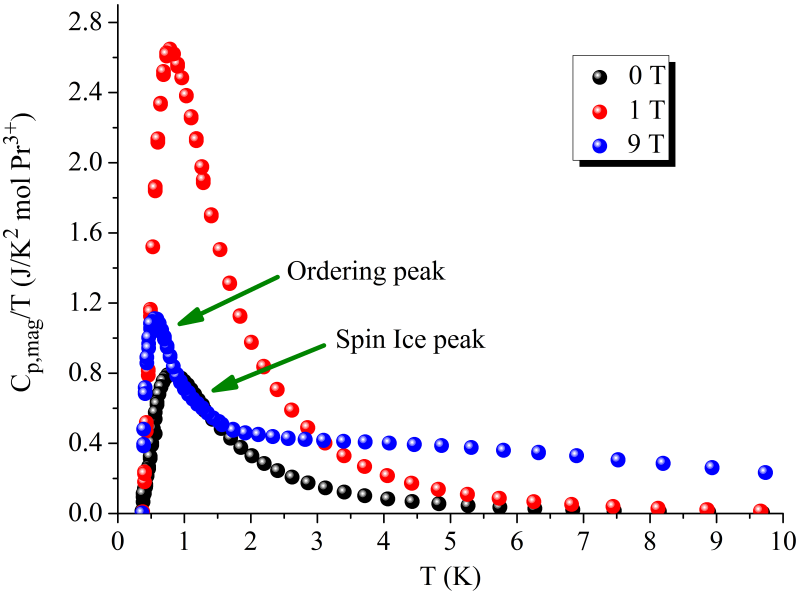

FIGURE 3.13: $\frac{C_{p,mag}(T)}{T}$ for $\mu_o H = 0$, 1 and 9 T demonstrating a shift from a dynamic spin ice state into an LRO magnetic state. At 0 T, there is a broad feature at T $\approx$ 1 K, characteristic of spin ices. At 1 T, there is a large, much sharper feature with a $\frac{1}{T^2}$ high temperature dependence, indicative of a possible Schottky anomaly. At 9 T, there is both a sharp feature at low temperature indicating the possible formation of a long range ordered magnetic state.

- In order to eliminate the ambiguity concerning the value of the external magnetic field required to transition away from the spin ice state, the magnetic entropy retrieved was calculated using the thermodynamic identity,

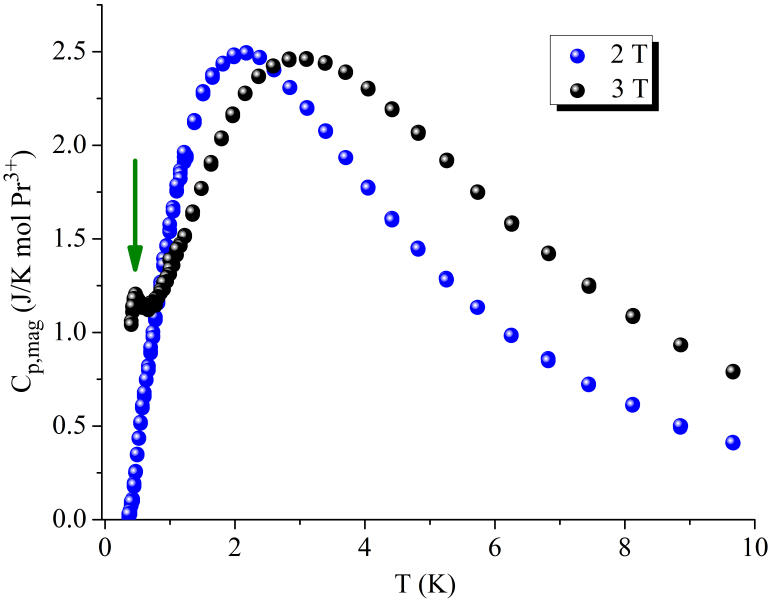

FIGURE 3.14: The appearance of a sharp feature in the magnetic isobaric heat capacity between an applied external magnetic field of 2 T and 3 T. This sharp feature indicates the formation of a long range ordered magnetic state that is clearly seen in figure 3.13.

$$\Delta S_{mag} = \int \frac{C_{p,mag}(T)}{T} dT, \tag{3.8}$$

where $C_{p,mag}$ is isobaric heat capacity after the lattce and nuclear subtraction. The integrated area (i.e. the magnetic entropy) as a function of applied external magnetic field is given in figure 3.15 below. As figure 3.15 demonstrates, the system is initially in a dynamic spin ice state characterised by the magnetic entropy being less than the Pauling entropy of R(ln2 - $\frac{1}{2}\ln\frac{3}{2}$) $\approx$ 4.1 J/K mol Pr^{3+} [31, 66]. As the external magnetic field is increased, the area approaches but still lies below Pauling entropy. After the application of an external magnetic field of 0.75 T, the entropy retrieved exceeds the Pauling entropy implying the system is no longer in the spin ice state. This significant increase can be seen directly by observing the evolution of the lattice and nuclear subtracted isobaric heat capacity between 0.5 T and 0.75 T as shown in figure 3.16 where the peak location does not shift but its magnitude increases substantially causing a significant increase in magnetic entropy being recovered. It should be noted that after 0.75 T, the magnetic entropy quickly increases towards the Rln2 (within error) — characteristic of a magnetic ground state doublet — and simply oscillates around the Rln2 limit. This oscillation, which is not significant within error, is purely artificial and represents the concomitant increase in magnetic entropy being retrieved from the formation of the long range ordered magnetic state and the shift of the Schottky

anomaly towards higher temperatures beyond the maximum temperature of 25 K where measurements and integration were performed.

As a result of the identification of the sharp peak accompanying the phase transition away from the spin ice state, an improved phase diagram — analogous to the *dipolar spin ice model* diagram from den Hertog *et al.* — can be calculated and is presented in figure 3.17. It should be noted that the phase diagram still contains some ambiguity due to the fact that the peak (accompanying the formation of the LRO magnetic state) in the isobaric heat capacity is not visible within the measured temperature range at lower fields. Consequently, the data points in figure 3.17 between 0.75 T and 2 T are simply upper limits of the value of $\frac{T}{D_{NN}}$. Furthermore, if one assumes that the LRO magnetic state's upper $\frac{\mathrm{T}}{\mathrm{D_{NN}}}$ boundary varies linearly, one can extrapolate a critical μ_{o}H value of 0.496(6) T. In fact, the phase diagram of den Hertog *et al.* demonstrates the behaviour of the LRO upper $\frac{\mathrm{T}}{\mathrm{D_{NN}}}$ boundary near the critical $\mathrm{J_{NN}/D_{NN}} \gtrsim$ -0.91 [20], descends more quickly relative to a linear trend and thus supports for a transition after an applied external field of 0.5 T. The value of 0.496(6) T, although an estimate, is quite similar to the μ_oH value obtained by Ross *et al.* for another quantum spin ice candidate $Yb_2Ti_2O_7$ [160]. As shown in figure 3.18, $Yb_2Ti_2O_7$ exhibits a field induced transition into an LRO magnetic state at approximately an external magnetic field of approximately 0.5 T. The initial proposal was that the low temperature-low field magnetic structure of $Yb_2Ti_2O_7$ consisted of three dimensional short range correlations. Inelastic neutron measurements two years later on different single crystal samples of $Yb_2Ti_2O_7$ identified this short ranged magnetic structure as the quantum spin ice state [34]. A comparison between figures 3.17 and 3.18 show strikingly similar behaviour with both similar temperature and magnetic field scales near the SI-LRO transition, supporting the classification of $Pr_2Sn_2O_7$ as a quantum spin ice candidate. Comparing the upper $\frac{\mathrm{T}}{\mathrm{D_{NN}}}$ boundary in the spin ice regime to the *dipolar spin ice model* phase diagram demonstrates that at a field of 0.01 T, the system is located at a largely positive $\mathrm{J_{NN}/D_{NN}}$ value in agreement with Zhou *et al.* [31] and Princep *et al.* [149], supporting the dynamic spin ice claim that was confirmed in figure 3.15. As the field is increased, the $\mathrm{J_{NN}/D_{NN}}$ value sharply decreases until the critical ratio is obtained. As the system enters the LRO magnetic state, large fields are required to tune the $\mathrm{J_{NN}/D_{NN}}$ away from the transition boundary, consistent with the large energetic requirements required for spin flips to create the $\mathbf{Q} = 0$ LRO AFM all-in-all-out structure [161, 162].

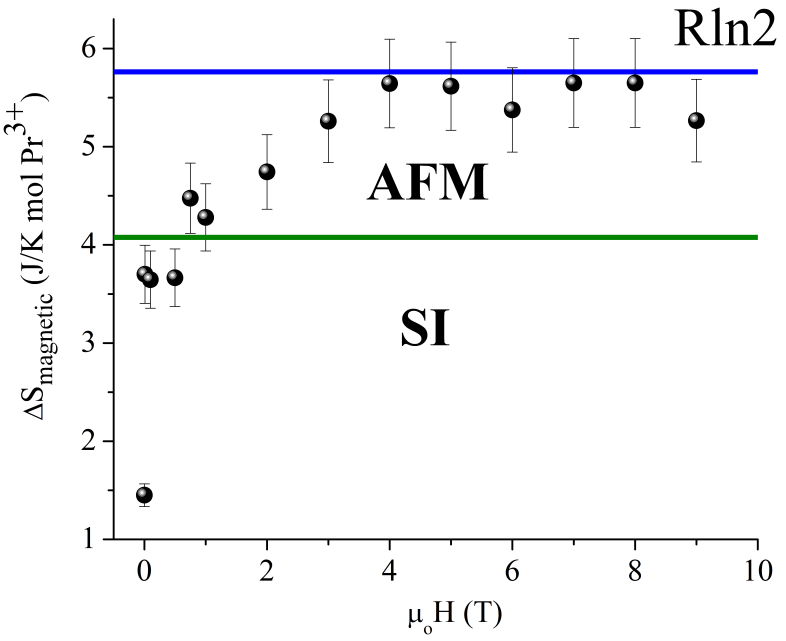

FIGURE 3.15: Magnetic entropy retrieved from 0.350 K to 25 K as a function of $\mu_o H$. The system is originally in a dynamic spin ice state due to the low value of the magnetic entropy retrieved but approaches the Pauling entropy (olive green line) with an increase in $\mu_o H$. The system exceeds the Pauling entropy, transitioning away from the spin ice state after an external applied field of ≈ 0.75 T and increases towards the Rln2 value (blue line) expected from a simple Schottky anomaly describing the magnetic ground state doublet.

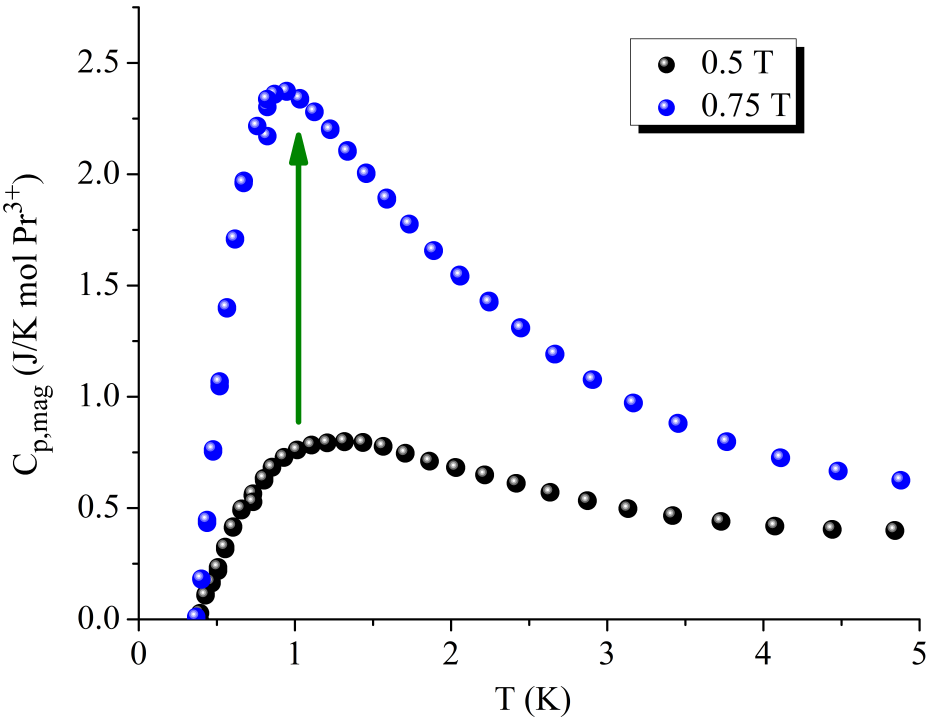

FIGURE 3.16: The magnetic component of the isobaric heat capacity for $\mu_o H = 0.5$ T and 0.75 T. The significant increase in the height of the heat capacity with little change in the peak's location provides an explanation for the area exceeding the Pauling entropy in figure 3.15 by a field of approximately 0.75 T.

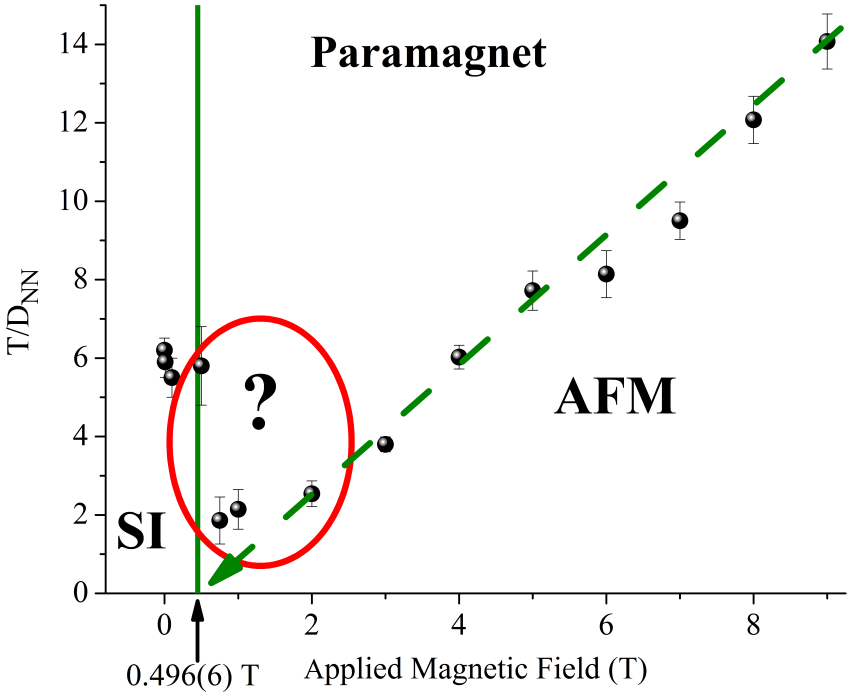

FIGURE 3.17: Phase diagram for $Pr_2Sn_2O_7$ calculated using isobaric heat capacity measurements. A critical value for μ_oH value of 0.496(6) T is noted and was calculated using a linear extrapolation from the high field upper $\frac{T}{D_{NN}}$ boundary. The red ellipse includes the lowest field measurements in the LRO $\mathbf{Q} = 0$ AFM state and represents only approximations to the actual upper $\frac{T}{D_{NN}}$ boundary. The application of an external magnetic field causes a shift away from a ferromagnetic nearest neighbour exchange dominated system to an AFM exchange dominated system. Once the critical $J_{NN}/D_{NN} \gtrsim$ -0.91 is crossed, large fields are required to tune the J_{NN}/D_{NN} ratio away from the SI-AFM transition due to the large energetic requirements for spin flipping that accompanies the formation of the LRO AFM state.

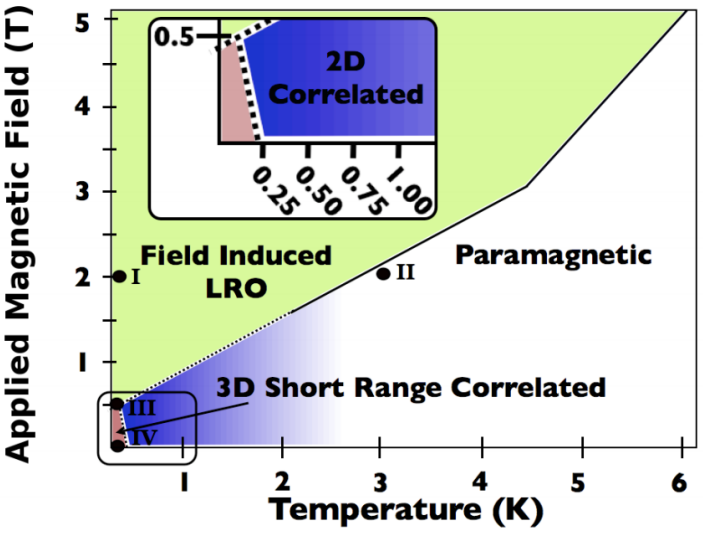

FIGURE 3.18: Proposed phase diagram for $Yb_2Ti_2O_7$ by Ross *et al.* [160]. Inset: highlighting the transition at $\mu_o H \approx 0.5$ T between short ranged 3D correlated magnetic structure and field-induced LRO magnetic state.

3.5 Neutron Scattering

Preliminary neutron powder diffraction experiments were conducted on the time-of-flight (TOF) **D**isc **C**hopper **S**pectrometer (DCS) installed on neutron guide NG4 at the **N**IST **C**enter for **N**eutron **R**esearch (NCNR). Measurements were performed at both 20 mK and 4-11 K using a dilution refrigerator and a standard orange cryostat, respectively, in the presence of 0, 1, 2, 3, 6 and 9 T applied magnetic fields provided by a vertical field cryomagnet. Wavelengths of 1.8 Å and 9 Å were chosen to provide both a large **Q** range and fine resolution at low **Q**, respectively. A neutron optical filter, supplemented by a pyrolytic graphite crystal filter removed γ-rays, fast neutrons and higher-order contamination, respectively, while seven $^{\text{natural}}Gd_2O_3$ choppers [163] along a 10 metre guide coated with ^{58}Ni equivalent supermirror material, act as both pulsers and monochromators, selecting the desired wavelengths while avoiding frame overlap [164].

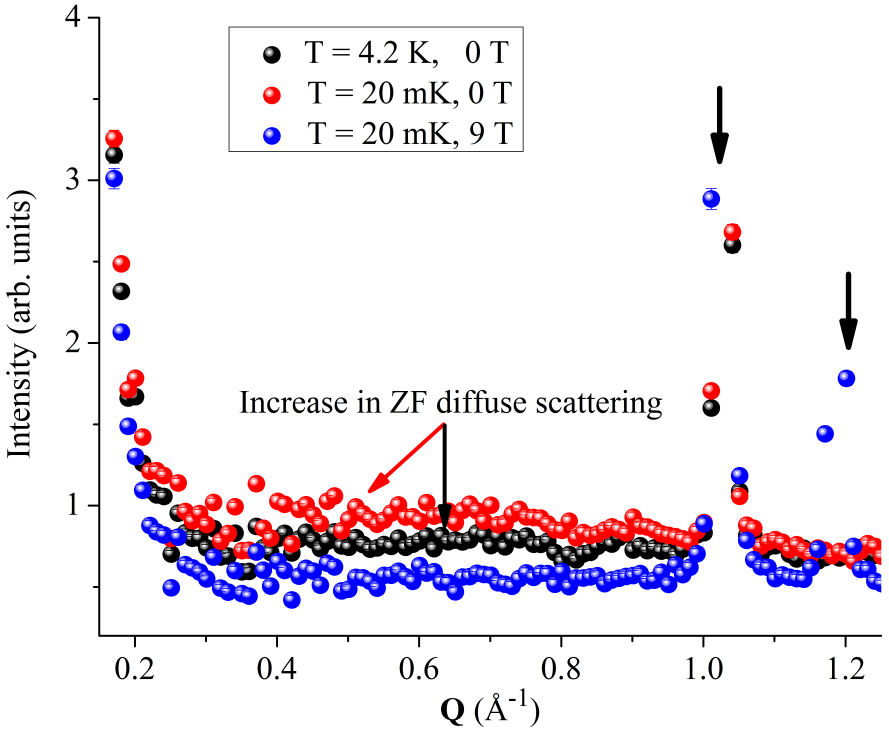

FIGURE 3.19: Comparison of elastic channel cuts along **Q** under 0 T at 20 mK and 4.2 K and 9 T at 20 mK. The elastic channel is integrated from [-0.05 meV, 0.05 meV] along **Q** with $\lambda = 9$ Å. The 4.2 K and 20 mK data sets both exhibit diffuse scattering buildup near $\mathbf{Q} = 0$, implying the presence of the spin ice state even at T $\sim$ 4 K. With the application of a magnetic field, the characteristic diffuse scattering disappears and accumulates on Bragg peaks implying the creation of a LRO magnetic state that accompanies the disappearance of the spin ice state.

Figure 3.19 compares elastic cuts (-0.05 meV $\leq E \leq$ 0.05 meV) along **Q** in an external applied magnetic field of μ_oH = 0 T and 9 T. In this figure, spin ice correlations —

indicated by significant amounts of diffuse scattering with a build-up of intensity near $\mathbf{Q} = 0$ representing the short range ferromagnetic correlations within individual tetrahedra — are present, even at temperatures of approximately 4 K. As the temperature is decreased to 20 mK, the characteristic diffuse scattering of the spin ice state, particularly near $\mathbf{Q} = 0$, increases, in agreement with the behaviour observed by Zhou *et al.* and Mirebeau *et al.* [31, 155]. It should be noted that the presence of the short range ferromagnetic spin ice correlations, even at temperatures ≈ 4 K, support the claim that the low temperature feature in figure 3.6 is indeed indicative of the spin ice state. As an external magnetic field is applied, the short range $\mathbf{Q} = 0$ ferromagnetic correlations disappear while the intensity on the Bragg reflection (111) increase substantially. Furthermore, an intense feature at $\mathbf{Q} \approx 1.19$ Å^{-1} — identified as the (200) Bragg reflection — appears. The disappearance of the magnetic diffuse scattering and the increase in intensity at the (111) and (200) magnetic Bragg reflections are consistent with a field induced transition.

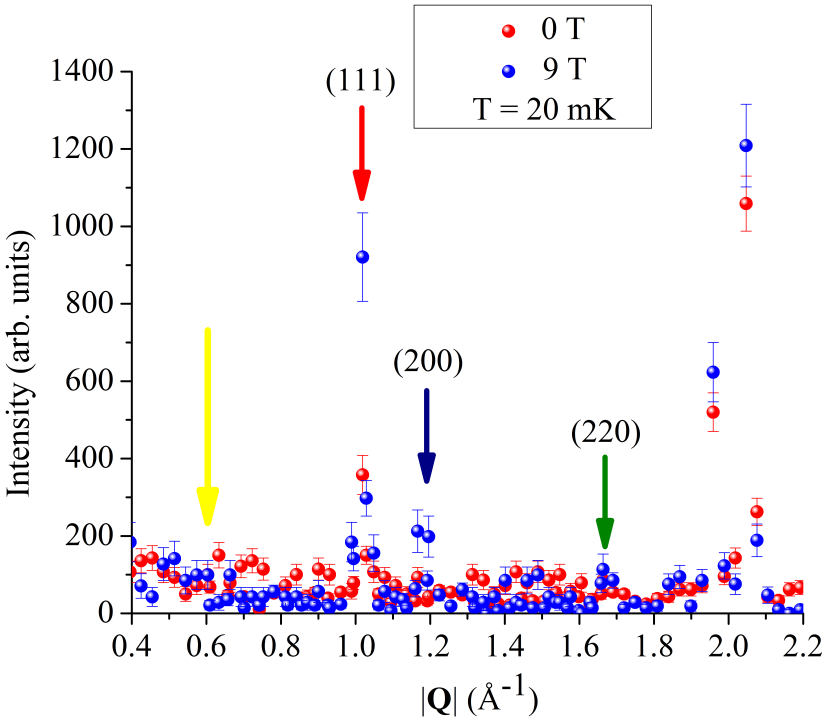

FIGURE 3.20: Comparison of elastic channel cuts along $\mathbf{Q}$ under 0 T and 9 T. The elastic channel is integrated from [-0.05 meV, 0.05 meV] along $\mathbf{Q}$ with $\lambda = 1.8$ Å at 20 mK. The increase in intensity for the (111), (200) and (220) peaks are indicated by red, dark blue and olive arrows, respectively.

As the system transitions away from the spin ice state, the characteristic short range ferromagnetic correlations (i.e. the diffuse scattering) disappears while the magnetic intensity shifts to individual Bragg peaks implying, not only an LRO magnetic state is

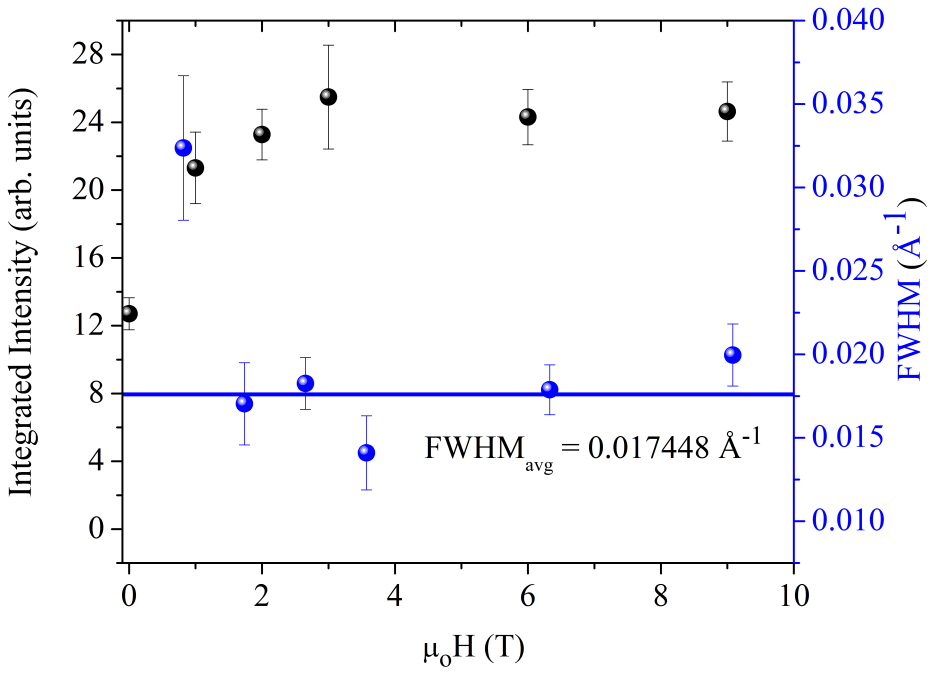

FIGURE 3.21: Integrated intensity and FWHM of the (111) peak as a function of applied external magnetic field for $\lambda = 1.8$ Å at 20 mK. As the external magnetic field is increased, the area saturates to a maximum while the FWHM decreases, both consistent with the formation of a LRO magnetic state. The saturation value of FWHM = 0.017448 Å^{-1} represents correlations over ≈ 5 unit cells. It should be noted that the reported value for the FWHM is clearly an underestimate of the true value, attributed to poor counting statistics.

being created but the propagation vector **q** must be zero, i.e. the magnetic cell is identical to the atomic/nuclear unit cell. Similar behaviour was observed for single crystals of $Dy_2Ti_2O_7$ by Fennell *et al.* under applied magnetic fields [165]. It is important to note that the inferences from an analogy between $Dy_2Ti_2O_7$ and $Pr_2Sn_2O_7$ is limited and should be interpreted with caution. The proposed ordering mechanism and resulting magnetic state by Fennell *et al.* [165] are both highly anisotropic, which cannot be deduced by powder elastic neutron diffraction. In particular, the application of a weak magnetic field (i.e. $\mu_o H \approx 0.7$ T) along [100] at 70 mK induces the disappearance of the spin ice diffuse scattering while saturating the Bragg reflections. This behaviour is strikingly similar to the behaviour observed for $Pr_2Sn_2O_7$, where the intensity of the Bragg reflections increases as seen in both figure 3.20 and eventually saturates as seen in figure 3.21 where the integrated area of the (111) magnetic Bragg reflection is already saturates at an externally applied magnetic field of 1 T. The diffuse scattering disappears as seen in figure 3.23 and elastic processes increasingly dominate as seen in figure 3.24. The [100] behaviour may be explained by the formation of a LRO $\mathbf{Q} = 0$ ferromagnetic state created by the removal of the six fold two-in-two-out spin ice degeneracy. Each

tetrahedron adopts the same two-in-two-out configuration aligning their net moment along the [100], i.e. the direction of the aligned field. Although the ferromagnetic ordering mechanism does account for the [100] behaviour, it cannot account for the behaviour in the [1-10] where the increase in intensity on the Bragg reflections is accompanied by an accumulation of the diffuse scattering around Q = X reflections (e.g. any Bragg peak that is located in the (*00l*) plane). Instead of forming the aforementioned simple LRO ferromagnetic structure as first proposed, the structure actually forms a Q = X structure which can be visualised as two interpenetrating alternating in-and-out chains as shown in figure 3.22. The anistropy of the Q = X structure accounts for both the increase intensity on the Bragg reflections (i.e. the Q = 0 intensity) but also the increase diffuse scattering buildup around Q = X reflections.

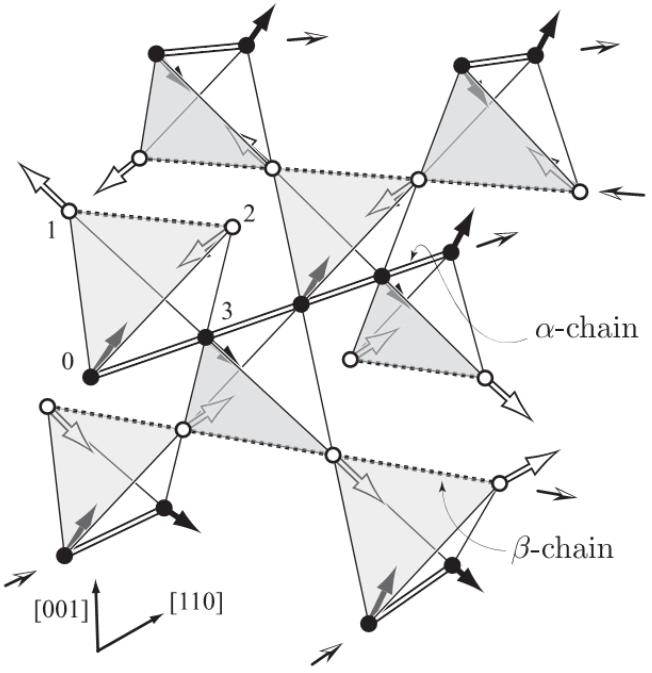

FIGURE 3.22: Pictorial representation of the **Q** = X magnetic structure for the canonical spin ices until a [110] applied external magnetic field. The magnetic moments are located on the vertices of the individual tetrahedra and each individual Ising (in this case trigonal ⟨111⟩) axis is labelled for clarity. The **Q** = X magnetic structure consists of two chains, commonly denoted as α and β, emphasised by the double and dotted line, respectively. Adapted from Yoshida *et al.* [166].

As a consequence of both the highly anistropic nature of the magnetic ordering mechanism and resulting magnetic structure, and since only polycrystalline samples of $Pr_2Sn_2O_7$ were measured, an alternative approach similar to $Ho_2Ru_2O_7$ [28] was used to characterise the magnetic ordering mechanism and the resulting structure *qualitatively*. The term qualitatively is emphasised because the elastic neutron data collected for $Pr_2Sn_2O_7$ on the DCS was simply preliminary and consequently, poor counting statistics

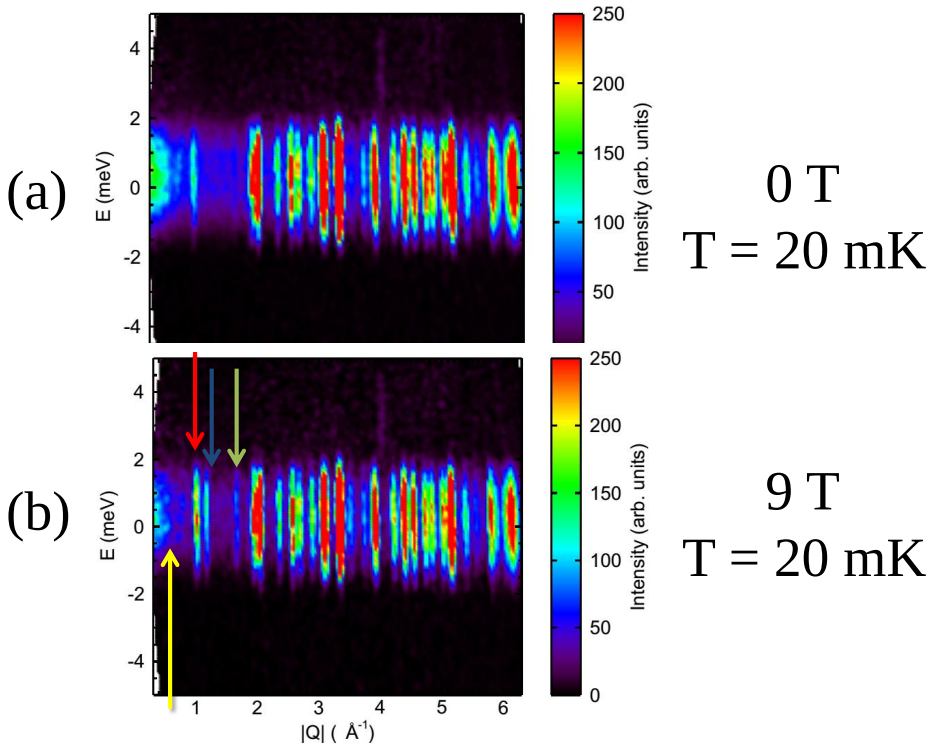

FIGURE 3.23: Comparison of energy-**Q** slices at 0 and 9 T with $\lambda = 1.8$ Å at 20 mK. With the application of the field, there is a reduction in diffuse scattering (particularly around $\mathbf{Q} = 0$) indicated by the yellow arrow, the (111) Bragg peak increases in intensity as indicated by the red arrow and two new Bragg peaks appear (200) and (220) indicated by the dark blue and olive arrows, respectively as shown in figure 3.20.

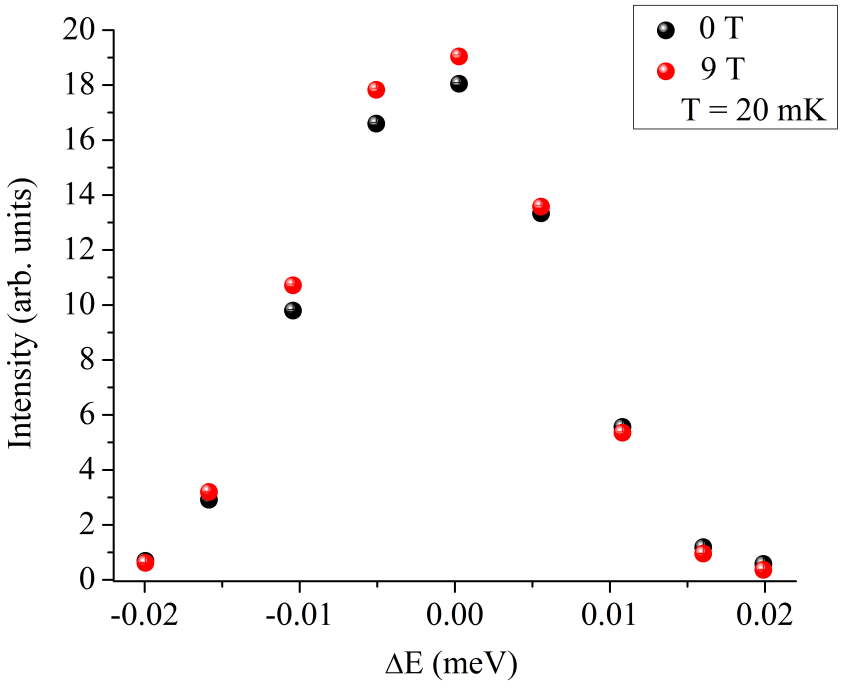

FIGURE 3.24: Comparison of cuts along energy integrated over all **Q** at 0 T and 9 T with $\lambda = 9$Å at 20 mK. There is an increase in intensity for the quasi-elastic channel and a sharpening of the quasi-elastic channel under the application of an external magnetic field . Both the increase in magnetic density and sharpening of the quasi-elastic channel are consistent with the formation of an LRO magnetic state.

and poor **Q** resolution for $\lambda = 1.8$ Å prohibits a possibility for a full magnetic structure refinement. Although it should also be emphasised that patterns can still be inferred and thus is the approach that will be taken for the remainder of this chapter. Recall that from DC magneometry and isobaric heat capacity measurements, the transition from the spin ice state to a LRO AFM was hypothesised to occur due to admixture of crystal fields. This admixture of crystal fields and the resulting shift in relative energies within the CF scheme was deduced by Wiebe *et al.* [28] to cause the Ho^{3+} moments to order antiferromagnetically at T ≈ 1.4 K but instead of an external magnetic field inducing the admixture, the admixture was caused by an internal magnetic field created by the ferromagnetic ordering of the Ru^{4+} moments that begins at T ≈ 95 K. In fact, crystal field contributions to the ordering mechanisms in pyorchlores have been well documented [87, 167, 168]. In a recently reported example, Tomiyasu *et al.* [169] deduced a similar phemonenon occurs in $Nd_2Ir_2O_7$ where the Ir^{4+} moments magnetically order below the metal-insulator transition temperature (T_{MI}) which creates a large enough static magnetic field at the Nd^{3+} sites to cause a large enough splitting of the ground state doublet to induce the formation of a LRO $\mathbf{Q} = 0$ AFM. It is worthwhile to note that before proceeding with the crystal field approach, another possible cause for magnetically ordering may be a structural transition which both Wiebe *et al.* [28] and Tomiyasu *et al.* [169] quickly disproved for $Ho_2Ru_2O_7$ and $Nd_2Ir_2O_7$, respectively. In a similar manner, elastic neutron scattering of $Pr_2Sn_2O_7$ on the DCS confirmed that the cause for the magnetic transition cannot be structural. A non-magnetic nuclear peak (i.e. a high **Q** peak), namely the (440) peak's centre location was plotted as a function of applied magnetic field. As figure 3.25 demonstrates, the peak does not shift (within error) implying no structural transition occurs as a consequence of the application of an external magnetic field and thus cannot be the cause for the observed spin ice-LRO AFM transition. The lack of any structural component is also confirmed by the absence of any peak splitting as shown in figures 3.19 and 3.20 after the application of a field since any deviation from ideal cubic symmetry would result in peak splitting due to removal of the equivalency of the crystalographic axes.

A first approach at the elucidating properties of magnetic structure was performed by conducting a systematic search, using the program **SARAh** and symmetry-representation analysis [170, 171]. The basis states of the irreducible representation (IR) Γ_9 of the $Fd\bar{3}m$ space group were identified and used for magnetic simulations using the program FULL-PROF to describe the praseodymium moments. By applying symmetry, only two basis states ψ_7 and ψ_8 of Γ_9 of the $Fd\bar{3}m$ space group were considered [28]. The need for only two basis states is due to the fact that all six basis states are simply three pairs of analogous basis states oriented with respect to the three individual crystallographic axes [28, 155]. These axes cannot be differentiated among one another by using powder

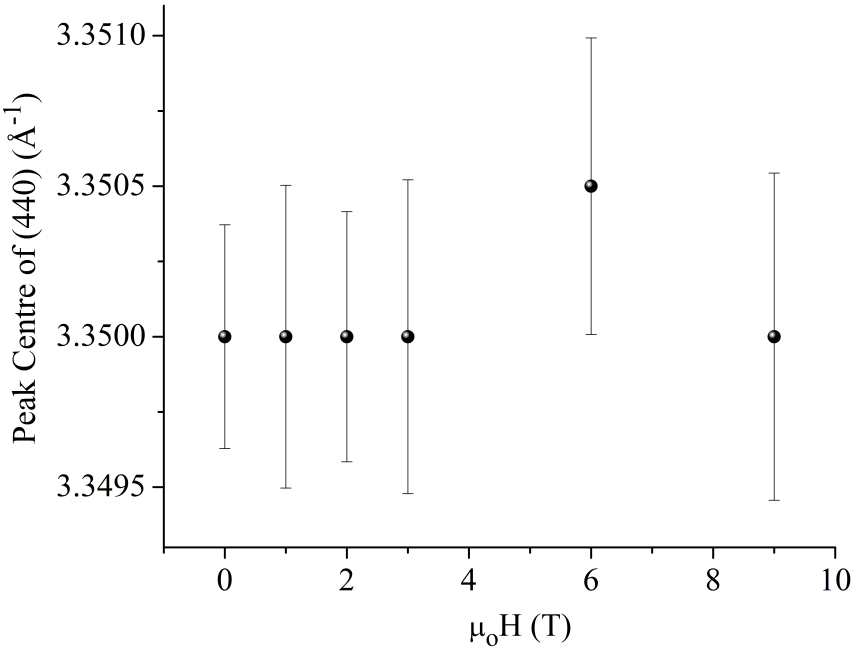

FIGURE 3.25: The location of the centre of the structural (440) peak as a function of applied external magnetic field for $\lambda = 1.8$ Å at 20 mK. The location of the peak's centre remains constant (within error), thus excluding the possibility of a structural distortion being responsible for the observed formation of the LRO magnetic state.

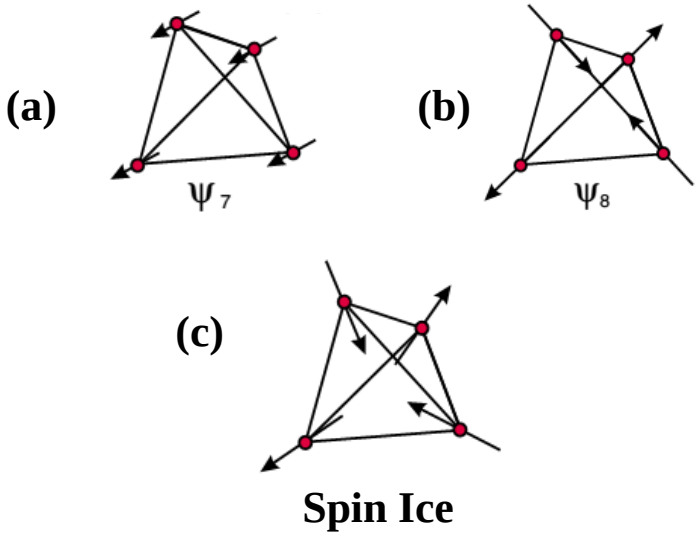

FIGURE 3.26: The basis vectors (a) ψ_7 and (b) ψ_8 of the irreducible representation (IR) Γ_9 of the Fd$\bar{3}$m space group retrieved from SARAh used in magnetic simulations of $Pr_2Sn_2O_7$. It is noted that an equal proportion of ψ_7 and ψ_8 yields the spin ice state in (c). The structures were retrieved from Wiebe *et al.* [28].

neutron diffraction and thus only two basis states were considered. The basis state of ψ_7 is a collinear ferromagnet where all the moments are aligned along the a axis. The basis state ψ_8 is an orthogonal antiferromagnet. It is worthwhile to note that an equal mixture of ψ_7 and ψ_8 yield the spin ice state, with the coefficients determining the magnitude of the magnetic moment on each vertex of the tetrahedron [28, 155]. All three structures are shown in figure 3.26.

Since a magnetic refinement was not possible, preliminary magnetic simulations were performed. The three simulations involved first assuming the entire paramagnetic moment detected by susceptometry (i.e. the value of $\mu_{\text{eff}} \approx 2.5\ \mu_{\text{B}}$ was used as a starting point and varied) was directed along the a axis forming the collinear ferromagnetic state described by ψ_7; recall was seen in $Dy_2Ti_2O_7$ along [100] [165]. The second simulation used an analogous procedure involving the assumption that the entire moment was directed within the b-c plane described by ψ_8, this would be similar to the situation in $Er_2Ti_2O_7$ [56]. The third simulation varied the contributions of both basis vectors ψ_7 and ψ_8 in a situation similar to $Ho_2Ru_2O_7$ [28]. The three simulations are shown below.

Figures 3.27 and 3.28 demonstrate that the magnetic structure of $Pr_2Sn_2O_7$ under an applied field cannot be described as a simple collinear ferromagnet or a simple XY antiferromagnet. The former possesses zero intensity contribution to the new prominent low $|\mathbf{Q}|$ Bragg reflections at (200) and (220). The latter extinguishes all intensity on multiple Bragg reflections including the (111), which is a magnetic Bragg peak that increases in intensity under the application of a field, as shown in figures 3.19 and 3.23. Instead, figure 3.29 demonstrates that there is a mixture of ferromagnetic and antiferromagnetic contributions to the magnetic structure. Through a systematic search, the best combination was concluded to be: $0.2297(2)\psi_7 + 0.847(5)\psi_8$ which both confirms the absence of the spin ice state due to the lack of a 1:1 ratio and the antiferromagnetic nature of the magnetic structure due to the larger coefficient of ψ_8. Furthermore, the linear combination of $0.2297(2)\psi_7 + 0.847(5)\psi_8$ corresponds to magnetic moment of 0.87(1) μ_{B} which is agreement with the susceptometry results (e.g. figure 3.6) that demonstrate a reduction in the magnetic moment of the Pr^{3+} ground state doublet. The transition from a 1:1 ratio to a larger XY AFM contribution with an accompanying reduction in the magnetic moment is also seen by $Ho_2Ru_2O_7$ which one may recall was shown to possess an accompanying change in the relative energy of the crystal field levels [28]. The identification of a significant XY AFM component is important for two reasons: the first is that this result is consistent with the pollution of non-axial $|M_J \neq J\rangle$ terms which was previously stated to drive the spin ice to LRO AFM transition and secondly, the large value of the XY component (relative to the collinear ferromagnetic component) suggests a highly anistropic XY AFM magnetic structure. This significant anistropy is consistent with the phenomenon of geometric frustration within the pyrochlores because

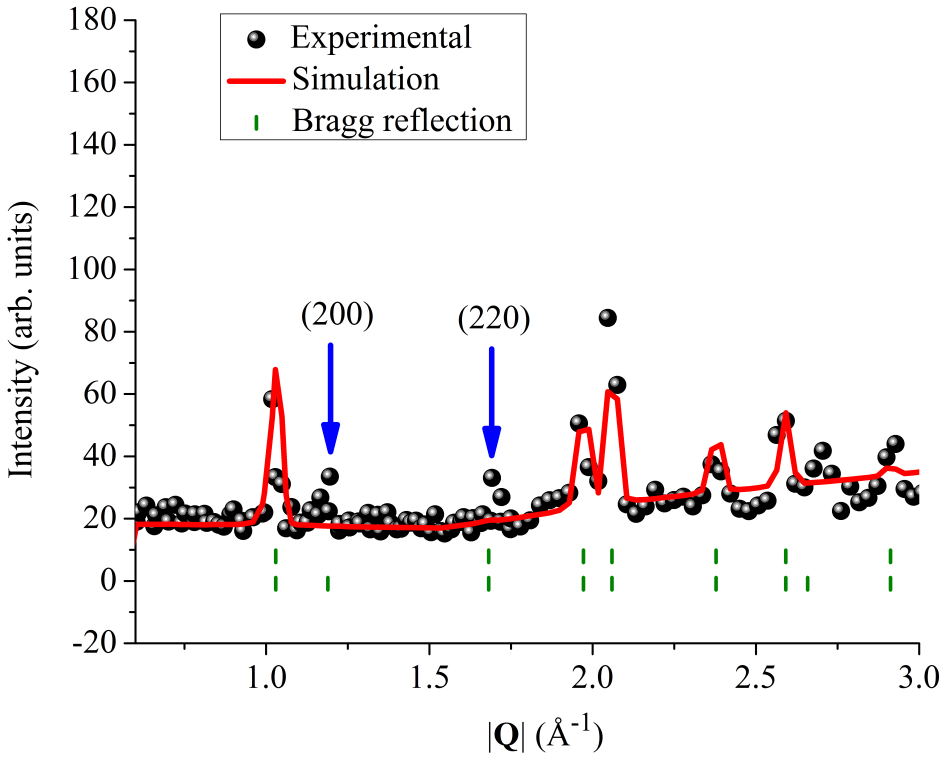

FIGURE 3.27: Preliminary magnetic simulation for the magnetic structure of $Pr_2Sn_2O_7$ in 1 T using only the basis vector ψ_7 of the irreducible representation (IR) Γ_9 of the $Fd\bar{3}m$ space group and a magnetic moment of 2.5 μ_B. Experimental data is given by the black spheres, the simulation is given by the red curve and the Bragg reflections' locations are given by the olive dashes with the set above and below are nuclear and magnetic reflections, respectively. The simulation is evidently of poor quality, particularly having no intensity on the new magnetic Bragg peaks of (200) and (220), labelled by blue arrows for reference. A qualitative comparison to figure 3.29 implies the magnetic structure of $Pr_2Sn_2O_7$ is not a simple collinear ferromagnet.

it has been seen that highly isotropic moments that are AFM coupled do not order due to geometric frustration, but once a large anistropy is introduced the geometric frustration is overwhelmed and a unique ground state is selected. A situation that occurs analogously for the Ir^{4+} moments in $Nd_2Ir_2O_7$ [169, 172].

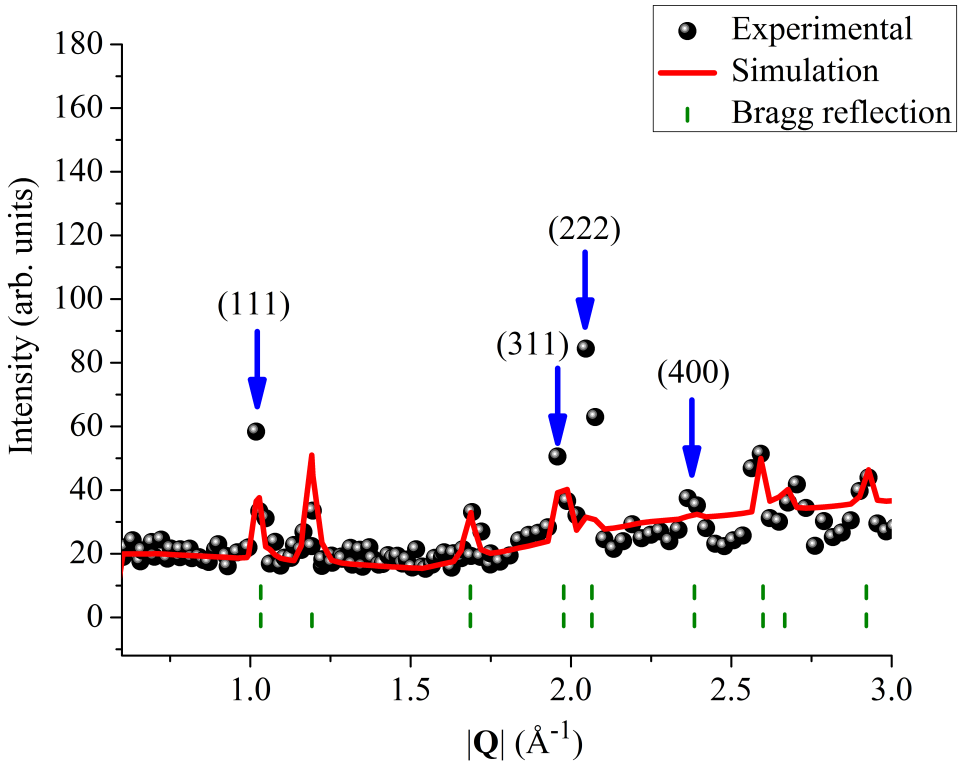

FIGURE 3.28: Preliminary magnetic simulation for the magnetic structure of $Pr_2Sn_2O_7$ in 1 T using only the basis vector ψ_8 of the irreducible representation (IR) Γ_9 of the $Fd\bar{3}m$ space group and a magnetic moment of 2.5 μ_B. Experimental data is given by the black spheres, the simulation is given by the red curve and the Bragg reflections' locations are given by the olive dashes with the set above and below are nuclear and magnetic reflections, respectively. The simulation is evidently of poor quality with multiple peaks' intensities being diminished, labelled by blue arrows for reference. A qualitative comparison to figure 3.29 implies the magnetic structure of $Pr_2Sn_2O_7$ is not a simple XY antiferromagnet.

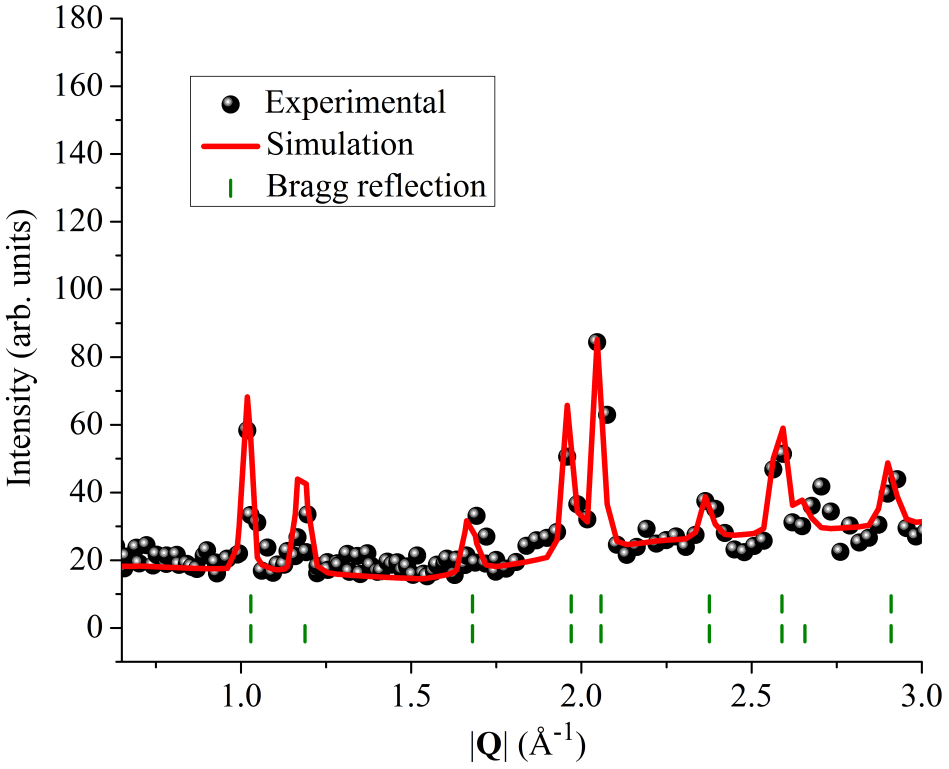

FIGURE 3.29: Preliminary magnetic simulation for the magnetic structure of $Pr_2Sn_2O_7$ in 1 T using both the basis vectors ψ_7 and ψ_8 of the irreducible representation (IR) Γ_9 of the $Fd\bar{3}m$ space group. The simulation is again of poor quality but many of the qualitative features at low $|Q|$ are captured, suggesting a possibility of a combination of ferromagnetism and antiferromagnetism similar to the magnetic behaviour of $Dy_2Ti_2O_7$ along [1-10] [165].

Chapter 4

Perturbation of the Dynamic Spin Ice State *via* Randomised Chemical Pressure: $Pr_2Sn_{2-x}Ti_xO_7$

4.1 Introduction and Motivation

The exotic spin ice state, as shown in Chapter 3, is extremely fragile when exposed to an external perturbation such as an applied magnetic field, requiring only a value of $\mu_o H \approx 0.5$ T to transition into an LRO antiferromagnetic state. An inevitable follow-up question would be since the spin ice state is so fragile towards an external stimulus, causing the system to cross the critical $\frac{J_{NN}}{D_{NN}}$ boundary in the *dipolar spin ice model* [20] with such weak magnetic fields, is there another method to allow experimentalists to possess the ability to fine tune the exchange-to-dipolar ratio with greater control in order to approach and probe the boundary between the spin ice and LRO AFM states? Recall that this spin ice-LRO AFM boundary is of particular interest due to the recent discovery that elementary excitations within the spin ice state behave similarly to deconfined magnetic monopoles as proposed by Bramwell *et al.* [173]. These elementary excitations — in the form of a defect three-out-one-in structure — possess an effective magnetic flux pattern that can be modelled as emenating from point-like magnetic charges (i.e. monopoles). Since these elementary excitations can disperse throughout the pyrochlore *A* tetrahedral sublattice, these excitations also mimic the property of fluidity, thus forming an effective magnetic Coulombic liquid state that has been probed extensively through polarised neutron scattering by Fennell *et al.* [174]. Despite the

discoveries of these deconfined magnetic monopoles in the spin ices, the current density of monopoles in canonical spin ice systems are vey low, prohibiting the ability of experimentalists to probe their magnetic properties. An attempt to remedy this low monopole density was accomplished through the substitution of the tetravalent titanium cation by the much smaller tetravalent germanium cation, creating a new class of pyrochlores called the *germanates* [43]. The substitution of a much smaller tetravalent cation in the 16*c* Wyckoff site places the germanates outside the critical radius ratio of 1.71, thus requiring the application of extremely large pressures during the heating routine in order to avoid the tetragonal pyrogermanate phase [43, 175]. The germanates represent a significant decease in the lattice parameter compared to the ambient pressure canonical spin ices and since the identity of the magnetic ions remains unchanged, the new class of pyrochlores represent a completely different scale of exchange interactions [176]. As summarised by Zhou *et al.* [32], the germanates have indeed provided the condensed matter community with a significantly higher density of magnetic monopoles that are much more correlated than the canonical spin ices. In particular, one member of the germanates, $Dy_2Ge_2O_7$ has been shown by Zhou *et al.* [144] to possess the closest $\frac{J_{NN}}{D_{NN}}$ value to the proposed SI-LRO AFM phase transition with a $\frac{J_{NN}}{D_{NN}} \approx$ -0.73. Despite the progress made through the germanates, the monopole density is still relatively low that it is still very difficult to probe this novel arena of monopole physics which has led to the condensed matter community seeking the substiution of even smaller tetravalent cations such as silicon under the application of even higher pressures [42]. Furthermore, despite the progress through the germanates, there still remains ambiguity of what occurs near the spin ice-LRO AFM transition.

Attempts to fine-tune the spin ice state at ambient pressures have consisted of two strategies. The first involved modifying the exchange interactions by introducing magnetic *A*-site cations into the 16*c* site, displacing titanium forming the stuffed spin ices $A_{2+x}Ti_{2-x}O_{7-\delta}$ such as $Ho_{2+x}Ti_{2-x}O_{7-\delta}$ by Lau *et al.* [177]. These stuffed spin ices were shown to not proceed towards the phase transition boundary, and the spin ice state remains intact despite large values of doping [178]. The second method involved artificially shrinking the lattice by substituting smaller tetravalent cations in the canonical spin ices' 16*c* Wyckoff site forming $A_2B_{2-x}C_xO_7$, where the C^{4+} dopant is randomly distributed among the 16*c* Wyckoff sites. Surprisingly, this strategy with disprosium and holmium stannates, using antimony, has revealed the spin ice state is quite robust against positional disorder [179]. The use of the much smaller Ti^{4+} among the stannates has only be used once by Dahlberg *et al.* [180] by doping $Tb_2Sn_2O_7$ resulting in a suppression of LRO ordering and eventual freezing of the system into a spin glass state, despite only very small values of x (i.e. $x \leq 0.20$). The stark contrast between the stuffed spin ices and the study by Dahlberg *et al.* revealed a crucial role of the identity

of the cation in the 16*c* Wyckoff and its distribution throughout the lattice for stannate pyrochlores. This observation by Dahlberg *et al.* suggests that in fact, the stannate pyrochlore system can have its exchange-to-dipolar ratio drastically altered so that the magnetic state assumed by the system can change, unlike the stuffed spin ices. Although terbium stannate readily forms a spin glass state, as one would expect from randomised exchange interactions due to positional disorder, the praseodymium analog is postulated to be behave completely differently, attributed to the starkly different crystal field energy schemes present in terbium and praseodymium, respectively [181]. Through a comparison from its stannate to titanate to germanate analog, dysprosium (and holmium) show that by shrinking the lattice *via* chemical pressure, the AFM superexchange is enhanced. Consequently, it is posulated that as the value of x in $Pr_2Sn_{2-x}Ti_xO_7$ increases, the $\frac{J_{NN}}{D_{NN}}$ ratio should become more negative and move towards the SI-LRO AFM transition. As the AFM superexchange interactions between spins increase, the correlations between monopoles should increase, eventually leading into a type of cooperative fluctuating antiferromagnetic state as seen in La_2CuO_4 by Yamada *et al.* [182]. As the system reaches a critical value x, a critical density of monopoles should theoretically recondense leading into the LRO AFM state proposed by den Hertog *et al.* [20] in the *dipolar spin ice model*. The set of questions this chapter attempts to address are all derived from one fundamental question: what are the consequences of applying randomised chemical pressure on the dynamic spin ice $Pr_2Sn_2O_7$? Does the perturbed system form an LRO magnetic state or does it form an exotic short range ordered correlated magnetic state such as a quantum antiferromagnet?

4.2 Synthesis of the $Pr_2Sn_{2-x}Ti_xO_7$ Pyrochlore Series

Polycrystalline samples of $Pr_2Sn_{2-x}Ti_xO_7$ (x = 0.05, 0.10, 0.20, 0.30, 0.40 and 0.60) were prepared by a standard solid state reaction of stoichiometric amounts of Pr_6O_{11} (99.99 %, Alfa Aesar), SnO_2 (99.99 %, Alfa Aesar) and TiO_2 (99.99 %, Alfa Aesar) as described in equation 4.1 below.

$$Pr_6O_{11(s)} + (6-3x)SnO_{2(s)} + 3xTiO_{2(s)} \longrightarrow 3Pr_2Sn_{2-x}Ti_xO_{7(s)} + O_{2(g)} \qquad (4.1)$$

All three powder reagents were mixed together, finely ground and pressed into a pellet form using a uniaxial press. The pellets were placed in an alumina crucible and were subjected to a heating routine adapted from Kennedy *et al.* [38]. The pellets were heated in air at 1000°C for 24 hours. The pellets were then reground, repelletised and heated in air at 1400°C for approximately 48 hours with intermittent grindings until powder x-ray

diffraction measurements confirmed both the absence of all starting reagents and the presence of the single pyrochlore phase. As shown in figure 4.1, by substituting more Sn(IV) for the smaller Ti(IV), the 2θ value for the (222) peak increases representing a decrease in the d-spacing between the (222) planes, corresponding to a decrease in the lattice parameter a. The room temperature powder x-ray diffraction pattern of the highest doped member of the $Pr_2Sn_{2-x}Ti_xO_7$ series, $Pr_2Sn_{1.4}Ti_{0.6}O_7$ and the subsequent Rietveld refinement with FULLPROF [152] is given in figure 4.2 below. The Rietveld refinements on each member of $Pr_2Sn_{2-x}Ti_xO_7$ pyrochlore series for $0 \leq x \leq 0.60$ confirmed the presence of single pyrochlore phase possessing $Fd\bar{3}m$ symmetry with no discernible impurities.

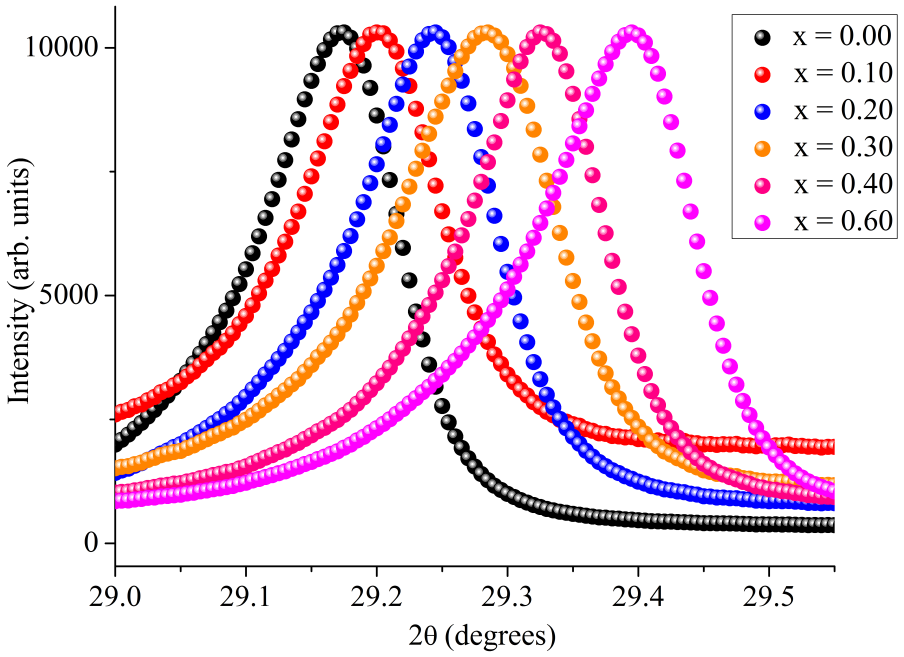

FIGURE 4.1: The measured (222) peak of the room temperature x-ray powder diffraction profiles for various members of the$Pr_2Sn_{2-x}Ti_xO_7$ pyrochlore series on a HUBER G670 imaging-plate powder diffraction Guinier camera with a $K_{\alpha,1}$ source. As the value of x increases, the (222) peak shifts to a higher 2θ value, indicating a smaller lattice parameter a, attributed to the Ti(IV) substitution for Sn(IV) in the $16c$ Wyckoff sites.

Rietveld refinements performed on the $Pr_2Sn_{2-x}Ti_xO_7$ series assumed that there was a random distribution of Sn(IV) and Ti(IV) among exclusively the six-coordinate $16c$ Wyckoff positions. In other words, the Rietveld refinement contained three important assumptions: (i) the Ti(IV) did not enter the eight-coordinate $16d$ Wyckoff position (i.e. the A-site), (ii) the Ti(IV) did not form local pockets of higher concentration (i.e. concentration gradients) and (iii) the introduction of the smaller Ti(VI) did not encourage stuffing (i.e. the introduction of Ti(IV) did not cause Pr(III) to enter the B-site). The validity of the first assumption is based on the observation that the larger

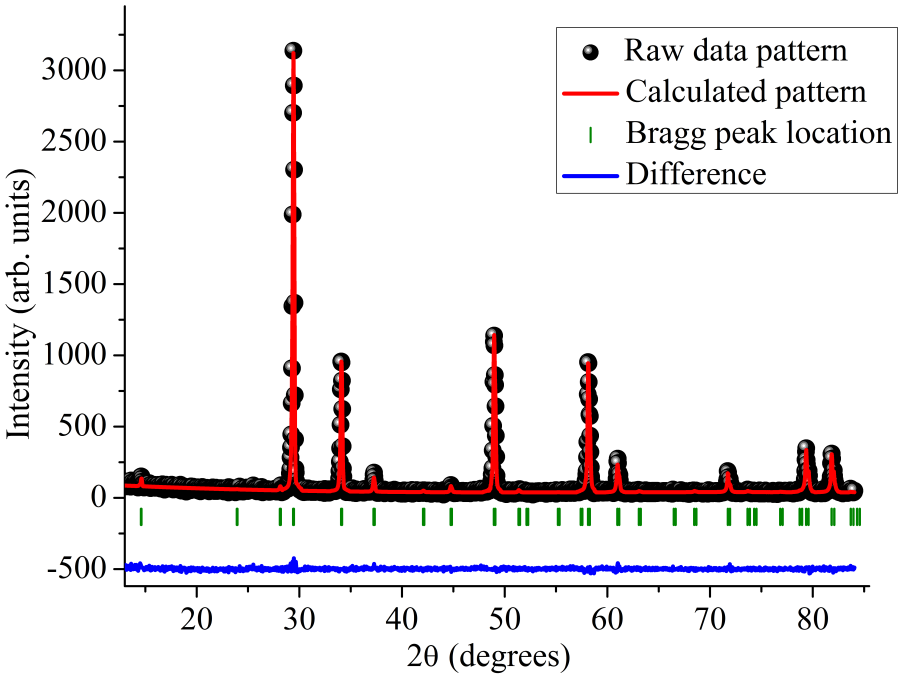

FIGURE 4.2: Measured, calculated and difference room temperature x-ray powder diffraction profiles for $Pr_2Sn_{1.4}Ti_{0.6}O_7$ on a Siemens D5000 diffractometer with a $K_{\alpha_{1,2}}Cu$ source. The measured intensity is given by the black spheres, the calculated intensity is given by the red curve and the difference is given by the blue curve. The Bragg reflections' locations are given by olive vertical lines. The absence of peak splitting (beyond that expected from the $K_{\alpha_{1,2}}Cu$ source) at high 2θ confirms the presence of a single pyrochlore phase. The Rietveld refinement assumes a random distribution of the Ti(IV) uniquely on the 16*c* Wyckoff position with no stuffing from the Pr(III).

Sn(IV) ($R_{Ti^{4+}} = 0.74 < R_{Sn^{4+}} = 0.81$ Å) does not enter the *A*-site; thus, a size argument would suggest no Ti^{4+} should enter the *A* site. The second assumption is based on the diffusion model of the ceramic method [183] used for the standard solid state reaction described in equation 4.1. The synthesis of the final product *via* the ceramic method involves the diffusion of the constitutent ions from the individual crystallites of unreacted starting reagents through contact surfaces. By both finely grinding the starting reagents and through subsequent intermittent grinding-reheating cycles, the distribution of the Ti(IV) ions should be completely randomised due to the initial randomisation of the constituent crystallite surface interfaces. The third assumption is based on the fact that there is no stuffing that was detected in the undoped sample $Pr_2Sn_2O_7$ by both Zhou *et al.* [31] and Princep *et al.* [149]. Recall that stuffing in pyrochlore oxides results from a situation when the radius of the *A*-site cation approaches the value of the B(IV) cation resulting in some *A*-site cations assuming the 16*c* position. Since no stuffing was observed in $Pr_2Sn_2O_7$ with a $\frac{R_{Pr^{3+}}}{R_{Sn^{4+}}}$ of 1.632, the larger $\frac{R_{Pr^{3+}}}{R_{Ti^{4+}}}$ of 1.861 would further discourage stuffing in the $Pr_2Sn_{2-x}Ti_xO_7$ series. The role of stuffing in pyrochlores — particularly in both canonical and quantum spin ices — has recently captured the

attention of the condensed matter community. The particular interest in the *stuffed canonical spin ices* — commonly denoted as SSI (stuffed spin ices) — is attributed to the fact that these SSI systems as aforementioned, exhibit the spin ice state up to very large values of stuffing (i.e. very large x values). The tolerance of the spin ice state with respect to stuffing is surprising because by introducing additional magnetic trivalent A-site cations into the $16c$ site, additional exchange pathways should be created. As a consequence of the creation of additional exchange pathways, interaction disorder should be present, thereby introducing additional constraints on the spin ice manifold formation which should lead to the freezing of the spin ice state. Instead, both Lau *et al.* [177] and Zhou *et al.* [178] experimentally determined that the SSI $Ho_{2+x}Ti_{2-x}O_{7-\delta}$ exhibited the same residual entropy per spin as the unstuffed canonical spin ice $Ho_2Ti_2O_7$. The particular interest concerning stuffing in the *quantum spin ices* is a result of the lack of consensus among experimentalists concerning the identity of magnetic ground state for the quantum spin ice $Yb_2Ti_2O_7$. In 2012, Ross *et al.* [54] — utilitizing the phase diagram from Balents *et al.* [34] — deduced that the presence of stuffing played a crucial role in the selection of magnetic ground states for the quantum spin ice candidate $Yb_2Ti_2O_7$. The particular reason why stuffing was so significant for $Yb_2Ti_2O_7$ is due to the great diversity of magnetic ground states separated by small energy scales due the quantum nature of $Yb_2Ti_2O_7$. Since $Pr_2Sn_2O_7$ is also a quantum spin ice, careful attention must be taken concerning any possibility of stuffing but as aforementioned, by substituting a smaller tetravalent B cation, stuffing is highly unlikely and will not be considered for the rest of this chapter.

TABLE 4.1: Comparison between experimentally[1] determined and calculated[2] lattice parameters for the newly synthesised $Pr_2Sn_{2-x}Ti_xO_7$ pyrochlore series

x	Experimental a (Å)	Calculated a (Å)	$\frac{R_{A^{3+}}}{R_{B^{4+}}}$
0	10.6024(3)	10.603(4)	1.63311(5)
0.10	10.589(3)	10.590(5)	1.6430(4)
0.20	10.574(2)	10.577(5)	1.6543(3)
0.30	10.565(3)	10.563(4)	1.6611(5)
0.40	10.547(2)	10.549(4)	1.6749(3)
0.60	10.523(3)	10.522(4)	1.6937(5)

[1] Refined lattice parameters from Rietveld refinements with Si and LaB_6 XRD SRMs
[2] Calculated using a linear regression with data from Table 4.2

The lattice parameters a for the $Pr_2Sn_{2-x}Ti_xO_7$ series ($0 \leq x \leq 0.60$) calculated from Rietveld refinements are summarised in table 4.1. Since this chapter constitutes

TABLE 4.2: Reported lattice constants and magnetic ground states for the $Pr_2B_2O_7$ pyrochlore series used to calculate the expected lattice parameter for the newly synthesised $Pr_2Sn_{2-x}Ti_xO_7$ pyrochlore series

B	B^{4+} radius[1] (Å)	Lattice Constant[2] (Å)	Magnetic Ground State[3]
Pb	0.775	10.872(3)	Quantum Spin Ice[4] [184]
Zr	0.72	10.71(4)	Quantum Spin Ice [82]
Sn	0.69	10.603(4)	Quantum Spin Ice [31]
Ir	0.625	10.394(6)	Metallic Quantum Spin Ice [60, 185] or Chiral Spin Liquid [59]
Ru	0.62	10.377(4)	Spin Liquid [186, 187]

[1] Radii for B^{4+} are Shannon-Prewitt ionic radii (VI coordinate) [88]
[2] Errors represent variability between literature reported values [188]
[3] Most recently **proposed** magnetic ground states
[4] Recent unpublished evidence suggests that $Pr_2Pb_2O_7$ in fact orders [189]

the first successful synthesis of the $Pr_2Sn_{2-x}Ti_xO_7$ pyrochlore series, a direct comparison between the experimentally determined lattice parameters and those in literature is not possible. Instead, a quantitative comparison between the experimentally determined lattice parameters and the expected lattice parameters was performed. The calculation of the expected lattice parameters for the $Pr_2Sn_{2-x}Ti_xO_7$ pyrochlore series was accomplished by first obtaining a relationship between the lattice parameter a of various praseodymium-based pyrochlores (i.e. $Pr_2B_2O_7$) and the Shannon-Prewitt ionic radius for the various tetravalent B cations summarised in table 4.2. A linear regression was subsequently performed on the data summarised in table 4.2, as shown in figure 4.3, providing the two parameters: slope, m and y-intercept, b relating the value of a and the Shannon-Prewitt ionic radius of tetravalent B-site cation. Since the $Pr_2Sn_{2-x}Ti_xO_7$ pyrochlore series is essentially a binary solid state mixture of two different tetravalent cations, an effective tetravalent B-site radius can be calculated with respect to x by a linear combination of the individual Shannon-Prewitt ionic radii of Sn(IV) and Ti(IV) as summarised by equation 4.2,

$$R_{\mathrm{B,effective}} = (1 - \mathrm{y}) \cdot \mathrm{R_B} + \mathrm{y} \cdot \mathrm{R_{B'}}, \tag{4.2}$$

where $\mathrm{y} = \frac{x}{2}$, $\mathrm{R_B}$ and $\mathrm{R_{B'}}$ are the Shannon-Prewitt ionic radii for six-coordinate Sn(IV) and Ti(IV), respectively. As shown in figure 4.4, the experimentally determined lattice parameter values for all members of the $Pr_2Sn_{2-x}Ti_xO_7$ pyrochlore series agree very well to the expected behaviour of the lattice parameter with respect to x. The observed

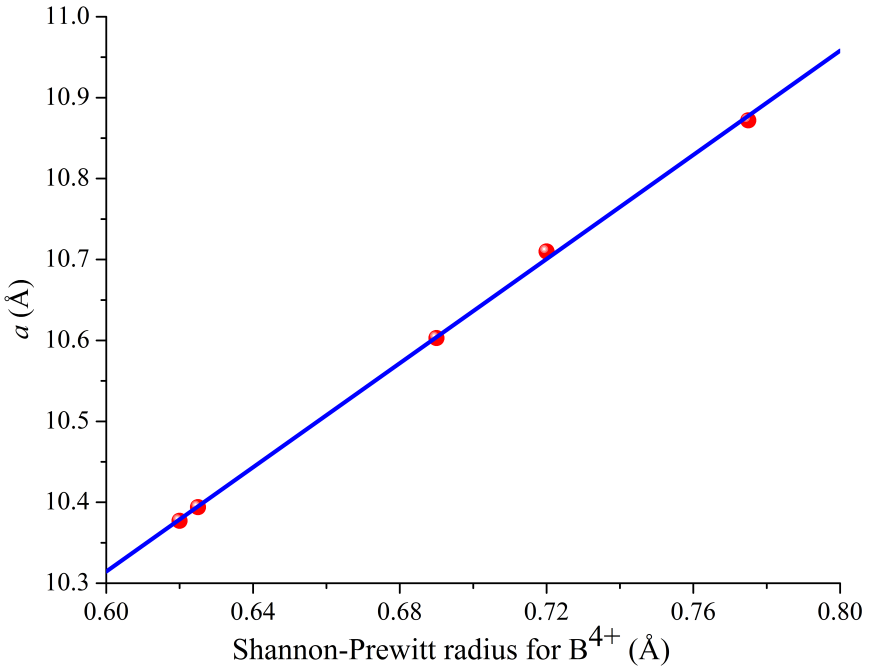

FIGURE 4.3: Reported lattice parameter for the $Pr_2B_2O_7$ pyrochlore series as a function of the calculated Shannon-Prewitt ionic radii for select six coordinate tetravalent B cations summarized in Table 4.2. Shown is the linear regression performed to calculate the expected lattice parameter for the newly synthesised $Pr_2Sn_{2-x}Ti_xO_7$ pyrochlore series reported in Table 4.1.

decrease in the lattice parameter a (as alluded to in figure 4.1) is linear with respect to x, following Vegard's law, as is expected for a simple binary solid state solution [190].

As table 4.1 demonstrates, as one increases the value of x, the $\frac{R_{Pr^{3+}}}{R_{B^{4+}_{effective}}}$ increases. The increase in the ratio between cationic radii is attributed to the reduction in the effective tetravalent B-site cation radius as the smaller Ti^{4+} substitutes for the larger Sn^{4+} described by equation 4.2. This increase in the value $\frac{R_{Pr^{3+}}}{R_{B^{4+}_{effective}}}$ provides an explanation as to why no member of the $Pr_2Sn_{2-x}Ti_xO_7$ series beyond x $\approx$ 0.60 could be synthesised possessing only the pyrochlore $Fd\bar{3}m$ phase. Utilising the definition of the effective tetravalent B-site ionic radius and the upper limit for the $\frac{R_{Pr^{3+}}}{R_{B^{4+}_{effective}}} \approx 1.71$ provided by Gardner *et al.* [11], the *expected* maximum value for x is approximately 0.74. Beyond the value of 0.74, one would expect the $Pr_2Sn_{2-x}Ti_xO_7$ series to assume both the pyrochlore $Fd\bar{3}m$ phase and the monoclinic $P2_1$ (No. 4/230) phase, the latter being the structure assumed by the titanium parent compound $Pr_2Ti_2O_7$ as deduced by Patwe *et al.* [191]. In fact, the value of x $\approx$ 0.74 has been proven experimentally to be an overestimate since $Pr_2Sn_{1.3}Ti_{0.7}O_7$ already exhibits a mixture of the pyrochlore $Fd\bar{3}m$ and monoclinic $P2_1$ phase as shown in figure 4.5, despite multiple regriding-reheating cycles.

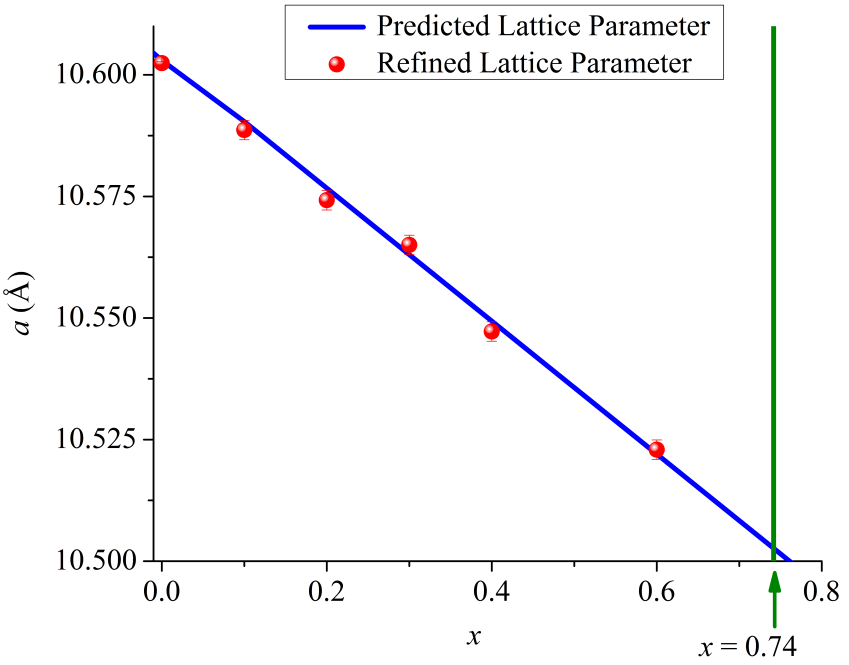

FIGURE 4.4: Experimentally determined lattice parameters and *expected* lattice parameters of the $Pr_2Sn_{2-x}Ti_xO_7$ pyochlore series as a function of x are plotted for comparison. The experimentally determined lattice parameters linearly decreases with x in agreement with Vegard's law and exhibits excellent agreement with the *expected* lattice parameter behaviour derived from a linear regression from data summarised in table 4.2. The maximum x value of ≈ 0.74 is noted by an olive line representing the value of x where the $Pr_2Sn_{2-x}Ti_xO_7$ series should no longer assume the pyrochlore $Fd\bar{3}m$ structure.

As a final note, the only adjustable crystallographic position parameter of the oxygen in the $48f$ Wyckoff position was refined for each member of the $Pr_2Sn_{2-x}Ti_xO_7$ pyrochlore series. As shown in figure 4.6, the value of the $48f$ oxygen's positional parameter increases approximately linearly with respect to x. This linear increase is in agreement with the inverse relationship between the lattice parameter and the $48f$ oxygen's parameter deduced by Kennedy *et al.* [38] since as the value of x increases — as shown in figure 4.4 — the lattice parameter decreases. The observed increase in the value of the $48f$ oxygen's positional parameter signifies that the local octahedral coordination environment of the $16c$ Wyckoff site (i.e. the B-site) becomes increasingly distorted while the cubic coordination environment of the $16d$ Wyckoff site (i.e. the A site) approaches ideal cubic symmetry. This distortion of the octahedral environment *via* the increase in the value of the $48f$ oxygen's positional parameter is consistent with the premise that the tetravalent B-site cation is the component that ultimately distorts the structure away from the pyrochlore phase. Once again, it should be noted that any structural conclusions or trends derived from refinements concerning oxygen from powder x-ray diffraction are limited due to the large discrepancy between the x-ray scattering of the high Z compounds of praseodymium, tin and titanium compared to oxygen.

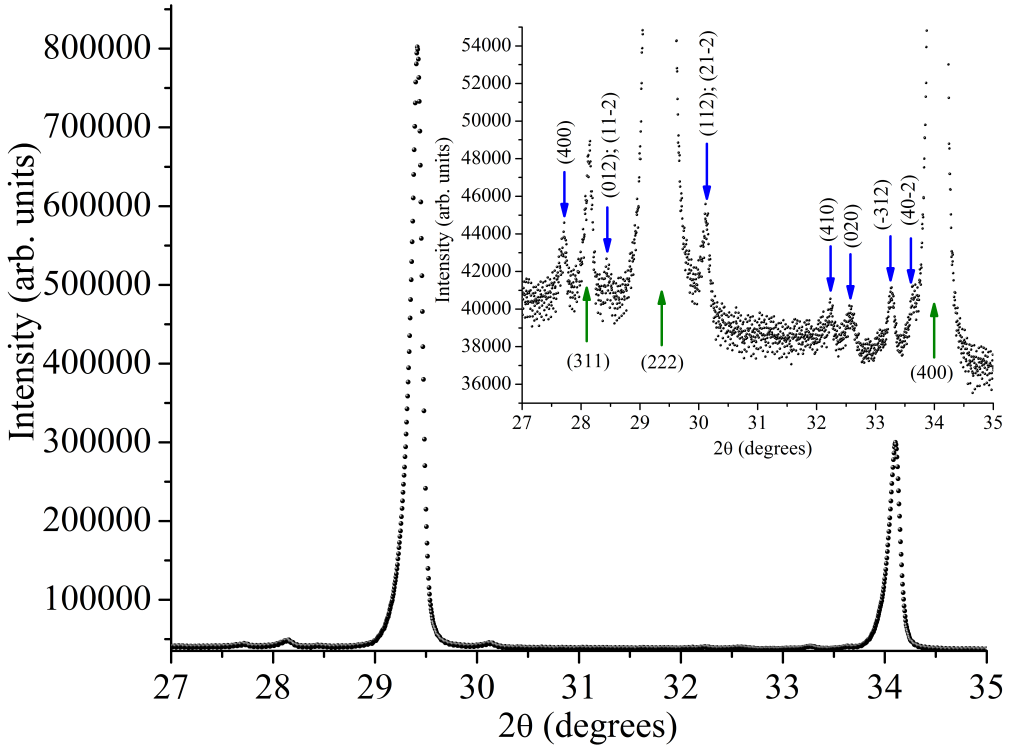

FIGURE 4.5: Measured room temperature powder x-ray diffraction profile for $Pr_2Sn_{1.3}Ti_{0.7}O_7$ on a HUBER G670 imaging-plate powder diffraction Guinier camera with a $K_{\alpha,1}$ source. Inset: The diffraction profile exhibits two distinct phases with a dominant pyrochlore $Fd\bar{3}m$ phase and a non-negligible monoclinic $P2_1$ phase, whose Bragg reflections are labelled by olive and blue arrows, respectively.

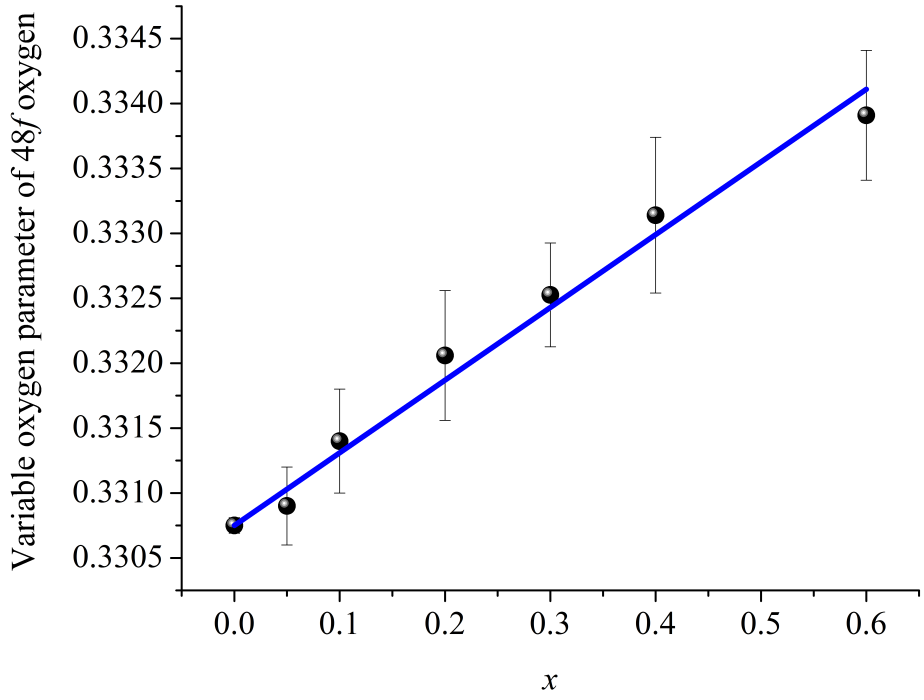

FIGURE 4.6: The variable positional parameter of the oxygen in the 48*f* Wyckoff position as a function of x. As the value of x increases, the unit cell lattice parameter a decreases — as shown in figure 4.4 — while the variable positional parameter of the 48*f* oxygen increases, in agreement with Kennedy *et al.* [38].

4.3 Susceptometry

4.3.1 DC Susceptometry of the $Pr_2Sn_{2-x}Ti_xO_7$ Pyrochlore Series

The DC magnetic susceptibility, χ, of each member of the $Pr_2Sn_{2-x}Ti_xO_7$ pyrochlore series was measured from 1.8 K to 30 K under an external applied magnetic field value of 0.01 T, 0.1 T and 1 T, respectively. The motivation for using the three aforementioned fields was based on the observation — which was the main conclusion of Chapter 3 — that the parent compound $Pr_2Sn_2O_7$ still remains in the spin ice regime until an external magnetic field $\mu_oH \approx 0.5$ T. Consequently, with the internal perturbation *via* chemical pressure, the fragility of the spin ice state in $Pr_2Sn_{2-x}Ti_xO_7$ was assumed to have increased. Thus two lower fields (0.01 T and 0.1 T) were chosen with the objective of probing the spin ice state. The significantly larger field of 1 T was chosen to probe the magnetic properties of the resulting magnetic state after the $Pr_2Sn_{2-x}Ti_xO_7$ pyrochlore series' members were completely out of the spin ice state. A comparison between the behaviour of different members under the three external applied magnetic fields — as shown in figures 4.7, 4.9 and 4.11, representing the behaviour for select members of the $Pr_2Sn_2O_7$ pyrochlore series under an external applied magnetic field of 0.01 T, 0.1 T and 1 T, respectively — reveals that in all three fields, no member exhibits any indication of the formation of an long range ordered magnetic state down to 1.8 K. Furthermore, for all external applied magnetic fields, as the value of x increases, there is an observed saturation of the magnetic susceptibility at higher temperatures. The observation of saturation at higher temperatures due to the increased value of x — indicated by the flattening of the DC magnetic susceptibility — is indicative that the increased value of x represents a deviation away from simple paramagnetic behaviour. Recall that this saturation of the DC susceptibility was also observed in the parent compound $Pr_2Sn_2O_7$ as the strength of the external applied magnetic field was increased. A comparison between the Weiss temperature and the Curie constant revealed that the drastic change in the net interaction energy scale between spins was caused by the large increase in the magnitude of the quantum mechanical exchange interaction compared to the comparatively smaller change in the dipolar moment. In an analogous manner to the application of an external magnetic field in Chapter 3, the Curie-Weiss parameters C and θ_{CW} were extracted with the Curie-Weiss law (equation 3.3) and shown in figures 4.13 and 4.14, respectively.

There is not only an approximate linear relationship between the value of θ_{CW} but the effect of the value of x is an order of magnitude higher than the effect on the nearest neighbour dipolar term D_{NN}. In particular, figure 4.14 clearly demonstrates that as one increases the value of x, the net interactions between spins become stronger and

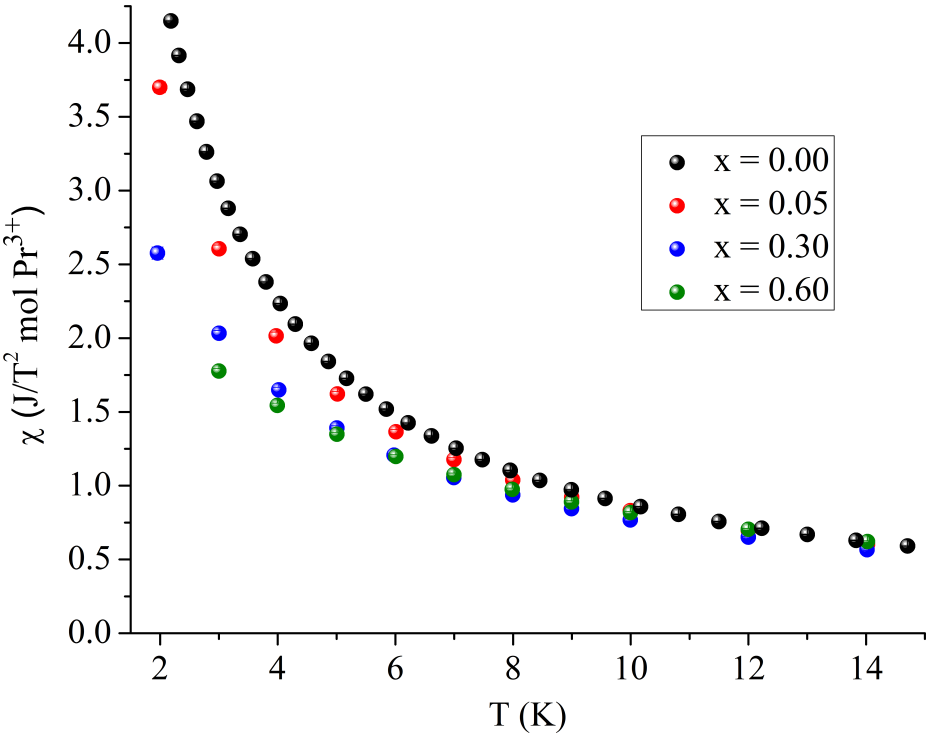

FIGURE 4.7: Molar DC ZFC magnetic susceptibility (M/H) of select members of the $Pr_2Sn_{2-x}Ti_xO_7$ pyrochlore series as a function of temperature with an external applied magnetic field $\mu_o H = 0.01$ T.

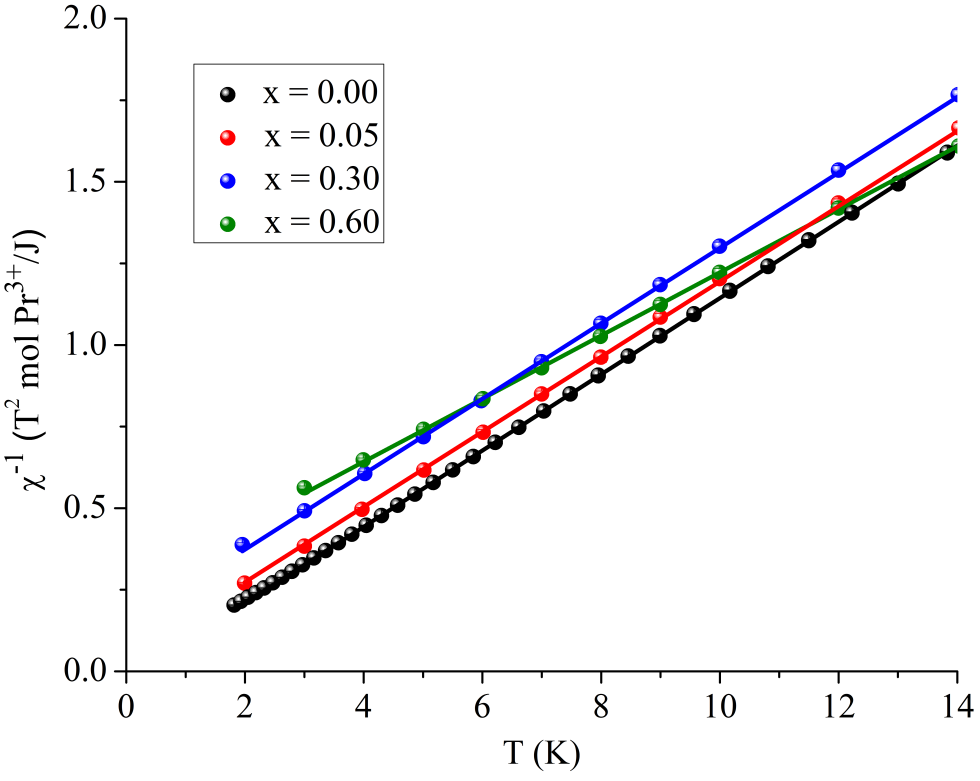

FIGURE 4.8: Inverse of the molar DC ZFC magnetic susceptibility (M/H) and Curie-Weiss fits for select members of the $Pr_2Sn_{2-x}Ti_xO_7$ pyrochlore series as a function of temperature with an external applied magnetic field $\mu_o H = 0.01$ T.

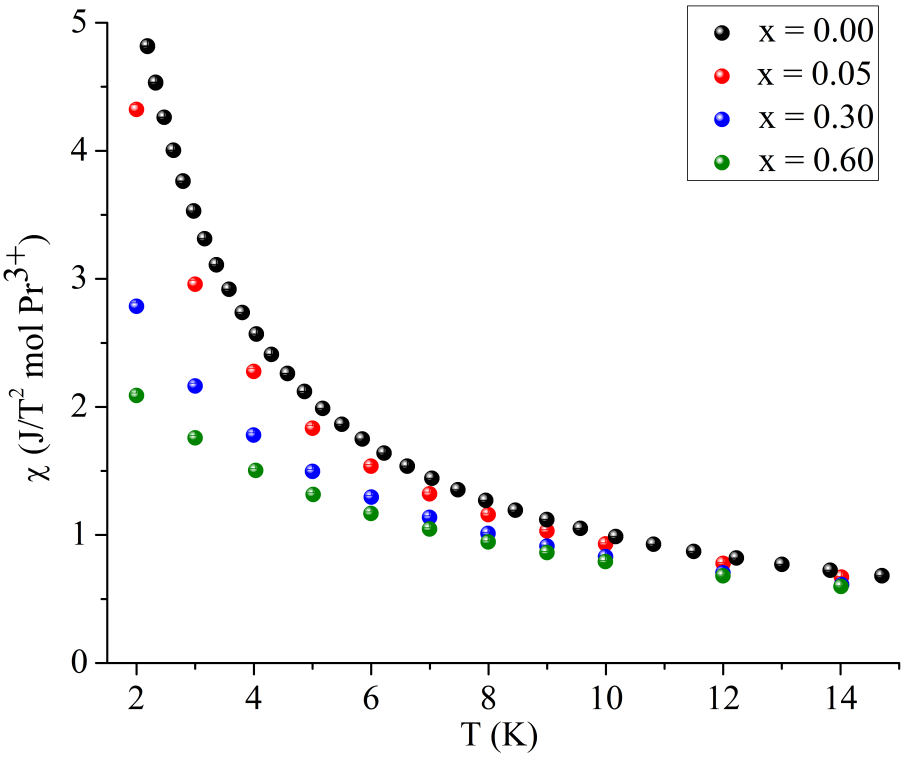

FIGURE 4.9: Molar DC ZFC magnetic susceptibility (M/H) of select members of the $Pr_2Sn_{2-x}Ti_xO_7$ pyrochlore series as a function of temperature with an external applied magnetic field $\mu_o H = 0.1$ T.

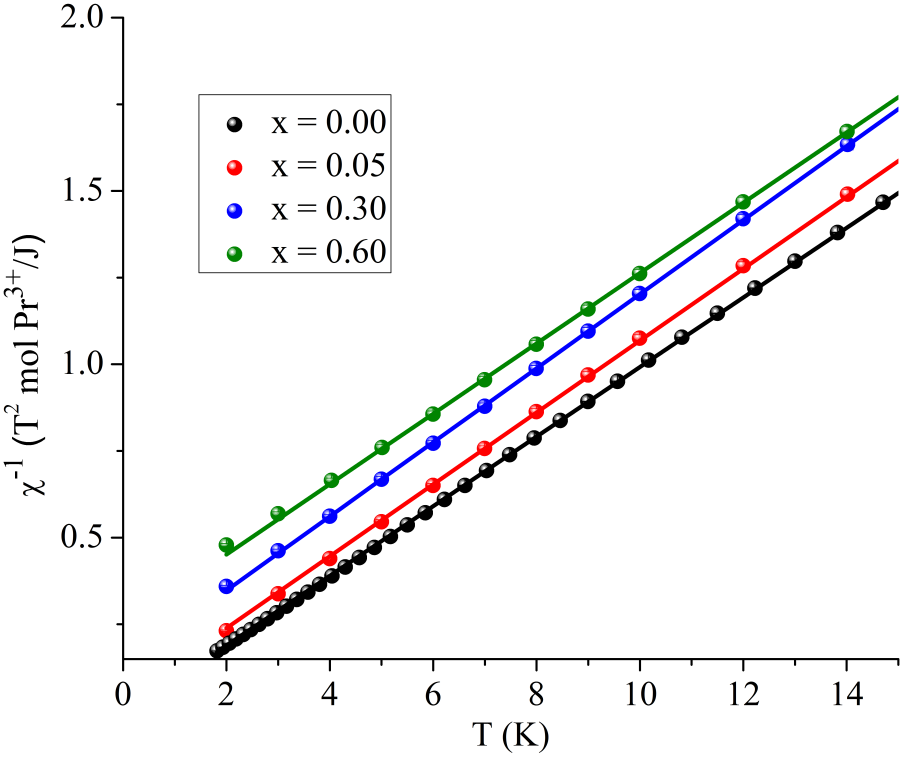

FIGURE 4.10: Inverse of the molar DC ZFC magnetic susceptibility (M/H) and Curie-Weiss fits for select members of the $Pr_2Sn_{2-x}Ti_xO_7$ pyrochlore series as a function of temperature with an external applied magnetic field $\mu_o H = 0.1$ T.

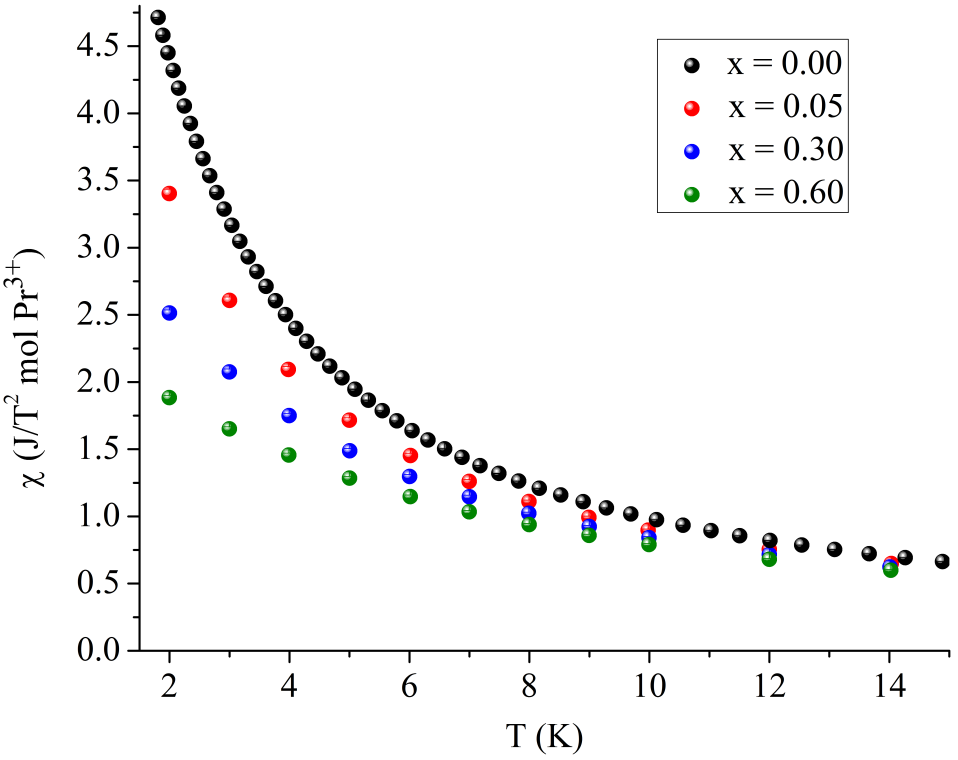

FIGURE 4.11: Molar DC ZFC magnetic susceptibility (M/H) of select members of the $Pr_2Sn_{2-x}Ti_xO_7$ pyrochlore series as a function of temperature with an external applied magnetic field $\mu_o H = 1$ T.

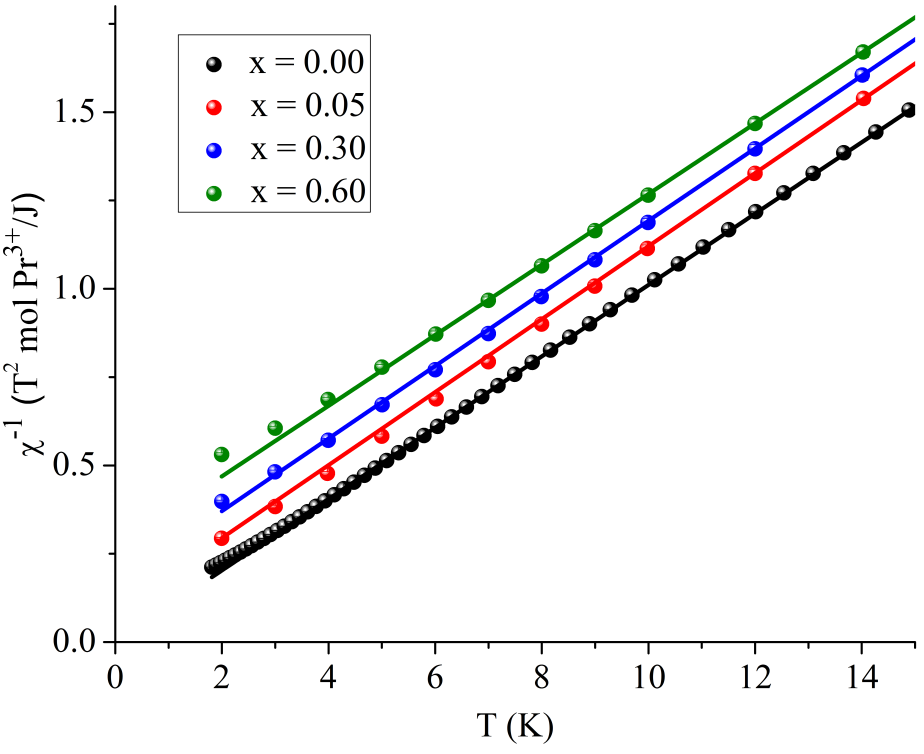

FIGURE 4.12: Inverse of the molar DC ZFC magnetic susceptibility (M/H) and Curie-Weiss fits for select members of the $Pr_2Sn_{2-x}Ti_xO_7$ pyrochlore series as a function of temperature with an external applied magnetic field $\mu_o H = 1$ T.

more importantly, are antiferromagnetic. This behaviour is completely analogous to the behaviour with the behaviour seen in Chapter 3 and thus suggests a possibility that the higher doped members (i.e. those members with high values of x) may form an LRO AFM state as proven for $Pr_2Sn_2O_7$ under large applied external magnetic fields.

As shown in figure 4.13, the effective magnetic moment μ_{eff} does not vary linearly as one would expect, instead, for an external applied magnetic field μ_oH of 0.01 T, there is a single sharp feature at $x \approx 0.3$ which may be indicative of a possible chemical pressure induced phase transition. As the field is increased from 0.01 T to 1 T, the feature at $x \approx 0.30$ substantially decreases while another feature at $x \approx 0.10$ appears and becomes more distinct. The decrease for $x \approx 0.30$ and concomitant increase for $x \approx 0.10$ feature with an increase in the external applied magnetic field are together indicative of larger net interactions between spins. The increase in the strength of the net spin-spin interactions is supported by figure 4.14 that demonstrates the 1 T Weiss temperature data set is more negative (within error) compared to both 0.01 and 0.1 T data sets. Figure 4.14 also reveals the fragility of the spin ice state with respect to chemical pressure. Recall from the *dipolar spin ice model*, the spin ice state can only exist if there are **net** ferromagnetic interactions, albeit the value of ferromagnetic dipolar interaction is allowed to be in close proximity to the value of an antiferromagnetic exchange interaction. Figure 4.14 demonstrates that the parent compound $Pr_2Sn_2O_7$ is pushed into a net AFM regime and thus away from the spin ice state with values of $x \approx 0.05$. Recall that this fragility of the spin ice state concerning chemical pressure involving the B^{4+} has also seen in $Tb_2Sn_2O_7$ by Dahlberg *et al.* [180]. Mirebeau *et al.* [181] using elastic neutron powder diffraction determined that $Tb_2Sn_2O_7$ switches from net antiferromagnetic to net ferromagnetic correlations at approximately 2 K. As the temperature is lowered to approximately 0.87 K, the system enters into an ordered ferromagnetic state indicated by the appearance of new magnetic Bragg peaks confirming the Curie temperature previously reported by Matsuhira *et al.* [192] three years prior using low temperature magnetic susceptibility. Mirebeau *et al.* determined that within the ferromagnetic structure were Tb^{3+} whose moments were reduced due to crystal field effects and who were slightly canted ($\theta \approx 13.3^o$) with respect to the local <111> direction. As a result of the net ferromagnetic interactions with slightly canted spins with respect the local $< 111 >$ direction, $Tb_2Sn_2O_7$ forms spin ice but since the system freezes into a long range ordered state, it is called an *ordered* spin ice. Although the system does enter the LRO FM state at $T_c \approx 0.87$ K, Mirebeau *et al.* [193] and Réotier *et al.* [194] demonstrated using heat capacity measurements and μSR relaxation spectroscopy, respectively, that there were collective spin fluctuations within the ordered spin ice state. These spin fluctuations were a result of clusters of ferromagnetic spins within the spin ice structure as deduced by Bert *et al.* [195] using μSR relaxation spectroscopy. The fact

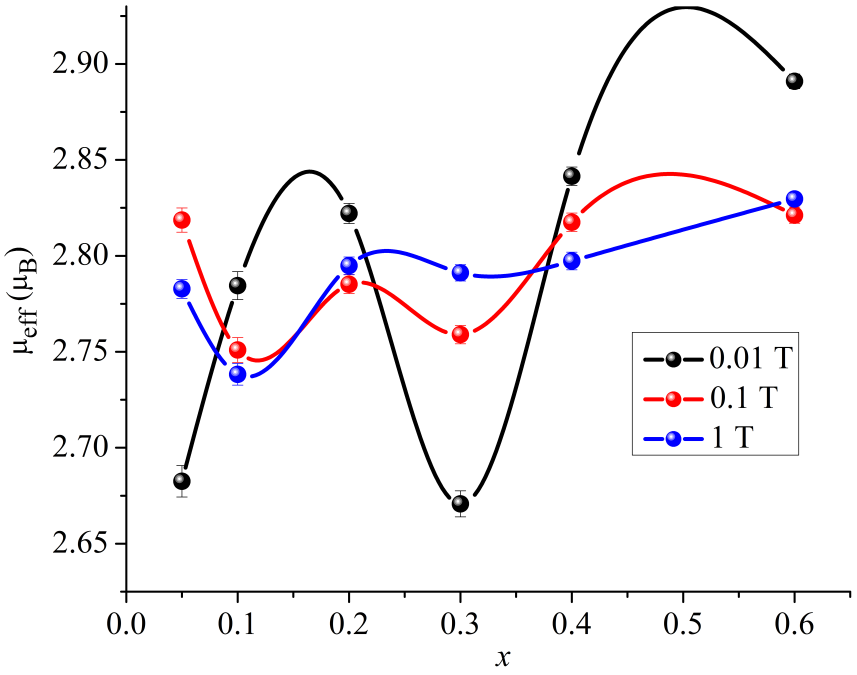

FIGURE 4.13: Calculated effective magnetic moment μ_{eff} as a function of doping x for the $Pr_2Sn_{2-x}Ti_xO_7$ pyrochlore series under an external magnetic field $\mu_o H$ of 0.01 T, 0.1 T and 1 T, respectively. The points constituting a data set are joined by splines to guide the reader and to emphasise discontinuities. At the lowest external applied magnetic field, there exists a discontinuity at $x \approx 0.30$ which is replaced by a discontinuity at $x \approx 0.10$ in the presence of higher external applied magnetic fields. These discontinuties are indicative of a possible chemical pressure induced phase transition.

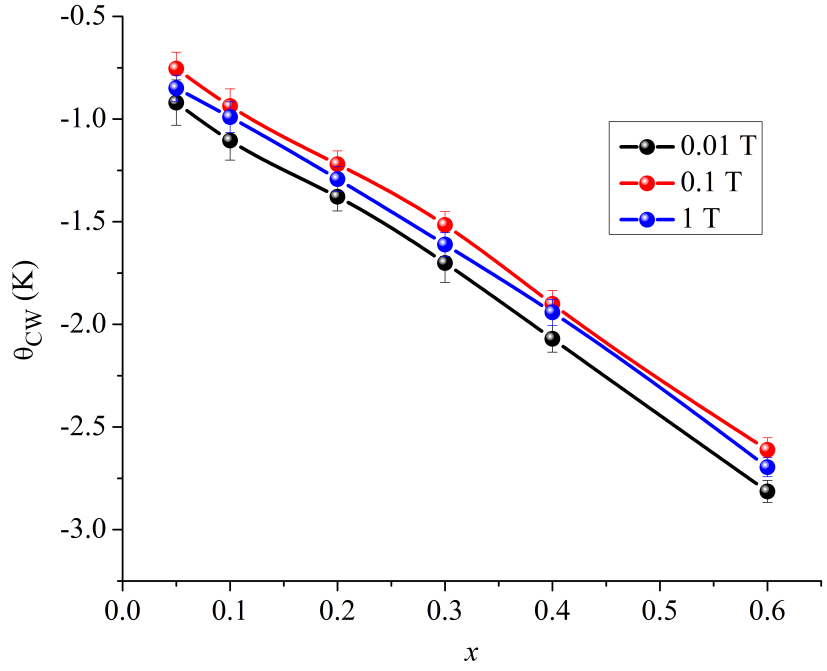

FIGURE 4.14: Calculated Weiss temperature, θ_{CW} as a function of doping x for the $Pr_2Sn_{2-x}Ti_xO_7$ pyrochlore series under an external applied magnetic field $\mu_o H$ of 0.01 T, 0.1 T and 1 T, respectively. The spin ice state exhibits great fragility with respect to doping. The fragility, indicated by the transition from a net ferromagnetic (FM) to net antiferromagnetic (AFM) regime occurs at very low values of x, i..e $0 < x < 0.05$.

that $Tb_2Sn_2O_7$ does indeed become static (on the μSR time scale) and loses part of the dynamic character characteristic of its titanate analog has been suggested by Mirebeau *et al.* [193] to be caused by the 3 % difference in lattice constants between the titanate and the stannate. The lattice expansion from the titanate to the stannate weakens the exchange interactions, thus allowing for the dipolar interactions to dominate leading to the system becoming static.

In 2011, Dahlberg *et al.* [180] were the first to explore the effects of the applying chemical pressure to a quantum spin ice. Recall from section 4.2 that systematic studies concerning doping in spin ices have often been limited to (i) canonical dipolar spin ices and (ii) stuffing of the A^{3+} cation into the 16*c* Wyckoff site. Unlike the stuffing in canonical dipolar spin ices, Dahlberg *et al.* discovered that $Tb_2Sn_2O_7$ exhibited the same hightened fragility as was exhibited by $Yb_2Ti_2O_7$. With a value of $x = 0.10$, the transition into an ordered spin ice state was completely surpressed, while a value of $x = 0.20$ resulted in a spin glass transition with $T_g \approx 250$ mK. Both $Tb_2Sn_2O_7$, $Yb_2Ti_2O_7$ and now $Pr_2Sn_2O_7$, demonstrate the fragility of the spin ice state with respect to doping. The fragility of the spin ice state can be observed by comparing the effective moment as a function of temperature.

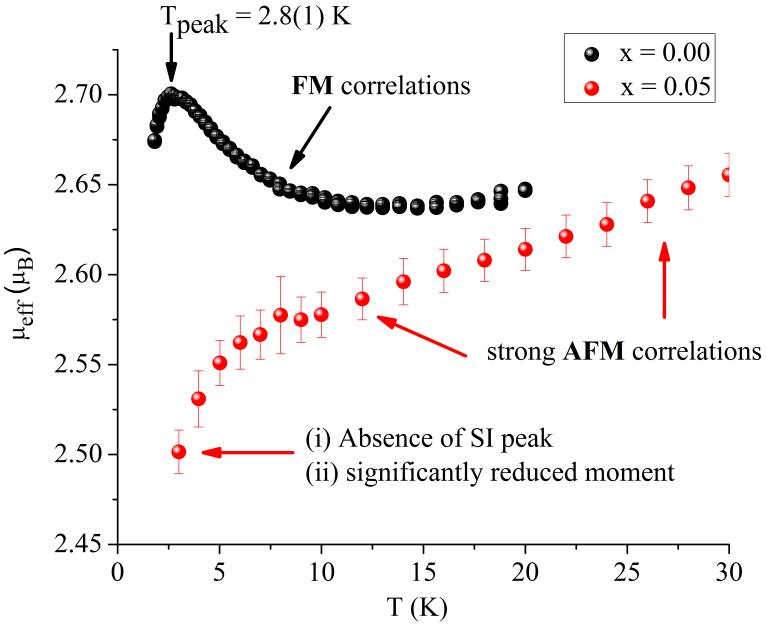

FIGURE 4.15: μ_{eff} as a function of temperature for the $Pr_2Sn_{2-x}Ti_xO_7$ pyrochlore series members $x = 0$ and 0.05, both under an external applied magnetic field μ_oH of 0.01 T. The parent compound exhibits both net ferromagnetic correlations and a broad peak at T = 2.8(1) K — characteristic of the spin ice state — both of which disappear in $Pr_2Sn_{1.95}Ti_{0.05}O_7$ which exhibits strong antiferromagnetic correlations with a significantly reduced ground state magnetic moment.

As shown in figure 4.15, the ferromagnetic correlations — characteristic of the spin

ice state — and the spin ice peak at 2.8(1) K are suppressed and replaced by strong antiferromagnetic interactions with a value of $x = 0.05$ under an applied external magnetic field of 0.01 T, in agreement with figure 4.14. Not only is the change between the parent compound $Pr_2Sn_2O_7$ and $Pr_2Sn_{1.95}Ti_{0.05}O_7$ abrupt in terms of the type of correlations present, but the magnetic moment of the ground state has been shown to be significantly reduced, below the value predicted by Princep *et al.* [149]. Since both compounds were measured under the (i) same and (ii) small external applied magnetic field of 0.01 T, the difference between the parent compound $Pr_2Sn_2O_7$ and $Pr_2Sn_{1.95}Ti_{0.05}O_7$ can only be explained by the presence of tetravalent titanium. It is important to note that the conclusion that the effect of doping $Pr_2Sn_2O_7$ results in (i) antiferromagnetic interactions that are (ii) stronger was deduced by both (i) the type of curvature and (ii) the value of the effective magnetic moment at comparable temperature scales, respectively. As seen in figure 4.14, the upward curvature of the temperature dependence of the effective magnetic moment of $Pr_2Sn_2O_7$ becomes distinctly downwards for $Pr_2Sn_{1.95}Ti_{0.05}O_7$ implying a net change in the type of interaction, while the curvature is much more prounounced between 1.8 K and 30 K. The enhanced curvature represents the presence of a larger energy gap beween crystal field states, Δ, which itself is indicative of stronger exchange interactions since J can be thought of as an internal field creating a local *energy scale*. As x increases from 0.05 to 0.20 under $\mu_o H = 0.01$ T, the compound behaves like a simple two level system whose exchange interactions monotonically increases with respect to doping as shown in figure 4.16.

Yet, as one transitions from $x = 0.20$ to $x = 0.30$ in the presence of 0.01 T, the curvature of the effective moment as a function of temperature does not increase, in fact, the curvature for $x = 0.30$ is similar to $x = 0.20$ but a significantly smaller scale (i.e. smaller moment). This behaviour is unexpected from a two simple level system because as one transitions from $x = 0.20$ to 0.30, the effective exchange spin-spin interaction's energy scale, J increases as seen by the increase in the magnitude of θ_{CW} in figure 4.14. If no other component of the system experienced any significant change, the internal field (derived from J) should increase and consequently the splitting and thus the curvature should increase. Instead, the curvature remains the same (implying a similar energy scale between $x = 0.20$ and 0.30) while the magnitude of the moment decreased, implying that the magnetic properties of the crystal field states involved in the probed transition must have changed (i.e. the $\left|^{2S+1}L_J, M_J\right\rangle$ basis vectors that constitute the crystal field levels must have changed). To confirm the claim of changing crystal field levels, the effective magnetic moment as a function of temperature was calculated under an external applied magnetic field of 0.1 T and 1 T for low values of x (i.e. $0 \leq x \leq 0.30$). The reason for choosing small values of x is because from figure 4.13, the apparent transition shifts from $x = 0.30$ in the presence of 0.01 T to $x \approx 0.1$ in the presence

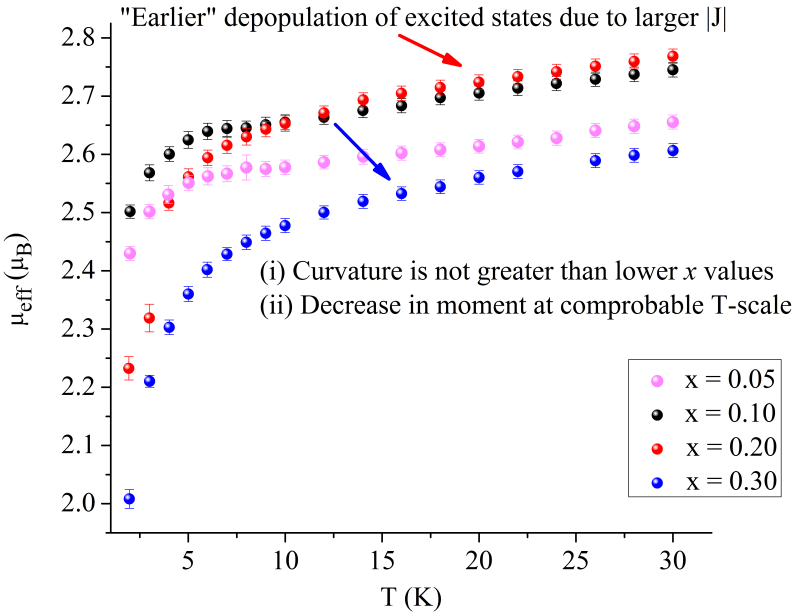

FIGURE 4.16: μ_{eff} as a function of temperature for the $Pr_2Sn_{2-x}Ti_xO_7$ pyrochlore series members $x = 0.05$, 0.10, 0.20 and 0.30, all under an external applied magnetic field μ_oH of 0.01 T. As one increases x from 0.05 to 0.20, the system acts as a simple two level system with increasing J as seen in figure 4.14. The curvature does not change significantly and the absolute value of the moment decreases from $x = 0.20$ to 0.30, supporting both the presence of a transition seen in figure 4.13 and the driving force behind this transition is a changing of constitutent $\left|^{2S+1}L_J, M_J\right\rangle$ basis vectors.

of 0.1 and 1 T. An additional benefit of choosing low values for x under 0.1 and 1 T is the observation that the value of J does not vary significantly from x values of 0.05 and 0.1. Consequently, if there are any drastic changes between the curvature of the effective moment's temperature dependence between $x = 0.05$ and 0.10 under applied magnetic fields of 0.1 T and 1 T, the effect must be caused by the change of the constituent $\left|^{2S+1}L_J, M_J\right\rangle$ basis vectors. As both figures 4.17 and 4.18 show, this distinct change between $x = 0.05$ and 0.1 does indeed exist in the presence of external applied magnetic fields of 0.1 T and 1 T, respectively, confirming the discontinuities present in figure 4.13. It should be noted that as the field is increased (i.e. comparing figure 4.16 to 4.18), the difference in curvature between $x = 0.20$ and 0.30 disappears (as seen in figure 4.13) and the system behaves as simple two level system which is expected since the transition for the larger external applied magnetic fields occurs at lower values of x. The role of the identity of the constitutent $\left|^{2S+1}L_J, M_J\right\rangle$ basis vectors, although crucial, is not surprising. As a crude first approximation, one can imagine the crystal field levels of the $Pr_2Sn_{2-x}Ti_xO_7$ pyrochlore series as a result from a linear combination of the crystal field schemes of the parent $Fd\bar{3}m$ pyrochlore compound $Pr_2Sn_2O_7$ and the monoclinic $P2_1$ $Pr_2Ti_2O_7$. The net result would be an effective *smearing* of the crystal field levels of $Pr_2Sn_2O_7$ (i.e. the bulk phase) which can be formally quantified by a change of constituent $\left|^{2S+1}L_J, M_J\right\rangle$ basis vectors for each crystal field level as was seen

for $Pr_{2-x}Bi_xRu_2O_7$ by van Duijin *et al.* [196]. The admixture of $\left|^{2S+1}L_J, M_J\right\rangle$ basis vectors constituting individual crystal field states induced by magnetic field and the admixture's role in driving the system into an LRO AFM state supports the hypothesis that the *smearing* effect caused by doping drives the system away from the spin ice state. An inevitable follow-up question would be if the *smearing* effect from doping $Pr_2Sn_2O_7$ with tetravelent titanium causes the system to depart from the spin ice state, does the *smaring* of the crystal field levels have the same effect as the admixture caused by the application of external magnetic fields? In other words, does doping cause the system to transition into an LRO AFM state and if not, what type of magnetic state does $Pr_2Sn_{2-x}Ti_xO_7$ possess? An attempt to answer this question will be the main focus for the remainder of the chapter.

4.3.2 Field Dependence of the Magnetic Properties of $Pr_2Sn_{1.4}Ti_{0.6}O_7$

As described in section 3.1 and subsection 4.3.1, the $Tb_2B_2O_7$ system where B = Sn^{4+} and Ti^{4+}, provides a useful analogy when attempting to characterise the magnetic properties of the magnetic state created by applying chemical pressure to a quantum spin ice. One may also be reminded that the analogy to the $Tb_2B_2O_7$ system is also limited because of the virtual excitation mechanism behind its *quantum* nature is different than the crystal field pollution seen in $Pr_2Sn_2O_7$, but nonetheless, the observations of Dahlberg *et al.* [180] provide some insight as to the possible effects of introducing tetravalent titanium into a stannate quantum spin ice. The $Pr_2Sn_{1.4}Ti_{0.6}O_7$ member of the $Pr_2Sn_{2-x}Ti_xO_7$ pyrochlore series was chosen because from figure 4.13, at the lowest external applied magnetic field of 0.01 T, there was evidence that there was a possible phase transition at $x = 0.30$ while at larger fields, the transition occurred at lower values of x. The objective of this study is to explore the final magnetic state and since figure 4.13 shows $Pr_2Sn_{1.4}Ti_{0.6}O_7$ is clearly in the new magnetic state, the highest doped member is thus a suitable candidate for study.

As shown in figure 4.19, DC susceptibility measurements down to 1.8 K with external applied magnetic fields from 0.01 T to 9 T, provided no anomalies that would be indicative of the formation of a long range ordered state. In a similar manner to $Pr_2Sn_2O_7$, the low temperature behaviour of the DC susceptibility is strongly correlated to the strength of the external applied magnetic field. The system exhibits simple paramagnetic behaviour (down to 1.8 K) in low magnetic fields while under the application of larger fields, the DC susceptibility saturates at a finite value of 0.82(1) J $\cdot$ (T^2 mol Pr^{3+})$^{-1}$ at 9 T, albeit lower than the value observed in $Pr_2Sn_2O_7$ which saturates at 0.91(1) J $\cdot$ (T^2 mol Pr^{3+})$^{-1}$. The significant change in curvature of the DC magnetic susceptibility suggests that in a similar manner to $Pr_2Sn_2O_7$, there is a possibility of

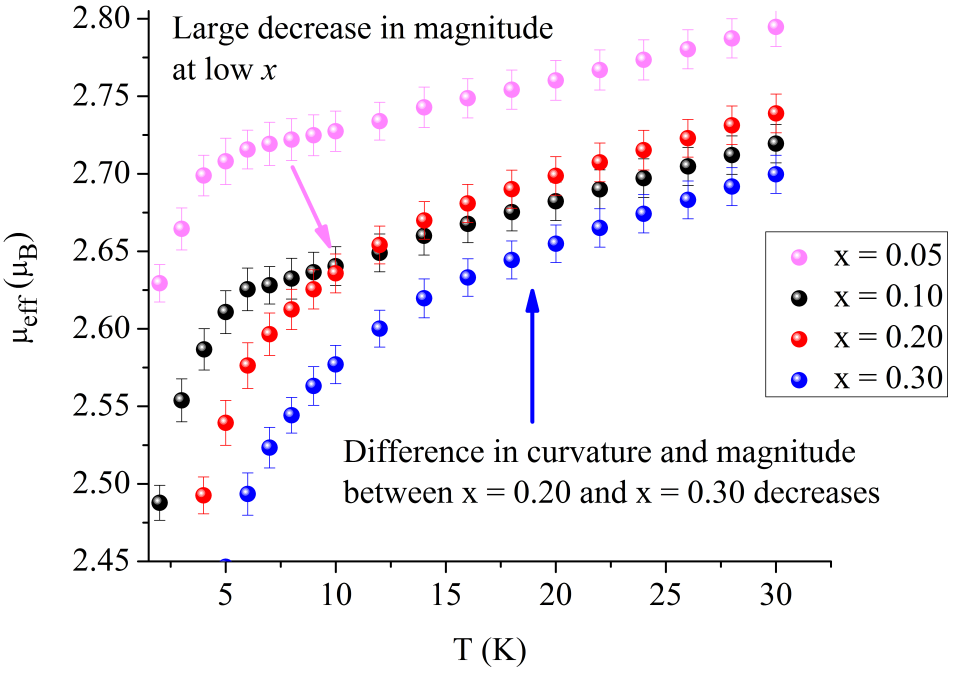

FIGURE 4.17: μ_{eff} as a function of temperature for the $Pr_2Sn_{2-x}Ti_xO_7$ pyrochlore series members $x = 0.05$, 0.10, 0.20 and 0.30, all under an external applied magnetic field μ_oH of 0.1 T. As seen in figure 4.13, the differences between $x = 0.20$ and 0.30 decreases, yet the difference at x 0.05 and 0.10 increases, once again indicative of a possible phase transition.

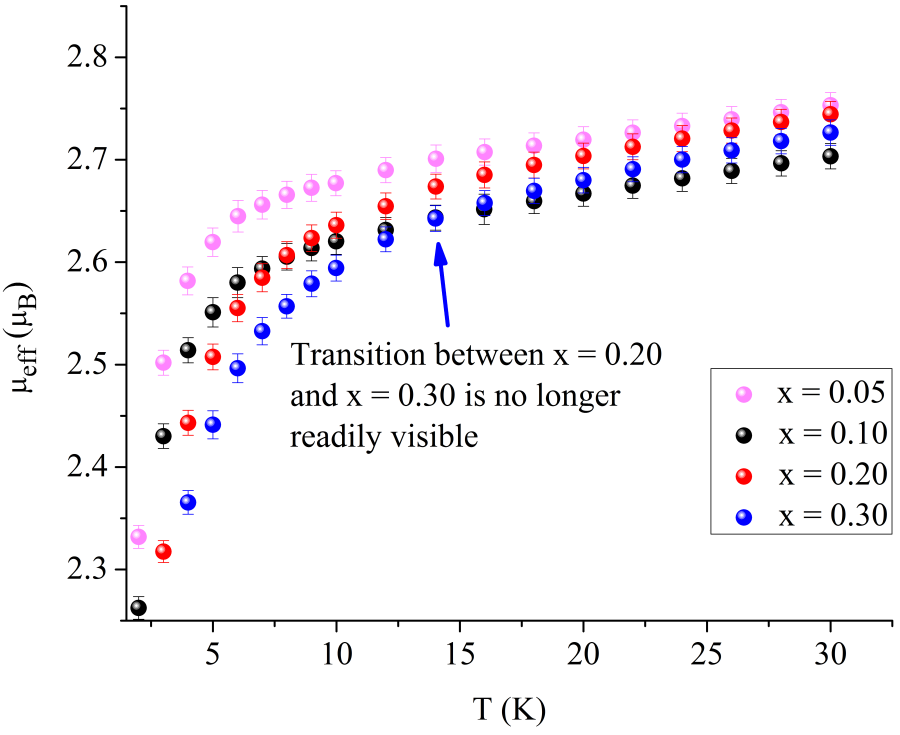

FIGURE 4.18: μ_{eff} as a function of temperature for the $Pr_2Sn_{2-x}Ti_xO_7$ pyrochlore series members $x = 0.05$, 0.10, 0.20 and 0.30, all under an external applied magnetic field μ_oH of 1 T. As seen in figure 4.13, the differences between $x = 0.20$ and 0.30 no longer exists, yet the difference at $x = 0.05$ and 0.10 increases, once again indicative of a phase transition. The similarity of the Weiss temperature θ_{CW} between $x = 0.05$ and 0.10 for 0.01 T and 1 T supports the hypothesis from figure 4.16 that the driving force behind the transition is a changing of constitutent $\left|^{2S+1}L_J, M_J\right\rangle$ basis vectors.

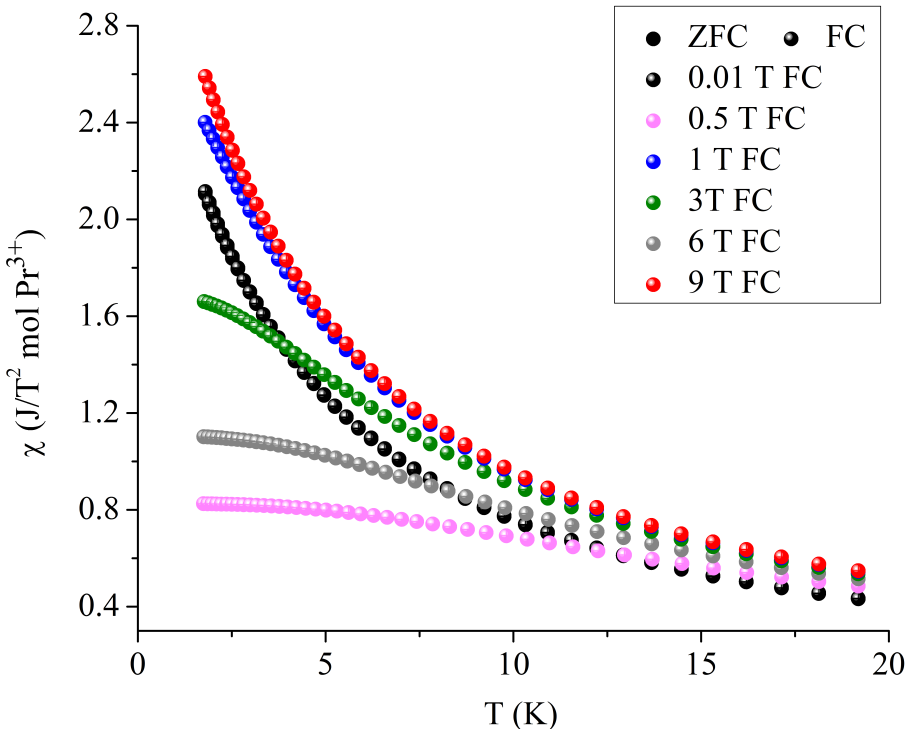

FIGURE 4.19: Molar DC ZFC magnetic susceptibility (M/H) of $Pr_2Sn_{1.4}Ti_{0.6}O_7$ as a function of temperature for select applied magnetic fields.

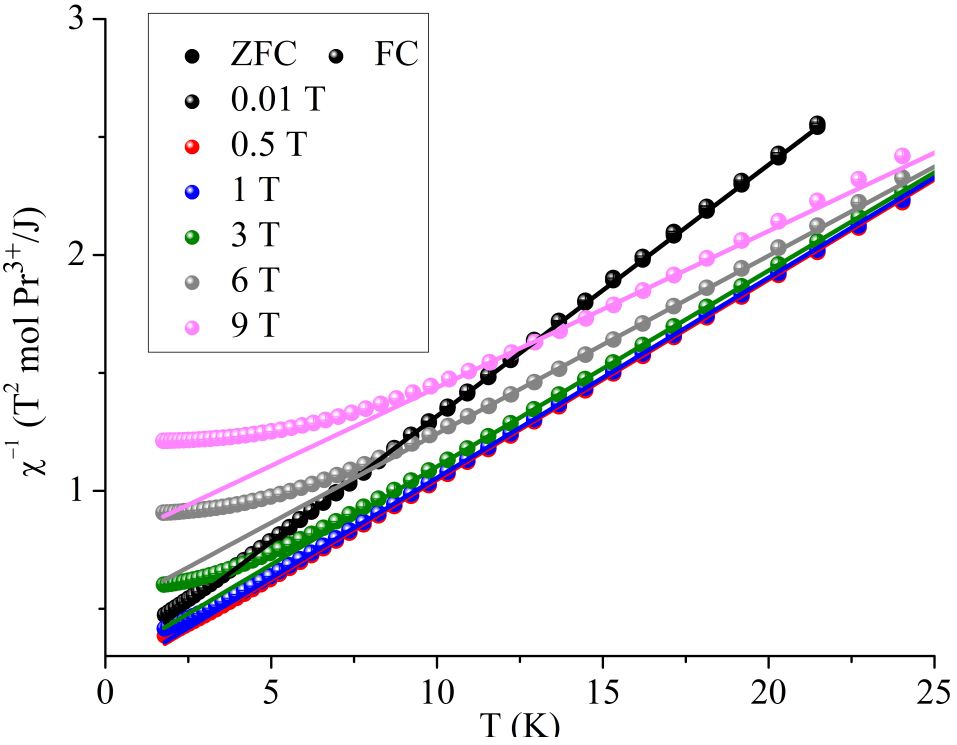

FIGURE 4.20: Inverse of the molar DC ZFC magnetic susceptibility and Curie-Weiss fits of $Pr_2Sn_{1.4}Ti_{0.6}O_7$ as a function of temperature for select applied magnetic fields.

a field induced transition. The possibility of a field induced transition was confirmed by examining the behaviour of the Curie-Weiss parameters θ_{CW} and C with respect to the external applied magnetic field as shown in figures 4.21 and 4.22, respectively. In a similar manner to $Pr_2Sn_2O_7$, the effective magnetic moment μ_{eff} experiences a significant increase from 0.01 T to 0.1 T but unlike $Pr_2Sn_2O_7$, the value of μ_{eff} does not experience a gradual increase and subsequent decrease at a low external applied magnetic field. The reader may recall from section 3.2, the sudden decrease in μ_{eff} provided the first piece of evidence suggesting a possible phase transition at approximately an external applied magnetic field of 0.5 T. Instead, as shown in figure 4.22, the value of μ_{eff} in $Pr_2Sn_{1.4}Ti_{0.6}O_7$ increases once again from 0.1 T to 0.5 T but then remains constant until an external applied magnetic field of approximately 3 T where its behaviour is completely analogous to that of $Pr_2Sn_2O_7$ after approximately 0.75 T, in other words, when $Pr_2Sn_2O_7$ is in its AFM state as proven by both isobaric heat capacity and elastic neutron diffraction. The distinctly different behaviour between $Pr_2Sn_{1.4}Ti_{0.6}O_7$ and $Pr_2Sn_2O_7$ is also observed with the Weiss temperature's field dependence behaviour. As shown in figure 4.21 — unlike the continuous decrease seen in $Pr_2Sn_2O_7$ — $Pr_2Sn_{1.4}Ti_{0.6}O_7$ experiences an initial increase in the Weiss tempeature from 0.01 T to 0.1 T while assuming a continuous decrease that continues to 9 T. The increase in the Weiss temperature — which is unexpected for a simple AFM — and the observation that the effective magnetic moment remains constant from 0.5 T to 3 T both imply that before an AFM is formed, there is some intermediate magnetic state that the system assumes after a field of ≈ 0.1 T.

The transition between 0.01 T and 0.1 T is made even more evident by plotting the effective magnetic moment as a function of temperature. As shown in figure 4.23, there is a stark difference between the effective magnetic moment of the excited crystal field states. Recall that if the system was a simple antiferromagnet, then as the temperature is decreased, thermal excitations between crystal field states slowly become statistically unlikely and thus the higher crystal field states depopulate. As the external applied magnetic field is increased, the internal field — related to the effective exchange J spin-spin interactions — increases as well which in turn causes a large crystal field splitting Δ which causes the system to depopulate at a larger temperature. Instead, what is observed from 0.01 T to 0.1 T is a drastic increase in the excited crystal field level's effective magnetic moment implying the possibility of some type of phase transition. In contrast, the claim that there is a transition at approximately 3 T is not clear from figure 4.23. Rather, the system behaves as the aforementioned two level crystal field system with $\Delta(\approx J)$. Instead, the possibility of transition at an external applied magnetic field of 3 T can be investigated by analysing the isothermal magnetisation at base temperature. As shown in figure 4.24, the behaviour of the isothermal magnetisation of $Pr_2Sn_2O_7$ is quite

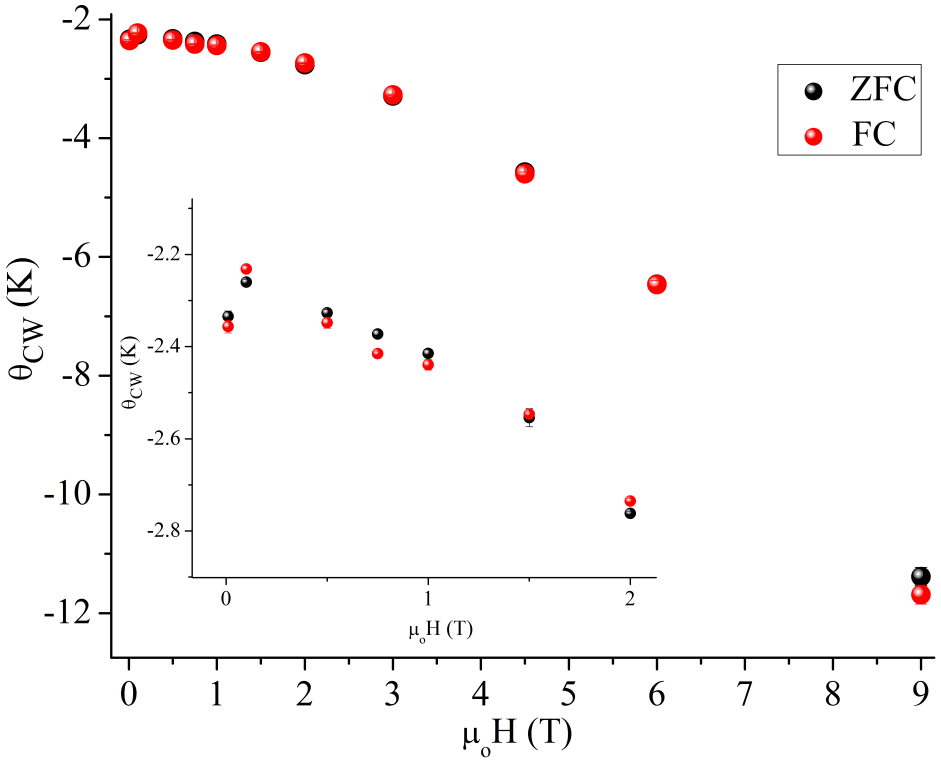

FIGURE 4.21: Calculated Weiss temperature, θ_{CW} as a function of applied field for $Pr_2Sn_2O_7$; Inset: The Weiss temperature increases from 0.01 to 0.1 T, indicating a possibility of a field induced phase transition.

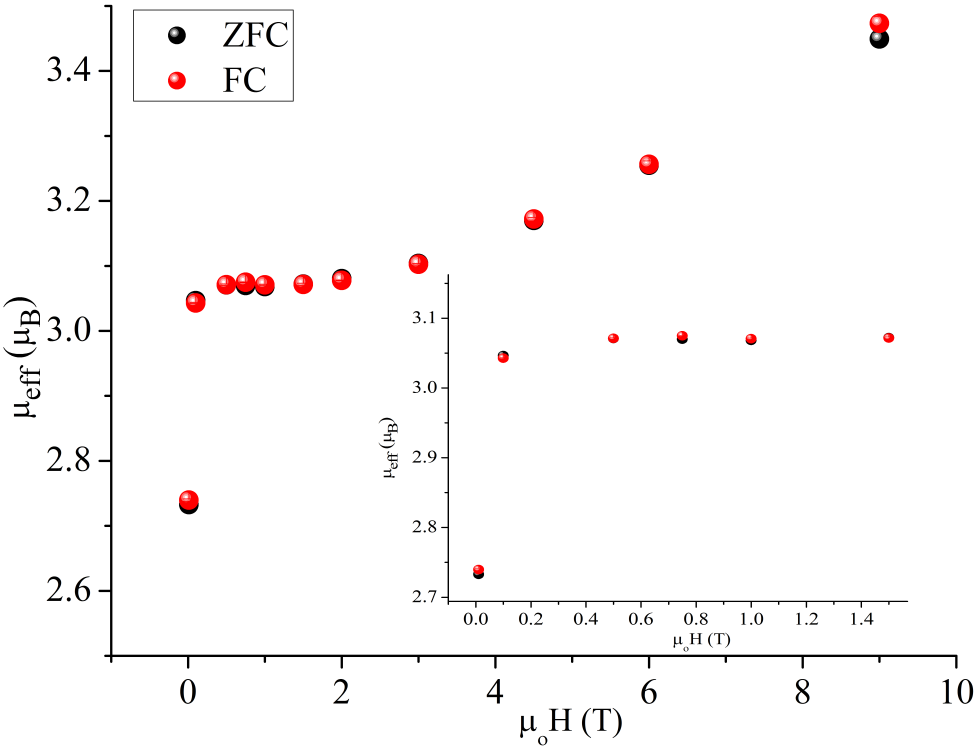

FIGURE 4.22: Calculated effective magnetic moment μ_{eff} as a function of applied external magnetic field for $Pr_2Sn_{1.4}Ti_{0.6}O_7$; Inset: The effective magnetic moment's non-linear behaviour at low applied external magnetic fields. The similarity of $Pr_2Sn_{1.4}Ti_{0.6}O_7$ and $Pr_2Sn_2O_7$ after $\mu_oH \approx 3$ T is an indication for a field induced phase transition into an LRO.

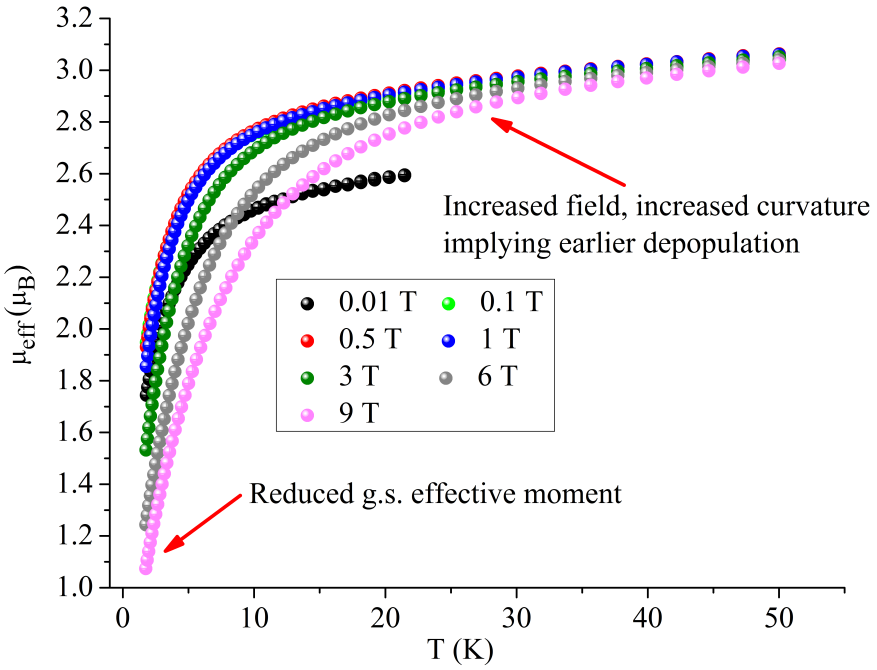

FIGURE 4.23: μ_{eff} as a function of temperature for various applied external magnetic fields. The stark difference in behaviour from 0.01 T and 0.1 T implies there exists a possibility for a field induced transition. The behaviour from 0.1 to 9 T corresponds to a simple two level system with $\Delta(\approx J)$, providing no indication of the 3 T transition deduced in figure 4.22.

different compared to that of $Pr_2Sn_{1.4}Ti_{0.6}O_7$. The former saturates at approximately one-half of the magnetisation predicted by the constituent $\left|^{2S+1}L_J, M_J\right\rangle$ basis vectors deduced by Princep *et al.* in agreement with the predictions of Matsuhira *et al.* [84]. The latter's magnetisation does not saturate, confirming the loss of the ferromagnetic spin ice correlations, instead implying the presence of strong net antiferromagnetic correlations as suspected from the values of the Weiss temperature observed in figure 4.21. Furthermore, as shown in figure 4.24, the isothermal magnetisation was subsequently modelled by a Brillouin function B_J (H,T) which provided an effective J of 1.45(1) and $\mu = 2.35(3)\ \mu_B$ confirming that the reduction in the Pr^{3+} moment and its total angular moment J. By taking the first derivative of the isothermal magnetisation $\left(\frac{\partial M}{\partial H}\right)_T$ as shown in figure 4.25, there is no evidence of a phase transition at approximately 3 T as deduced from the Curie-Weiss parameters extracted from DC susceptometry measurements. The lack of a drastic change in $\left(\frac{\partial M}{\partial H}\right)_T$ (e.g. a maximum or minimum) does not confirm the phase transition suspected in figure 4.22. Instead, a maximum is shown at an externally applied magnetic field of approximately 0.1 T, providing support for the claim that the compound enters an intermediate magnetic state, as seen in figures 4.21 and 4.22.

To summarise, magnetic field studies using DC magetisation on $Pr_2Sn_{1.4}Ti_{0.6}O_7$ has

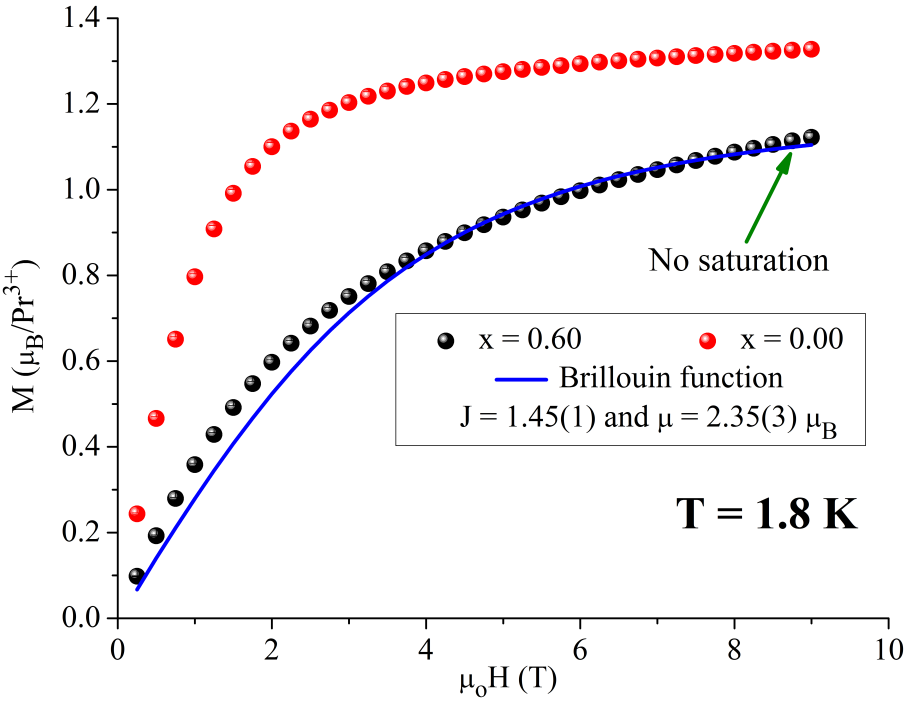

FIGURE 4.24: Isothermal magnetisation M as a function of applied external magnetic field for $Pr_2Sn_{1.4}Ti_{0.6}O_7$at 1.8 K. The isothermal magnetisation of $Pr_2Sn_2O_7$ is also included for comparison. The isothermal magnetisation of $Pr_2Sn_{1.4}Ti_{0.6}O_7$ unlike $Pr_2Sn_2O_7$ does not satuarate implying net AFM correlations. A fit to a Brillouin function was performed providing a J = 1.45(1) and a moment of μ = 2.35(3) μ_B, both values are significantly reduced compared to the free ion values, implying strong crystal field effects.

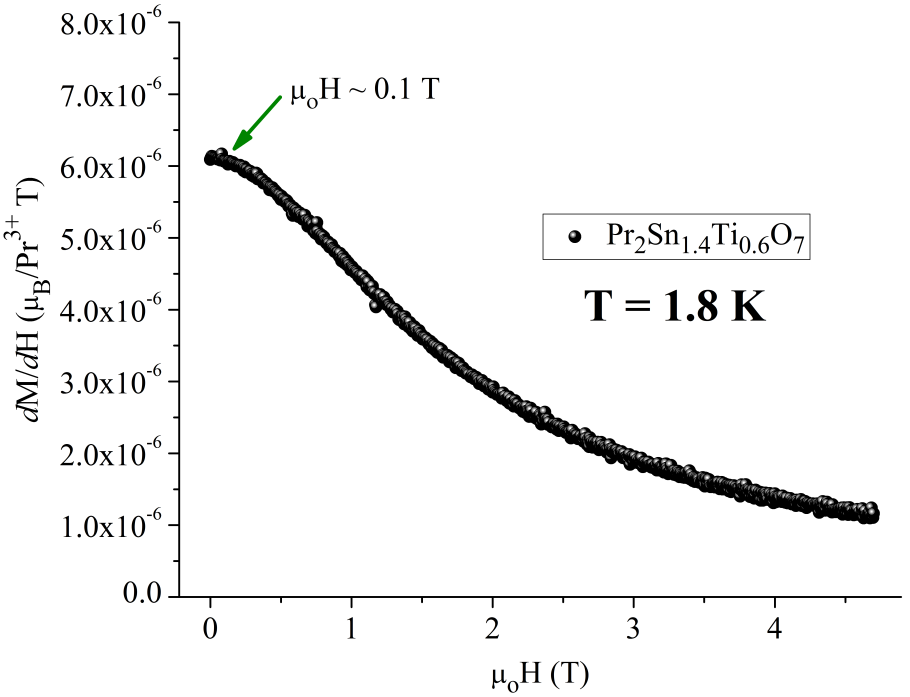

FIGURE 4.25: First order derivative of high resolution (remeasurement of data in figure 4.24) isothermal magnetisation $\left(\frac{\partial M}{\partial H}\right)_T$ at 1.8 K for $Pr_2Sn_{1.4}Ti_{0.6}O_7$. There is an absence of a sharp feature at approximately 3 T, providing no indication that the system undergoes a transition into an AFM state by 3 T. A maximum at $\mu_o H \approx 0.1$ T is indicated by the olive arrow, providing further evidence of a possible transition into an intermediate magnetic state.

revealed distinctly different behaviour compared to the parent compound $Pr_2Sn_2O_7$. DC magnetisation implies that $Pr_2Sn_{1.4}Ti_{0.6}O_7$ enters a new magnetic state at approximately 0.1 T confirmed by the temperature dependence of μ_{eff} and the anomalous rise in the Weiss temperature in figure 4.21. This intermediate magnetic state is quite robust as the possible transition into an LRO AFM state is suspected to occur at 3 T, deduced from the magnetic field dependence of μ_{eff}, although isothermal magnetisation provides no further experimental support for this possible transition claim. The fact that experimental evidence suggests that it requires an external magnetic field of 3 T to cause the transition into an LRO AFM state is indeed surprising considering that the magnitude of the Weiss temperature for $Pr_2Sn_{1.4}Ti_{0.6}O_7$ is significantly larger than $Pr_2Sn_2O_7$ at similar field strengths. The increased magnitude of the Weiss temperatures in figure 4.21 would suggest — if one were to make a one-to-one correspondence to $Pr_2Sn_2O_7$— that the system would be already in the LRO AFM regime since the dipolar interactions are relatively unchanged compared to $Pr_2Sn_2O_7$ since the effective moments in figure 4.22 are quite similar to those observed in $Pr_2Sn_2O_7$. The lack of an LRO AFM, despite stronger AFM correlations, imply that the AFM correlations must be short ranged (i.e. the greatest contribution to θ_{CW} must be J_{NN}) and thus prohibits the formation of a LRO AFM state without a large external perturbation. This conclusion implies the presence of small clusters of Pr^{3+} spins with strong AFM correlations that are limited to its neighbours within the cluster. This antiferromagnetic cluster hypothesis, although drastically different from the simple LRO AFM in $Pr_2Sn_2O_7$, is a possibility considering the inherent disordered nature of the magnetism in $Pr_2Sn_{1.4}Ti_{0.6}O_7$. Recall that the $Pr_2Sn_{2-x}Ti_xO_7$ pyrochlore series was synthesised by replacing tetravalent tin in the 16*c* Wyckoff site with titanium. The location of the titanium is assumed to be completely random, although limited to the 16*c* site. The random nature of the titanium distribution within the pyrochlore unit cell would introduce random structural deviations within the $Pr_2Sn_2O_7$ ideal structure. If random structural deviations are introduced in $Pr_2Sn_2O_7$ structure, the local crystal field environments — as seen in the preceeding subsection — and thus the magnetism would inevitably change. One would suspect that the introduction of the random deviations would subject the system to additional constraints but as seen in $Tb_2Sn_2O_7$ by Dahlberg *et al.* [180], the additional constraints do not encourage an LRO to be formed, rather it destroys the LRO and causes a spin glass state to form if the Tb^{3+} are diluted enough. A similar situation may be occurring in $Pr_2Sn_{1.4}Ti_{0.6}O_7$, where the random distribution of Ti^{4+} surpresses the ability of an external stimulus (in this case, an external magnetic field) to perturb the system into an LRO. The inevitable question is since $Pr_2Sn_{1.4}Ti_{0.6}O_7$ represents the highest doped member of the $Pr_2Sn_{2-x}Ti_xO_7$ pyrochlore series, is the intermediate magnetic phase (i.e. the magnetic phase before 3 T in $Pr_2Sn_{1.4}Ti_{0.6}O_7$), a spin glass? The lack of a T_g in the DC susceptibility suggests that $Pr_2Sn_{1.4}Ti_{0.6}O_7$ does not assume a spin glass state

down to 1.8 K and this was confirmed using AC susceptometry which is the subject of the next subsection.

4.3.3 AC susceptometry of the $Pr_2Sn_{2-x}Ti_xO_7$ Pyrochlore Series

From Chapter 3 — in particular, section 3.5 — the parent compound $Pr_2Sn_2O_7$, forms a long range ordered magnetic state with an externally applied magnetic field $\mu_oH \leq 1$ T while DC susceptometry on $Pr_2Sn_{1.4}Ti_{0.6}O_7$ described in subsection 4.3.2 provides some indication towards the formation of a long range ordered magnetic state at an externally applied magnetic field $\mu_oH \approx 3$ T. In both cases, for $Pr_2Sn_2O_7$ and for $Pr_2Sn_{1.4}Ti_{0.6}O_7$, there still remains ambiguity concerning the intermediate magnetic structure both systems assume before the external magnetic field induces an LRO magnetic state. AC susceptometry was performed on each member of the $Pr_2Sn_{2-x}Ti_xO_7$ pyrochlore series from 1.8 K to 15 K in the absence of an external magnetic field with a small oscillating field ($H_{osc} < 1$ Oe) with variable frequencies between $f = 10$ Hz to 1 KHz. As shown in figures 4.26, 4.27, 4.28 and 4.29, each member of the $Pr_2Sn_{2-x}Ti_xO_7$ pyrochlore series exhibits no evidence of a static magnetic structure being formed for all driving frequencies. For example, if a static magnetic structure was formed, this would be indicated by a cusp in the in-phase or *dynamic susceptibility* χ'. The cusp in χ' would indicate that at a particular frequency *f*, the relaxation of the spins are much slower than the driving frequency of AC magnetic field implying the spin dynamics in the system appear static (at the time scale of AC susceptometry) as is seen in the cases of stuffed canonical spin ices such as $Ho_{2-x}A_xTi_xO_{7-\delta}$ by Synder *et al.* [132]. The lack of these static features in figure 4.26 confirms persistent fluctuations down to 1.8 K in the parent compound $Pr_2Sn_2O_7$ but once again these results imply that the system is still fluctuating only on the time scale of the AC susceptibility. Zhou *et al.* [31] experimentally determined that these highly correlated spin fluctuations are no longer thermally activated but are in fact located in a quantum mechanical regime with the characteristic relaxation time τ on the order of nanoseconds. Thus the dynamic system is on the time scale probed by AC susceptometry. As aforementioned, each member of the $Pr_2Sn_{2-x}Ti_xO_7$ pyrochlore series ($x = 0.05$, 0.40 and 0.60 are shown in figures 4.27, 4.29 and 4.28, respectively) demonstrate persistent spin fluctuations down to 1.8 K. These persistent spin fluctuations are important because although the parent compound's relaxation dynamics are on such a smaller time scale compared to the AC driving frequency *f* at 1.8 K, any dilution of the magnetism — particularly on the 16*c* Wyckoff site — is expected to drastically change the energetics and thus the time scale of these fluctuations.

Recall Dahlberg *et al.* [180] demonstrated that $Tb_2Sn_{2-x}Ti_xO_7$ when $x = 0.10$, the transition associated with $Tb_2Sn_2O_7$ entering the ordered spin ice state was suppressed

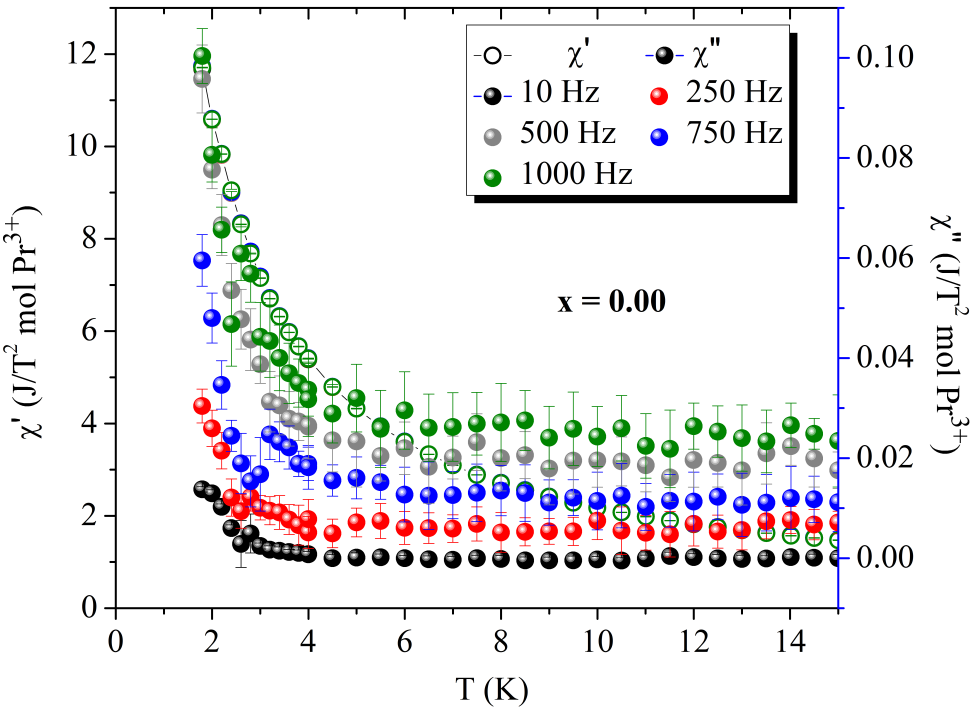

FIGURE 4.26: Low-temperature AC susceptibility of $Pr_2Sn_2O_7$ in zero external applied magnetic field. Open symbols show the in-phase χ'(T) while the closed symbols show the out-of-phase χ"(T).

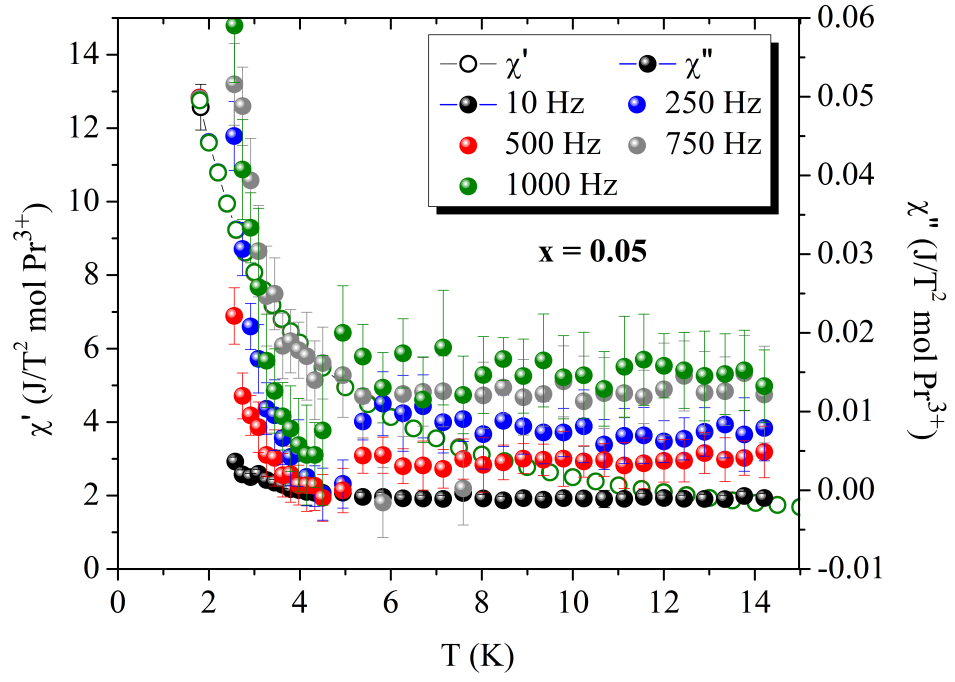

FIGURE 4.27: Low-temperature AC susceptibility of $Pr_2Sn_{1.95}Ti_{0.05}O_7$ in zero external applied magnetic field. Open symbols show the in-phase χ'(T) while the closed symbols show the out-of-phase χ"(T).

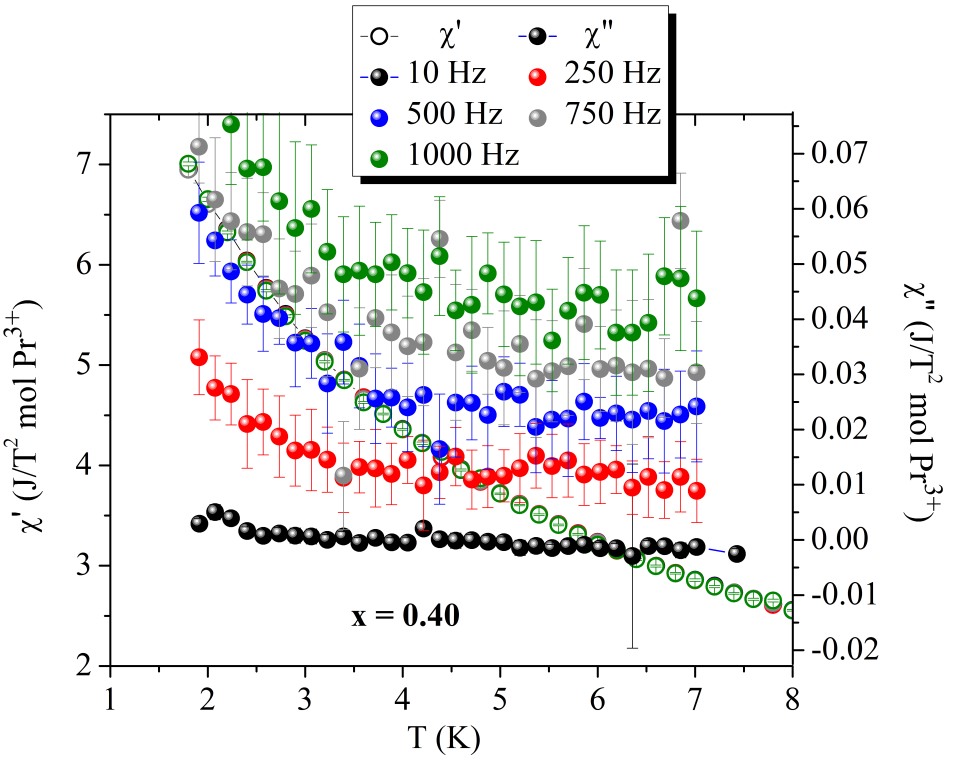

FIGURE 4.28: Low-temperature AC susceptibility of $Pr_2Sn_{1.6}Ti_{0.4}O_7$ in zero external applied magnetic field. Open symbols show the in-phase χ'(T) while the closed symbols show the out-of-phase χ"(T).

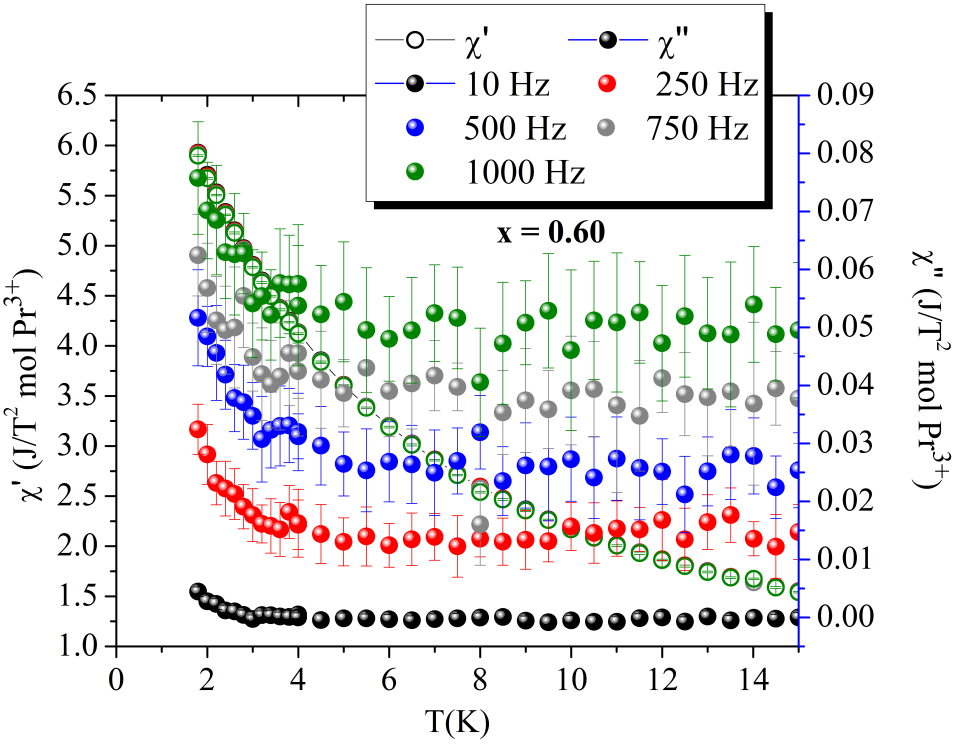

FIGURE 4.29: Low-temperature AC susceptibility of $Pr_2Sn_{1.4}Ti_{0.6}O_7$ in zero external applied magnetic field. Open symbols show the in-phase χ'(T) while the closed symbols show the out-of-phase χ"(T).

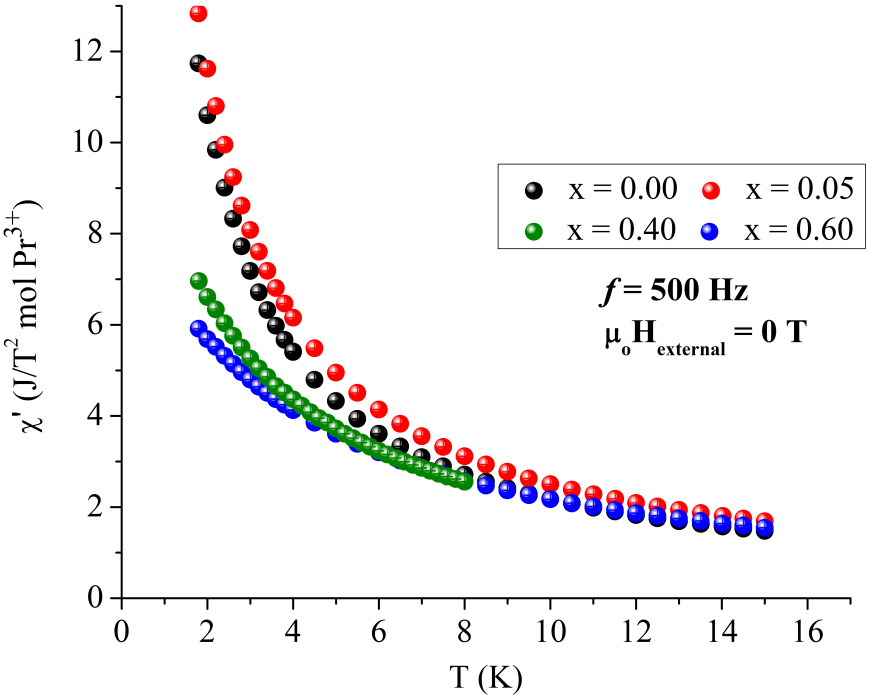

FIGURE 4.30: The dynamic in-phase χ' of the low-temperature AC susceptibility of various members of the $Pr_2Sn_{2-x}Ti_xO_7$ pyrochlore series in zero external applied magnetic field and driving frequency $f = 500$ Hz.

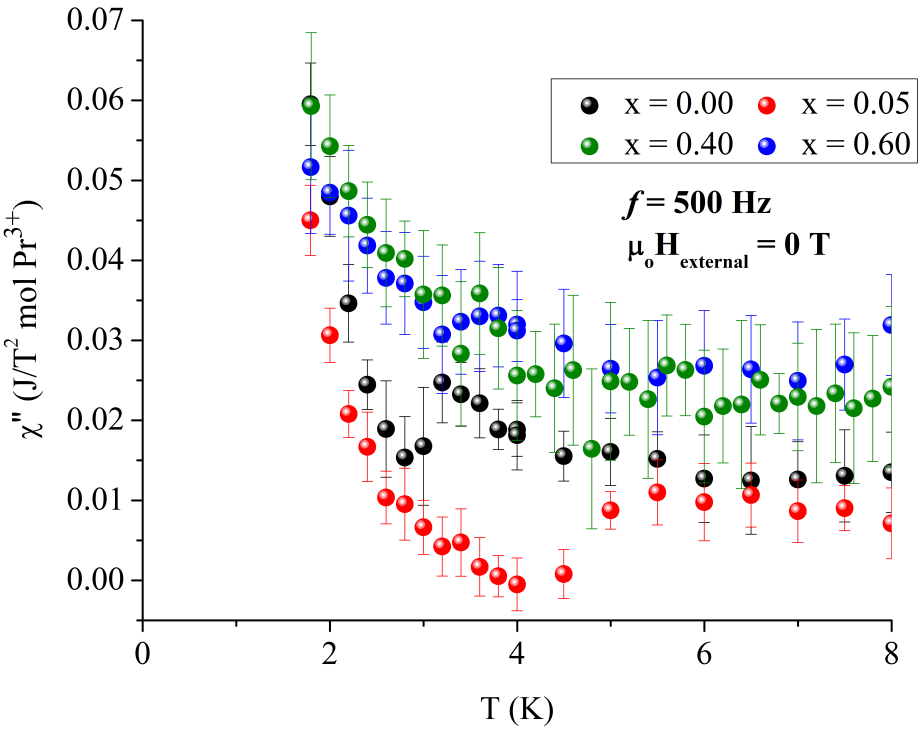

FIGURE 4.31: The out-of-phase χ" of the low-temperature AC susceptibility of various members of the $Pr_2Sn_{2-x}Ti_xO_7$ pyrochlore series in zero external applied magnetic field and driving frequency $f = 500$ Hz.

and eventually with higher values of x, a spin ice state was formed. Our AC results on the $Pr_2Sn_{2-x}Ti_xO_7$ series do not show either feature. By comparing different members of the $Pr_2Sn_{2-x}Ti_xO_7$ pyrochlore series in figures 4.30 and 4.31 at a particular frequency, there remains a distinct upward turn at low temperatures for χ' for all members implying no indication that a transition is being suppressed. This behaviour was seen by Dahlberg *et al.* [180] in $Tb_2Sn_2O_7$ and replaced the transition at T $\approx$ 800 mK. Consequently, one may speculate that if there was a transition — indicated by the prominent low temperature feature — that the saturation with larger values of x imply that the transition is being surpressed but this is purely speculation and requires much lower temperature AC susceptibility. Furthermore, there is no indication of the system freezing into a spin glass, even up to the highest doped member $Pr_2Sn_{1.4}Ti_{0.6}O_7$. The freezing of the system, i.e. the transition from a paramagnet into an amorphous static magnetic structure, would be indicated by a frequency dependence, particularly in the out-of-phase χ" component of the AC susceptibility as is seen in numerous pyrochlore oxides including $Y_2Mo_2O_7$ by Dusinger *et al.* [197] and $Tb_2Mo_2O_7$ by Gaulin *et al.* [57]. The frequency dependence — which can be intuitively interpreted as the irreversibility of the dynamics present in the system — is not observed in any members of the $Pr_2Sn_{2-x}Ti_xO_7$ pyrochlore series. The fact that there is no evidence for a spin glass present, even for $Pr_2Sn_{1.4}Ti_{0.6}O_7$, is significant because it demonstrates that the $Pr_2Sn_{2-x}Ti_xO_7$ system does not act like its terbium analog. The fact that the $Pr_2Sn_{2-x}Ti_xO_7$ system does not freeze as x increases is a surprising result because as aforementioned, Dalhberg *et al.* [180] and Mirebeau *et al.* [181] provided mounting evidence that the freezing mechanism in $Tb_2Sn_2O_7$ was attributed to either the disorder of the exchange interactions and/or to the tuning of the dipolar/exchange interaction influence on spin-spin correlations. If either one or both of these considerations were ultimately the parameter that causes the spin glass transition, the $Pr_2Sn_{2-x}Ti_xO_7$ system should theoretically exhibit the same surpression of the spin ice transition and a spin glass freezing. A possibility that should be mentioned is that $Pr_2Sn_2O_7$ and $Tb_2Sn_2O_7$ have completely different fluctuation energy scales at base temperature, once again due to their completely different mechanisms causing quantum fluctuations. All the aforementioned features for $Tb_2Sn_2O_7$ in AC susceptibility were seen between base and 800 mK and thus it can may be speculated that a spin glass transition *may* appear if the $Pr_2Sn_{2-x}Ti_xO_7$ members, in particular, $Pr_2Sn_{1.4}Ti_{0.6}O_7$, were cooled to a low enough temperature. To summarise, AC susceptibility simply indicates that the system remains dynamic down to 1.8 K with fluctuations of characteristic internal frequencies greater than 1 kHz. Ultimately, the results from AC susceptibility do not support but more importantly do not reject the possibility of the intermediate magnetic phase being composed of weakly antiferromagnetic clusters.

4.4 Isobaric Heat Capacity

As an attempt to both (i) characterise the intermediate magnetic state of the $Pr_2Sn_{2-x}Ti_xO_7$ pyrochlore series ($0 < x \leq 0.60$) and (ii) confirm if the transition into an LRO magnetic state occurs at an external applied magnetic field $\mu_oH \approx 3$ T, the isobaric heat capacity of polycrystalline $Pr_2Sn_{1.4}Ti_{0.6}O_7$ was measured under multiple external applied magnetic fields. Phase pure $Pr_2Sn_{1.4}Ti_{0.6}O_7$ was reground, repelleted and sintered at 1000^{o}C for 12 hours in air to provide internal cohesion for the pellet. The isobaric heat capacity was measured by the thermal relaxation method down to a base temperature of approximately 350 mK under various fields ranging from $\mu_oH =$ 0 to 9 T. The total mass normalised isobaric heat capacity for select external applied magnetic fields is shown in figure 4.32 below.

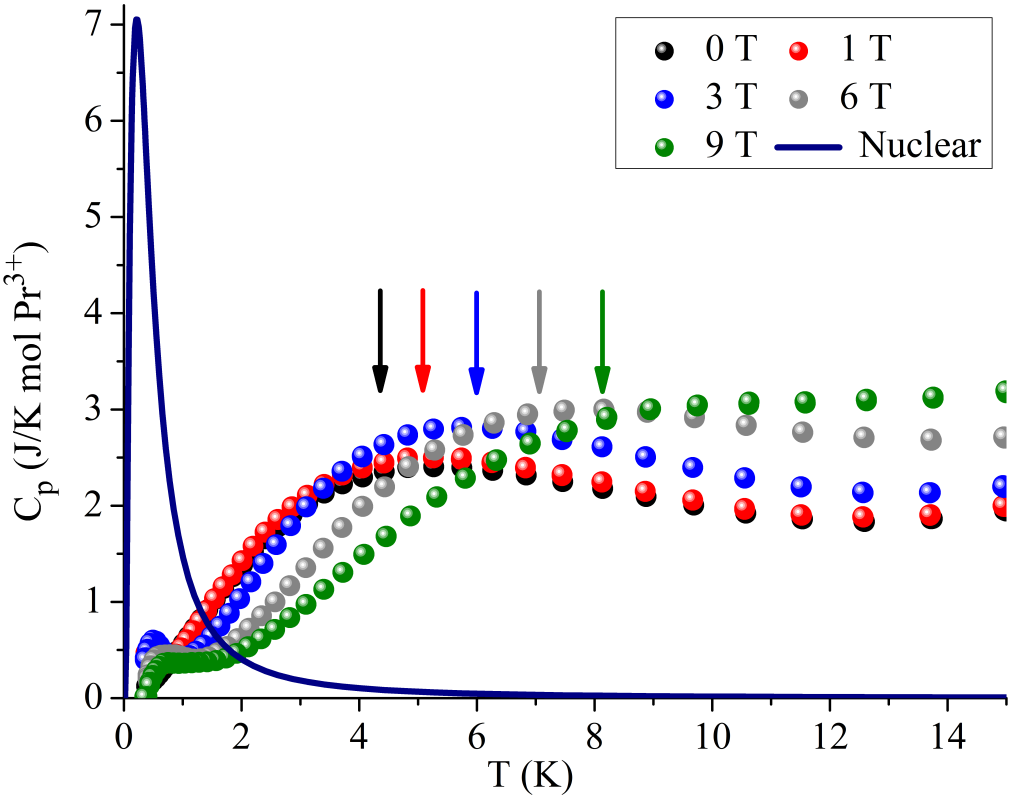

FIGURE 4.32: Mass normalised isobaric heat capacity for $Pr_2Sn_{1.4}Ti_{0.6}O_7$ as a function of temperature for select applied magnetic fields. The evolution of the high temperature feature is indicated by arrows with each arrow indicating the peak position for a particular field, shown more explicitly in figure 4.33. Instead of a distinct sharp nuclear Schottky anomaly — characteristic of praseodymium-based pyrochlores — there is only an appearance of a broad low temperature anomaly that is magnetic in origin. The nuclear Schottky that is expected for a free Pr^{3+} $^3H_4$ is included for comparison.

In a similar manner to the parent compound $Pr_2Sn_2O_7$, the isobaric heat capacity of $Pr_2Sn_{1.4}Ti_{0.6}O_7$ exhibits **two** distinct features, one located at base temperatures and a

Schottky-type of anomaly at temperatures ranging from approximately 5 to 10 K. Both of these features were concluded to be magnetic in origin due to their clear dependence on the strength of the external applied magnetic field with the latter's movement shown explicitly in figure 4.33.

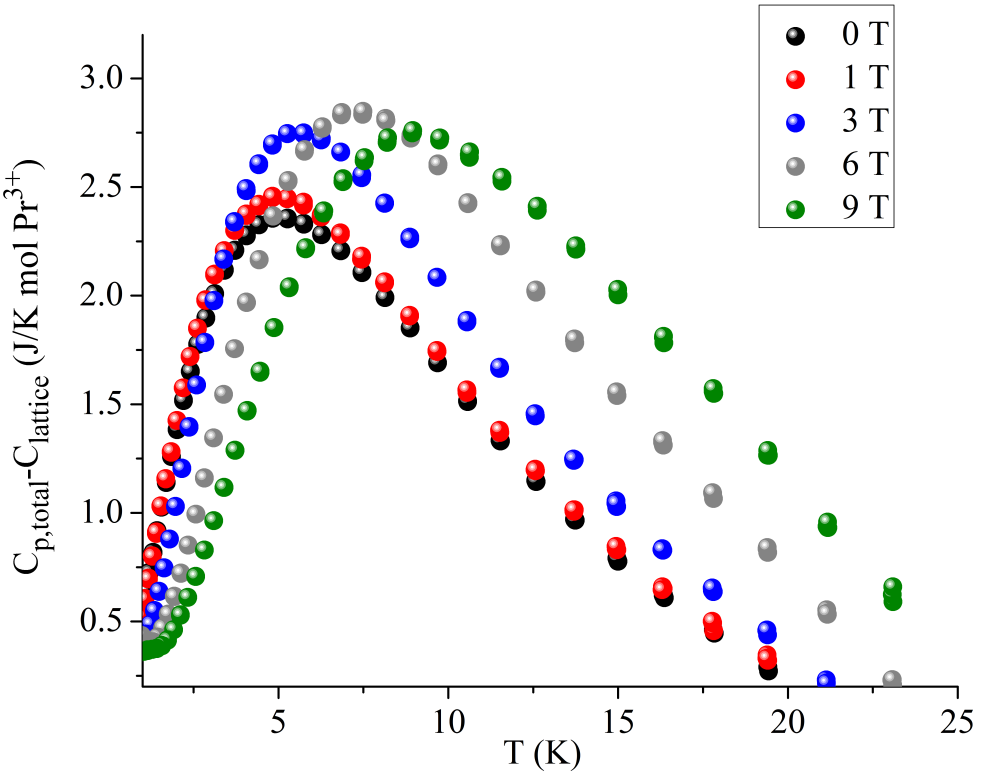

FIGURE 4.33: Lattice subtracted isobaric heat capacity of the high temperature Schottky-type magnetic anomaly for $Pr_2Sn_{1.4}Ti_{0.6}O_7$ under various external applied magnetic fields.

Another and most striking similarility between $Pr_2Sn_{1.4}Ti_{0.6}O_7$ and $Pr_2Sn_2O_7$ is the lack of a sharp anomaly, even up to an external applied magnetic field of 9 T, implying no LRO magnetic state has formed down to 350 mK in an external applied magnetic field up to 9 T. This lack of ordering — in other words, a distinct transition into an LRO — contradict the expectations drawn from DC susceptometry in subsection 4.3.2 since field dependence studies using DC susceptometry on $Pr_2Sn_{1.4}Ti_{0.6}O_7$, implies that $Pr_2Sn_{1.4}Ti_{0.6}O_7$ should enter an LRO at approximately 3 T. It should be noted that the lack of a sharp peak down to 350 mK, although contradictory to the findings of the DC susceptometry, is consistent with both $Tb_2Sn_2O_7$ and more importantly, the parent compound $Pr_2Sn_2O_7$. Recall from section 3.4, $Pr_2Sn_2O_7$ did not exhibit any sign of a transition into an LRO until approximately 3 T as explicitly shown by heat capacity at 350 mK in figure 3.14, despite DC susceptometry predicting that an external magnetic field $\mu_oH \leq 1$ T should cause such a transition, ultimately proven by neutron scattering. Ultimately it was concluded that $Pr_2Sn_2O_7$ was simply not cooled to low

enough temperatures to achieve this LRO magnetic state. This situation may be what is occurring for $Pr_2Sn_{1.4}Ti_{0.6}O_7$ and what is ultimately seen in $Tb_2Sn_{2-x}Ti_xO_7$ where spin freezing occurs at 200 mK.

Although $Pr_2Sn_{1.4}Ti_{0.6}O_7$ shares some key characteristics in the isobaric heat capacity with its parent compound, there are distinct differences that provide important inferences on the intermediate magnetic state assumed by $Pr_2Sn_{1.4}Ti_{0.6}O_7$. As shown in figure 4.32, there is a distinct absence of the prominent nuclear Schottky anomaly that dominates both the low temperature isobaric heat capacity of $Pr_2Sn_2O_7$ seen in section 3.4 and many praseodymium based magnetic pyrochlore oxides [82, 198]. Both the particular absence of a nuclear Schottky and a spin ice transition can be seen quite explicitly at 0 T as shown in figure 4.34.

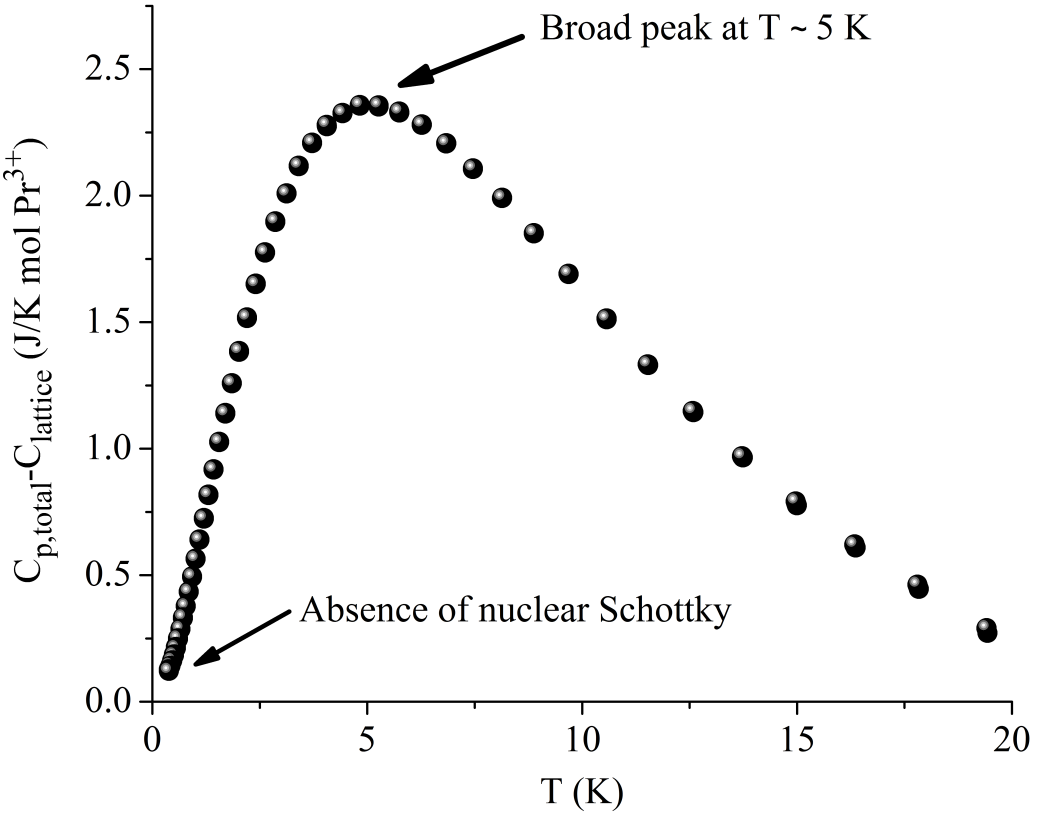

FIGURE 4.34: Lattice subtracted isobaric heat capacity of $Pr_2Sn_{1.4}Ti_{0.6}O_7$ in zero external applied magnetic field. The presence of a broad peak at 5 K and the absence of a nuclear Schottky contribution are explicitly noted. $Pr_2Sn_2O_7$ in zero external applied magnetic field exhibits a prominent low temperature nuclear Schottky and a relatively sharp feature below 1 K indicative of the spin ice transition. This transition is clearly surpressed in $Pr_2Sn_{1.4}Ti_{0.6}O_7$.

The spin ice transition at approximately 1 K is completely suppressed and replaced by a broad feature at 5 K indicating the spin ice state has been suppressed as suspected

by the large negative Weiss temperature retrieved from DC susceptometry. Furthermore, unlike the rapid increase at low temperatures seen in figure 3.11 for $Pr_2Sn_2O_7$, there is a monotonic decrease of the isobaric heat capacity in the limit of $T \to 0$ for the $Pr_2Sn_{1.4}Ti_{0.6}O_7$ case. One possible explanation to account for the lack of the distinct low temperature nuclear Schottky anomaly — characteristic of praseodymium magnetic pyrochlore oxides — is the claim that at 0 T, the nuclear Schottky is present but it is located at such low temperatures that it cannot be observed directly down to 350 mK. This explanation is based on the observation that as one increases the external applied magnetic field from 0 T to 1 T, one recovers an upward curvature that *appears* characteristic of a nuclear Schottky anomaly that would the result of a hyperfine field resulting from a static electronic praseodymium moment of 0.805(2) μ_B. The aforementioned static praseodymium moment of 0.805(2) μ_B was calculated using equation 3.6 and signifies that the electronic moments that the nucleus experiences — on the time scale of nuclear thermal relaxation — is significantly reduced from the free ion moment of approximately 3.5 μ_B for Pr^{3+} [3]. This reduction in the electronic moment may be indicative of the praseodymium spins pairing up antiferromagnetically, thus effectively cancelling their individual magnetic moments seen by the nucleus as is common in frustrated magnets such as what is seen in some FCC magnets [199]. Another explanation for the reduction in the electronic moment seen by the nucleus could be caused by the fact that the electronic spin fluctuations occur at a much faster time scale than the nuclear thermal relaxation time scale. This was suspected by Calder *et al.* to explain the lack of a nuclear Schottky in holmium based double perovskite Ba_2HoSbO_6 [200] for example. In fact, the explanation by Calder *et al.* can be quickly rejected by observing the low temperature feature — shown explicitly for various magnetic fields in figure 4.35 — as a function of temperature and applied magnetic field. In particular, if one claims that the nuclear Schottky was simply not visible at 0 T but becomes visible as one applies field due to the increased static electronic moment felt by the nucleus due to increased induced polarisation of the Pr^{3+} spins, then the value of the isobaric heat capacity at a specific temperature should simply monotonically increase with field until a saturation value is reached as determined by equation 3.8 using the free ion moment of Pr^{3+}. As shown in figure 4.36, the value of the isobaric heat capacity at a temperature of 0.4 K increases initially — as one would expect if the low temperature feature observed was indeed a nuclear Schottky — but in fact, the low temperature feature's value decreases after an external applied magnetic field $\mu_oH \approx 2$ T, and decreases monotonically as the external applied magnetic field is increased. One may argue that since the decrease occurs between 2 T and 3 T (recall that a transition was suspected at an external applied magnetic field of approximately 3 T). This decrease may be indicative of a possible phase transition.

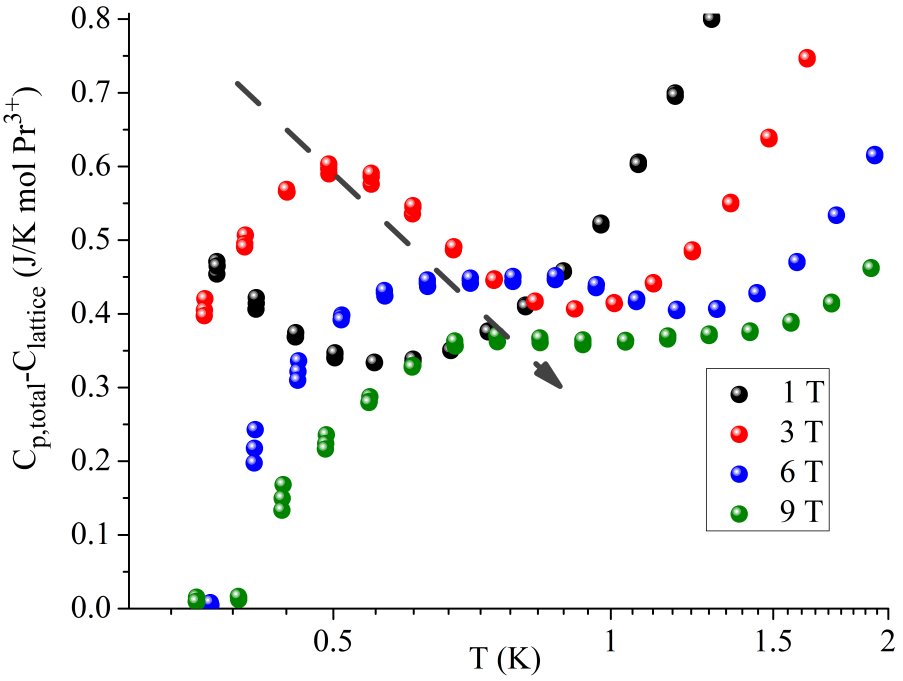

FIGURE 4.35: The temperature dependence of the lattice subtracted isobaric heat capacity for the low temperature magnetic feature for various external applied magnetic fields. The rise seen at low temperatures for 1 T is not the high temperature tail a nuclear Schottky but rather the high temperature tail of the low temperature broad feature.

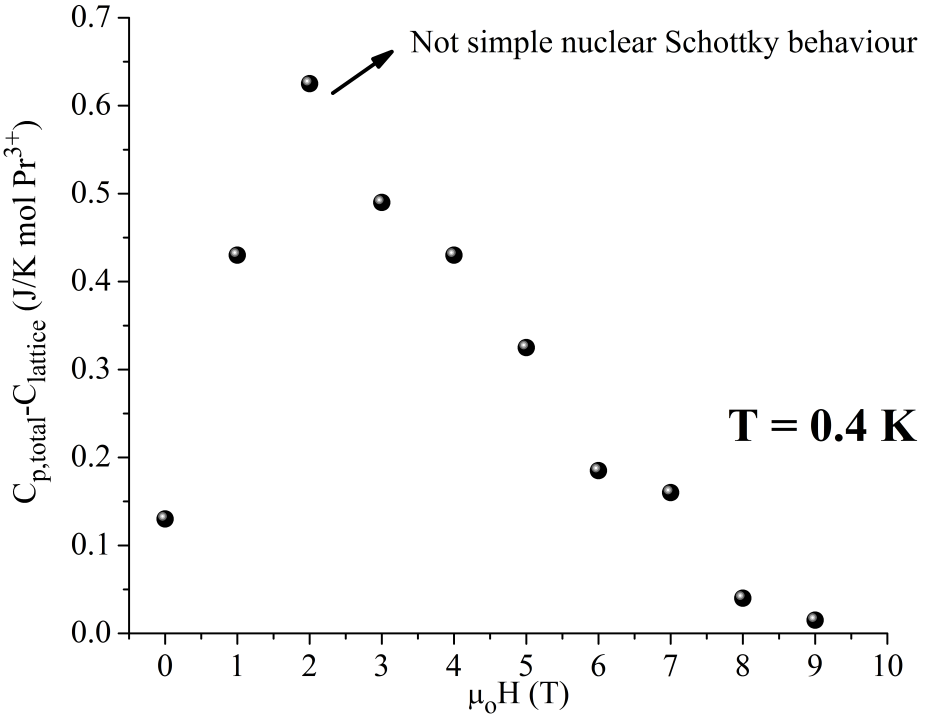

FIGURE 4.36: The value of the lattice subtracted isobaric heat capacity at 0.4 K as a function of external applied magnetic field. Instead of a monotonic increase — as expected for the behaviour of a simple nuclear Schottky — there is a distinct decrease between 2 T and 3 T which may indicate a possible phase transition. The fact that the isobaric heat capacity decreases so rapidly at 0.4 K implies that the nuclear Schottky contribution's to the isobaric heat capacity at low temperatures is extremely small.

As an attempt to eliminate some ambiguity concerning the intermediate magnetic state assumed by $Pr_2Sn_{1.4}Ti_{0.6}O_7$, the lattice component (i.e. the phonon contribution) to the total isobaric heat capacity was first estimated by measuring the isobaric heat capacity of the mass corrected non-magnetic isostructural $Y_2Sn_{1.4}Ti_{0.6}O_7$, then subtracting the value for the total isobaric heat capacity. The reason yttrium and not lanthanum was placed on the 16*d* Wyckoff site was because six coordinate La^{3+} is large enough compared to six coordinate Pr^{3+} that it pushes the radius ratio between the 16*d* to 16*c* for $La_2Sn_{1.4}Ti_{0.6}O_7$ beyond the critical value of 1.71 and the monoclinic $P2_1$ $La_2Ti_2O_7$ was observed *via* room temperature powder x-ray diffraction. Once subtracted, the quotient of the isobaric heat capacity and temperature was plotted as a function of temperature as shown in figure 4.37. Recall from equation 2.49 that the integral of figure 4.37 represents the entropy released as one decreases temperature, shown explicitly in figure 4.38.

The behaviour in figure 4.37 rejects the applicability of the mechanism proposed by Calder *et al.* for Ba_2HoSbO_6 to the current system of $Pr_2Sn_{1.4}Ti_{0.6}O_7$. The reason for rejecting the fluctuating spins hypothesis is because the upward turn observed in figure 4.35 with the application of 1 T is not a nuclear Schottky but rather the high temperature tail of a broad anomalous magnetic feature that becomes almost completely visible by approximately 3 T. It must be conceded that there is a nuclear component in the low temperature magnetic feature but its contribution is relatively small as shown by the drastic reduction as the feature moves to higher temperatures as the external magnetic field increases. As presented in figure 4.37, the low temperature magnetic anomaly increases in intensity and appears at higher temperatures. Both observations indicate a larger amount of entropy is being released at higher temperatures, in agreement with stronger spin-spin correlations or collective spin-spin correlations. The former case is much more likely because the peaks, even at an external applied magnetic field of 3 T are significantly broadened, emphasised by the fact that the data is presented on a logarithm temperature scale. The observation that the low temperature portion of the data has a peak but is broad implies that $Pr_2Sn_{1.4}Ti_{0.6}O_7$ does assume a short range ordered magnetic structure for low magnetic fields. Furthermore, as the field is progressively increased, the energy of spins' correlations with their nearest neighbours increase — in agreement with the increase in the magnitude of θ_{CW} — proven by the observation that the broad peak moves to higher temperatures as field is increased. It is worth noting that the magnetic entropy for all fields are above the Pauling entropy, confirming that $Pr_2Sn_{1.4}Ti_{0.6}O_7$ is no longer in the spin ice regime, in agreement with the DC susceptometry results. Furthermore, for all fields, the entropy approaches the value of Rln2 as one would expect for a simple two level system. The decrease in released entropy observed for higher fields is completely artificial and is attributed to the fact

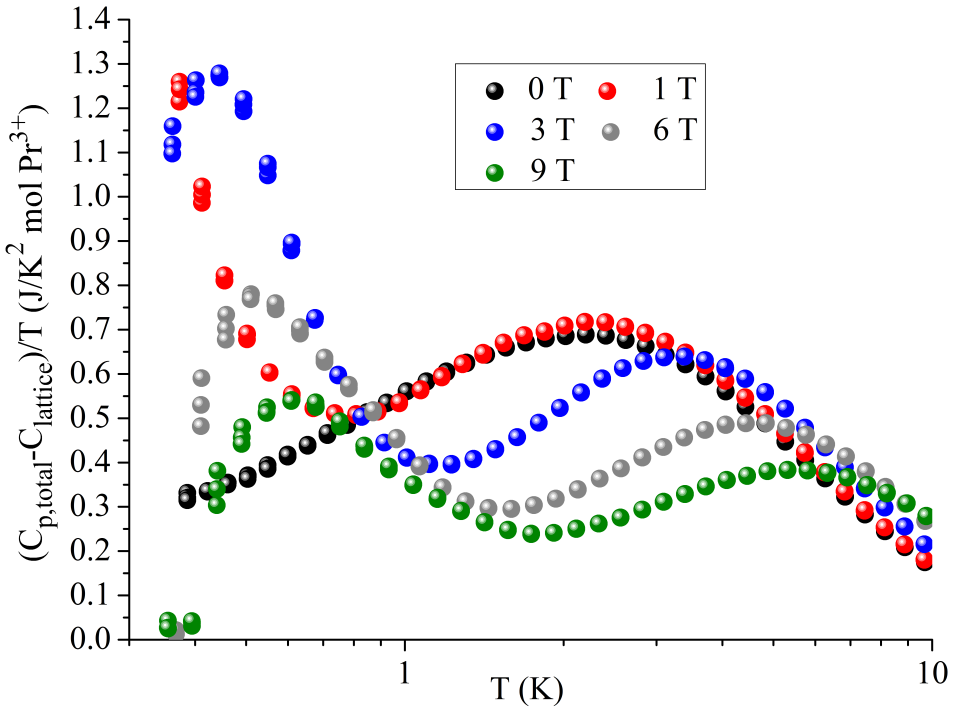

FIGURE 4.37: $\frac{C_p(T)}{T}$ for $Pr_2Sn_{1.4}Ti_{0.6}O_7$ under select external applied magnetic fields showing both the high temperature Schottky-like anomaly and the low temperature broad feature implying weak short range spin-spin correlations. Comparison between 2 T and 3 T data sets reveals that the rapid increase at low temperature from 0 T to 1 T is not a nuclear Schottky as first suspected but is the hgh temperature tail of this low temperature feature.

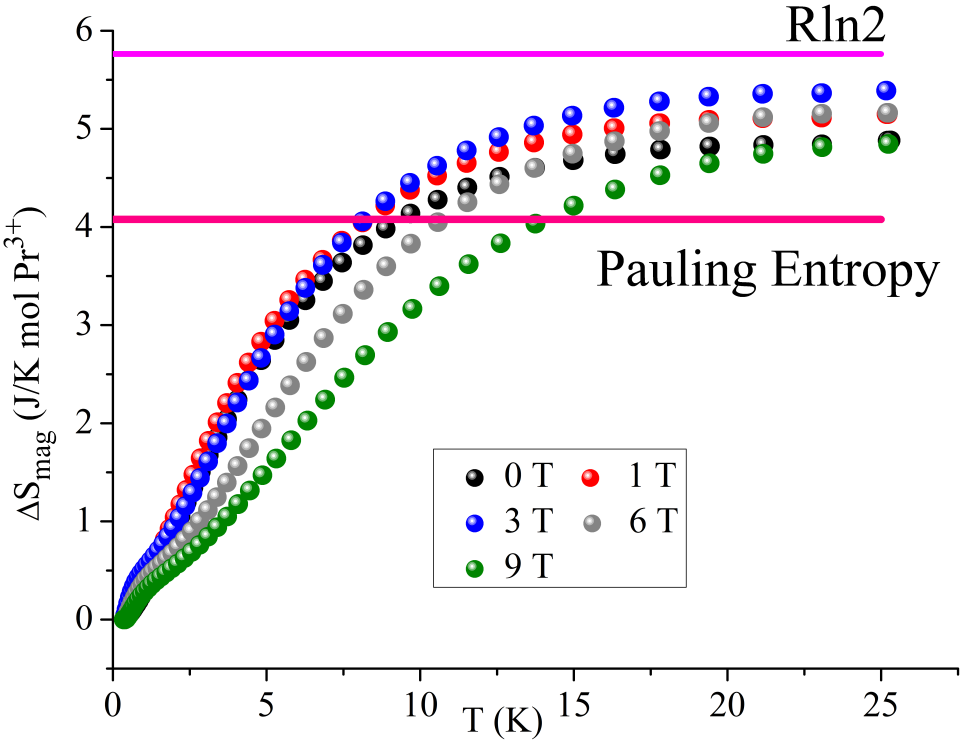

FIGURE 4.38: Magnetic entropy recovered as a function of temperature from 350 mK to 25 K determined by numerical integration of figure 4.37. For all fields, the magnetic entropy exceeds the Pauling entropy confirming that $Pr_2Sn_{1.4}Ti_{0.6}O_7$ is no longer in the spin ice regime. The entropy recovered for each field approaches Rln2 implying a simple doublet system. The decrease in the total magnetic entropy is simply an artifact caused by the higher temperature featuring moving beyond the limits of integration.

that the higher temperature is sequentially moving to temperatures beyond the temperature range of integration (i.e. 0.35 K $\leq$ T $\leq$ 25 K). The conclusion of a possible transition at an external applied magnetic field of approximately 3 T is supported by the observation that the low temperature anomaly not only decreases rapidly from 3 T to 6 T, but its width increases as well.

The observed behaviour of the isobaric heat capacity of $Pr_2Sn_{1.4}Ti_{0.6}O_7$ shares some similarities to another quantum spin ice candiate $Yb_2Ti_2O_7$. In 1969, Blöte *et al.* [77] observed an extremely broad feature in the isobaric heat capacity centered about 4 K, suggestive of short ranged correlations. This broad peak was then followed by an extremely sharp feature at approximately 200 mK, suggestive of the formation of an LRO magnetic state. In 2009, Ross *et al.* [160], using high precision TOF neutron scattering spectroscopy on a $Yb_2Ti_2O_7$ single crystal, suggested that the 4 K broad feature in the heat capacity was in fact 2D SRO correlations. The same study suggested that the sharp feature at approximately 250 mK was a 3D SRO correlated system and not an LRO magnetic state. The study went even further and determined that a field-induced LRO magnetic state from the 2D SRO magnetic state occurs at an external field of μ_oH $\approx$ 0.5 T. Although the work by Ross *et al.* suggests a transition into a 3D correlated SRO magnetic state and not an LRO as originally suspected, the nature of the transition between 200-300 mK is still quite controversial. In 2013, D'Ortenzio *et al.* [201], using isobaric heat capacity and μSR spectroscopy, concluded that the 200-300 mK transition was in fact a transition into an unknown "unconventional ground state", providing some suggestion of the presence of a quantum spin ice state. The 2013 study concluded that this low field magnetic structure was both not glassy and long ranged. In fact, this controversy of the 200 mK-300 mK transition began in the early 2000's, Bramwell *et al.* [202], using magnetisation studies determined that $Yb_2Ti_2O_7$ possessed weak net ferromagnetic spin correlations ($\theta_{CW} \sim 0.6$ K), suggesting a strong superexchange component. Hodges *et al.* [203] using Mössbauer spectroscopy determined that $Yb_2Ti_2O_7$ was a well isolated ground state Kramers' doublet with a dominant XY anisotropy and a $\Delta \sim 600$ K suggesting the system was an effective S = $\frac{1}{2}$ system, i.e. an extremely quantum system. In 2002, Hodges *et al.* [204] performed further Mössbauer spectroscopy measurements, determined that the ground state was not frozen after the transition at 240 mK. Continuing with μSR and elastic powder neutron scattering experiments, Hodges *et al.* determined that the 240 mK transition was followed by three orders of magnitude decrease in the fluctuation rate but the spins were in fact still fluctuating down to base temperature. In 2003, Yasui *et al.* [205] provided evidence that $Yb_2Ti_2O_7$ did indeed transition into a static ferromagnetic state at 240 mK by recording a buildup of extra intensity on the Bragg peaks. This controversial study by Yasui *et al.* led Gardner *et al.* [206] to perform polarised neutron scattering experiments in 2004 which conclusively

confirmed that the magnetic ground state was no static on the neutron time scale which has recently been challenged by a neutron scattering study by Chang *et al.* [207] in 2014. Despite the current controversy of the magnetic ground state of $Yb_2Ti_2O_7$, the analogy between the $Pr_2Sn_{1.4}Ti_{0.6}O_7$ system and $Yb_2Ti_2O_7$ is quite useful for multiple reasons:

- Despite the strong anistropic character of Pr^{3+} in the parent compound $Pr_2Sn_2O_7$, DC susceptometry has confirmed the possibility of *smearing* of the crystal fields in $Pr_2Sn_{1.4}Ti_{0.6}O_7$ by introducing Ti/Sn randomised substitutions. Recall from Chapter 3 that the effect of the application of a magnetic field caused a large amount of admixture between individual crystal field states resulting in an LRO magnetic state with dominant XY character, instead of the original Ising-like character of the spin ice state. The shift of Ising to dominant XY anistropy in the $Pr_2Sn_{1.4}Ti_{0.6}O_7$ system naturally suggests a comparison between the $Pr_2Sn_{1.4}Ti_{0.6}O_7$ system and $Yb_2Ti_2O_7$, especially when one considers the quantitative similarities between the effective magnetic moments.

- The preceding discussion concerning $Pr_2Sn_{1.4}Ti_{0.6}O_7$ and $Yb_2Ti_2O_7$ attempted to provide an analogy of the formation of an SRO through a very broad feature before a possible LRO magnetic state shown through a sharp feature. Another argument using $Yb_2Ti_2O_7$ as a direct comparison is the observation of sample dependence issues with $Yb_2Ti_2O_7$ by Ross *et al.* [54]. Ross *et al.* determined that the discrepancy between the reported ground states for $Yb_2Ti_2O_7$ in literature was due to stuffing of Yb^{3+} in the 16*c* Wyckoff site. The amount and effects on the physical properties of stuffing was particularly prominent in single crystals. In single crystals, the 240 mK peak became much broader and lower in intensity, attributed to the randomisation of the exchange interactions, meaning that there is some removal of the interactions' spatial symmetry. So in fact, the broad feature that is observed in the heat capacity of $Pr_2Sn_{1.4}Ti_{0.6}O_7$, may be a type of SRO-LRO transition but its intensity and sharpness are being obscured by the randomisation of exchange interactions caused by the randomised substitution of Ti^{4+} for Sn^{4+}.

- Unlike the titanate, Dun *et al.* [208] showed that $Yb_2Sn_2O_7$ does in fact transition into an LRO ferromagnetic state at 0.11 K, albeit with persistent spin dynamics down to 0.05 K due to its proximity to a quantum critical point. The stark differences between the stannate and the titanate members of the ytterbium family of pyrochlores demonstrates the fragility of the spin correlations that is analogous to the behaviour being currently observed in the $Pr_2Sn_{1.4}Ti_{0.6}O_7$ pyrochlore series.

This fragility of the spin ice state in $Pr_2Sn_2O_7$ was confirmed by the observation that the isobaric heat capacity for intermediate members of the $Pr_2Sn_{2-x}Ti_xO_7$ pyrochlore

series exhibits identical properties to $Pr_2Sn_{1.4}Ti_{0.6}O_7$. As an example, one can see in figures 4.39 and 4.40 that $Pr_2Sn_{1.6}Ti_{0.4}O_7$ exhibits (i) no distinct nuclear anomaly at the lowest temperatures, (ii) only a broad peak appears at the lowest temperatures, (iii) the broad feature distinctly decreases at external applied magnetic higher fields while (iv) the magnetic entropy is above that of the Pauling entropy and approaches Rln2 implying a simple two level system.

To summarise, isobaric heat capacity provides ample evidence for not only a possible transition at 3 T but also provides support for the claim that the intermediate magnetic state assumed by $Pr_2Sn_{1.4}Ti_{0.6}O_7$ does indeed consist of weakly correlated AFM clusters, deduced from DC susceptometry in subsection 4.3.2. These AFM clusters themselves would significantly reduce the static electronic moment of Pr^{3+} seen by the nucleus due to the antiferromagnetic arrangement and would account for the absence of the distinct nuclear Schottky seen in $Pr_2Sn_2O_7$ and other praseodymium-based pyrochlores such as $Pr_2Zr_2O_7$ [82]. The cluster stucture would account for the short range spin-spin correlation seen in the low temperature feature for low fields. The distinct decrease in intensity of the proposed short range ordered state's contribution to the magnetic entropy is consistent with the behaviour of another the short range ordered magnetic state in the Heisenberg pyrochlore AFM magnet preceeding the formation of an LRO at lower temperatures.

4.5 Elastic Neutron Scattering

In order to investigate both the low temperature crystal and magnetic structure, elastic neutron scattering measurements were performed on polycrystalline samples of $Pr_2Sn_2O_7$ and $Pr_2Sn_{1.7}Ti_{0.3}O_7$ on the high resolution C2 800-wire powder diffractometer (DUALSPEC) at the NRU at the Canadian Neutron Beam Centre (CNBC), Chalk River Laboratories, Ontario, Canada. Both polycrystalline samples used for the scattering experiments at the CNBC were loaded in a sealed aluminum can in a ^{4}He exchange gas and mounted in a pumped ^{4}He or ^{3}He cryostat, in order to achieve temperatures of 4 K and 300 mK, respectively. The neutron diffraction patterns were measured at both temperatures in 0.05° steps with a standard 2θ range of 5° to 85° [209], using a Si#17 (531) monochromator selecting a neutron wavelength λ of 2.3654 Å, supplemented by a pyrolytic graphite filter to suppress higher order contamination. The neutron wavelength λ of 2.3654 Å was selected due to its high flux on the C2 thermal neutron beamline and its ability to provide fine resolution for large d spacing, i.e. low $\mathbf{Q}$ regions, where magnetic contributions are most prominent.

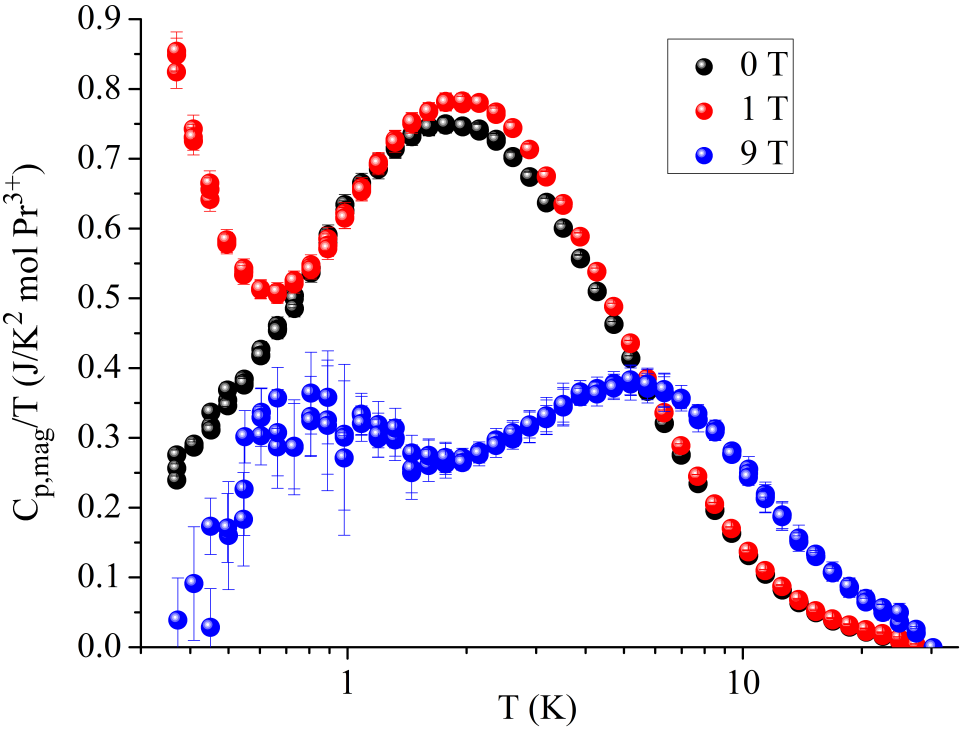

FIGURE 4.39: $\frac{C_p(T)}{T}$ for $Pr_2Sn_{1.6}Ti_{0.4}O_7$ under select external applied magnetic fields showing both the high temperature Schottky-like anomaly and the low temperature broad feature implying weak short range spin-spin correlations. The behaviour of the isobaric heat capacity of $Pr_2Sn_{1.6}Ti_{0.4}O_7$ is identical to the behaviour of $Pr_2Sn_{1.4}Ti_{0.6}O_7$ shown in figure 4.37 confirming the fragility of the spin ice state relative to chemical doping on the 16*c* Wyckoff site.

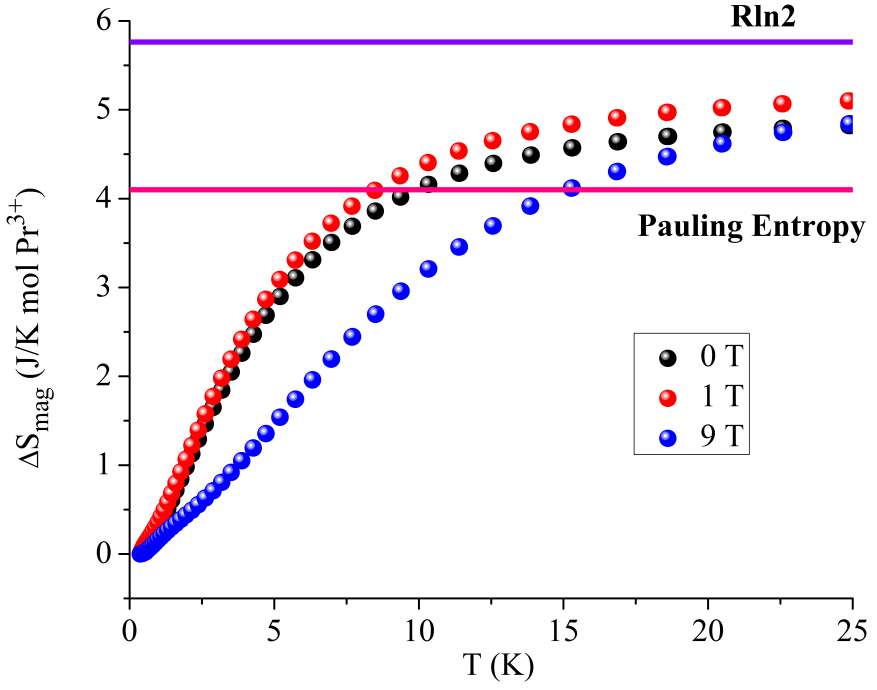

FIGURE 4.40: Magnetic entropy recovered as a function of temperature from 350 mK to 25 K determined by numerical integration of figure 4.39. For all fields, the behaviour of $Pr_2Sn_{1.6}Ti_{0.4}O_7$ is qualitatively similar to that seen for $Pr_2Sn_{1.4}Ti_{0.6}O_7$ in figure 4.38 where the magnetic entropy exceeds the Pauling entropy confirming that $Pr_2Sn_{1.6}Ti_{0.4}O_7$ is no longer in the spin ice regime.

4.5.1 Magnetic Diffuse Scattering

As shown in both figures 4.41 and 4.42, upon cooling the system from 4 K to 300 mK, there are no new Bragg peaks that appear at low **Q** for $Pr_2Sn_2O_7$ and $Pr_2Sn_{1.7}Ti_{0.3}O_7$. It should be noted that a small amount (< 1 %) of unreacted SnO_2 was detected in $Pr_2Sn_{1.7}Ti_{0.3}O_7$ in figure 4.42 that was not detected by room temperature x-ray diffraction. The absence of new low **Q** Bragg peaks at 300 mK indicates that both $Pr_2Sn_2O_7$ and $Pr_2Sn_{1.7}Ti_{0.3}O_7$ do not form an LRO magnetic state down to 300 mK in zero applied magnetic field since it was concluded from magnetic property measurements that both magnetic systems do not form an LRO magnetic state by 4 K.

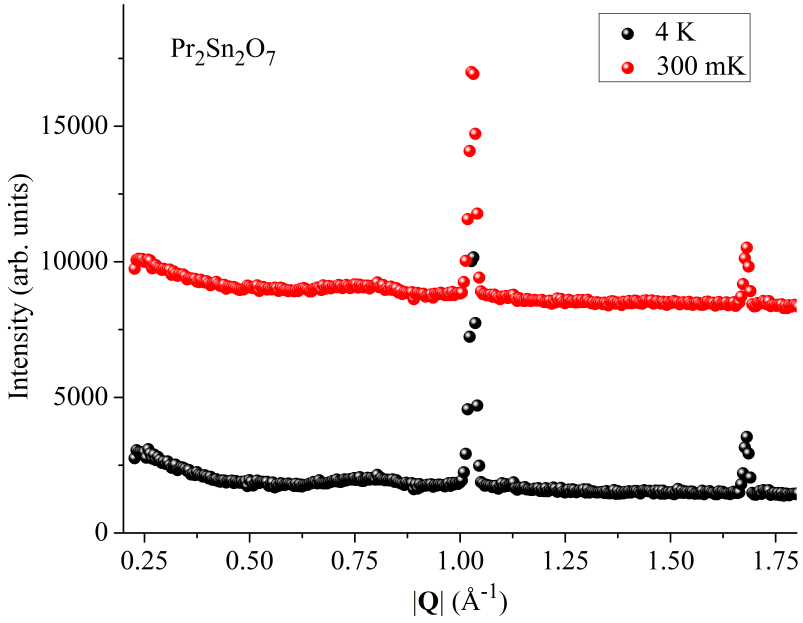

FIGURE 4.41: Low **Q** region of the raw neutron diffraction pattern for $Pr_2Sn_2O_7$ at 4 K and 300 mK (vertically offset) collected on the high resolution C2 800-wire powder diffractometer (DUALSPEC) with a neutron wavelength λ of 2.3654 Å. Comparison between 300 mK and 4 K diffraction profiles provide no indication of any magnetic ordering down to 300 mK.

Although both systems do not exhibit a clear magnetic transition by 300 mK, isobaric heat capacity provides evidence of short range magnetic correlations for both $Pr_2Sn_2O_7$ and the members of the $Pr_2Sn_{2-x}Ti_xO_7$ pyrochlore system in section 3.4 and subsection 4.4, respectively. The presence of these short range correlations — with resolution limited nuclear Bragg peaks superimposed — can be seen in figures 4.43 and 4.44 for $Pr_2Sn_2O_7$ and $Pr_2Sn_{1.7}Ti_{0.3}O_7$, respectively.

For both compounds, the magnetic component of the scattering intensity was isolated by subtracting the high temperature 4 K data set from the base temperature 300 mK data set. Recall from subsection 2.1.4 that the magnetic scattering cross-section function — given by equation 2.24 which is simply a re-written form of equation 7.73 in

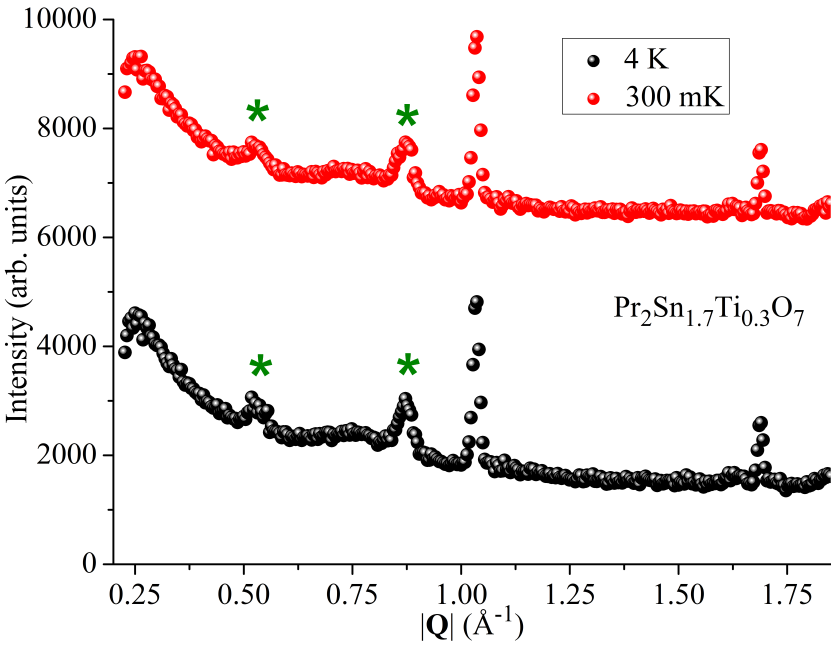

FIGURE 4.42: Low **Q** region of the raw neutron diffraction pattern for$Pr_2Sn_{1.7}Ti_{0.3}O_7$ at 4 K and 300 mK (vertically offset) collected on the high resolution C2 800-wire powder diffractometer (DUALSPEC) with a neutron wavelength λ of 2.3654 Å. The Bragg reflections from unreacted SnO_2 are noted with olive asterisks and represent intensities $< 1\%$ of the intensities of the main phase structural Bragg peaks. Comparison between 300 mK and 4 K diffraction profiles provide no indication of any magnetic ordering down to 300 mK.

Squires' *Introduction to Thermal Neutron Scattering* [111] — may be intuitively interpreted as stating the scattering intensity is proportional to the square of the magnetic form factor $F(\mathbf{Q})$ multiplied by the Fourier transform of the spin correlation function as explicitly stated in equation 2.25. Since only elastic neutron scattering was performed, by correcting the net intensity for the $|\mathbf{Q}|$ dependence due to the Pr^{3+} magnetic form factor shown in figure 4.45.

The resulting intensity is in fact the Fourier transform of the static spin correlation instead of the dynamic correlation function given in the last term in the definition 2.25 for equation 2.24. Figures 4.43 and 4.44 demonstrate two significantly types of behaviour exhibited by $Pr_2Sn_2O_7$ and $Pr_2Sn_{1.7}Ti_{0.3}O_7$. The former exhibits a broad low **Q** with finite intensity as $\mathbf{Q} \rightarrow 0$ Å^{-1}, indicative of the presence of net short range ferromagnetic correlations. The presence of these net FM short range correlations that exhibit a build-up at $\mathbf{Q} \rightarrow 0$ Å^{-1} is definitive source of experimental evidence that $Pr_2Sn_2O_7$ assumes the spin ice state by 300 mK in agreement wtih Zhou *et al.* [31]. The diffuse scattering of spin ices have been well chacterised through polarised neutron scattering by Fennell *et al.* [155] and its quantiative behaviour by Kadowaki *et al.* [211]. A simplified version of the quantiative description by Kadowaki *et al.* given by Bertaut *et al.* as equation 4.3 [212],

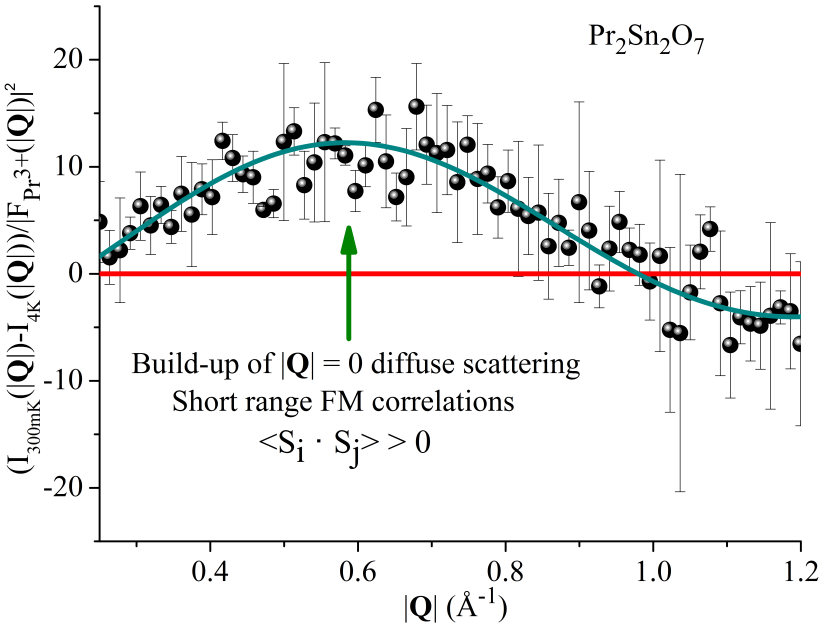

FIGURE 4.43: Background subtracted and form factor corrected low $|\mathbf{Q}|$ neutron scattering intensity at 300 mK for $Pr_2Sn_2O_7$ collected on the high resolution C2 powder diffractometer λ of 2.3654 Å. Zero scattering intensity is given by the red line for reference. The positive build-up of $|\mathbf{Q}| \to 0$ Å^{-1} diffuse scattering is characteristic of short ranged magnetic FM correlations indicative of the spin ice state, confirmed by employing the nearest neighbour isotropic spin correlation model from equation 4.3.

$$S(|\mathbf{Q}|) = \sum_{i,j} \langle S_i \cdot S_j \rangle \frac{\sin(|\mathbf{Q}||\mathbf{R_{ij}}|)}{|\mathbf{Q}||\mathbf{R_{ij}}|} \sim \langle S_i S_j \rangle \frac{sin(|\mathbf{Q}||\mathbf{R_{ij}}|)}{|\mathbf{Q}||\mathbf{R_{ij}}|}, \tag{4.3}$$

where $|\mathbf{R}_{ij}|$ is the distance between spins S_i and S_j, the individual spins in the sum are assumed to behave approximately isotropic and where the last approximation assumes only nearest neighbour spin-spin correlations. Equation 4.3 is particularly useful for determining the dominant type of short range correlations since

$$\lim_{|\mathbf{Q}| \to 0} \frac{\sin(|\mathbf{Q}||\mathbf{R_{ij}}|)}{|\mathbf{Q}||\mathbf{R_{ij}}|} \to 1, \tag{4.4}$$

then since *via* the second equality in equation 4.3, then

$$\lim_{|\mathbf{Q}| \to 0} S(|\mathbf{Q}|) \to \sim \langle S_i S_j \rangle, \tag{4.5}$$

implying positive scattering intensity as $\mathbf{Q} \to 0$ is indicative of ferromagnetic correlations and negative for antiferromagnetic correlations. Despite the highly anisotropic nature of the $^3H_4$ ground state for Pr^{3+} in $Pr_2Sn_2O_7$, the main qualitative features of the diffuse scattering is captured by the nearest neighbour isotropic spin model as shown in

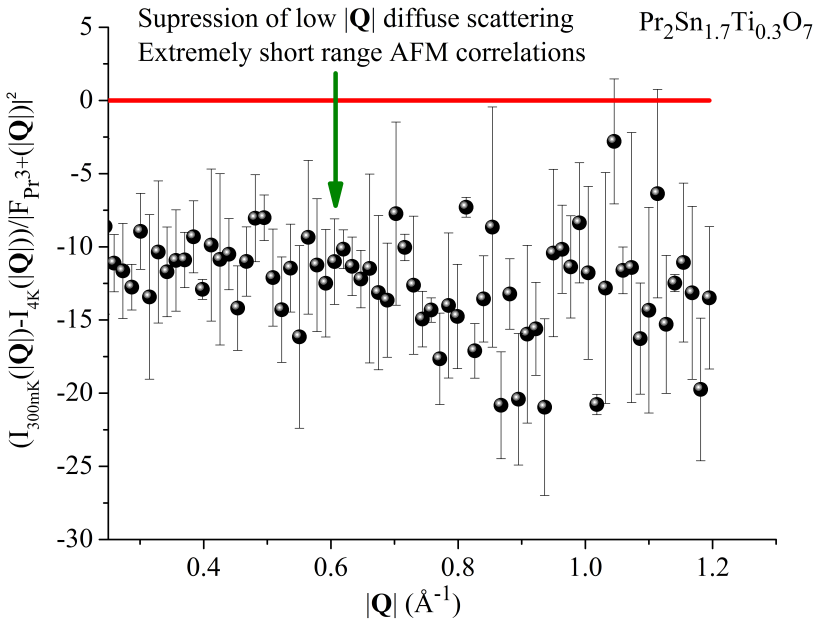

FIGURE 4.44: Background subtracted and form factor corrected low $|\mathbf{Q}|$ neutron scattering intensity at 300 mK for $Pr_2Sn_{1.7}Ti_{0.3}O_7$ collected on the high resolution C2 powder diffractometer with λ of 2.3654 Å. Zero scattering intensity is given by the red line for reference. The depletion of $|\mathbf{Q}| \to 0$ Å^{-1} diffuse scattering is indicative of the absence of FM spin correlations, confirming that $Pr_2Sn_{1.7}Ti_{0.3}O_7$ is longer in the spin ice state. The extremely broad curve implies that the AFM spin correlations are extremely short ranged, confirming the conclusions from the physical property measurements.

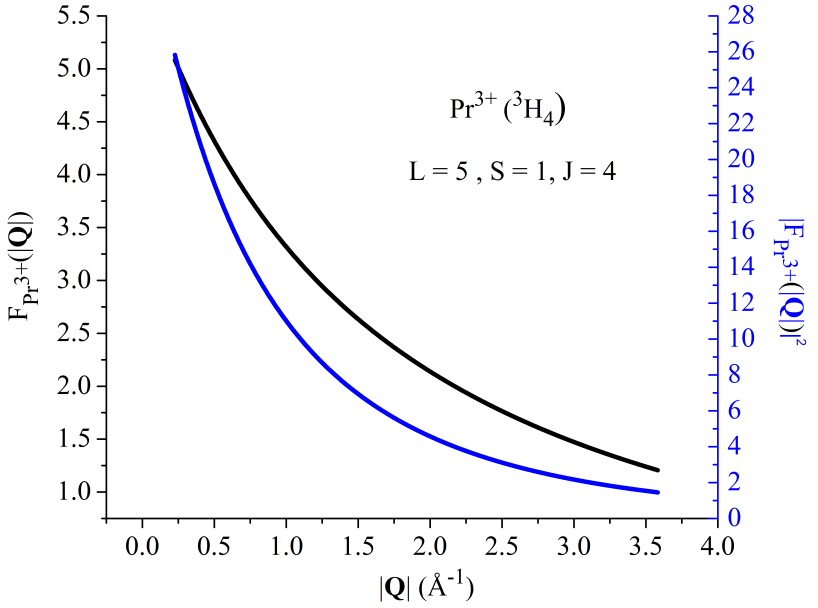

FIGURE 4.45: The calculated magnetic form factor F($|\mathbf{Q}|$) and form factor squared $|F(|\mathbf{Q}|)|^2$ for $^3H_4$ Pr^{3+} as a function of $|\mathbf{Q}|$ using parameters from Stassis *et al.* [210].

figure 4.43. The successful fit at low $\mathbf{Q}$ confirmed net ferromagnetic nearest neighbour spin-spin correlations since $\langle S_i \cdot S_j \rangle > 0$. A comparison of the diffuse scattering for both

$Ho_2Ti_2O_7$ and $Ho_2Ge_2O_7$ at T $\sim$ 50 mK in figure 4.46 with $Pr_2Sn_2O_7$ at T $\sim$ 300 mK in figure 4.43 exhibit quite similar qualitative behaviours, supporting the claim by Zhou *et al.* [31] that $Pr_2Sn_2O_7$ is indeed a spin ice. On the contrary, $Pr_2Sn_{1.7}Ti_{0.3}O_7$ exhibits an extremely broad feature (in **Q**) with a depletion of $\mathbf{Q} \to 0$ Å^{-1} intensity with the net corrected intensity being clearly negative near 0 Å^{-1}. The depletion of $|\mathbf{Q}| = 0$ scattering indicates that there is an absence of the ferromagnetic interactions in a similar finding by Gardner *et al.* for $Tb_2Ti_2O_7$ [213], thus confirming that the spin ice state is no longer present in the $Pr_2Sn_{2-x}Ti_xO_7$ members as deduced from both magnetic susceptibility and heat capacity and in agreement with the *dipolar spin ice model* [20]. Secondly, the extremely broad curve implies — *via* the interpretation that the scattering intensity is the Fourier transform of the static spin correlation function — that the spatial coherence of the AFM interactions are extremely short ranged, once again confirming the conclusions from susceptometry and heat capacity.

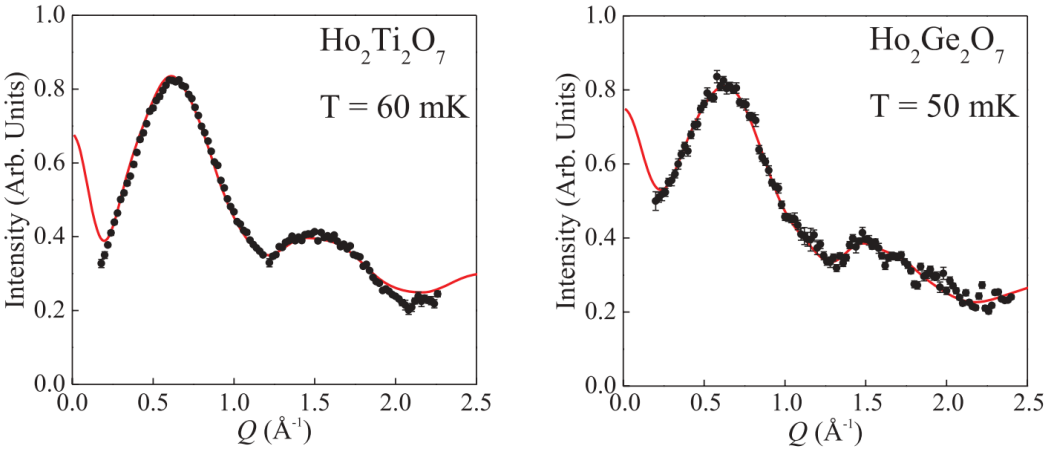

FIGURE 4.46: Experimental low **Q** neutron powder diffraction data for the spin ice materials (*left*) $Ho_2Ti_2O_7$ and (*right*) $Ho_2Ge_2O_7$ collected on the D7 diffuse scattering spectrometer at the Institut Laue-Langevin from Fennell *et al.* [81] and Hallas *et al.* [214], respectively. The measured intensity is given by the black points, a reverse Monte Carlo fit is represented by the red curve and the error bars represent an uncertainty of $\pm\sigma$. Both materials exhibit a build-up of positive scattering intensity as $\mathbf{Q} \to 0$ indicative of short range ferromagnetic correlations that are characteristic of the spin ice state.

4.5.2 Low Temperature Crystal Structure

From both DC and AC susceptometry, it is evident that no member of the $Pr_2Sn_{2-x}Ti_xO_7$ pyrochlore series forms a magnetic LRO state down to 1.8 K and subsequently confirmed by isobaric heat capacity down to 350 mK. Instead of an LRO magnetic state, it was proposed in subsection 4.4 that the members of $Pr_2Sn_{2-x}Ti_xO_7$ series assumed an intermediate magnetic state consisting of weakly coupled AFM clusters.

Effectively, the system could be considered as acting as an extremely weak cooperative paramagnet, whereby the local AFM clusters continuously fluctuate and do not order, attributed to their poor intercluster interactions. So far, the magnetic property measurements on the $Pr_2Sn_{2-x}Ti_xO_7$ members provide no explanation as to how this potential weak cooperative paramagnetic state is achieved. One possible explanation for this exotic magnetic state may be provided by once again applying the analogy between the $Pr_2Sn_{2-x}Ti_xO_7$ series and $Tb_2Ti_2O_7$, the enigmatic spin liquid. Recall that $Tb_2Ti_2O_7$, unlike its stannate counterpart, does not form any detectable LRO magnetic state down to 50 mK [215]. Instead, the titanate exhibits continuous fluctuations down to 50 mK but these fluctuations are in fact correlated, as deduced by the presence of distinct diffuse scattering measured by Gardner *et al.* [213]. As an attempt to explain how the cooperative paramagnetic state is achieved in $Tb_2Ti_2O_7$, Ruff *et al.* [216] used high precision neutron diffraction to provide evidence of the appearance Jahn-Teller cubic-to-tetragonal distortion that was concident with the onset of the development of the cooperative paramagnetic state at T $\approx$ 20 K (although this distortion has been questioned by a recent study by de Réotier *et al.* [217]). The importance of strong coupling between magnetic and lattice degrees of freedom have been shown to have dramatic effects on cubic spinel antiferromagnets such as $ZnCr_2O_4$ that exhibits a tetragonal distortion at approximately 12.5 K [218]. It has been proposed by Tchernyshyov [219] that these distortions would assist the pyrochlore lattice's frustrated AFM interactions and thus prohibit the formation of any LRO magnetic state. In order to explore such a possibility, the lattice parameters for both $Pr_2Sn_2O_7$ and $Pr_2Sn_{1.7}Ti_{0.3}O_7$ retrieved from Rietveld refinements of the powder neutron diffraction data — as shown in figures 4.47 and 4.48, respectively for 300 mK — were compared in table 4.3. The Rietveld refinement of the powder neutron diffraction profile for $Pr_2Sn_2O_7$ confirmed the presence of single phase pure $Pr_2Sn_2O_7$ possessing $Fd\bar{3}m$ symmetry with no discernible impurities, with the exception of aluminum powder lines from the aluminum sample container. The Rietveld refinement of the powder neutron diffraction profile for $Pr_2Sn_{1.7}Ti_{0.3}O_7$ confirmed the presence of $Pr_2Sn_{1.7}Ti_{0.3}O_7$ possessing $Fd\bar{3}m$ symmetry with a small unreacted SnO_2 impurity (< 1 %) in addition to the aluminum powder lines.

TABLE 4.3: Lattice parameters of $Pr_2Sn_2O_7$ and $Pr_2Sn_{1.7}Ti_{0.3}O_7$ retrieved from Rietveld refinements of room temperature powder x-ray diffraction using a $K_{\alpha_{1,2}}$ Cu source on a Siemens D5000 diffractometer and powder neutron diffraction at 4 K and 300 mK using the high resolution C2 diffractometer with λ of 2.3654 Å.

x	298 K (Å)	4 K (Å)	300 mK (Å)	$\frac{a_{298K}-a_{4K}}{a_{4K}} \times 10^4$
0.00	10.6024(3)	10.584(5)	10.588(3)	17.384(9)
0.30	10.565(3)	10.546(6)	10.542(7)	18.02(2)

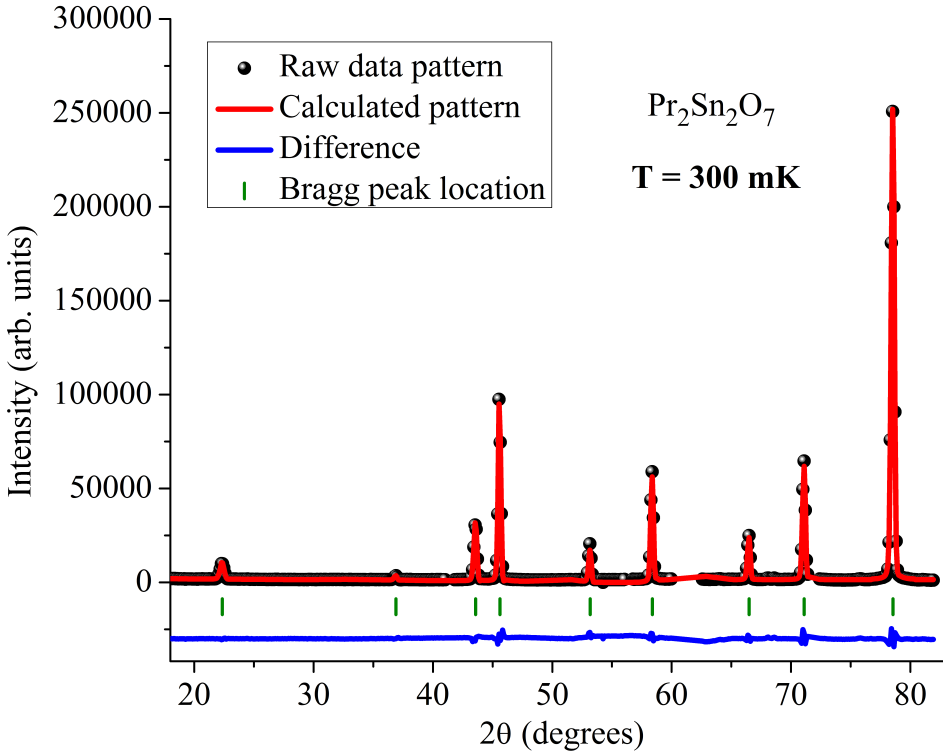

FIGURE 4.47: Measured, calculated and difference neutron powder diffraction profiles for $Pr_2Sn_2O_7$ at 300 mK collected on the C2 powder diffractometer with λ of 2.3654 Å. The measured intensity is given by the black spheres, the calculated intensity is given by the red curve and the difference is given by the blue curve. The Bragg reflections' locations are given by the olive vertical lines. The portions of the profiles containing aluminum Bragg peaks were excluded from the refinement.

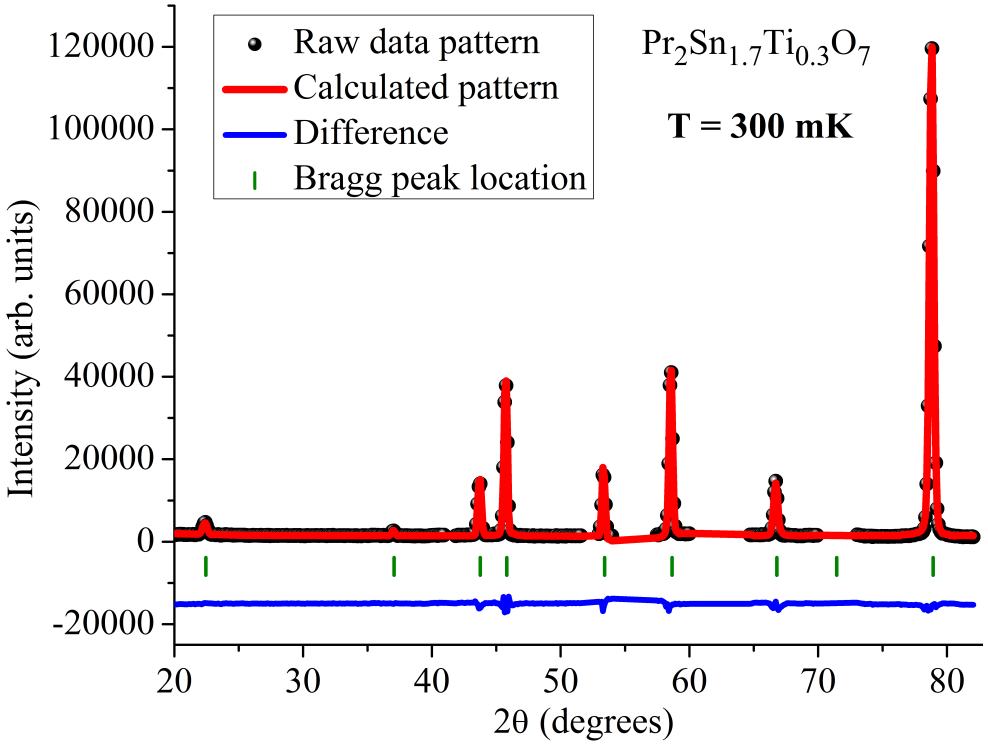

FIGURE 4.48: Measured, calculated and difference neutron powder diffraction profiles for $Pr_2Sn_{1.7}Ti_{0.3}O_7$ at 300 mK collected on the C2 powder diffractometer with λ of 2.3654 Å. The measured intensity is given by the black spheres, the calculated intensity is given by the red curve and the difference is given by the blue curve. The Bragg reflections' locations are given by the olive vertical lines. The portions of the profiles containing aluminum and unreacted SnO_2 Bragg peaks were excluded from the refinement.

The unit cell parameter for both $Pr_2Sn_2O_7$ and $Pr_2Sn_{1.7}Ti_{0.3}O_7$ exhibits normal thermal contraction from 300 K to 4 K with a value of $\frac{\Delta a}{a} \times 10^4$ of 17.384(9) and 18.02(2), respectively, which is very similar to both $Tb_2Ti_2O_7$ and $Y_2Ti_2O_7$ [216]. But, unlike the anomalous increase as the temperature is lowered in unit cell parameter as seen in $Tb_2Ti_2O_7$ by Ruff *et al.*, the lattice parameter for both $Pr_2Sn_2O_7$ and $Pr_2Sn_{1.7}Ti_{0.3}O_7$ remains unchanged (within error) between 4 K and 300 mK. This is similar to the behaviour of most pyrochlores like $Y_2Ti_2O_7$ as was seen within the same study by Ruff *et al.* [216]. In fact, for both $Pr_2Sn_2O_7$ and $Pr_2Sn_{1.7}Ti_{0.3}O_7$, there is no evidence for any structural distortion. As seen in figures 4.49 and 4.50, the distinctly structural peak (i.e. high $\mathbf{Q}$) (440) exhibits no evidence of broadening with lowering temperature as was seen in the case of $Tb_2Ti_2O_7$, thus implying no temperature dependence in spatial correlations between 4 K and 300 mK and consequently, no evidence for a structural contribution to the proposed weak cooperative parmagnetic state in the $Pr_2Sn_{2-x}Ti_xO_7$ members.

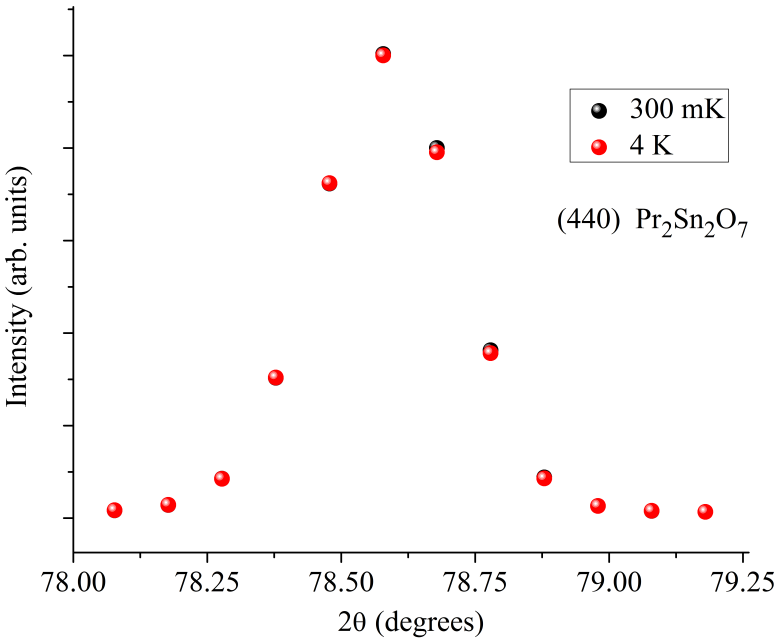

FIGURE 4.49: Comparison of the (440) neutron Bragg peak profiles measured at 300 mK and 4 K for $Pr_2Sn_2O_7$ on the high resolution C2 800-wire powder diffractometer (DUALSPEC) with a neutron wavelength λ of 2.3654 Å. The FWHM values of the (440) Bragg peak are 0.029(1) and 0.029(3) $Å^{-1}$ at 300 mK and 4 K, respectively, confirming no peak broadening and thus no structural contribution to the proposed weak cooperative parmagnetic state in $Pr_2Sn_2O_7$.

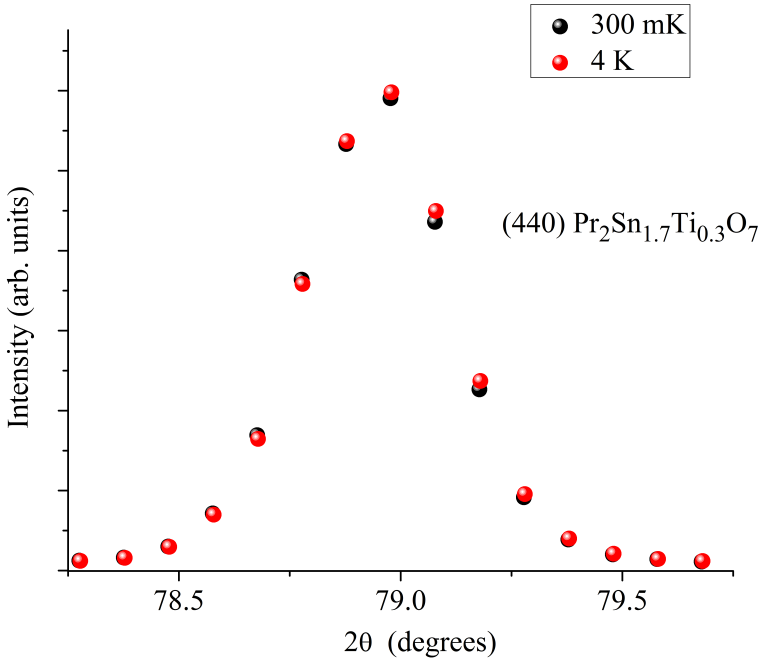

FIGURE 4.50: Comparison of the (440) neutron Bragg peak profiles measured at 300 mK and 4 K for $Pr_2Sn_{1.7}Ti_{0.3}O_7$ on the high resolution C2 800-wire powder diffractometer (DUALSPEC) with a neutron wavelength λ of 2.3654 Å. The FWHM values of the (440) Bragg peak are 0.037(2) and 0.037(6) $Å^{-1}$ at 300 mK and 4 K, respectively, confirming no peak broadening and thus no structural contribution to the proposed weak cooperative parmagnetic state in $Pr_2Sn_{1.7}Ti_{0.3}O_7$.

Chapter 5

Concluding Remarks & Future Directions

A variety of different experimental probes, from x-ray and neutron diffraction, DC and AC susceptometry and isobaric heat capacity experiments, were utilised to investigate the structural and magnetic properties of $Pr_2Sn_2O_7$ when the dynamic spin ice is perturbed. The first perturbation through the application of an external applied magnetic field was found to induce a transition from a dynamic spin ice state into a long ranged ordered antiferromagnet. The second perturbation through chemical pressure was accomplished by synthesising the new pyrochlore series $Pr_2Sn_{2-x}Ti_xO_7$ ($0.05 \leq x \leq 0.60$) *via* the substitution of Sn^{4+} by the much smaller Ti^{4+}, randomly distributed on the 16*c* Wyckoff site. The application of this *randomised* chemical pressure was found to not only suppress the formation of the spin ice state at small values of x ($x \lesssim 0.05$) but induces a highly disorded magnetic state consisting of poorly coupled antiferromagnetic spins. This intermediate magnetic state possesses little spatial coherence with short range AFM correlations down to 300 mK.

Several important questions concerning how the presence of a magnetic field influences the spin ice state were addressed with the study described in Chapter 3. The first basic result was the confirmation that the dynamic spin ice state, like the canonical spin ice state in $Ho_2Ti_2O_7$ and $Dy_2Ti_2O_7$, is extremely fragile with respect to the presence of a magnetic field, requiring only $\mu_oH \approx 0.5$ T to transition away from the spin ice state. Another important result is that the application of an external applied magnetic field induces a transition into a long ranged ordered antiferromagnetic state as predicted in the *dipolar spin ice model* by den Hertog *et al.* [20]. Both laboratory magnetic property measurements and neutron diffraction experiments indicate that the driving mechanism behind the spin ice to LRO AFM transition consists of an admixture of

non-axial $|M_J \neq \pm J\rangle$ terms in the ground state crystal field non-Kramers doublet. This driving mechanism is similar to that in $Ho_2Ru_2O_7$ as determined by Wiebe *et al.* [28], whereby the magnetic Ru^{4+}, instead of an external applied source, is the magnetic field felt by Ho^{3+} inducing the transition into an LRO AFM. The analogy to $Ho_2Ru_2O_7$ provides a clear avenue for future work. In a similar manner to Wiebe *et al.*, the proposed admixture of constituent $|M_J\rangle$ bases driving the transition into the LRO AFM state can be probed directly by inelastic powder neutron diffraction experiments under various applied magnetic fields on spectrometers such as the DCS (NCNR) or SEQUOIA (SNS) that have excellent resolution in the inelastic channel at large energy transfers. The experiment would consist of tracking the temperature-dependent $|\mathbf{Q}|$-independent (i.e. non or minimally dispersive) inelastic features as a function of applied magnetic field. If the proposed mechanism is indeed correct, the location of these inelastic features should change as a function of magnetic field. The results from the inelastic neutron scattering experiment can be further complemented by directly modelling the crystal field levels by (i) applying statistical mechanical approximations to the DC susceptibility *via* the Van Vleck formula, (ii) applying a Zeeman splitting term to the crystal field Hamiltonian and using this Hamiltonian to model the isothermal magnetisation and (iii) applying a hyperfine correction *via* a first order effective nuclear spin correction term in the Hamiltonian and once again using a Hamiltonian to model the isobaric heat capacity. All three aforementioned modelling methods are discussed by Calder *et al.* and were used to model the non-magnetic CF ground doublet in Ba_2HoSbO_6 [200]. A final unanswered question pertains to the magnetic structure of the LRO AFM state. Through representational analysis, modelling the $|\mathbf{Q}|$-integrated elastic channel from the DCS using a linear combination of basis vectors ψ_7 and ψ_8 of the irreducible representation Γ_9 of the cubic $Fd\bar{3}m$ space group, a significant XY component was detected with a significantly reduced effective Pr^{3+} moment. This significant XY component, representing a transition away from the initial Ising anisotropy in the spin ice regime, provided further experimental evidence for the admixture mechanism driving the SI-LRO AFM transition. The determination of the actual magnetic structure (i.e. the coefficients of ψ_7 and ψ_8) and the effective moment of Pr^{3+} would require a Rietveld refinement on elastic powder neutron diffraction experiment data collected on diffractometers with high $|\mathbf{Q}|$ resolution such as C2 (CNBC) in the presence of an external applied magnetic field.

The final portion of this thesis concerned the magnetic properties of the newly synthesised $Pr_2Sn_{2-x}Ti_xO_7$ pyrochlore series ($0.05 \leq x \leq 0.60$). These materials were synthesised to investigate the effects of applying *randomised* chemical pressure on the dynamic spin ice state in $Pr_2Sn_2O_7$. In particular, the substitution of Sn^{4+} by the much smaller Ti^{4+}, distributed randomly on the $16c$ Wyckoff site, was an attempt to both (i) artificially tune the $\frac{J_{NN}}{D_{NN}}$ ratio towards the vicinity of the SI-LRO AFM transition

where quantum fluctuations are strongest in the *dipolar spin ice model* [20] and (ii) to increase the magnetic monopole density beyond what is currently available, even densities present in high pressure spin ice phases such as the germanates $X_2Ge_2O_7$ (X = Dy, Ho) [32, 42, 43, 176, 220]. The study of cation substitution has been surprisngly limited (almost) exclusively to stuffing, whereby excess magnetic A-site cations reside on the 16c site. Studies by Lau *et al.* [177] and Zhou *et al.* [178] have demonstrated that the spin ice state remains intact despite large values of x. Contrarily, most studies involving the substitution of the 16c Wyckoff site used similar sized cations as an attempt to explore the effects of positional disorder on the spin ice state such as the study performed by Ke *et al.* [179]. In fact, the only study of applying *randomised* **chemical pressure** on a spin ice system by substituting a larger Sn^{4+} by the much smaller Ti^{4+} in a stannate spin ice was performed by Dalhberg *et al.* [180] in $Tb_2Sn_2O_7$. The application of chemical pressure on the terbium stannate system revealed the surprising fragility of the spin ice state with respect to doping on the B site. Dahlberg *et al.* determined that by minimal doping ($x \lesssim 0.10$), the ordered spin ice transition at T $\approx$ 900 mK was suppressed and by a value of $x \lesssim 0.20$, the $Tb_2Sn_{2-x}Ti_xO_7$ system froze into a spin glass state. The work in Chapter 4 confirmed the extreme fragility of the spin ice state in $Pr_2Sn_2O_7$ against *randomised* chemical pressure brought about by Ti^{4+} substitution, requiring only a minimal amount ($x \lesssim 0.05$) to suppress the spin ice state. In a similar manner to its terbium counterpart, magnetic property measurements provided no evidence that any member of the $Pr_2Sn_{2-x}Ti_xO_7$ pyrochlore series formed an LRO magnetic state, but even more surprising was unlike $Tb_2Sn_{2-x}Ti_xO_7$, there was no evidence of any member — even up to a value of $x \approx 0.60$ — freezing into a spin glass state down to 350 mK. Instead of an LRO magnetic state or freezing, the characteristic ferromagnetic buildup of $|\mathbf{Q}| \to 0$ diffuse scattering indicative of a spin ice state was replaced by a depletion of diffuse scattering with an extremely broad pattern at low $|\mathbf{Q}|$ indicative of extremely short ranged AFM spatial spin correlations down to 300 mK. The lack of freezing, even with extremely large amounts of titanium present (i.e. $x \approx 0.60$) is surprising for numerous reasons. Susceptometry has revealed that as the value of x increases, the magnitude of the Weiss temperature θ_{CW} increases substantially as well, implying strong exchange interactions are present and thus the system should order. Furthermore, it has been proposed by Mirebeau *et al.* [181] that the freezing in the $Tb_2Sn_{2-x}Ti_xO_7$ can be caused by the application of chemical pressure due to either (i) a modification of the $\frac{J_{NN}}{D_{NN}}$ ratio due to the lattice contraction and/or (ii) alterations of the crystal field levels' constitutent $|M_J\rangle$ bases. If the possible explanations proposed by Mirebeau *et al.* were correct, the $Pr_2Sn_{2-x}Ti_xO_7$ members — especially the highest doped member — should freeze into a spin glass state. Although the chemical disorder prohibits the $Pr_2Sn_{2-x}Ti_xO_7$ members from forming the spin ice state of its parent compound, each member in fact strongly interacts with only its nearest neighbours as

seen by the extremely broad diffuse scattering in $|\mathbf{Q}|$ space and a broad feature in the isobaric heat capacity. But not only do the spins only interact strongly with their nearest neighbours forming cluster type structures but these clusters have extremely weak intercluster interactions. Indications of such poor intercluster interactions was deduced by two experimental observations: (i) the system does not exhibit linear behaviour in the Curie-Weiss parameters until a value of $\mu_o H \approx 3$ T and (ii) the lack of a distinct nuclear Schottky anomaly in the isobaric heat capacity, characteristic of praseodymium systems [82, 198]. With such poor intercluster coupling and strong antiferromagnetic intracluster correlations, the static hyperfine field from the electronic moments seen by the nucleus will be significantly reduced and thus cause an absence of a nuclear Schottky at base temperatures. The formation of an effective paramagnet with such short AFM correlations was indeed unexpected and represents a unique energetic compromise that cannot be explained by current literature. Future studies would involve measuring AC susceptibility at much lower temperatures (i.e. in the mK range) in order to confirm the absence of a spin glass transition. Further work would consist of using neutron spectrometers such as BASIS (SNS) or HFBS (NCNR) with high quasi-elastic resolution with a large $|\mathbf{Q}|$ range to measure the extremely broad diffuse scattering in order to better characterise the proposed exotic intermediate magnetic structure.

Ultimately, the work summarised in this thesis reveals that careful attention must be taken when selecting the B-site cation residing in $16c$ Wyckoff site of the $Fd\bar{3}m$ pyrochlore structure, if one desires to have a spin ice state. With the work described in Chapter 3, it has been confirmed that the ambient magnetic field detected by the magnetic A^{3+} on the $16d$ Wyckoff site has a stark effect on the spin ice state induced a spin ice transition at very low fields ($\mu_o H \ll 1$ T). Consequently, pyrochlores containing magnetic B site cations (where A-site cation is different than the B-site cation) residing in the $16c$ Wyckoff sites, are expected not to be spin ices or if they do assume a spin ice state, it would be very close to a SI-LRO AFM transition in the *dipolar spin ice model*. Although the results in Chapter 4 provide experimental evidence for an exotic intermediate magnetic state, the suppression of the spin ice state in $Pr_2Sn_2O_7$ ultimately demonstrates the need for high pressure phases such as the germanates and the proposed silicates [221]. These high pressure phases, although still difficult to synthesise, provide uniform chemical pressure, allowing experimentalists to fine tune spin ice properties, in particular, the effective monopole density such as has been seen in the germanates [32, 42, 173, 174]. Chapter 4 confirms the experimental conclusions from Dahlberg *et al.* [180], demonstrating that *randomised* chemical pressure — despite resulting in the formation of exotic magnetic states — does not allow the pyrochlore system to retain spin ice physics, even to minute levels of chemical disorder with a much smaller dopant such as Ti^{4+}.

Appendix A

Rietveld Refinement of Room Temperature X-ray Diffraction Patterns for $Pr_2Sn_{2-x}Ti_xO_7$ Series

TABLE A.1: Refined parameters obtained from Rietveld refinements using FULLPROF suite [152] performed on room temperature x-ray diffraction patterns of $Pr_2Sn_{2-x}Ti_xO_7$ series. Room temperature diffraction patterns were collected using Bragg-Bretano geometry on a Siemens D5000 x-ray diffractometer (Cu $K_{\alpha 1,\alpha 2}$ source) at the University of Winnipeg.

Refined Parameters	x = 0	x = 0.10	x = 0.20	x = 0.30	x = 0.40	x = 0.60
a	10.6024(3)	10.589(3)	10.574(2)	10.565(3)	10.547(2)	10.523(3)
$x^{\dagger}$	0.33075(6)	0.3314(4)	0.3321(5)	0.3325(4)	0.3331(6)	0.3339(5)
χ^2	1.62	1.92	2.01	1.88	2.11	1.95
R_p	6.10	11.95	13.6	11.15	16.52	12.6
R_{wp}	7.24	13.40	16.8	13.10	19.60	15.9

† Refined variable $48f$ oxygen parameter

Appendix B

Rietveld Refinements of 300 mK and 4 K Neutron Diffraction Patterns for $Pr_2Sn_2O_7$ and $Pr_2Sn_{1.7}Ti_{0.3}O_7$ (C2 CNBC)

TABLE B.1: Refined parameters obtained from Rietveld refinements using FULLPROF suite [152] performed on neutron diffraction patterns for $Pr_2Sn_2O_7$ and $Pr_2Sn_{1.3}Ti_{0.7}O_7$ at 4 K and 300 mK collected using the high resolution C2 diffractometer (CNBC) with λ of 2.3654 Å.

Refined Parameters	x = 0 (300 mK)	x = 0 (4 K)	x = 0.30 (300 mK)	x = 0.30 (4 K)
a	10.588(3)	10.584(5)	10.542(7)	10.546(6)
x	0.3311(3)	0.3321(7)	0.3328(4)	0.3330(6)
χ^2	2.11	2.94	2.77	2.27
R_p	18.7	25.9	24.2	19.7
R_{wp}	21.3	31.5	29.8	26.7

† Refined variable $48f$ oxygen parameter

Bibliography

[1] A. Auerbach, *Interacting Electrons and Quantum Magnetism*, 2nd ed., Vol. 1 (Springer, Berlin, Germany, 1998).

[2] R. White and B. Bayne, *Quantum Theory of Magnetism*, 1st ed., Vol. 1 (Springer, Berlin, Germany, 1983).

[3] C. Kittel, *Introduction to Solid State Physics*, 8th ed. (John Wiley & Sons, Inc., New York, NY, 2004).

[4] J. Stratton, *Electromagnetic Theory*, Vol. 33 (Adams Press, New York, NY, 2007).

[5] R. Feynman, Physical Review **80**, 440 (1950).

[6] D. Griffiths, *Introduction to Quantum Mechanics*, 2nd ed. (Addison-Wesley, Boston, MA, 2004).

[7] J. Sakurai and J. Napolitano, *Modern Quantum Mechanics*, 2nd ed. (Addison-Wesley, Boston, MA, 2010).

[8] S. Clark, *Handbook of physical constants*, Vol. 97 (Geological Society of America, 1966).

[9] W. Gerlach and O. Stern, Physica **8**, 110 (1922).

[10] K. Taylor and M. Darby, *Physics of Rare Earth Solids*, 1st ed. (Chapman and Hall, New York, NY, 1972).

[11] J. Gardner, M. Gingras, and J. Greedan, Reviews of Modern Physics **82**, 53 (2010).

[12] J. Jensen and A. Mackintosh, *Rare Earth Magnetism*, 1st ed. (Clarendonr, Oxford, U.K., 1991).

[13] M. Getzlaff, *Solid State Magnetism*, 1st ed. (Springer, Berlin, Germany, 2008).

[14] P. Mohn, *Magnetism in the Solid State: An Introduction*, 2nd ed. (Springer, Berlin, Germany, 2005).

[15] A. Avella and F. Mancini, *Strongly Correlated Systems*, 1st ed., Vol. 176 (Springer, Berlin, Germany, 2013).

[16] A. West, *Solid State Chemistry and its Applications*, 2nd ed. (John Wiley & Sons, New York, NY, 2014).

[17] T. Kaplan and S. Mahanti, Europhysics Letters **87**, 17002 (2009).

[18] U. Schollwöck and R. Bishop, *Quantum Rare Earth Magnetism*, 1st ed., Vol. 645 (Springer, Berlin, Germany, 2004).

[19] M. Bieringer, *Magnetic Frustration in Transition Metal Oxides with Triangular, Tetrahedral and Square Planar Magnetic Sublattices*, Ph.D. thesis, McMaster University, Hamilton, ON (2000).

[20] B. den Hertog and M. Gingras, Physical Review Letters **84**, 3430 (2000).

[21] J. Greedan, Journal of Alloys and Compounds **408**, 444 (2006).

[22] J. Greedan, *Geometrically Frustrated Magnetic Materials*, 1st ed., Vol. 12 (John Wiley & Sons, Ltd., New York, NY, 2011).

[23] J. B. Goodenough, Journal of Physics and Chemistry of Solids **6**, 287 (1958).

[24] H. Diep, *Frustrated Spin Systems*, 1st ed., Vol. 1 (World Scientific, New York, NY, 2004).

[25] L. Girifalco, *Statistical Physics of Materials*, 1st ed., Vol. 1 (Oxford University Press, Oxford, U.K., 2003).

[26] K. Lee, J. Lee, C. Lee, and M.-H. Whangbo, Bulletin of the Korean Chemical Society **35**, 1277 (2014).

[27] L. Balents, Nature **464**, 199 (2010).

[28] C. Wiebe, J. Gardner, S.-J. Kim, G. Luke, A. Wills, B. Gaulin, J. Greedan, I. Swainson, Y. Qiu, and C. Jones, Physical Review Letters **93**, 076403 (2004).

[29] A. Ramirez, Annual Review of Materials Science **24**, 453 (1994).

[30] D. Dai and M.-H. Whangbo, The Journal of Chemical Physics **121**, 672 (2004).

[31] H. Zhou, C. Wiebe, J. Janik, L. Balicas, Y. Yo, Y. Qiu, J. Copley, and J. Gardner, Physical Review Letters **101**, 227204 (2008).

[32] H. Zhou, S. Bramwell, J. Cheng, C. Wiebe, G. Li, L. Balicas, J. Bloxsom, H. Silverstein, J. Zhou, J. Goodenough, *et al.*, Nature Communications **2**, 478 (2011).

[33] C. Schröder, H. Nojiri, J. Schnack, P. Hage, M. Luban, and P. Kögerler, Physical Review Letters **94**, 017205 (2005).

[34] K. Ross, L. Savary, B. Gaulin, and L. Balents, Physical Review X **1**, 021002 (2011).

[35] P. Anderson, Materials Research Bulletin **8**, 153 (1973).

[36] K. A. Ross, *Neutron Scattering Studies of the Quantum Spin Ice Material* $Yb_2Ti_2O_7$, Ph.D. thesis, McMaster University (2012).

[37] M. Subramanian and A. Sleight, Handbook on the Physics and Chemistry of Rare Earths **16**, 225 (1993).

[38] B. Kennedy, B. Hunter, and C. Howard, Journal of Solid State Chemistry **130**, 58 (1997).

[39] M. Subramanian, G. Aravamudan, and G. Rao, Progress in Solid State Chemistry **15**, 55 (1983).

[40] T. Hahn, *International Tables for Crystallography*, Vol. A (Springer).

[41] H. Karunadasa, Q. Huang, B. Ueland, P. Schiffer, and R. Cava, Proceedings of the National Academy of Sciences **100**, 8097 (2003).

[42] A. M. Hallas, $Ho_2Ge_2O_7$ *and* $Pr_2Zr_2O_7$*: A Tale of Two Spin Ices*, Master's thesis, University of Manitoba, Winnipeg, MB (2013).

[43] C. Wiebe and J. Greedan, Physics in Canada **68**, 103 (2012).

[44] N. Taira, M. Wakeshima, and Y. Hinatsu, Journal of Physics: Condensed Matter **11**, 6983 (1999).

[45] E. Tkachenko and P. Fedorov, Inorganic Materials **39**, S25 (2003).

[46] J. Kilner, Solid State Ionics **129**, 13 (2000).

[47] L. Minervini, R. Grimes, and K. Sickafus, Journal of the American Ceramic Society **83**, 1873 (2000).

[48] P. Wilde and C. Catlow, Solid State Ionics **112**, 173 (1998).

[49] R. Doshi, V. Richards, J. Carter, X. Wang, and M. Krumpelt, Journal of The Electrochemical Society **146**, 1273 (1999).

[50] E. Aluri and A. Grosvenor, Journal of Physics and Chemistry of Solids **74**, 830 (2013).

[51] E. Aluri and A. Grosvenor, Journal of Alloys and Compounds **616**, 516 (2014).

[52] E. Aluri, J. Hayes, J. Walker, and A. Grosvenor, Journal of Physical Chemistry C **118**, 7910 (2013).

[53] M. Hatnean, C. Decorse, M. Lees, O. Petrenko, D. Keeble, and G. Balakrishnan, Materials Research Express **1**, 026109 (2014).

[54] K. Ross, T. Proffen, H. Dabkowska, J. Quilliam, L. Yaraskavitch, J. Kycia, and B. Gaulin, Physical Review B **86**, 174424 (2012).

[55] J. Greedan, Materials Research Bulletin **14**, 13 (1979).

[56] A. Poole, A. Wills, and E. Lelievre-Berna, Journal of Physics: Condensed Matter **19**, 452201 (2007).

[57] S. Petit, P. Bonville, I. Mirebeau, H. Mutka, and J. Robert, Physical Review B **85**, 54428 (2012).

[58] J. Reimers, J. Greedan, and M. Sato, Journal of Solid State Chemistry **72**, 390 (1988).

[59] R. Flint and T. Senthil, Physical Review B **87**, 125147 (2013).

[60] Y. Tokiwa, J. Ishikawa, S. Nakatsuji, and P. Gegenwart, Nature Materials **13**, 356 (2014).

[61] S. Bramwell, M. Harris, B. Den Hertog, M. Gingras, J. Gardner, D. McMorrow, A. Wildes, A. Cornelius, J. Champion, R. Melko, *et al.*, Physical Review Letters **87**, 047205 (2001).

[62] M. Harris, S. Bramwell, D. McMorrow, T. Zeiske, and K. Godfrey, Physical Review Letters **79**, 2554 (1997).

[63] S. Bramwell and M. Gingras, Science **294**, 1495 (2001).

[64] W. Giauque and J. Stout, Journal of the American Chemical Society **58**, 1144 (1936).

[65] P. Debye, Annalen der Physik **39**, 789 (1912).

[66] L. Pauling, Journal of the American Chemical Society **57**, 2680 (1935).

[67] J. Bernal and R. Fowler, Journal of Chemical Physics **1**, 515 (1933).

[68] S. Bramwell, Annual Reports Section A **96**, 505 (2000).

[69] D. Bitko, T. Rosenbaum, and G. Aeppli, Physical Review Letters **77**, 940 (1996).

[70] J. Friedman, M. Sarachik, J. Tejada, and R. Ziolo, Physical Review Letters **76**, 3830 (1996).

[71] J. Champion, S. Bramwell, P. Holdsworth, and M. Harris, Europhysics Letters **57**, 93 (2002).

[72] S. Bramwell and M. Gingras, Science **294**, 1495 (2001).

[73] H. Van Kempen, A. Miedema, and W. Huiskamp, Physica **30**, 229 (1964).

[74] R. Siddharthan, B. Shastry, A. Ramirez, and A. Hayashi, Physical Review Letters **83**, 1854 (1999).

[75] A. Ramirez, A. Hayashi, R. Cava, R. Siddharthan, and B. Shastry, Nature **399**, 333 (1999).

[76] R. Bauminger, S. Cohen, A. Marinov, and S. Ofer, Physical Review Letters **6**, 467 (1961).

[77] H. Blöte, R. Wielinga, and W. Huiskamp, Physica **43**, 549 (1969).

[78] M. Kanada, Y. Yasui, Y. Kondo, S. Iikubo, M. Ito, H. Harashina, M. Sato, H. Okumura, K. Kakurai, and H. Kadowaki, Journal of the Physical Society of Japan **71**, 313 (2002).

[79] M. Shores, E. Nytko, B. Bartlett, and D. Nocera, Journal of the american chemical society **127**, 13462 (2005).

[80] K. Matsuhira, Y. Hinatsu, and T. Sakakibara, Journal of Physics: Condensed Matter **13**, L737 (2001).

[81] T. Fennell, P. Deen, A. Wildes, K. Schmalzl, D. Prabhakaran, A. Boothroyd, R. Aldus, D. McMorrow, and S. Bramwell, Science **326**, 415 (2009).

[82] K. Kimura, S. Nakatsuji, J. Wen, C. Broholm, M. Stone, E. Nishibori, and H. Sawa, Nature Communications **4** (2013).

[83] S. Rosenkranz, A. Ramirez, A. Hayashi, R. Cava, R. Siddharthan, and B. Shastry, Journal of Applied Physics **87**, 5914 (2000).

[84] K. Matsuhira, Y. Hinatsu, K. Tenya, and T. Sakakibara, Journal of Physics: Condensed Matter **12**, L649 (2000).

[85] D. Byström, *Ground State Order in Spin Ice Without Long-Range Interactions*, Master's thesis, Royal Institute of Technology, Stockholm, Sweden (2013).

[86] M. Omar, *Elementary Solid State Physics: Principles and Applications*, 1st ed., Vol. 1 (Addison-Wesley, Boston, MA, 1993).

[87] R. Melko and M. Gingras, Journal of Physics: Condensed Matter **16**, R1277 (2004).

[88] R. Shannon, Acta Crystallographica Section A: Crystal Physics, Diffraction, Theoretical and General Crystallography **32**, 751 (1976).

[89] J. Shackelford and M. Clode, *Introduction to Materials Science for Engineers*, 8th ed., Vol. 1 (Pearson/Prentice Hall, Upper Sadder River, NJ, 2014).

[90] G. Bacon, *Neutron Diffraction*, 1st ed., Vol. 1 (Clarendon, Oxford, U.K., 1955).

[91] A. Hall, Notes and Records of the Royal Society of London **44**, 13 (1990).

[92] T. Young, Philosophical transactions of the Royal Society of London , 12 (1802).

[93] F. Selleri, *Wave-Particle Duality*, 2nd ed., Vol. 1 (Springer, Berlin, Germany, 2012).

[94] C. Hammond and C. Hammond, *The Basics of Crystallography and Diffraction*, 3rd ed., Vol. 1 (Oxford University Press Oxford, Oxford, U.K., 2009).

[95] W. Bragg, Nature **90**, 410 (1912).

[96] M. Born and E. Wolf, *Principles of Optics: Electromagnetic Theory of Propagation, Interference and Diffraction of Light*, 7th ed., Vol. 1 (Cambridge University Press, Cambridge, U.K., 1999).

[97] B. Warren, *X-ray Diffraction*, 1st ed., Vol. 1 (Courier Corporation, New York, NY, 1969).

[98] P. Ewald, Proceedings of the Physical Society **52**, 167 (1940).

[99] C. R. Wiebe, *Studies of Magnetism in Rhenium and Manganese Based Perovskite Oxides*, Ph.D. thesis (2002).

[100] W. Röntgen, Science **3**, 227 (1896).

[101] D. Moore and R. Reynolds, *X-ray Diffraction and the Identification and Analysis of Clay Minerals*, 2nd ed., Vol. 1 (Oxford university press Oxford, Oxford, U.K., 1999).

[102] J. Stangl, C. Mocuta, V. Chamard, and D. Carbone, *Nanobeam X-Ray Scattering: Probing Matter at the Nanoscale*, 1st ed., Vol. 4 (Wiley-VCH, Weinheim, Germany, 2013).

[103] R. Hill and C. Howard, Journal of Applied Crystallography **20**, 467 (1987).

[104] H. Klug, L. Alexander, *et al.*, *X-ray Diffraction Procedures*, 2nd ed., Vol. 1 (Wiley-Interscience, New York, NY, 1974).

[105] Q. Shen, Physical Review Letters **80**, 3268 (1998).

[106] L. d. Broglie, Philosophical Magazine Series 6 **47**, 446 (1924).

[107] M. Fagen, A. Joel, S. Millman, and G. Schindler, *A History of Engineering and Science in the Bell System: Physical Sciences (1925-1980)*, 1st ed., Vol. 4 (Bell Telephone Laboratories, Murray Hill, NJ, 1983).

[108] C. Shull, W. Strauser, and E. Wollan, Physical Review **83**, 333 (1951).

[109] B. Brockhouse, T. Arase, G. Caglioti, M. Sakamoto, R. Sinclair, and A. Woods, IAEA, Vienna **113** (1961).

[110] Y. Izyumov, *Magnetic Neutron Diffraction*, 1st ed., Vol. 1 (Springer Science & Business Media, Berlin, Germany, 2012).

[111] G. Squires, *Introduction to the Theory of Thermal Neutron Scattering*, 3rd ed., Vol. 1 (Cambridge University Press, Cambridge, U.K., 2012).

[112] V. Sears, Neutron News **3**, 26 (1992).

[113] M. Hillery, Physical Review A **24**, 933 (1981).

[114] M. Das, *Condensed Matter: New Research*, 1st ed., Vol. 1 (Nova Publishers, New York, N.Y., 2007).

[115] O. Halpern and M. Johnson, Physical Review **55**, 898 (1939).

[116] T. Egami and S. Billinge, *Underneath the Bragg peaks: Structural Analysis of Complex Materials*, 1st ed., Vol. 16 (Pergamon, Oxford, U.K., 2003).

[117] H. Rietveld, Journal of Applied Crystallography **2**, 65 (1969).

[118] W. Yinghua, Journal of Applied Crystallography **20**, 258 (1987).

[119] G. Caglioti, A. Paoletti, and F. Ricci, Nuclear Instruments **3**, 223 (1958).

[120] L. McCusker, R. Von Dreele, D. Cox, D. Louer, and P. Scardi, Journal of Applied Crystallography **32**, 36 (1999).

[121] B. Cullity and C. Graham, *Introduction to Magnetic Materials*, 2nd ed., Vol. 1 (Wiley-IEEE Press, New York, NY, 2008).

[122] S. Blundell, *Magnetism in Condensed Matter*, 1st ed., Vol. 1 (Oxford University Press, Oxford, U.K., 2001).

[123] A. Muxworthy, Earth and Planetary Science Letters **169**, 51 (1999).

[124] H. Weinstock, IEEE Transactions on Magnetics **27**, 3231 (1991).

[125] B. Josephson, Physics Letters **1**, 251 (1962).

[126] J. Clarke and A. Braginski, *The SQUID Handbook: Fundamentals and Technology of SQUIDs and SQUID Systems*, Vol. 1 (John Wiley & Sons, 2005).

[127] M. Sawicki, W. Stefanowicz, and A. Ney, Semiconductor Science and Technology **26**, 064006 (2011).

[128] *Physical Property Measurement System: Vibrating Sample Magnetometer (VSM) Option Users Manual*, Quantum Design Inc., San Diego, CA, 1st ed. (2004).

[129] *PPMS Heat Capacity Option Users Manual*, Quantum Design Inc., San Diego, CA, 1st ed. (2009).

[130] *Magnetic Property Measurement Systems: MPMS-XL User Manual*, Quantum Design Ltd., San Diego, CA, 1st ed. (2002).

[131] D. Bruce, D. O'Hare, and R. Walton, *Molecular Materials*, Vol. 14 (John Wiley & Sons, 2011).

[132] J. Snyder, B. Ueland, A. Mizel, J. Slusky, H. Karunadasa, R. Cava, and P. Schiffer, Physical Review B **70**, 184431 (2004).

[133] V. Peikov, K. Jeon, and A. Lane, Journal of Magnetism and Magnetic Materials **193**, 307 (1999).

[134] T. Francavilla, R. Hein, and D. Liebenberg, *Magnetic Susceptibility of Superconductors and Other Spin Systems* (Springer US, 2013).

[135] H. Buchdahl, *The Concepts of Classical Thermodynamics*, 1st ed., Vol. 1 (Cambridge University Press, Cambridge, U.K., 2009).

[136] A. Münster, *Classical Thermodynamics*, 1st ed., Vol. 1 (John Wiley & Sons, Hoboken, NJ, 1970).

[137] J. Waldram, *The Theory of Thermodynamics*, 1st ed., Vol. 1 (Cambridge University Press, Cambridge, U.K., 1985).

[138] T. Hill, *An Introduction to Statistical Thermodynamics*, 1st ed., Vol. 1 (Dover Publications, New York, NY, 1987).

[139] B. Roy, *Fundamentals of Classical and Statistical Thermodynamics*, 1st ed., Vol. 1 (John Wiley & Sons, Hoboken, NJ, 2002).

[140] H. Stanley, *Introduction to Phase Transitions and Critical Phenomena*, 1st ed., Vol. 1 (Oxford University Press, New York, NY, 1987).

[141] A. Cooke, T. Thorp, and M. Wells, Proceedings of the Physical Society **92**, 400 (1967).

[142] J. Lashley, M. Hundley, A. Migliori, J. Sarrao, P. Pagliuso, T. Darling, M. Jaime, J. Cooley, W. Hults, L. Morales, *et al.*, Cryogenics **43**, 369 (2003).

[143] H. Fukazawa, R. Melko, R. Higashinaka, Y. Maeno, and M. Gingras, Physical Review B **65**, 054410 (2002).

[144] H. Zhou, J. Cheng, A. Hallas, C. Wiebe, G. Li, L. Balicas, J. Zhou, J. Goodenough, J. Gardner, and E. Choi, Physical Review Letters **108**, 207206 (2012).

[145] P. Bonville, I. Mirebeau, A. Gukasov, S. Petit, and J. Robert, Journal of Physics: Conference Series **320**, 012006 (2011).

[146] S. Rosenkranz, A. P. Ramirez, A. Hayashi, R. J. Cava, R. Siddharthan, and B. S. Shastry, Journal of Applied Physics **87**, 5914 (2000).

[147] K. Stevens, Proceedings of the Physical Society. Section A **65**, 209 (1952).

[148] K. Fritsch, E. Kermarrec, K. Ross, Y. Qiu, J. Copley, D. Pomaranski, J. Kycia, H. Dabkowska, and B. Gaulin, Physical Review B **90**, 014429 (2014).

[149] A. Princep, D. Prabhakaran, A. Boothroyd, and D. Adroja, Physical Review B **88**, 104421 (2013).

[150] H. Molavian, M. Gingras, and B. Canals, Physical Review Letters **98**, 157204 (2007).

[151] H. Zhou, S. Bramwell, J. Cheng, C. Wiebe, G. Li, L. Balicas, J. Bloxsom, H. Silverstein, J. Zhou, J. Goodenough, *et al.*, Nature Communications **2**, 478 (2011).

[152] J. Rodríguez-Carvajal, Physica B: Condensed Matter **192**, 55 (1993).

[153] B. Kennedy, Journal of Solid State Chemistry **123**, 14 (1996).

[154] B. Kennedy, Materials Research Bulletin **32**, 479 (1997).

[155] I. Mirebeau, A. Apeteri, J. Rodriguez-Carvajal, P. Bonville, A. Forget, D. Colson, V. Glazkov, J. Sanchez, O. Isnard, and E. Suard, arXiv preprint cond-mat/0503377 (2005).

[156] Z. Avanaki and A. Hassanzadeh, Journal of Theoretical and Applied Physics **7**, 1 (2013).

[157] B. Holmström, A. Anderson, and M. Krusius, Physical Review **188**, 888 (1969).

[158] J. Kondo, Journal of the Physical Society of Japan **16**, 1690 (1961).

[159] B. Bleaney, Journal of Applied Physics **34**, 1024 (1963).

[160] K. Ross, J. Ruff, C. Adams, J. Gardner, H. Dabkowska, Y. Qiu, J. Copley, and B. Gaulin, Physical Review Letters **103**, 227202 (2009).

[161] I. Makhfudz, Physical Review B **89**, 024401 (2014).

[162] L. Chang, Y. Su, Y.-J. Kao, Y. Chou, R. Mittal, H. Schneider, T. Brückel, G. Balakrishnan, and M. Lees, Physical Review B **82**, 172403 (2010).

[163] J. Copley and J. Cook, Physica B: Condensed Matter **283**, 386 (2000).

[164] J. Copley and J. Cook, Chemical Physics **292**, 477 (2003).

[165] T. Fennell, O. Petrenko, B. Fåk, J. Gardner, S. Bramwell, and B. Ouladdiaf, Physical Review B **72**, 224411 (2005).

[166] S.-i. Yoshida, K. Nemoto, and K. Wada, Journal of the Physical Society of Japan **73**, 1619 (2004).

[167] J. Snyder, J. Slusky, R. Cava, and P. Schiffer, Nature **413**, 48 (2001).

[168] H. Fukazawa, R. Melko, R. Higashinaka, Y. Maeno, and M. Gingras, Physical Review B **65**, 054410 (2002).

[169] K. Tomiyasu, K. Matsuhira, K. Iwasa, M. Watahiki, S. Takagi, M. Wakeshima, Y. Hinatsu, M. Yokoyama, K. Ohoyama, and K. Yamada, Journal of the Physical Society of Japan **81** (2012).

[170] A. Wills, Journal of Materials Chemistry **15**, 245 (2005).

[171] A. Poole, E. Lelievre-Berna, and A. Wills, Physica B: Condensed Matter **404**, 2535 (2009).

[172] K. Tomiyasu, H. Suzuki, M. Toki, S. Itoh, M. Matsuura, N. Aso, and K. Yamada, Physical Review Letters **101**, 177401 (2008).

[173] S. Bramwell, S. Giblin, S. Calder, R. Aldus, D. Prabhakaran, and T. Fennell, Nature **461**, 956 (2009).

[174] T. Fennell, P. Deen, A. Wildes, K. Schmalzl, D. Prabhakaran, A. Boothroyd, R. Aldus, D. McMorrow, and S. Bramwell, Science **326**, 415 (2009).

[175] Y. Smolin, Soviet Physics — Crystallography **15**, 36 (1970).

[176] C. Wiebe and A. Hallas, APL Materials **3**, 041519 (2015).

[177] G. Lau, R. Freitas, B. Ueland, B. Muegge, E. Duncan, P. Schiffer, and R. Cava, Nature Physics **2**, 249 (2006).

[178] H. Zhou, C. Wiebe, Y. Jo, L. Balicas, Y. Qiu, J. Copley, G. Ehlers, P. Fouquet, and J. Gardner, Journal of Physics: Condensed Matter **19**, 342201 (2007).

[179] X. Ke, B. Ueland, D. West, M. Dahlberg, R. Cava, and P. Schiffer, Physical Review B **76**, 214413 (2007).

[180] M. Dahlberg, M. Matthews, P. Jiramongkolchai, R. Cava, and P. Schiffer, Physical Review B **83**, 140410 (2011).

[181] I. Mirebeau, A. Apetrei, J. Rodriguez-Carvajal, P. Bonville, A. Forget, D. Colson, V. Glazkov, J. Sanchez, O. Isnard, and E. Suard, Physical Review Letters **94**, 246402 (2005).

[182] K. Yamada, K. Kakurai, Y. Endoh, T. Thurston, M. Kastner, R. Birgeneau, G. Shirane, Y. Hidaka, and T. Murakami, Physical Review B **40**, 4557 (1989).

[183] L. Smart and E. Moore, *Solid State Chemistry: An Introduction*, 3rd ed. (CRC press: Taylor & Francis Group, Boca Raton, FL, 2012).

[184] A. M. Hallas, A. M. Arevalo-Lopez, A. Z. Sharma, T. Munsie, J. P. Attfield, C. R. Wiebe, and G. M. Luke, Phys. Rev. B **91**, 104417 (2015).

[185] L. Balents, Nature **464**, 199 (2010).

[186] S. Zouari, R. Ballou, A. Cheikhrouhou, and P. Strobel, Journal of Alloys and Compounds **476**, 43 (2009).

[187] M. Tachibana, Y. Kohama, T. Atake, and E. Takayama-Muromachi, Journal of Applied Physics **101**, 09D502 (2007).

[188] M. Brik and A. Srivastava, Journal of the American Ceramic Society **95**, 1454 (2012).

[189] A. Hallas, Private Communication (2015).

[190] A. Denton and N. Ashcroft, Physical Review A **43**, 3161 (1991).

[191] S. Patwe, V. Katari, N. Salke, S. Deshpande, R. Rao, M. Gupta, R. Mittal, S. Achary, and A. Tyagi, Journal of Materials Chemistry C **3**, 4570 (2015).

[192] K. Matsuhira, Y. Hinatsu, K. Tenya, H. Amitsuka, and T. Sakakibara, Journal of the Physical Society of Japan **71**, 1576 (2002).

[193] I. Mirebeau, A. Apetrei, I. Goncharenko, and R. Moessner, Physica B: Condensed Matter **385**, 307 (2006).

[194] P. De Réotier, A. Yaouanc, L. Keller, A. Cervellino, B. Roessli, C. Baines, A. Forget, C. Vaju, P. Gubbens, A. Amato, *et al.*, Physical Review Letters **96**, 127202 (2006).

[195] F. Bert, P. Mendels, A. Olariu, N. Blanchard, G. Collin, A. Amato, C. Baines, and A. Hillier, Physical Review Letters **97**, 117203 (2006).

[196] J. van Duijn, K. Kim, N. Hur, D. Adroja, F. Bridges, A. Daoud-Aladine, F. Fernandez-Alonso, R. Ruiz-Bustos, J. Wen, V. Kearney, *et al.*, arXiv preprint arXiv:1407.0661 (2014).

[197] S. Dunsiger, R. Kiefl, K. Chow, B. Gaulin, M. Gingras, J. Greedan, A. Keren, K. Kojima, G. Luke, W. MacFarlane, *et al.*, Physical Review B **54**, 9019 (1996).

[198] O. Lounasmaa, Physical Review **133**, A211 (1964).

[199] E. Granado, J. Lynn, R. Jardim, and M. Torikachvili, Physical Review Letters **110**, 017202 (2013).

[200] S. Calder, X. Ke, F. Bert, A. Amato, C. Baines, C. Carboni, R. Cava, A. Daoud-Aladine, P. Deen, T. Fennell, *et al.*, Physical Review B **81**, 064425 (2010).

[201] R. DOrtenzio, H. Dabkowska, S. Dunsiger, B. Gaulin, M. Gingras, T. Goko, J. Kycia, L. Liu, T. Medina, T. Munsie, *et al.*, Physical Review B **88**, 134428 (2013).

[202] S. Bramwell and M. Gingras, Science **294**, 1495 (2001).

[203] J. Hodges, P. Bonville, A. Forget, M. Rams, K. Królas, and G. Dhalenne, Journal of Physics: Condensed Matter **13**, 9301 (2001).

[204] J. Hodges, P. Bonville, A. Forget, A. Yaouanc, P. De Réotier, G. André, M. Rams, K. Królas, C. Ritter, P. Gubbens, *et al.*, Physical Review Letters **88**, 077204 (2002).

[205] Y. Yasui, M. Soda, M. S. M. Iikubo, S.and Ito, N. Hamaguchi, T. Matsushita, N. Wada, T. Takeuchi, N. Aso, *et al.*, Journal of the Physical Society of Japan **72**, 3014 (2003).

[206] J. Gardner, G. Ehlers, N. Rosov, R. Erwin, and C. Petrovic, Physical Review B **70**, 180404 (2004).

[207] L.-J. Chang, M. Lees, I. Watanabe, A. Hillier, Y. Yasui, and S. Onoda, Physical Review B **89**, 184416 (2014).

[208] Z. Dun, E. Choi, H. Zhou, A. Hallas, H. Silverstein, Y. Qiu, J. Copley, J. Gardner, and C. Wiebe, Physical Review B **87**, 134408 (2013).

[209] M. Potter, H. Fritzsche, D. Ryan, and L. Cranswick, Journal of Applied Crystallography **40**, 489 (2007).

[210] C. Stassis, H. Deckman, B. Harmon, J. Desclaux, and A. Freeman, Physical Review B **15**, 369 (1977).

[211] H. Kadowaki, Y. Ishii, K. Matsuhira, and Y. Hinatsu, Physical Review B **65**, 144421 (2002).

[212] E. Bertaut and P. Burlet, Solid State Communications **5**, 279 (1967).

[213] J. Gardner, A. Keren, G. Ehlers, C. Stock, E. Segal, J. Roper, B. Fåk, M. Stone, P. Hammar, D. Reich, *et al.*, Physical Review B **68**, 180401 (2003).

[214] A. Hallas, J. Paddison, H. Silverstein, A. Goodwin, J. Stewart, A. Wildes, J. Cheng, J. Zhou, J. Goodenough, E. Choi, *et al.*, Physical Review B **86**, 134431 (2012).

[215] J. Gardner, B. Gaulin, A. Berlinsky, P. Waldron, S. Dunsiger, N. Raju, and J. Greedan, Physical Review B **64**, 224416 (2001).

[216] J. Ruff, B. Gaulin, J. Castellan, K. Rule, J. Clancy, J. Rodriguez, and H. Dabkowska, Physical Review Letters **99**, 237202 (2007).

[217] P. de Réotier, A. Yaouanc, A. Bertin, C. Marin, S. Vanishri, D. Sheptyakov, A. Cervellino, B. Roessli, and C. Baines, Journal of Physics: Conference Series **551**, 012021 (2014).

[218] S.-H. Lee, C. Broholm, W. Ratcliff, G. Gasparovic, Q. Huang, T. Kim, and S.-W. Cheong, Nature **418**, 856 (2002).

[219] O. Tchernyshyov, R. Moessner, and S. Sondhi, Physical Review B **66**, 064403 (2002).

[220] Z. Dun, M. Lee, E. Choi, A. Hallas, C. Wiebe, J. Gardner, E. Arrighi, R. Freitas, A. Arevalo-Lopez, J. Attfield, *et al.*, Physical Review B **89**, 064401 (2014).

[221] A. Reid, C. Li, and A. Ringwood, Journal of Solid State Chemistry **20**, 219 (1977).